

## ABSTRACT

Title of Dissertation:       MODELING AND TESTING OF ETHERNET  
TRANSFORMERS

David Bowen, Doctor of Philosophy, 2011

Dissertation directed by:   Professor Isaak D. Mayergoyz

Department of Electrical and Computer Engineering

Twisted-pair Ethernet is now the standard home and office last-mile network technology. For decades, the IEEE standard that defines Ethernet has required electrical isolation between the twisted pair cable and the Ethernet device. So, for decades, every Ethernet interface has used magnetic core Ethernet transformers to isolate Ethernet devices and keep users safe in the event of a potentially dangerous fault on the network media. The current state-of-the-art Ethernet transformers are miniature (<5mm diameter) ferrite-core toroids wrapped with approximately 10 to 30 turns of wire. As small as current Ethernet transformers are, they still limit further Ethernet device miniaturization and require a separate bulky package or jack housing. New coupler designs must be explored which are capable of exceptional miniaturization or on-chip fabrication.

This dissertation thoroughly explores the performance of the current commercial Ethernet transformers to both increase understanding of the device's behavior and outline performance parameters for replacement devices. Lumped element and distributed circuit models are derived; testing schemes are developed and used to extract model parameters from commercial Ethernet devices. Transfer relation measurements of the commercial Ethernet transformers are compared against the model's behavior and it is found that the tuned, distributed models produce the best transfer relation match to the measured data.

Process descriptions and testing results on fabricated thin-film dielectric-core toroid transformers are presented. The best results were found for a 32-turn transformer loaded with  $100\Omega$ , the impedance of twisted pair cable. This transformer gave a flat response from about 10MHz to 40MHz with a height of approximately 0.45. For the fabricated transformer structures, theoretical methods to determine resistance, capacitance and inductance are presented. A special analytical and numerical analysis of the fabricated transformer inductance is presented. Planar cuts of magnetic slope fields around the dielectric-core toroid are shown that describe the effect of core height and winding density on flux uniformity without a magnetic core.

# MODELING AND TESTING OF ETHERNET TRANSFORMERS

By

David Bowen

Dissertation submitted to the Faculty of the Graduate School of the  
University of Maryland, College Park in partial fulfillment  
of the requirements for the degree of  
Doctor of Philosophy  
2011

## Advisory Committee:

Professor Isaak D. Mayergoyz, Chair  
Professor Reza Ghodssi  
Professor Thomas E. Murphy  
Professor Robert Newcomb  
Professor Mario Dagenais  
Professor A. Udaya Shankar, Dean's Representative

©Copyright by  
David Bowen  
2011

## Acknowledgements

I have had the enriching opportunity to work with many people on multiple research projects during my time at the University of Maryland. I would first like to acknowledge the long standing support of my research advisor, Professor Isaak Mayergoyz. Our many project discussions and debates over the years have been invaluable educational and have served to significantly improve my technical communication. I am also indebted to Professor Mayergoyz on his insistence of my academic enrichment, involving me with the administration of his power electronics courses as well as multiple areas of research, but also strongly supporting my coursework.

I would like to thank Dr. Charles Krafft of the Laboratory for Physical Sciences for his material and intellectual support of all of the research projects on which I have been involved. Dr. Krafft has taught me much about the practical aspects of research, both in and outside an academic environment. I would also like to acknowledge a fellow graduate student, Sergiy Tkachuck, with which I have worked and collaborated for my entire time at the university. Also, Professor Reza Ghodssi and his student Mustafa Beyaz were instrumental in determining the approach to the fabrication aspect of the project. Also, thanks to Professor Tom Murphy for his advice and feedback along the way.

I also wish to acknowledge the support of many of the staff at the Laboratory for Physical Sciences. I would like to thank Steve Brown for his initial support and orientation during the start-up of fabrication. I would also like to thank Dan Hinkel and Warren Burke for their continued support and advice throughout fabrication. Thanks to Paul Kolb for his assistance in

device FEA computations, as well as Ben Palmer and Bill Johnson for their assistance in circuit board design and network analyzer measurements. Thanks also to Chris Richardson for his advice on mask drawing, and the LPS management for supporting the project. I would also like to express my general gratitude to everyone at LPS from which I have borrowed equipment.

Finally, I would like to thank my family for their support over my many years of higher education. Special thanks to my fiancé, Ann, for her support and understanding of my erratic schedule over the past year.

## Table of Contents

LIST OF PUBLICATIONS .....	viii
LIST OF TABLES .....	ix
LIST OF FIGURES .....	x
Chapter 1 : Introduction .....	1
1.1 Introduction .....	1
Chapter 2 : Electrical isolation and signal modes .....	1
2.1. Introduction .....	1
2.2. Signal Modes.....	2
Chapter 3 : Transformers: Design and operation.....	8
3.1. Magnetic coupling, transformer theory, and the ideal transformer.....	8
3.2 The real transformer: Description and lumped equivalent circuit.....	14
3.2.1 Real transformer lumped equivalent circuit model: Frequency domain.....	16
3.2.2 Losses in magnetic core materials .....	22
3.2.2.1 Hysteresis loss .....	23
3.2.2.2 Eddy current loss .....	28
3.2.3 Alternate derivation of lumped element transformer model.....	36
3.2.4 Capacitances in the transformer lumped equivalent circuit model.....	42
Chapter 4 : Characterization of lumped parameters and ferrites .....	46
4.1 Classic transformer tests.....	46
4.1.1 Classic short circuit test .....	46
4.1.2 Classic open circuit test .....	49
4.1.3 DC resistance test.....	52
4.2 Novel high frequency transformer tests .....	53
4.2.1. Quasi-short circuit test (QSCT) .....	53
4.2.2. Quasi-open circuit test (QOCT).....	56
4.2.3. Measured transfer characteristics.....	64
Chapter 5 : Modeling with distributed parameters .....	68
5.1. Distributed analysis introduction .....	68
5.2. Differential mode .....	69

5.2.1.	Differential-mode distributed model analysis.....	70
5.3.	Common-mode model.....	88
5.3.1.	Common mode distributed model analysis.....	90
5.4.	Summary .....	102
Chapter 6 :	Testing of commercial Ethernet transformers.....	103
6.1.	Introduction .....	103
6.2.	Differential-mode Ethernet transformer testing.....	105
6.2.1.	1GBase-T Ethernet transformer.....	112
6.2.1.1.	Transfer relation .....	112
6.2.1.2.	Mutual inductance .....	114
6.2.1.3.	Leakage inductance .....	115
6.2.1.4.	Line resistance .....	116
6.2.1.5.	Core loss resistance .....	117
6.2.2.	10GBase-T Ethernet transformer.....	118
6.2.2.1.	Differential-mode transfer relation.....	119
6.2.2.2.	Mutual inductance .....	120
6.2.2.3.	Leakage inductance .....	121
6.2.2.4.	Line resistance .....	121
6.2.2.5.	Core loss resistance .....	122
6.2.3.	Large PVC-core transformer.....	124
6.2.3.1.	Differential-mode transfer relation.....	126
6.2.3.2.	Mutual inductance .....	127
6.2.3.3.	Leakage inductance .....	128
6.2.3.4.	Line resistance .....	129
6.2.3.5.	Core loss resistance .....	130
6.3.	Common-mode Ethernet transformer testing.....	131
6.3.1.	Common-mode signal suppression.....	133
6.3.1.1.	Common-mode signal suppression by grounding the winding center tap.....	134
6.3.1.2.	Common-mode signal suppression by choke .....	137
6.3.2.	1GBase-T Ethernet transformer.....	138
6.3.2.1.	Cross-winding capacitance .....	140

6.3.2.2.	Intra-winding capacitance.....	141
6.3.3.	10GBase-T Ethernet transformer .....	141
6.3.3.1.	Cross-winding capacitance .....	142
6.3.3.2.	Intra-winding capacitance.....	143
6.3.3.3.	Effectiveness of choke on common-mode suppression.....	144
6.3.4.	Large PVC-core transformer.....	145
6.4.	Summary of extracted values .....	147
6.5.	Model comparison.....	148
6.5.1.	Introduction.....	148
6.5.2.	Differential-mode lumped element models .....	148
6.5.2.1.	1GBase-T transformer lumped equivalent circuit comparison.....	149
6.5.2.2.	10GBase-T transformer lumped equivalent circuit comparison.....	150
6.5.2.3.	PVC-core transformer lumped equivalent circuit comparison .....	151
6.5.3.	Differential-mode distributed models .....	152
6.5.3.1	1GBase-T differential-mode model comparisons.....	155
6.5.3.2	10GBase-T transformer differential-mode model comparisons.....	156
6.5.3.3	PVC-core transformer differential-mode model comparison .....	158
6.5.4.	Differential-mode model comparison summary .....	159
6.5.5.	Common-mode distributed models.....	160
6.5.5.1.	1GBase-T common-mode model transfer function comparison .....	163
6.5.5.2.	10GBase-T transformer distributed common-mode transfer function comparison.....	164
6.5.6.	Testing of commercial Ethernet transformers summary.....	166
Chapter 7 :	Dielectric-core toroid transformer: Fabrication and analysis.....	167
7.1.	Introduction and background .....	167
7.2.	Thin-film dielectric-core transformers: Fabrication and analysis .....	176
7.2.1.	Introduction.....	176
7.2.2.	Rectangular line design.....	185
7.2.2.1	Design and mask drawing.....	185
7.2.2.2	Resistance .....	188
7.2.2.3	Calculation of total capacitance of straight lined toroid transformer .....	191

7.2.2.4	Inductance.....	198
7.2.2.5	Fabrication.....	199
7.2.2.6	Measurement scheme and results .....	205
7.2.3.	Wedge shaped line design.....	212
7.2.3.1	Design and mask drawing.....	212
7.2.3.2	Wedge line resistance calculation.....	214
7.2.3.3	Calculation of total capacitance for wedge shaped winding toroid transformer 222	
7.2.3.4	Inductance.....	225
7.2.3.5	Fabrication.....	225
7.2.3.6	Results .....	227
7.3.	Numerical analysis of magnetic flux and inductance of air-core toroid inductors and transformers.....	229
7.3.1.	Introduction.....	229
7.3.2.	Magnetic flux density .....	230
7.3.3.	Structure.....	249
7.3.4.	Nested windings.....	264
7.4.	PVC-core measured and predicted value comparison.....	267
7.5.	Summary .....	268
Chapter 8 : Summary .....		269
8.1.	Problem restatement and chapter review .....	269
8.2.	Future work .....	271
Appendix A	: VNA calibration theory.....	272
Appendix B	: ABCD parameters cascade.....	298
Appendix C	: 2-port parameter conversions.....	299
Appendix D	: In-house transfer relation measurement system.....	301
Appendix E	: Formation of T-type and $\pi$ -type equivalent circuits.....	303
Bibliography .....		306

## LIST OF PUBLICATIONS

- 1) **Bowen, D.** Mayergoyz, I. Krafft, C. Kroop, D. Beyaz, M. “On design of air-core Ethernet transformers,” *Journal of Applied Physics*, **105**, 07A307 (2009)
- 2) **Bowen, D.** Mayergoyz, I. Zhang, Z. McAvoy, P. Krafft, C. Kroop, D. “Modeling and testing of Ethernet Transformers,” *IEEE Transactions On Magnetics*, 45, 10, 4793 (2009)
- 3) **Bowen, D.** Mayergoyz, I. Krafft, C. “Electromagnetic Modeling of Ethernet Transformers,” *IEEE Transactions On Magnetics*, 46, 2, 563 (2010)
- 4) **Bowen, D.** Mayergoyz, I. Krafft, C. “Common Mode Analysis of Ethernet Transformers,” *IEEE Magnetics Letters*, 1, 0500204 (2010)
- 5) **Bowen, D.** Mayergoyz, I. Krafft, C. “Fabrication and testing of a microelectromechanical systems type dielectric core Ethernet transformer,” *Journal of Applied Physics*, 109, 07E503 (2011)
- 6) **Bowen, D.** Mayergoyz, I. Krafft, C. “Testing and analysis of common mode characteristics of Ethernet transformers,” *Journal of Applied Physics*, 109, 07E705 (2011)
- 7) Bowen, D. Krafft, C. “Discrete Cosine Transform Technique for Measuring Domain Widths in Magneto-optic Garnet Films,” *IEEE Magnetics Letters*, To Be Published (2011)
- 8) Tkachuk, S. **Bowen, D.** Nistor, I. Mayergoyz, I. Krafft, C. “Study of etched (210)-oriented thin garnet films,” *Journal of Applied Physics*, **103**, 07E503 (2008)
- 9) Tkachuk, S. **Bowen, D.** Krafft, C. Mayergoyz, I. “Imaging capabilities of etched (100) and (210) garnet films,” *Journal of Applied Physics*, **105**, 07A524 (2009)
- 10) Tkachuk, S. **Bowen, D.** Krafft, C. Mayergoyz, I. “Controllability of Anisotropy of Bi and Pr Containing Garnet Films Grown on (210)-Oriented Substrates,” *IEEE Transactions On Magnetics*, 44, 11 (2008)
- 11) Mayergoyz, I. Zhang, Z. McAvoy, P. **Bowen, D.** Krafft, C. “Electromagnetic Analysis of Plasmon-Resonance Based All-Optical Magnetic Recording,” *IEEE Transactions On Magnetics*, 45, 3 (2009)
- 12) Mayergoyz, I. Zhang, Z. McAvoy, P. **Bowen, D.** Krafft, C. “Application of Circularly Polarized Plasmon Resonance Modes to All-Optical Magnetic Recording,” *IEEE Transactions On Magnetics*, 44, 11 (2008)
- 13) Mayergoyz, I. Zhang, Z. McAvoy, P. Lang, G. **Bowen, D.** Krafft, C. “Excitation and dephasing of circularly polarized plasmon modes in spherical nanoshells for application in all-optical magnetic recording,” *Journal of Applied Physics*, 105, 07B904 (2009)
- 14) Krafft, C. Tkachuk, S. Lang, G. Bowen, D. Mayergoyz, I., “Magneto-Optic Indicator Films for Forensics,” *Materials Research Society Proceedings*, 1291, (2010)

## LIST OF TABLES

Table 6.1. Bandwidths for DM and CM signals for different Ethernet standards [25], [26].....	104
Table 6.2. Network parameter descriptions [28]. .....	107
Table 6.3. 1GBase-T Ethernet transformer physical dimensions. ....	112
Table 6.4. 10GBase-T Ethernet transformer physical dimensions. ....	118
Table 6.5. PVC-core transformer physical dimensions. ....	125
Table 6.6. Summary of all transformers extracted parameters. ....	148
Table 7.1. Fabricated rectangular line transformer physical dimensions. ....	203
Table 7.2. Fabricated transformer theoretically predicted resistance, inductance, and cross-winding capacitance.....	203
Table 7.3. DC resistance measurements of fabricated transformers.....	206
Table 7.4. Summary of performance metrics for fabricated and commercial Ethernet transformers. ....	212
Table 7.5. Fabricated wedge-lined transformer physical parameters. ....	226
Table 7.6. Theoretical parameters for wedge-lined fabricated transformers. ....	226
Table 7.7. Fabricated wedge-lined transformers measured DC resistance.....	227
Table 7.8. Analytical inductance for toroid rectangular cross-section transformers with various turn numbers ( $h = 2\mu\text{m}$ , $a = 5\text{mm}$ , $b = 2\text{mm}$ ). ....	262
Table 7.9. Analytical mutual and leakage inductance for toroid rectangular cross-section transformers with various turn numbers ( $h = 2\mu\text{m}$ , $a = 5\text{mm}$ , $b = 2\text{mm}$ ). ....	264
Table 7.10. Ratios of calculated mutual and leakage inductance to self inductance for various turn numbers. ....	264
Table 7.11. Nested-winding numerical inductance analysis values. ....	266
Table 7.12. Comparison of measured and predicted inductance and capacitance for the large PVC-core transformer.....	268

## LIST OF FIGURES

FIG. 1.1 Commercial Ethernet transformers (a) In package next to US Penny (b) microscope image of an Ethernet transformer removed from its package.....	3
FIG. 2.1. End of balanced transmission line.....	2
FIG. 2.2. Depiction of signal with both common-mode and differential mode components. (a) Sum of common mode and differential mode (b) Differential mode and common mode signals separated. ....	3
FIG. 2.3. A 2-device network connection in a real environment.....	4
FIG. 2.4. 1Gbps spectra (a) Common-mode (b) Differential-mode .....	6
FIG. 2.5. 100Mbps spectra (a) Common-mode (b) Differential-mode.....	7
FIG. 3.1. Schematic drawing of a classic transformer. (Ulaby, Fawwaz T. Fundamentals of Applied Electromagnetics. Media Edition, © 2004. pg. 235, Reprinted by permission of Pearson Education, Inc., Upper Sadle River, New Jersey) [5].....	8
FIG. 3.2. Winding depicting Faraday’s Law (Ulaby, Fawwaz T. Fundamentals of Applied Electromagnetics. Media Edition, ©2004. Pg. 237, Reprinted by permission of Pearson Education, Inc., Upper Sadle River, New Jersey) [5].....	11
FIG. 3.3. Torus core inductor with leakage flux. (Cheng, David K. Field and Wave Electromagnetics, 2nd ed., ©1989. pg. 252, Reprinted by permission of Pearson Education, Inc., Upper Sadle River, New Jersey) [7] .....	15
FIG. 3.4. Real transformer analysis diagram. ....	16
FIG. 3.5. Real transformer equivalent circuit. ....	22
FIG. 3.6. Generic ferromagnetic material hysteresis curve .....	24
FIG. 3.7. Generic hysteresis curves for relatively hard, soft, and softer magnetic materials .....	25
FIG. 3.8. Eddy currents diagram. (Young,/ Freedman/Sandin/Ford. Sear’s and Zemansky’s University Physics, 10 <sup>th</sup> ed., (c)2000, pg. 1016, Reprinted by permission of Pearson Education, Inc., Upper Sadle River, New Jersey) [10] .....	30
FIG. 3.9. Diagram of core material with flux and eddy currents. [11] .....	30
FIG. 3.10. Mn-Zn complex magnetic permeability dispersion curve. [13] .....	33
FIG. 3.11. Transformer equivalent circuit with core loss resistor. ....	36
FIG. 3.12. Equivalent circuit derived by alternative method.....	40
FIG. 3.13. Parallel to Series impedance conversion. ....	40
FIG. 3.14. Image of bifilar wound Ethernet transformer extracted from package. ....	43
FIG. 3.15. Capacitance placement in the equivalent circuit. ....	44
FIG. 3.16. Common transformer equivalent circuit including capacitance.....	44
FIG. 4.1. Measurement scheme for classic transformer tests. ....	46
FIG. 4.2. Phasor diagram for SCT approximate equivalent circuit. ....	47
FIG. 4.3. Modified equivalent circuit for the short circuit test. ....	47
FIG. 4.4. Approximate equivalent circuit for open circuit test. ....	50
FIG. 4.5. Phasor diagram for OCT equivalent circuit.....	50
FIG. 4.6. Measurement setup to determine primary and secondary winding resistances.....	52
FIG. 4.7. Quasi-short circuit test experimental setup. ....	54
FIG. 4.8. Quasi-short circuit test phasor diagram.....	55
FIG. 4.9. Quasi Open Circuit test measurement setup.....	57
FIG. 4.10. Quasi-open circuit test phasor diagram. ....	58
FIG. 4.11. Phasor Diagram for the quasi-open circuit test. ....	59

FIG. 4.12. Measured core properties using the quasi open circuit test. [14] .....	62
FIG. 4.13. Complex permeability of Mn-Zn Ferrite (a) Real (b) Imaginary [20] .....	63
FIG. 4.14. Comparison of measured and calculated transfer characteristics.....	66
FIG. 4.15. Common-mode transfer characteristic measurement setup.....	66
FIG. 4.16. Common-mode transfer characteristic for a 1Gbase-T commercial Ethernet transformer.....	67
FIG. 5.1. External terminal diagram of differential-mode distributed transformer model with boundary conditions.....	72
FIG. 5.2. Single cell of differential-mode distributed model.....	73
FIG. 5.3. Distributed model without inductance transfer characteristic (varying alpha prime)..	86
FIG. 5.4. Distributed model without inductance transfer characteristic (varying Lambda). .....	86
FIG. 5.5. Plot of transformer input impedance calculated by the analytical distributed model equations. ....	88
FIG. 5.6. Single cell of common-mode distributed model. ....	90
FIG. 5.7. External terminal diagram of common-mode distributed transformer half-model with boundary conditions.....	92
FIG. 6.1. Isolation clause in IEEE 802.3 Base-T Ethernet standard. [25] .....	103
FIG. 6.2. Differential mode VNA testing scheme. ....	105
FIG. 6.3. 1GBase-T differential-mode VNA testing custom circuit boards (a) without device (b) with device .....	105
FIG. 6.4. T-Type equivalent circuit .....	110
FIG. 6.5. $\Pi$ -type equivalent circuit .....	110
FIG. 6.6. 1GBase-T Ethernet Transformer transfer relation.....	113
FIG. 6.7. 1GBase-T infinite loaded transfer relation with in-house system supplemental data.	114
FIG. 6.8. 1GBase-T Ethernet transformer mutual inductance extraction. ....	115
FIG. 6.9. 1GBase-T Ethernet transformer leakage inductance extraction.....	116
FIG. 6.10. 1GBase-T transformer line resistance. ....	117
FIG. 6.11. 1GBase-T Ethernet transformer core loss resistance.....	118
FIG. 6.12. 10GBase-T Ethernet transformer measured transfer relation with different loads. ..	119
FIG. 6.13. 10GBase-T Ethernet transformer measured transfer relation with in-house system low frequency data. ....	120
FIG. 6.14. 10GBase-T Ethernet transformer extracted mutual inductance. ....	120
FIG. 6.15. 10GBase-T Ethernet transformer extracted leakage inductance. ....	121
FIG. 6.16. 10GBase-T Ethernet transformer line resistance.....	122
FIG. 6.17. 10GBase-T Ethernet transformer core loss resistance.....	123
FIG. 6.18. Comparison of series core parameters for 1GBase-T and 10GBase-T transformers.	124
FIG. 6.19. PVC-core transformer with coffee cup to present scale.....	125
FIG. 6.20. PVC-core transformer top view.....	125
FIG. 6.21. PVC-core transformer VNA measured differential-mode transfer relation for different loads.....	127
FIG. 6.22. PVC-core transformer in-house system measure differential-mode transfer relation. .....	127
FIG. 6.23. PVC-core transformer extracted mutual inductance. ....	128
FIG. 6.24. PVC-core transformer extracted leakage inductance. ....	129
FIG. 6.25. PVC-core transformer extracted line resistance. ....	130
FIG. 6.26. PVC-core transformer extracted core loss resistance.....	131

FIG. 6.27. Common-mode measurement scheme.....	133
FIG. 6.28. Custom circuit boards for common-mode measurements (a) without device package (b) with device package. ....	133
FIG. 6.29. Diagram of common-mode flux cancelation in a transformer winding with a grounded center tap. ....	135
FIG. 6.30. Common-mode currents on a traditional transformer with load. ....	136
FIG. 6.31. Common-mode currents on a transformer with a grounded center tap.....	136
FIG. 6.32. Description of currents in common-mode chokes.....	138
FIG. 6.33. Diagram of flux cancelation and common-mode current suppression using a common- mode choke. ....	138
FIG. 6.34. 1GBase-T Ethernet transformer common-mode transfer relation [31]. ....	139
FIG. 6.35. 1GBase-T Ethernet transformer cross-winding capacitance analysis. ....	140
FIG. 6.36. 1GBase-T Ethernet transformer intra-winding capacitance analysis. ....	141
FIG. 6.37. 10GBase-T Ethernet transformer common-mode transfer relation [31]. ....	142
FIG. 6.38. 10GBase-T Ethernet transformer cross-winding capacitance analysis. ....	143
FIG. 6.39. 10GBase-T Ethernet transformer intra-winding capacitance analysis. ....	144
FIG. 6.40. 10GBase-T Ethernet transformer common-mode transfer relation with and without common-mode chokes [31].....	145
FIG. 6.41. PVC-core transformer common-mode transfer relation.....	146
FIG. 6.42. PVC-core transformer extracted cross-winding capacitance. ....	147
FIG. 6.43. Lumped element equivalent circuit used for comparison to measured transfer relations.....	149
FIG. 6.44. 1GBase-T Ethernet Transformer lumped equivalent circuit transfer relation comparison.....	150
FIG. 6.45. 10GBase-T Ethernet Transformer lumped equivalent circuit transfer relation comparison.....	151
FIG. 6.46. PVC-core Transformer lumped equivalent circuit transfer relation comparison. ....	152
FIG. 6.47. Differential-mode distributed circuit cell. ....	153
FIG. 6.48. Chosen differential-mode per-length impedance topology. ....	154
FIG. 6.49. Chosen differential-mode per-length admittance topology.....	154
FIG. 6.50. Chosen differential-mode per-length mutual impedance topology. ....	154
FIG. 6.51. 1GBase-T Ethernet transformer differential-mode model comparison - exact extracted values. ....	155
FIG. 6.52. 1GBase-T Ethernet transformer differential-mode model comparison - Tuned values. .....	156
FIG. 6.53 10GBase-T Ethernet transformer differential-mode model comparison - exact extracted values.....	157
FIG. 6.54. 10GBase-T Ethernet transformer differential-mode model comparison - Tuned values. .....	157
FIG. 6.55. PVC-core transformer differential-mode model comparison - exact extracted values. .....	158
FIG. 6.56. PVC-core transformer differential-mode model comparison - Tuned values. ....	159
FIG. 6.57. Distributed infinitesimal circuit cell for the common-mode model. ....	161
FIG. 6.58. Circuit topology for the distributed common-mode model per-length series impedance .....	162

FIG. 6.59. Circuit topology for the distributed common-mode model per-length cross-winding admittance. ....	162
FIG. 6.60. Tuning topology for the per-length impedance of the common-mode distributed model.....	162
FIG. 6.61. 1GBase-T transformer: Common-mode distributed model transfer relation with extracted parameter values.....	163
FIG. 6.62. 1GBase-T transformer: Common-mode distributed model transfer relation with tuned parameter values [31].....	164
FIG. 6.63. 10GBase-T transformer: Common-mode distributed model transfer relation with extracted parameter values.....	165
FIG. 6.64. 10GBase-T transformer: Common-mode distributed model transfer relation with tuned parameter values [31].....	165
FIG. 7.1. Magnetic fields of a long solenoid. (Plonus, M. Applied Electromagnetics. McGraw Hill, 1978. Reproduced with permission of The McGraw-Hill Companies) [38] .....	169
FIG. 7.2. Magnetic field depiction of a single current carrying loop cross-section. (Plonus, M. Applied Electromagnetics. McGraw Hill, 1978. Reproduced with permission of The McGraw-Hill Companies) [38] .....	170
FIG. 7.3. Net field perpendicular to the cross-section between two filaments carrying identical current in the same direction. ( $\Delta$ is the distance between filament centers).....	171
FIG. 7.4. Cross-section flux density slope field for adjacent wires at $x=2\text{mm}$ and $x=3\text{mm}$ with current flowing into the page. Line lengths indicate flux magnitude. ....	173
FIG. 7.5. Adjacent winding turns field interaction. ....	174
FIG. 7.6. Flux diagram of rectangular cross-section toroid inductor. (Young,/ Freedman/Sandin/Ford. Sear's and Zemansky's University Physics, 10 <sup>th</sup> ed., (c)2000, Reprinted by permission of Pearson Education, Inc., Upper Sadle River, New Jersey) [10] .....	175
FIG. 7.7. Square cross-section torus with labeled dimensions. (a) top view (b) side view .....	178
FIG. 7.8. Torus core and metal conductor cross section labeled dimensions.....	178
FIG. 7.9. 32-turn toroid transformer coordinate lattice. ....	183
FIG. 7.10. Top view of 3D rendering of bifilar wound toroidal transformer with core structure. ....	186
FIG. 7.11. Top view of 3D rendering of bifilar wound toroidal transformer without core structure.....	186
FIG. 7.12. Width Budget of torus geometry. ....	187
FIG. 7.13. Oblique view of 3D model of rectangular lined 32-turn bifilar-wound transformer. ....	189
FIG. 7.14. Coplanar stripline cross sectional dimensions.....	191
FIG. 7.15. Image of aluminum sidewall cracking over Su-8.....	200
FIG. 7.16. Enhanced image of aluminum sidewall cracking over Su-8. ....	201
FIG. 7.17. Probe station micrograph of a 32-turn fabricated silicon dioxide core transformer with probe contacts. ....	204
FIG. 7.18. 3-inch silicon wafer with 32, 64, 128, and 256-turn rectangular line devices. ....	204
FIG. 7.19. Cascade Microtech M150 probe station used to characterize fabricated transformers. ....	205
FIG. 7.20. Close-up photo of probe station RF probes over sample. ....	206
FIG. 7.21. Decomposition of the measured scattering parameters into pad impedance and winding performance. ....	209
FIG. 7.22. 32-turn fabricated transformer transfer relation for various loads. ....	210

FIG. 7.23. 64-turn fabricated transformer transfer relation for various loads. ....	211
FIG. 7.24. Top view: 3D model of 16-turn wedge shaped transformer.....	214
FIG. 7.25. 3D model of toroid transformer with wedge shaped lines. ....	216
FIG. 7.26. Wedge line layout (a) real line layout with skew (b) approximate layout for analysis .....	218
FIG. 7.27. Probe station images of wedge transformers (a) 8-turn H-scale (b) 16-turn H-scale	226
FIG. 7.28 Microscope photographs of transformer lines (a) 16-turn G-scale transformer lines and contact pads (b) 16-turn H-scale transformer lines.....	226
FIG. 7.29. Measured transfer relations for fabricated wedge-lined transformers.....	228
FIG. 7.30. Schematic of a single wire loop with current flowing around it. ....	230
FIG. 7.31. Flux density slope field around a wire loop in the XY plane. ....	242
FIG. 7.32. Flux density slope field superimposed over turn map of toroidal inductor.....	242
FIG. 7.33. Magnetic slope field for a dielectric-core toroid transformer: N=6. ....	243
FIG. 7.34. Magnetic slope field for a dielectric-core toroid transformer: N=8. ....	244
FIG. 7.35. Magnetic slope field for a dielectric-core toroid transformer: N=16. ....	245
FIG. 7.36. Magnetic slope field for a dielectric-core toroid transformer: N=32. ....	246
FIG. 7.37. Magnetic slope field for a dielectric-core toroid transformer: N=64. ....	247
FIG. 7.38. Theta direction magnetic field around the core of an N=16 toroid transformer with varying core height. ....	248
FIG. 7.39. Theta direction magnetic field around the core of an h=1mm toroid transformer with varying turn number.....	249
FIG. 7.40. Observing turn locations around toroid.....	252
FIG. 7.41. Diagram of dA calculation. ....	253
FIG. 7.42. Total normal flux through turns as numbered in FIG. 7.43, N = 32. ....	259
FIG. 7.43. Primary toroid winding indexed turn map, N = 32. ....	260
FIG. 7.44. Total normal flux through turns as numbered in FIG. 7.45, N = 128. ....	261
FIG. 7.45. Primary toroid winding indexed turn map, N = 128. ....	261
FIG. 7.46. Total normal flux through turns as numbered in FIG. 7.47, N = 32. ....	263
FIG. 7.47. Secondary toroid winding indexed turn map, N = 32. ....	263
FIG. 7.48. 3D rendering of a nested winding thin-film transformer structure.....	265
FIG. 7.49. Magnetic slope field around nested windings: Primary = Magenta, Secondary = Green.....	266
Appendix Fig. A.1. 1-port error model from Hackborn's 1968 article [44]. ....	273
Appendix Fig. A.2. Hackborn's obsolete <i>through</i> connection error model [44]. ....	276
Appendix Fig. A.3. B. P. Hand's depiction of the modern VNA error model [46]. ....	277
Appendix Fig. A.4. Forward direction port 2 error network with load match reflection branch. .....	278
Appendix Fig. A.5. Reverse direction port 2 error network with load match reflection branch.	279
Appendix Fig. A.6. <i>Through</i> connection error model in the forward direction.....	281
Appendix Fig. A.7. <i>Through</i> connection error model in the reverse direction.....	283
Appendix Fig. A.8. Hand's isolation terms signal flow graph. ....	285
Appendix Fig. A.9. Full error model with DUT in place in the forward direction.....	286
Appendix Fig. A.10. Full error model with DUT in place in the reverse direction.....	289
Appendix Fig. B.1. Cascade of two 2-port devices: X and Y with voltages and currents labeled. .....	298

Appendix Fig. C.1. Table taken from microwave engineering text by Pozar [28] showing the conversion formulas between 2-port network parameters, assuming a single system characteristic impedance. ....	299
Appendix Fig. C.2. Table taken from [50] showing the conversion from 2-port scattering parameters only to all other parameters, accounting for different characteristic impedances on port 1 and port 2. (Reprinted with permission from IEEE). ....	300
Appendix Fig. D.1. In-house built setup for measuring the transfer relation of a DUT.....	301
Appendix Fig. E.1. T-type equivalent circuit .....	303
Appendix Fig. E.2. $\pi$ -type equivalent circuit.....	305

## Chapter 1 : Introduction

### 1.1 Introduction

Over the past 50 years, computer networking has changed the world. Computer networks link people around the planet, communicating information in a fraction of a second. Databases make information readily accessible and electronic mail has become indispensable. Computers and, as a result, computer networks have revolutionized the way people live.

Such a revolutionary technology did not catch on like a technological pandemic. Computer networks grew and evolved from their military roots into increasingly faster and complex hardware and protocols. Early computer networks were small and inefficient, linking computers for the sole purpose of file sharing across rooms or, at farthest, buildings. The first design to take on the challenge of uniting dissimilar scattered networks was ARPAnet, commissioned by DARPA in the late 1960's. ARPAnet was one of the first networks to use packet switching instead of circuit switching. Packet switching made communication over an arbitrarily large network of interconnected terminals efficient and realizable useful.

ALOHAnet at the University of Hawaii which most engineers study in school is built upon the packet switching concepts of ARPAnet. ALOHAnet, built in 1970, used hubs in a star configuration and teletype machines to link the widespread university campus over radio channels. The network had a novel approach to collision detection involving acknowledgements and randomization which greatly influenced Bob Metcalfe at Xerox PARC.

In 1973, Bob Metcalfe, David Bogs and a Xerox engineering team would go on to design and build the first Ethernet network, connected using heavily shielded coaxial cable. In *Thicknet*

Ethernet, terminals were electrically connected in parallel along an RG-8 coaxial cable backbone and vampire taps were used to make links to individual computers. It was not so long ago that office networks were effectively using *Thinnet* Ethernet, in which RG-58 coaxial cable served as the backbone, and terminals would connect in parallel using BNC T-connectors. Increasing data rates and the high cost of coaxial cable has made *Thinnet* and *Thicknet* obsolete in favor of twisted pair cable networks. Category 5e unshielded twisted pair (UTP) cable is currently the networking standard, delivering data rates of 100Mbps and 1Gbps ( [1], [2]).

Network protocols are defined by the maximum distance of their cabling, or *network radius*, from which the bounds on the network implementation are derived. Networks range from *local area networks* (LANs) in homes, offices, and buildings to *wide area networks* (WANs) spanning thousands of miles. Over the last few decades, many different network protocols have been implemented for various ranges of network communication. At the LAN level, Ethernet over twisted-pair cable has emerged as the dominant LAN technology in the market, making up over 80% of LAN implementations [3]. Ethernet fiber optic protocols are also capable of midrange networks spanning tens of miles in a single link. Though high data rate and longer range Ethernet backbones are fiber optic, implementing office LANs (or “last-mile installations”) with fiber optics is not cost effective. In the stable market price limit, copper UTP cable implementations will still be less expensive by half the price of the equivalent fiber installation, making copper UTP the preferred last-mile network implementation [4].

The expanse of a given twisted-pair Ethernet LAN can be hundreds of computers and multiple buildings, using miles of cable. With all of this unprotected cable running around or between buildings, there is a real danger of a high voltage fault from incorrect wiring, anomalous short circuits, or random lightning strikes. The faulted cable connects to a network switch that

could short circuit to all of the computer terminals, possibly giving exposed computer components high voltage and ultimately causing a hazardous condition for the user. In practice, however, high voltage faults never reach computer terminals. This is because the network is protected by widely deploying techniques in electrical isolation. The device used principally in electrical isolation of twisted-pair cable networks is the Ethernet transformer. These isolation signal transformers are of a toroid geometry approximately 5mm in diameter with a ferrite core (usually Mn-Zn) and wound with fine gauge wire (See FIG. 1.1).

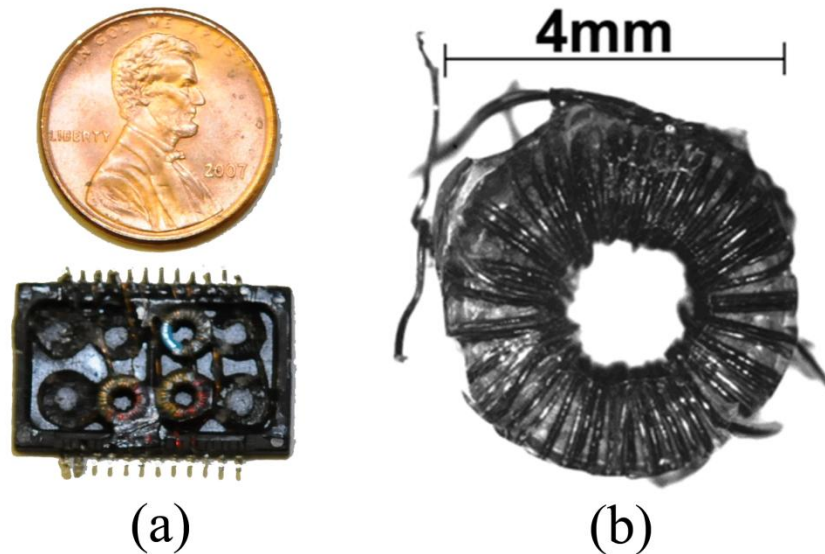


**FIG. 1.1 Commercial Ethernet transformers (a) In package next to US Penny (b) microscope image of an Ethernet transformer removed from its package.**

Though the current state of the art has delivered impressively small Ethernet transformers, it is becoming clear that transformers are the limiting component to further miniaturization of wired Ethernet devices. A single network link requires four transformers. Even the smallest transformers will require a separate package up to an inch long and 0.125 inches high. This not only limits the size of the Ethernet device that must reserve room for the transformer package footprint, but also adds a step to manufacturing, since using transformers

will always require the attachment of a separate package. It is clear that an isolation coupler that can be fabricated and integrated within a chip would allow devices to be smaller and accelerate manufacturing.

To this end, current ferrite core Ethernet transformers must be studied and modeled to predict quantitatively how a new thin-film air-core transformer design will perform. This dissertation will discuss the details of Ethernet transformers including the following: how and why they are currently used, modeling with classic and distributed circuit models in differential and common signal modes, techniques for the characterization of transformer ferrites, advanced differential and common mode measurement and parameter extraction, novel device fabrication and testing, and theoretical analysis of fabricated transformer structures. Following is a list outlining the novel contributions of this research.

1. **Quasi classical test development** – This measurement scheme employs phasor analysis and voltage amplitude measurements to characterize transformers over a range of frequencies, using the well known lumped element circuit model. These novel tests improve upon the classically used tests by being able to characterize a device over a range of frequencies. **See Section 4.2** for details.
2. **Distributed circuit model:** development and analysis – To properly include capacitances in the transformer equivalent circuit, a new distributed circuit model is developed for both differential and common mode signals. The model is then analyzed to find closed form expressions for input impedance and the transformer relations. These models are novel in their application to transformers and in their unique treatment of a device with distributed magnetic coupling. **See Chapter 5** for details.

3. **High quality commercial transformer measurements** – Special fixtures and analysis techniques were used to measure transfer relations and extract device parameters of commercial Ethernet transformers in both the differential and common mode signal configurations. Comparisons of these measurements with distributed model predictions revealed very good agreement, validating the new distributed model. **See Chapter 6 for details.**
  
4. **Fabrication** – A thin-film transformer was designed with varying turn numbers, a process was developed, and the devices were fabricated and tested (**See section 7.2 for details**). At the point of the writing of this dissertation, similar transformer designs are rare in the literature, usually for power applications with low turn numbers and a different fabrication process. Also, the designed 3D structure was analyzed and numerical methods were used to evaluate magnetic flux around the device and extract inductance (**See section 7.3 for details**). In no publications known to this author has the analysis been as thorough as was done in this research and reported in this dissertation.

## **Chapter 2 : Electrical isolation and signal modes**

### **2.1. Introduction**

In practice, electrical isolation means that in connected devices, current cannot flow directly from one device to others and vice versa. Network fault protection requires devices be electrically isolated at the fundamental physical layer of the medium, whether using coaxial cable or unshielded twisted pair. Isolation is used at all cable-device interfaces from network cards in computers and multiport network switches up to servers.

For decades, the principal solution for electrical isolation in Ethernet networks is the use of Ethernet transformers at all cable-device interfaces. Since transformers use electromagnetic coupling to link port 1 (the primary) to port 2 (the secondary), it is impossible in normal operation for currents to flow through the device from port 1 to port 2.

Electrical isolation transformers are not only useful in fault conditions, however. In normal operation, network cabling can stretch between buildings with different ground references. If the transmitting terminal sends a signal with 0 Volts DC offset referenced to local transmitter ground, it could be a 50 or 500 volt DC offset signal at the receiving terminal when referenced to local receiver ground. Without electrical isolation, large currents would flow into the receiving terminals creating potentially dangerous conditions for the user. However, with isolation transformers used at both the transmitter and receiver, all signals remain at safe levels at each point in transmission.

## 2.2. Signal Modes

To further discuss advantages of signal transformers in general, the signals must first be described. A signal can be decomposed into differential-mode ( $V_{dm}$ ) and common-mode ( $V_{cm}$ ) components as defined below:

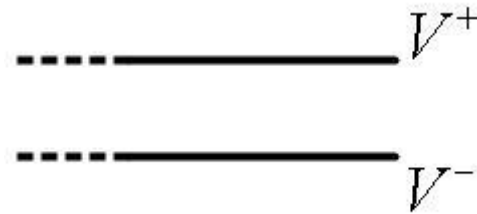


**FIG. 2.1. End of balanced transmission line.**

$$V^+ = \frac{V_{dm}}{2} + V_{cm} \quad 2.1$$

$$V^- = -\frac{V_{dm}}{2} + V_{cm} \quad 2.2$$

$$V^+ - V^- = \frac{V_{dm}}{2} + V_{cm} - \left( -\frac{V_{dm}}{2} + V_{cm} \right) = V_{dm} \quad 2.3$$

If  $V^+$  and  $V^-$  were measured with reference to Earth ground potential, the differential-mode part of the signal will invert polarity from line  $V^+$  to line  $V^-$ . The common-mode part of the signal will be the same with the same polarity on each terminal.

$$V_{dm}^+ = -V_{dm}^- \quad 2.4$$

and

$$V_{cm}^- = V_{cm}^+ \quad 2.5$$

As an example, consider FIG. 2.2. Both  $V^+$  and  $V^-$  have a common-mode 1Hz portion with an amplitude of 5V. The differential-mode signal is a 4 Hz sine with an amplitude of 10V.

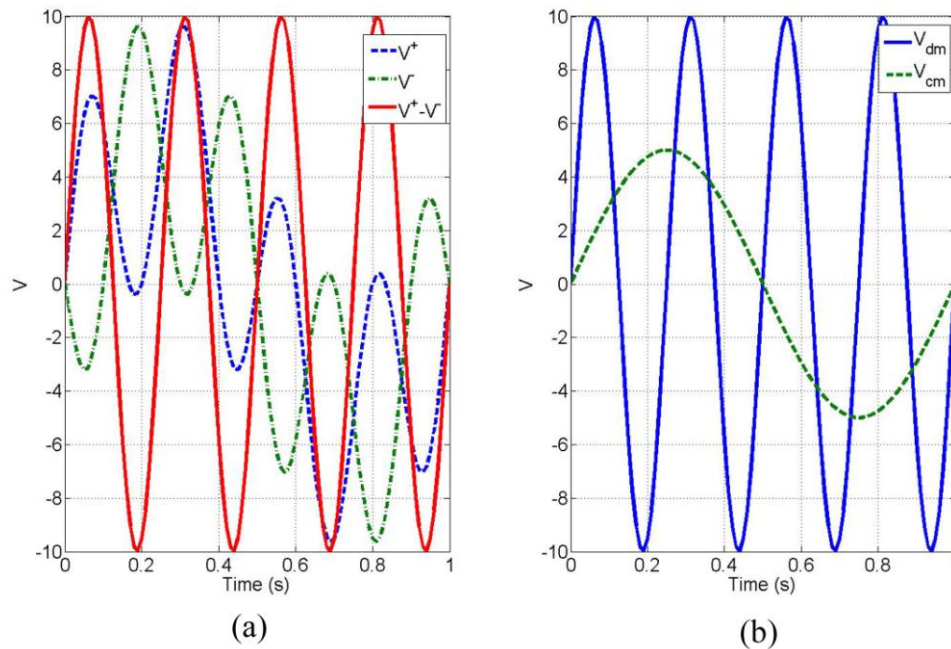


**FIG. 2.2. Depiction of signal with both common-mode and differential mode components. (a) Sum of common mode and differential mode (b) Differential mode and common mode signals separated.**

Now consider the current standard Ethernet network connected with unshielded twisted pair (UTP) cable. Consider a transmission over a single pair of wires from device A to device B (see FIG. 2.3).

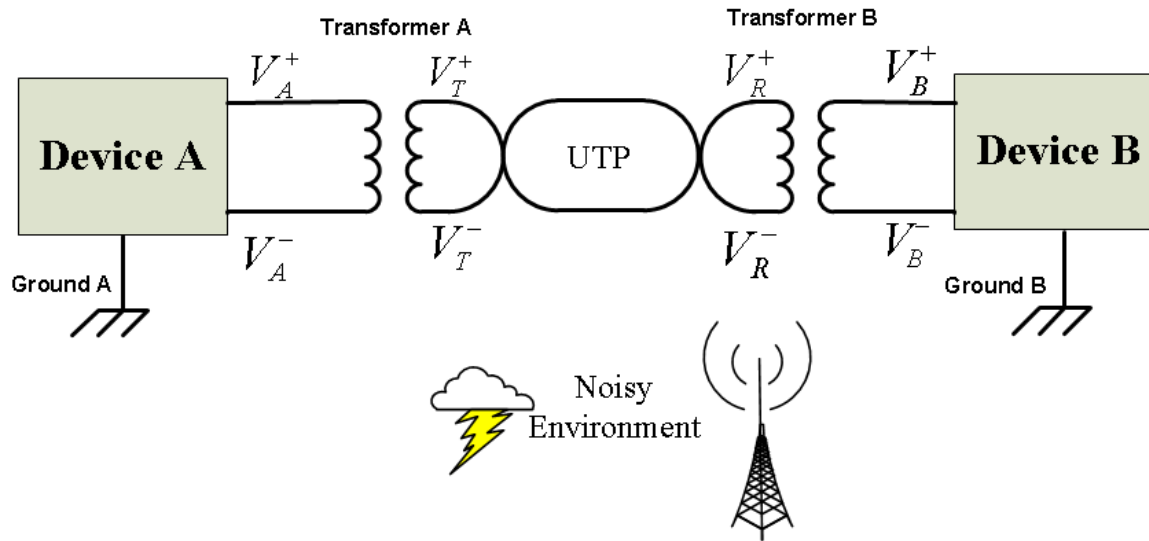


FIG. 2.3. A 2-device network connection in a real environment.

Device A will transmit data by putting a sequence of voltages on the twisted pair line. This is known as balanced transmission, balanced line transmission, or differential-mode transmission. Balanced transmission works well for long distance signal travel. Device B will receive the potential differences and process them digitally to recover the data. Following is a description of the signal along the path from device A to device B.

The output of device A before the first isolation transformer is given below, with both differential-mode and common-mode components.

$$V_A^+ = \frac{V_{A,dm}}{2} + V_{A,cm} \quad 2.6$$

$$V_A^- = -\frac{V_{A,dm}}{2} + V_{A,cm} \quad 2.7$$

For reasons that will be described in later sections, the isolation transformer (ideally) passes only the differential-mode portion of the signal.

$$V_T^+ = \frac{V_{A,dm}}{2} \quad 2.8$$

$$V_T^- = -\frac{V_{A,dm}}{2} \quad 2.9$$

As the signal travels down the twisted pair line, it picks up interference power from the environment. This interference power can be correctly assumed to couple equally to both lines of the twisted pair cable, given the close proximity of the two lines. It is clear from the equations that the interference voltage that appears on the lines is common-mode.

$$V_R^+ = \frac{V_{A,dm}}{2} + V_{Interference} \quad 2.10$$

$$V_R^- = -\frac{V_{A,dm}}{2} + V_{Interference} \quad 2.11$$

However, now the signal passes through the receiver's (device B) transformer, and again, common-mode is removed. Depending on the wiring of the receiver, the common-mode may be set intentionally for digital processing, which will be discussed in later sections.

$$V_B^+ = \frac{V_{A,dm}}{2} + V_{B,cm} \quad 2.12$$

$$V_B^- = -\frac{V_{A,dm}}{2} + V_{B,cm} \quad 2.13$$

The twisted pair network scheme with isolation transformers analyzed above will ideally deliver to the receiver a signal free from interference. Given the inexpensive unshielded cables used for networks, the isolation transformers are largely responsible for interference suppression. In the following chapter, the basic design and principal of operation of transformers will be

discussed. It will become clear in the following discussion how transformers effectively isolate and reject common-mode interference.

In FIG. 2.4 and FIG. 2.5 below is shown the measured spectra of 1Gbps and 100Mbps networks. These show empirically that the magnitudes of common-mode and differential-mode signals that exist on UTP cable between nodes of an Ethernet network are largely different. The common-mode signal currents are much greater than the differential-mode currents. Without an interface with large common-mode rejection, any subsequent processing would have great difficulty recovering the information carrying differential-mode signal.

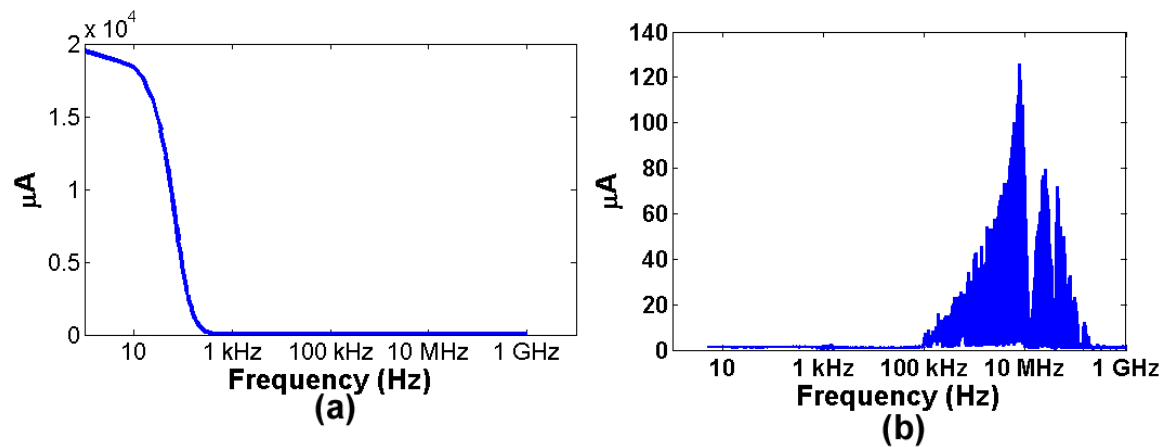


**FIG. 2.4. 1Gbps spectra (a) Common-mode (b) Differential-mode**

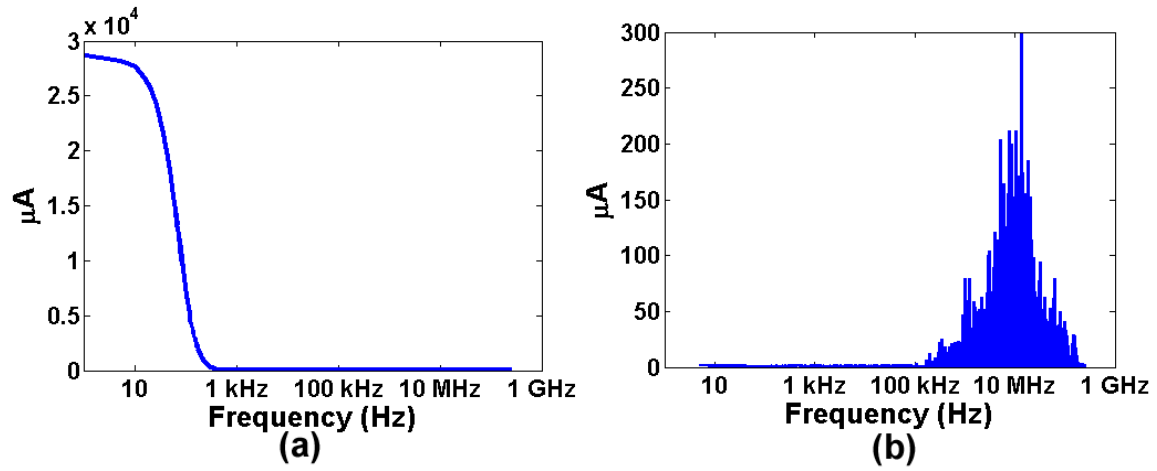
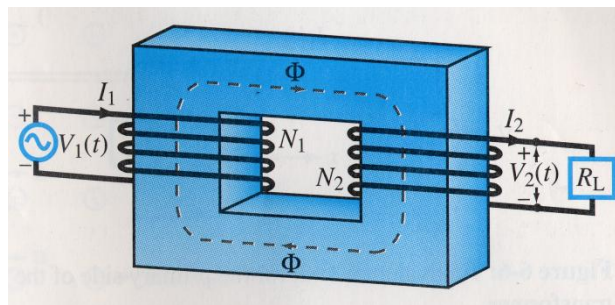


FIG. 2.5. 100Mbps spectra (a) Common-mode (b) Differential-mode

## Chapter 3 : Transformers: Design and operation

### 3.1. Magnetic coupling, transformer theory, and the ideal transformer

A transformer, whether *power* or *signal*, is an electromagnetic device. A signal or single phase power transformer consists of two windings of wire, the primary windings and the secondary windings. The windings are wrapped around such a material or in such geometry so as to have high mutual magnetic flux (see FIG. 3.1). Classic designs are as shown in FIG. 3.1, where the primary and secondary are wrapped around the same high magnetic permeability material. Using arguments of magnetic circuitry and parallel reluctance, the core material with low reluctance effectively guides the flux from the primary winding to the secondary winding.



**FIG. 3.1. Schematic drawing of a classic transformer.** (Ulaby, Fawwaz T. Fundamentals of Applied Electromagnetics. Media Edition, © 2004. pg. 235, Reprinted by permission of Pearson Education, Inc., Upper Saddle River, New Jersey) [5]

The clearest approach to describing the principal of operation of the generic transformer is to use an input to output progression. Considering the primary as the input (or port 1), a time-varying voltage  $\hat{V}_1$  is applied across the terminals. The primary winding will be assumed for the moment to be a pure inductance (part of the ideal transformer assumption), and the volume within the winding will be referred to as the winding *core*. The current  $\hat{I}_1$  will flow in the primary winding. Depending on the geometry of the winding, the core material used, and signal amplitudes, there will be a magnetic flux density,  $\hat{B}$ , around the winding that is proportional to the current  $\hat{I}_1$ . Considering a single isolated turn of the winding, integrating  $\hat{B}_{1\text{-turn}} \cdot dA$  over the

turn cross section will give the total magnetic flux,  $\hat{\phi}_{1-turn}$ , which is also proportional to  $\hat{I}_1$ . It is important at this point to differentiate between the flux through a single isolated turn,  $\hat{\phi}_{1-turn}$ , and the flux through the winding core,  $\hat{\phi}_{core}$ . These values are not the same as will be discussed next.

The flux through and shared by each turn of an  $N$ -turn winding ( $\hat{\phi}_{core}$ ) will be a superposition of the flux contributions from all proximate turns. In the ideal case, it is assumed that each turn couples entirely to all other turns, meaning that the flux from each turn is shared with each other turn. Thus, the total core flux will be the product of the flux from a single turn and  $N$ , as shown below.

$$\hat{\phi}_{core} = N\hat{\phi}_{1-turn} = N\hat{B}_{1-turn} \cdot dA \quad 3.1$$

Faraday's Law (determined empirically) states that the derivative of the flux through a loop of wire is equal to minus the loop terminal voltage (see equation 3.2 and FIG. 3.2). For a winding, Faraday's law is rephrased to state that the *winding* terminal voltage is equal to minus the derivative of the winding *flux linkages*. Flux linkages will be discussed in the next paragraph. However, it is important to note here that if the winding is ideal, each turn will share a common flux,  $\hat{\phi}_{core}$ . The single-turn voltage equation is given in equation 3.3 and the Faraday's law winding-terminal voltage equation is given in equation 3.4.

In equation 3.4, the turn number,  $N$ , is combined with the core flux to give the *flux linkages* ( $\hat{\psi}$ , see equation 3.5). [5] defines flux linkage as "the total magnetic flux linking a given circuit or structure." However, the flux linkages can be thought of conceptually in two ways. The first way, which is closer to the way that most textbooks describe flux linkage, is that any  $N$ -turn winding can be equated to an imaginary single, larger turn with a larger effective

area. Integrating the flux density over the effective area of the larger turn would be equal to the discrete sum of the flux density integrals of each turn of the winding. In this way, the flux linkage is the discrete sum of the flux through each turn. In the ideal winding, this is given by equation 3.5. The winding terminal voltage would then be proportional to the derivative of the flux through the effective area (see equation 3.4).

The second way to conceptualize flux linkages is in the context of Faraday's Law (equation 3.2). The terminal voltage of a single turn can be thought of as a single voltage source,  $\hat{V}_{1-turn}$  (see equation 3.3). The winding voltage would then be like a battery of single turn voltages. In the ideal winding case, each turn shares the same core flux, and will thus have equal single-turn voltages. The winding voltage will then be the sum of the  $N$  single-turn voltages (see equation 3.4).

$$\hat{V}_{emf} = -\frac{d\hat{\phi}}{dt} \quad 3.2$$

$$\hat{V}_{1-turn} = -\frac{d\hat{\phi}_{core}}{dt} \quad 3.3$$

$$\hat{V}_{winding} = N\hat{V}_{1-turn} = -N \frac{d\hat{\phi}_{core}}{dt} = -\frac{d(N\hat{\phi}_{core})}{dt} = -\frac{d(\hat{\psi})}{dt} \quad 3.4$$

$$\hat{\psi} = N\hat{\phi}_{core} \quad 3.5$$

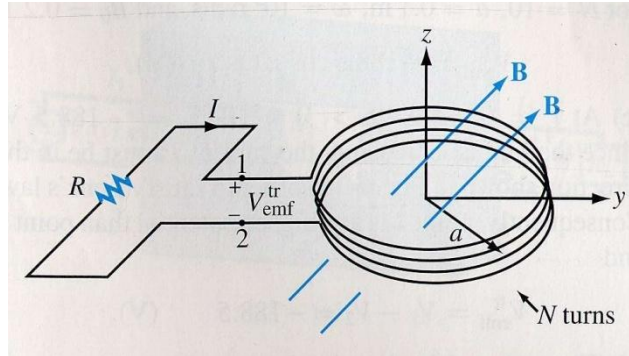


**FIG. 3.2. Winding depicting Faraday's Law** (Ulaby, Fawwaz T. Fundamentals of Applied Electromagnetics. Media Edition, ©2004. Pg. 237, Reprinted by permission of Pearson Education, Inc., Upper Sadle River, New Jersey) [5].

Flux linkages in the primary and secondary windings are given by the following expressions:

$$\hat{\psi}_1 = N_1\hat{\phi}_1 \quad 3.6$$

$$\hat{\psi}_2 = N_2\hat{\phi}_2 \quad 3.7$$

The core flux due to the primary is given by  $\hat{\psi}_1$  which is time dependent and in phase with the primary current  $\hat{I}_1$ . The primary and secondary windings are magnetically coupled by either a guiding core material that fills the core of both windings, or a geometry such that flux from the primary winding travels through the secondary winding. From Faraday's Law,

$$\hat{V}_2 = -\frac{d\hat{\psi}_2}{dt} = -N_2 \frac{d\hat{\phi}_2}{dt} \quad 3.8$$

The voltage on the secondary terminals will be the time derivative of the flux through the secondary winding times the number of secondary winding turns. Assuming ideal (total) magnetic coupling between the primary and secondary windings, the following is true:

$$\hat{\phi}_1 = \hat{\phi}_2 \text{ and } \frac{d\hat{\phi}_1}{dt} = \frac{d\hat{\phi}_2}{dt} \quad 3.9$$

and

$$\hat{V}_2 = -N_2 \frac{d\hat{\phi}_2}{dt} = -N_2 \frac{d\hat{\phi}_1}{dt} \quad 3.10$$

Using similar reasoning of Faraday's law, the following is also true:

$$\hat{V}_1 = -N_1 \frac{d\hat{\phi}_1}{dt} = -\frac{N_1}{N_2} N_2 \frac{d\hat{\phi}_1}{dt} = \frac{N_1}{N_2} \hat{V}_2 = a\hat{V}_2 \quad 3.11$$

where  $a = \frac{N_1}{N_2}$ , the turns ratio. This leads to the first ideal transformer relation between voltages.

$$\frac{\hat{V}_1}{\hat{V}_2} = \frac{N_1}{N_2} \quad 3.12$$

Assuming ideal power coupling, where the power into port 1 equals the power out of port 2, the following is true:

$$\begin{aligned}
P_1 &= P_2 & 3.13 \\
\hat{V}_1 \hat{I}_1 &= \hat{V}_2 \hat{I}_2 \\
a \hat{V}_2 \hat{I}_1 &= \hat{V}_2 \hat{I}_2 \\
\frac{\hat{I}_1}{\hat{I}_2} &= \frac{1}{a}
\end{aligned}$$

The final equation is the second ideal transformer relation between currents. Equations 3.12 and 3.13 can then be used to find an expression for the ideal primary input impedance given a load  $Z_L$  on the secondary winding. Thus, obvious uses of a transformer are stepping up and stepping down voltage and impedance matching in power applications by controlling the turn ratio.

$$\frac{\hat{V}_1}{\hat{I}_1} = \frac{a \hat{V}_2}{\frac{\hat{I}_2}{a}} = a^2 \frac{\hat{V}_2}{\hat{I}_2} = a^2 Z_L \quad 3.14$$

One conclusion from the above analysis is that transformers reject common-mode interference through magnetic coupling. From the above discussion, the secondary winding will have a voltage that is proportional to the time derivative of the core flux. This core flux is proportional to the primary current, and so the secondary voltage is proportional to the time derivative of the primary current. With the primary voltage composed of both differential-mode and common-mode signal, only the differential-mode part will result in primary currents. The common-mode part of the signal will be the same at both ends of the primary winding, resulting in no current and no flux contribution to the core.

An important thing to note is that this is not simply a DC rejection of signal. The common-mode signal can be any frequency and still contribute no primary winding current flow. With no common-mode currents, there will be no common-mode voltage signal on the secondary. However, the coupling of the primary voltages and currents to the secondary voltages

and currents obeys the equations above only in the idealized transformer model. The real transformer has winding resistance, core material losses, and leakage flux. In the next section, real transformers will be discussed and the equivalent circuit model will be derived.

### **3.2 The real transformer: Description and lumped equivalent circuit**

Idealized analyses are useful to evaluate the advantages or disadvantages of a concept or method, such as electromagnetically coupled circuits. As shown in the previous section, the ideal magnetically coupled transformer can control voltage and current to the secondary by changing only the turns ratio while delivering the same power, and can be used to match impedances.

However, the ideal transformer analysis neglects factors that affect performance under certain circumstances or are important when operation efficiency is being considered. The following device parameters need to be considered in a more complete analysis [6]:

1. **Winding resistance** – Wire windings are made from metals with finite conductivity. As the turn number approaches thousands, the length of wire has a non-negligible resistance. Thus, there will be a resistive contribution to the terminal voltage.
2. **Leakage flux** – In the ideal analysis, it is assumed that the same flux is shared by the primary winding and the secondary winding. However, with core materials of finite magnetic permeability, some flux from the primary winding will follow a path partly through the core and partly through the air. This is a parallel magnetic reluctance circuit, which can be compared to a parallel electric resistive circuit where some current flows through each branch (see FIG. 3.3).

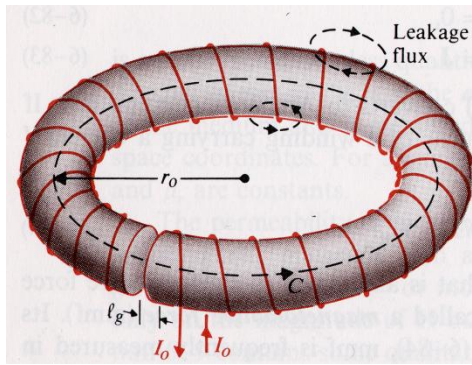


**FIG. 3.3. Torus core inductor with leakage flux.** (Cheng, David K. *Field and Wave Electromagnetics*, 2nd ed., ©1989, pg. 252, Reprinted by permission of Pearson Education, Inc., Upper Saddle River, New Jersey) [7]

Like the electric parallel circuit, the magnetic circuit flux will flow mostly

through the path of lower reluctance, the high permeability core. This flux that does take the path through the air will not couple the primary winding to the secondary, but instead will leak out of the core. For this reason, it is called *leakage flux* and will further change the relationship between the primary and secondary voltages and currents. The term *leakage inductance* will be used in later sections to represent the leakage flux that contributes to the self-inductance of the primary winding but does not couple to the secondary winding.

3. **Core losses** – The core material not only has finite magnetic permeability, but it also has finite resistance. Magnetic flux in the core causes currents to flow in circuitual paths around the cross section of the core (*eddy currents*), leading to ohmic losses.

Also, as will be discussed more in later sections, the core material is not perfectly soft, indicated by width in the materials hysteresis curve. This means that a field (*coercive field*) must be applied to return the material magnetization to zero, which requires energy. In AC applications when the material is being continually and cyclically switched, this switching energy is undesirably lost to material heating and must be accounted for in the device analysis.

In the following sections, the equivalent circuit of the real transformer is derived incorporating the winding resistance, the leakage flux, and the core losses.

### 3.2.1 Real transformer lumped equivalent circuit model: Frequency domain

In this section, the equivalent circuit for a real transformer will be derived by analyzing the Kirchoff's voltage law (KVL) equations on the primary and secondary windings in AC steady state. Below is a reference diagram for the real transformer.

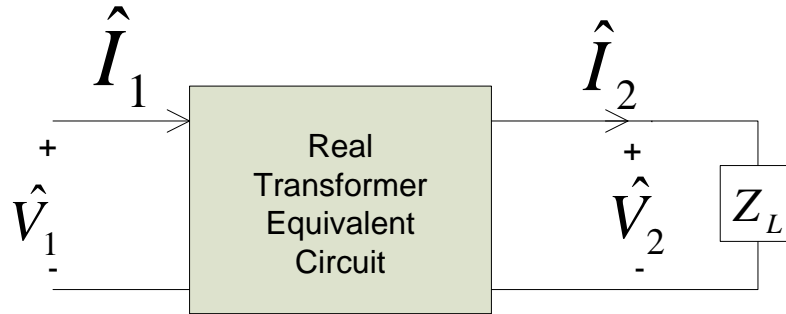


FIG. 3.4. Real transformer analysis diagram.

Performing KVL on the primary winding loop and the secondary winding loop gives rise to the following coupled circuit equations.

$$v_1(t) = R_1 i_1(t) + L_{11} \frac{di_1(t)}{dt} - M_{12} \frac{di_2(t)}{dt} \quad 3.15$$

$$v_2(t) = R_2 i_2(t) + L_{22} \frac{di_2(t)}{dt} - M_{21} \frac{di_1(t)}{dt} \quad 3.16$$

with the parameters defined below:

- 1)  $R_1$  - resistance of primary winding.
- 2)  $R_2$  - resistance of secondary winding.
- 3)  $L_{11}$  - inductance of primary winding.
- 4)  $L_{22}$  - inductance of secondary winding.
- 5)  $M_{12}$  - Mutual coupling factor (mutual inductance) of secondary to primary.
- 6)  $M_{21}$  - Mutual coupling factor (mutual inductance) of primary to secondary.

Taking equations 3.15 and 3.16 in AC steady state and using phasors for sinusoidal quantities gives the following forms.

$$\hat{V}_1 = R_1 \hat{I}_1 + j\omega L_{11} \hat{I}_1 - j\omega M_{12} \hat{I}_2 \quad 3.17$$

$$\hat{V}_2 = R_2 \hat{I}_2 + j\omega L_{22} \hat{I}_2 - j\omega M_{21} \hat{I}_1 \quad 3.18$$

Before continuing, the winding inductances should be discussed to elucidate how leakage flux is accounted for. Inductance is defined as the flux linkages divided by the current.

$$L = \frac{\hat{\psi}}{\hat{I}} \quad 3.19$$

Thus, the primary and secondary self inductances are defined as follows:

$$L_{11} = \frac{\hat{\psi}_1}{\hat{I}_1} = \frac{N_1 \hat{\phi}_1}{\hat{I}_1} = \frac{N_1 (\hat{\phi}_1^{core} + \hat{\phi}_1^{leakage})}{\hat{I}_1} = \frac{N_1 \hat{\phi}_1^{core}}{\hat{I}_1} + \frac{N_1 \hat{\phi}_1^{leakage}}{\hat{I}_1} = L_1^m + L_1^l \quad 3.20$$

$$L_1^m = \frac{N_1 \hat{\phi}_1^{core}}{\hat{I}_1} \quad 3.21$$

$$L_1^l = \frac{N_1 \hat{\phi}_1^{leakage}}{\hat{I}_1} \quad 3.22$$

$$L_{22} = \frac{\hat{\psi}_2}{\hat{I}_2} = \frac{N_2 \hat{\phi}_2}{\hat{I}_2} = \frac{N_1 (\hat{\phi}_2^{core} + \hat{\phi}_2^{leakage})}{\hat{I}_2} = \frac{N_2 \hat{\phi}_2^{core}}{\hat{I}_2} + \frac{N_2 \hat{\phi}_2^{leakage}}{\hat{I}_2} = L_2^m + L_2^l \quad 3.23$$

$$L_2^m = \frac{N_2 \hat{\phi}_2^{core}}{\hat{I}_2} \quad 3.24$$

$$L_2^l = \frac{N_2 \hat{\phi}_2^{leakage}}{\hat{I}_2} \quad 3.25$$

where the new inductances have the following definition

- 1)  $L_1^m$  - Primary main inductance. This is the larger fraction of the primary inductance and is proportional to core flux.
- 2)  $L_2^m$  - Secondary main inductance. This is the larger fraction of the secondary inductance and is proportional to core flux.
- 3)  $L_1^l$  - Primary leakage inductance – This is the smaller fraction of primary inductance and is proportional to leakage flux.
- 4)  $L_2^l$  - Secondary leakage inductance – This is the smaller fraction of secondary inductance and is proportional to leakage flux.

The primary mutual inductance  $M$  is defined as the secondary flux linkage of primary core flux  $\hat{\psi}_{21}$  divided by primary current  $\hat{I}_1$ .

$$M_{21} = \frac{\hat{\psi}_{21}}{\hat{I}_1} = \frac{N_2 \hat{\phi}_1^{Core}}{\hat{I}_1} \quad 3.26$$

Further manipulation of equation 3.26 isolates the primary main inductance.

$$M_{21} = \frac{N_2 \hat{\phi}_1^{Core}}{\hat{I}_1} = \frac{N_2}{N_1} \frac{N_1 \hat{\phi}_1^{Core}}{\hat{I}_1} = \frac{1}{a} L_1^m \quad 3.27$$

Similarly, manipulation with the secondary mutual inductance expression gives the following:

$$M_{12} = \frac{N_1 \hat{\phi}_2^{Core}}{\hat{I}_2} = \frac{N_1}{N_2} \frac{N_2 \hat{\phi}_2^{Core}}{\hat{I}_2} = a L_2^m \quad 3.28$$

Given the reciprocal nature of the geometry,

$$M_{12} = M_{21} = M \quad 3.29$$

Proceeding with the model analysis, it is the goal by manipulation of equations 3.17 and 3.18 to allow the isolation of a leakage flux term and get a coupled form that can be represented by an equivalent circuit.

First, equations 3.17 and 3.18 are rewritten to isolate the respective leakage inductances.

Adding the zero value quantities  $j\omega(aM\hat{I}_1 - aM\hat{I}_1)$  and  $j\omega\left(\frac{M\hat{I}_2 - M\hat{I}_2}{a}\right)$  to 3.17 and 3.18

respectively gives the following.

$$\hat{V}_1 = R_1 \hat{I}_1 + j\omega(L_{11} - aM)\hat{I}_1 - j\omega aM\left(\frac{\hat{I}_2}{a} - \hat{I}_1\right) \quad 3.30$$

$$\hat{V}_2 = R_2 \hat{I}_2 + j\omega\left(L_{22} - \frac{M}{a}\right)\hat{I}_2 - j\omega\frac{M}{a}(a\hat{I}_1 - \hat{I}_2) \quad 3.31$$

Substituting 3.27 into 3.30, and 3.28 into 3.31, the leakage inductance is isolated in the coupled circuit equations.

$$\hat{V}_1 = R_1 \hat{I}_1 + j\omega(L_1^l)\hat{I}_1 - j\omega aM\left(\frac{\hat{I}_2}{a} - \hat{I}_1\right) \quad 3.32$$

$$\hat{V}_2 = R_2 \hat{I}_2 + j\omega(L_2^l)\hat{I}_2 - j\omega\frac{M}{a}(a\hat{I}_1 - \hat{I}_2) \quad 3.33$$

Multiplying equation 3.33 by the turn ratio 'a' scales the physical quantities.

$$\hat{V}_1 = R_1 \hat{I}_1 + j\omega(L_1^l)\hat{I}_1 - j\omega aM\left(\frac{\hat{I}_2}{a} - \hat{I}_1\right) \quad 3.34$$

$$a\hat{V}_2 = a^2 R_2 \frac{\hat{I}_2}{a} + j\omega(a^2 L_2^l)\frac{\hat{I}_2}{a} - j\omega aM\left(\hat{I}_1 - \frac{\hat{I}_2}{a}\right) \quad 3.35$$

The new scaled quantities are as follows:

$$\hat{V}_2' = a\hat{V}_2 \quad 3.36$$

$$R_2' = a^2 R_2 \quad 3.37$$

$$L_2^l = a^2 L_2^l \quad 3.38$$

$$\hat{I}_2' = \frac{\hat{I}_2}{a} \quad 3.39$$

Substituting the scaled quantities, equation 3.34 and 3.35 become

$$\hat{V}_1 = R_1 \hat{I}_1 + j\omega(L_1^l) \hat{I}_1 - j\omega aM(\hat{I}'_2 - \hat{I}_1) \quad 3.34$$

$$\hat{V}'_2 = R'_2 \hat{I}'_2 + j\omega(L_2^l) \hat{I}'_2 - j\omega aM(\hat{I}_1 - \hat{I}'_2) \quad 3.35$$

More substitutions can be made in 3.34 and 3.35:  $aM = a\left(\frac{1}{a}L_1^m\right) = L_1^m$ ,  $X_{12} = \omega L_1^m$ ,  $X_1^l = \omega L_1^l$ ,

$X_2^l = \omega L_2^l$  and equations 3.34 and 3.35 become

$$\hat{V}_1 = R_1 \hat{I}_1 + jX_1^l \hat{I}_1 - j\omega X_{12}(\hat{I}'_2 - \hat{I}_1) \quad 3.40$$

$$\hat{V}'_2 = R'_2 \hat{I}'_2 + j(X_2^l) \hat{I}'_2 - j\omega X_{12}(\hat{I}_1 - \hat{I}'_2) \quad 3.41$$

In equations 3.40 and 3.41, the leakage inductance term has been isolated. Reversing KVL on the coupled equations 3.40 and 3.41, an equivalent circuit can be formed. However, loading the secondary takes extra considerations when using scaled quantities in the circuit. Consider the load impedance as shown below.

$$Z_L = \frac{\hat{V}_2}{\hat{I}_2} = \frac{\hat{V}'_2}{a^2 \hat{I}'_2} = \frac{Z'_L}{a^2}$$

Thus,

$$Z'_L = a^2 Z_L \quad 3.42$$

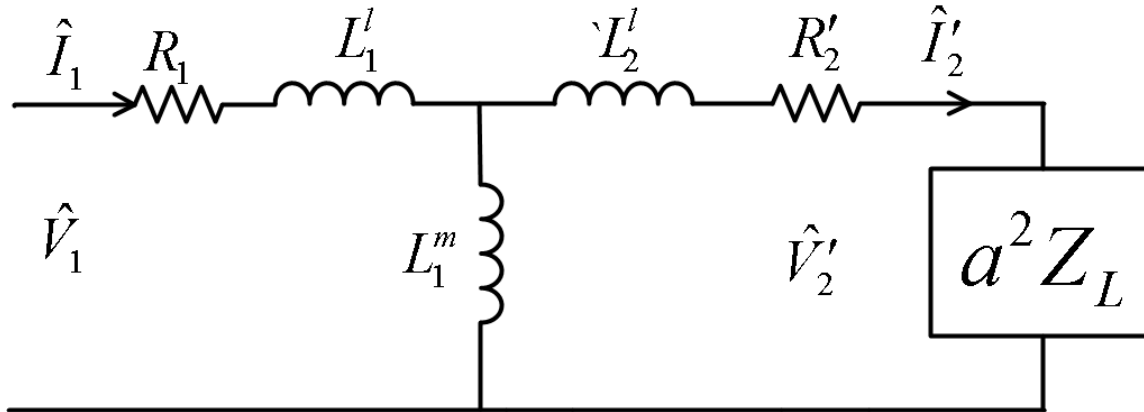


FIG. 3.5. Real transformer equivalent circuit.

FIG. 3.5 shows the equivalent circuit that results from frequency domain (AC steady state) analysis of a transformer's coupled circuit equations. This is not the final circuit, however, as will be shown later in this chapter. Further modifications will be made to accommodate prevailing physical effects from new transformer implementations.

### 3.2.2 Losses in magnetic core materials

Neglected in the previous analysis of real transformers are power losses in the core material. In the following section, the primary causes of core loss will be discussed, as well as how to account for them in the equivalent circuit.

It is the main purpose of the magnetic core material of a transformer to guide flux between windings with a low reluctance path. Magnetic reluctance of a magnetic material is inversely proportional to the material's magnetic permeability (see equation 3.43). Highly permeable materials exhibit low magnetic reluctance. High permeability core material also has the benefit of allowing high total flux to couple between the windings.

$$\text{Reluctance}_{\text{path}} = \frac{\text{length}_{\text{path}}}{\mu_r \mu_0 \text{Area}_{\text{cross-section}}}$$

Magnetic materials can be classified generally into three types: *diamagnetic* (bismuth, gold, etc), *paramagnetic* (aluminum, titanium, etc), and ferromagnetic (nickel, cobalt, iron). Diamagnetic materials have magnetization in slight opposition to the applied magnetic field, paramagnetic materials have magnetization slightly enhancing the applied magnetic field, and ferromagnetic materials have magnetizations that greatly enhance the applied magnetic field but with complex behavior such as non-linearity, hysteresis, and saturation. Diamagnetic materials have lower relative permeability than air ( $\sim 0.9998$ ), and paramagnetic materials have a relative permeability only slightly higher than air ( $\sim 1.0005$ ). For effective flux guiding, ferromagnetic materials are required, with a relative permeability from 250 to 100,000. The  $B$ - $H$  curve for ferromagnetic cores is discussed in the next section.

Ferromagnetic cores sink power primarily by two mechanisms: eddy currents and hysteresis. The consideration of these mechanisms is absent in the ideal transformer analysis since it is assumed that the core material has zero conductivity (no eddy currents) and is a perfectly soft magnetic material (requires no energy to switch magnetically). The following subsections will discuss in detail the dependencies of these loss mechanisms and how the loss can be incorporated into the equivalent circuit.

### 3.2.2.1 Hysteresis loss

Ferromagnetic materials are described as being magnetically “hard” or “soft”. These distinctions come from the materials hysteresis curve. Below is a generic ferromagnetic hysteresis curve, where the material magnetization,  $\vec{M}$ , is on the vertical axis and the applied

magnetic field,  $\vec{H}$ , is on the horizontal axis.  $\vec{M}$  is in units of magnetic flux density (Webers per square meter), making the total flux density ( $\vec{B}$ ) for a reasonably large volume within the material as follows.

$$\vec{B} = \vec{M} + \mu_0 \vec{H} \quad 3.44$$

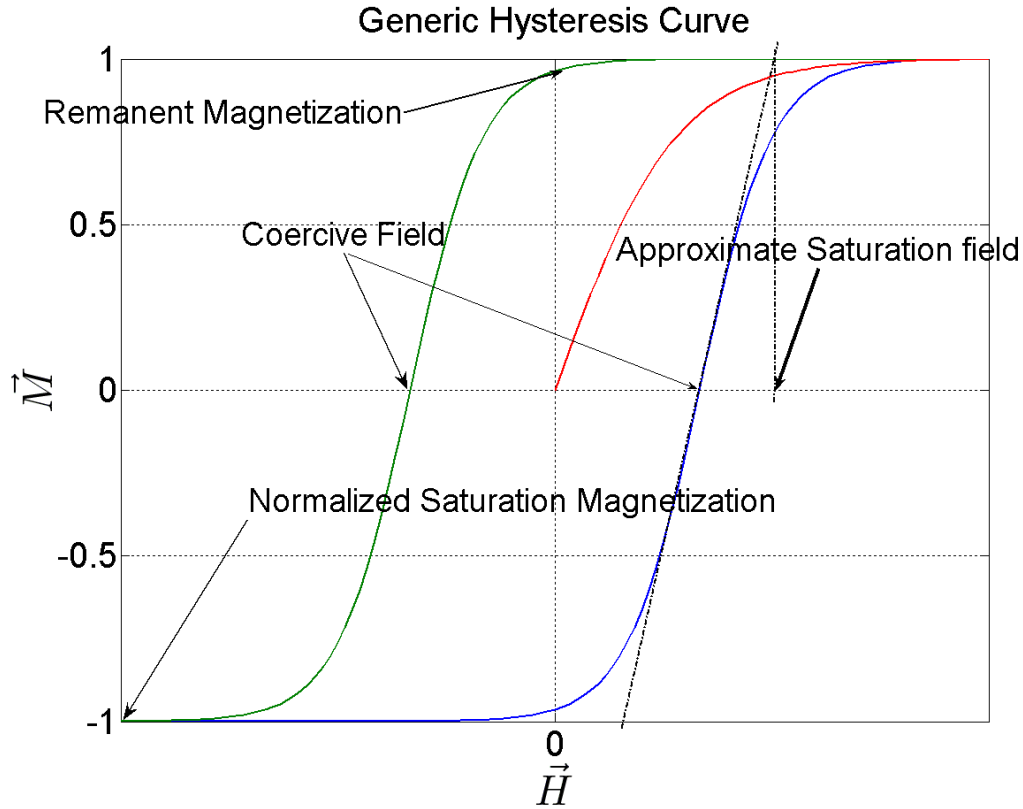


FIG. 3.6. Generic ferromagnetic material hysteresis curve

Equation 3.44 is written to isolate the material magnetization term. This equation can be rewritten to factor out the applied magnetic field, knowing that the material magnetization is proportional to the applied magnetic field, as shown in equation 3.45.

$$\vec{B} = \vec{M} + \mu_0 \vec{H} = \mu_0 \chi_m \vec{H} + \mu_0 \vec{H} = \mu_0 (1 + \chi_m) \vec{H} \quad 3.45$$

In equation 3.45,  $\vec{M} = \mu_0 \chi_m \vec{H}$  and  $\chi_m$  is the magnetic susceptibility specific to the material.

Equation 3.45 gives the net flux density that would be observed in a material with a given

applied magnetic field which is the sum of the material magnetization flux density and the applied flux density. For the purpose of material hysteretic classification, however, only the material magnetization ( $\vec{M} = \mu_0 \chi_m \vec{H}$ ) is important.

Hard materials usually exhibit wide hysteresis curves, with large coercive fields and generally high saturation fields. Soft materials have narrow hysteresis curves, with low coercive fields and generally small saturation fields. Note, however, that both materials could have high remnant magnetization. Below in FIG. 3.7 are the hysteresis curves for materials that are relatively magnetically hard and soft.

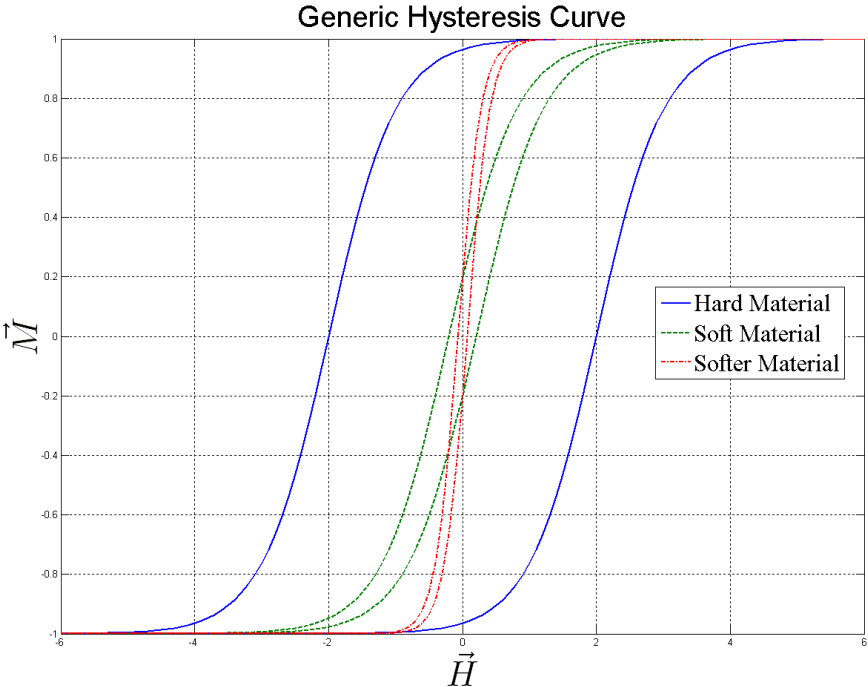


**FIG. 3.7. Generic hysteresis curves for relatively hard, soft, and softer magnetic materials**

Hard magnetic materials are useful for making permanent magnets, magnetic media, and other applications requiring magnets that do not change magnetization with ambient magnetic fields. These materials require large fields to set the magnetization, but also require a large

opposing field to demagnetize them. Thus, they can be placed in environments with considerably large stray magnetic fields and still retain their original magnetization.

Soft magnetic materials are used in magnetic recording heads, electromagnetic machines, and other flux guided devices. Soft materials are suited to applications that require the material magnetization to reverse direction often in use, such as transformer cores. Soft magnetic materials are also necessary for sensitive applications such as recording heads where the material magnetization must follow the applied magnetic field closely around the zero field point.

Electromagnetic machines use flux guiding as part of their principles of operation. This flux is time-varying, and will reverse the magnetization of the material at high frequency. As will be explained in the following section, hard magnetic materials are hard because of the large amount of energy needed to switch the direction of magnetic domains. Soft materials require low switching energies, and thus do not exhibit high magnetic losses when guiding time-varying magnetic flux in machines.

Hysteresis energy losses arise from energy expended in changing the magnetization direction of the material. Some of this energy is briefly stored as potential energy, but most is lost to thermal dissipation [8]. There is a magnetic energy associated with a volume of material under an applied magnetic field. This per volume energy is equal to the product of the applied field and the magnetic flux density of the material.

$$Energy = \vec{M} \cdot \vec{H} * Volume \quad 3.46$$

Switching energy is the energy required to reverse the magnetization of a material, calculated as the integral of the product  $\vec{H} \cdot d\vec{M}$  as the material goes between flux saturation in both directions.

$$Energy_{Switching} = Volume \int_{-M_{sat}}^{M_{sat}} \vec{H} \cdot d\vec{M} \quad 3.47$$

This energy is hysteresis loss, and depending on the switching frequency, a power loss can be calculated. A useful assumption can be made which makes this discussion on hysteresis loss more quantitative. The switch energy integral of equation 3.47 for an entire switch cycle (from  $-M_{sat}$  to  $M_{sat}$  and back to  $-M_{sat}$ ) is equal to the area of the hysteresis loop. In either region of the integral, the integral is a measure of the area between the curve and the y-axis. Assuming that the area of the hysteresis loop is known, the following energy-loss-per-cycle equation can be written.

$$Energy_{Cycle\_Loss} = Volume * A_{loop} \quad 3.48$$

With a switching frequency  $f$ , the power loss can be written as follow.

$$P_{loss} = \frac{Energy_{Cycle\_Loss}}{T_{Cycle}} = Volume * f * A_{loop} \quad 3.49$$

This can be modified further, approximating the loop area with the peak flux density.

$$A_{loop} \approx \eta B_{max}^n \quad 3.50$$

$\eta$  and  $n$  are determined empirically for a material.  $n$  can vary from 1.5 to 2.5. Thus, the power loss from hysteresis is given by

$$P_{loss,hysteresis} \approx Volume * f * \eta B_{max}^n \quad 3.51$$

The important conclusion from the hysteresis loss analysis is the dependence of the loss on the area of the hysteresis loop. From this, it is clear that soft materials with very narrow loops

will exhibit considerably less loss in switching than hard materials with broad hysteresis loops [9].

Besides hysteresis losses in domain switching, magnetic core materials also possess ohmic losses from eddy currents. Eddy current losses will be discussed in the next section.

### 3.2.2.2 Eddy current loss

Magnetic cores can be made from pure metallic elements including nickel, cobalt, and iron, alloys of these ferromagnetic metals, or ferrites. It will be shown in the following section that power is lost by circulating currents that come from loops of electric fields that surround the magnetic flux lines guided by the core. Thus, by reducing the conductivity of the core, the circulating currents will be reduced along with power losses.

Beginning with the differential form of Faraday's law, the time-varying magnetic flux in the core can be related to the circulating currents.

$$\nabla \times \vec{E} = -\frac{\partial \vec{B}}{\partial t} \quad 3.52$$

Integrating 3.52 over a bounded surface gives the following:

$$\int_s \nabla \times \vec{E} \cdot d\vec{s} = \int_s -\frac{\partial \vec{B}}{\partial t} \cdot d\vec{s} \quad 3.53$$

Using Stoke's theorem, the surface integral of the curl of electric field in 3.53 can be changed to a circulation integral.

$$\int_s \nabla \times \vec{E} \cdot d\vec{s} = \oint_c \vec{E} \cdot d\vec{l} = -\frac{\partial}{\partial t} \int_s \vec{B} \cdot d\vec{s} = -\frac{\partial \phi}{\partial t} \quad 3.54$$

From this form of Faraday's law, some physical considerations about eddy currents in ferromagnetic cores become clear. With a time varying magnetic flux in the core, equation 3.54 is non-zero. Thus, the circulation of the electric field is non-zero. In electrostatics, the electric field is conservative, so the integral of  $\vec{E} \cdot d\vec{l}$  around any path that returns to the initial point will be zero. However, with a time dependent flux, the circulation (which is a line integral that starts and ends at the same point) of the electric field is not zero. Recalling the electric field and voltage relationship shown in equation 3.55, this non-zero circulation indicates a potential difference between the two ends of the path. Where there exists a potential difference and a material with finite conductivity, there will exist a current and ohmic loss.

$$\int_a^b \vec{E} \cdot d\vec{l} = V(b) - V(a) \quad 3.55$$

For those engineers with vivid imaginations, it can be pictured that the net electric field along a closed path will give rise to current density by

$$\sigma \vec{E} = \vec{J} \quad 3.56$$

where  $\sigma$  is the material conductivity and  $\vec{J}$  is a current density. Consider, then, the continuity equation,

$$\nabla \cdot \vec{J} = 0 \quad 3.57$$

Since the time-varying flux is non-zero, the electric field must be non-zero (see Equation 3.54).

Since the electric field is non-zero, the current density must be non-zero (see equation 3.56).

Since the current density is non-zero, then from equation 3.57 the currents must follow closed paths within the material to have zero divergence.

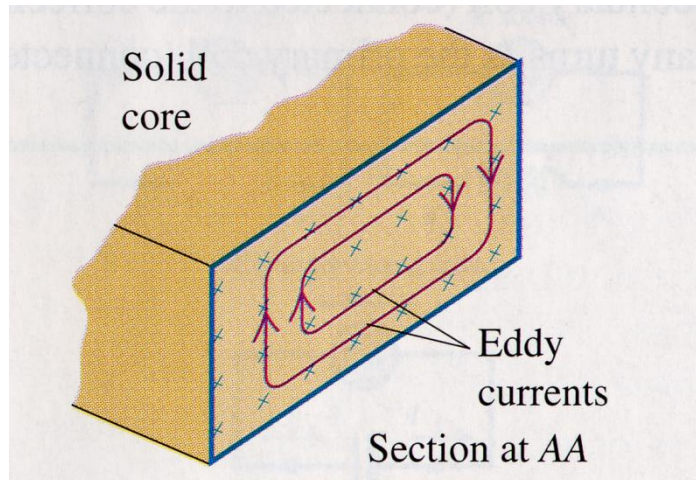


**FIG. 3.8. Eddy currents diagram.** (Young/ Freedman/Sandin/Ford. Sear's and Zemansky's University Physics, 10<sup>th</sup> ed., (c)2000, pg. 1016, Reprinted by permission of Pearson Education, Inc., Upper Sadle River, New Jersey) [10]

To further develop the expression for eddy current loss, consider a core with a rectangular cross section where magnetic flux is perfectly uniform and perpendicular to the cross section. Consider FIG. 3.9 below.

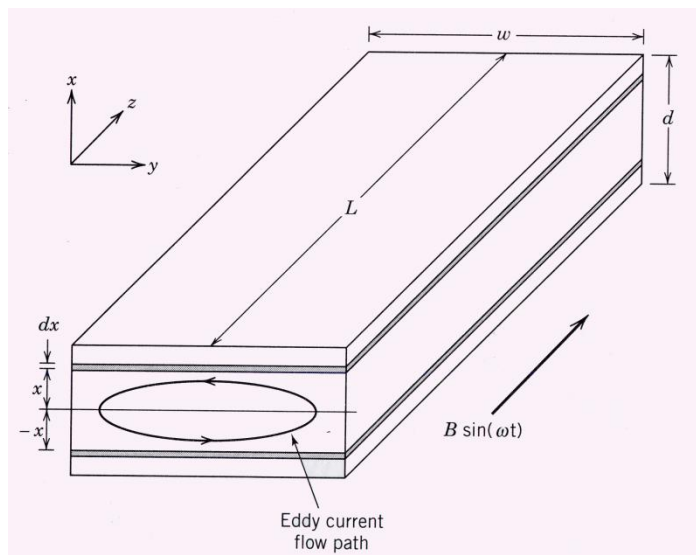


**FIG. 3.9. Diagram of core material with flux and eddy currents.** [11]

Assuming an axial core flux density defined by

$$\vec{B}(t) = B_0 \sin(\omega t) \quad 3.58$$

equation 3.54 can be evaluated.

$$\oint_c \vec{E} \cdot d\vec{l} = -\frac{\partial \phi}{\partial t} = -\frac{\partial}{\partial t} \left( \int_s B_0 \sin(\omega t) \cdot ds \right) = B_0 \omega \cos(\omega t) \int_s ds = B_0 \omega \cos(\omega t) (2xw) \quad 3.59$$

To evaluate the total resistance along the current path ( $r_p$ ), a high aspect ratio core is made.

Assuming  $d \ll w$ ,  $r_p$  can be approximated as follows:

$$r_p = \rho_{core} \frac{l}{A} = \rho_{core} \frac{2w + 4x}{Ldx} \approx \rho_{core} \frac{2w}{Ldx} \quad 3.60$$

The eddy current power loss of a single current loop is now given by substituting equation 3.59

for potential difference around the loop giving the following.

$$dP_{loss,eddy} = \frac{v^2(t)}{r_p} \cong \frac{\left( \oint_c \vec{E} \cdot d\vec{l} \right)^2}{\rho_{core} \frac{2w}{Ldx}} = \frac{B_0^2 \omega^2 \cos^2(\omega t) (4x^2 w^2)}{\rho_{core} \frac{2w}{Ldx}} \quad 3.61$$

The total power loss of all current loops is given by the integral of all loops.

$$\langle P_{loss,eddy} \rangle = \frac{4}{T} \int_0^T \int_0^{d/2} \frac{B_0^2 \omega^2 \cos^2(\omega t) (x^2 w^2) Ldx}{\rho_{core} 2w} dt = \frac{2}{T} \int_0^T \int_0^{d/2} \frac{B_0^2 \omega^2 \cos^2(\omega t) (x^2 w^2) Ldx}{\rho_{core}} dt =$$

$$\begin{aligned}
&= \frac{2B_0^2 wL \omega^2}{T \rho_{core}} \int_0^T \cos^2(\omega t) \left[ \int_0^{d/2} (x^2) dx \right] dt = \frac{2B_0^2 wL \omega^2}{T \rho_{core}} \int_0^T \cos^2(\omega t) \left[ \frac{d/2}{0} \left| \frac{x^3}{3} \right| \right] dt \\
&= \frac{2B_0^2 wL \omega^2 d^3}{24 T \rho_{core}} \int_0^T \cos^2(\omega t) dt = \frac{B_0^2 wL \omega^2 d^3}{24 \rho_{core}} = \frac{V B_0^2 \omega^2 d^2}{24 \rho_{core}} = \langle P_{loss, eddy} \rangle
\end{aligned} \tag{3.62}$$

Equation 3.62 represents the time averaged eddy current loss in a core of volume  $V$ , with peak magnetic flux density of  $B_0$ , thickness  $d$ , and resistivity  $\rho_{core}$ . To reduce eddy current losses, one could either increase resistivity, reduce volume, reduce flux density strength, or make the core thinner (reduce  $d$ ).

This eddy current equation illuminates the purpose of the different core designs. In an effort to reduce  $d$ , cores are laminated to take one sheet of thickness  $d$  and make  $n$  sheets of thickness  $\frac{d}{n}$ . Consider how this changes equation 3.62.

$$\frac{V B_0^2 \omega^2 \left( \frac{d}{n} \right)^2}{24 \rho_{core}} = \frac{\left( n(wL \frac{d}{n}) \right) B_0^2 \omega^2 \left( \frac{d}{n} \right)^2}{24 \rho_{core}} = \frac{V B_0^2 \omega^2 d^2}{n^2 24 \rho_{core}} = \langle P_{loss, eddy} \rangle \tag{3.63}$$

Laminating by a factor of  $n$  reduces losses by a factor  $n^2$ .

Another method to reduce eddy current loss is to increase the core resistivity without greatly compromising the magnetic permeability. To that end, core materials have been doped with semiconductor material to increase resistivity without impacting the magnetic moments.

Ferrite materials have high permeability as well as high resistivities; up to 10,000 Ohms per meter. Ferrites, however, are not ferromagnetic but ferrimagnetic, resulting in saturation magnetization that is about a tenth of ferromagnetic materials. One type of ferrite is a complex

crystalline magnetic spinel structure with the formula  $XO \cdot Fe_2O_3$  where X is a divalent metallic ion such as iron, cobalt, nickel, manganese, magnesium, zinc, or cadmium [12]. Each of these core types contains magnetic metals, but the crystal structure containing iron oxide causes the resistivity to be much higher than bulk metals. These high resistivities make ferrites ideal core materials where power conservation and high coupling coefficient is critical. A popular ferrite for signal transformers is Mn-Zn ferrite. FIG. 3.10 shows a theoretical dispersion relation for Mn-Zn ferrite.

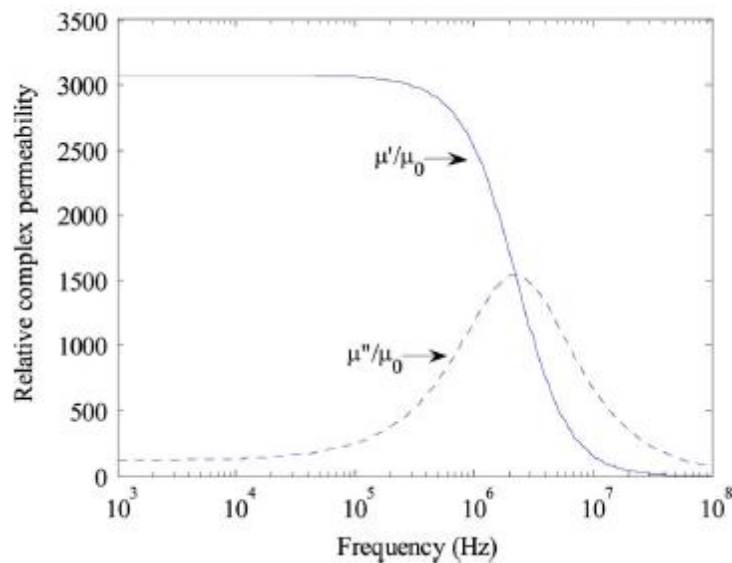


FIG. 3.10. Mn-Zn complex magnetic permeability dispersion curve. [13]

From FIG. 3.10, one can see that as signal frequencies increase above 1 MHz, the core material becomes unstable and loses permeability as the real part of permeability falls. Other techniques must be exercised at high frequencies to maintain coupling which will be discussed in later sections.

As interesting as techniques to reduce core losses are, the purpose of this discussion is to understand the origins of loss. Now that both eddy current loss and hysteresis loss have been

expressed in terms of physical or controllable quantities, these losses can be included in the model. Note how both hysteresis loss (equation 3.51) and eddy current loss (equation 3.63) both depend on physical parameters and peak magnetic flux density. Assuming flux density is constant over a cross-section of the core, the electro motive force (*emf*) voltage from the flux that couples the primary to the secondary can be expressed in the following way:

$$\begin{aligned}
 V_{emf}(t) &= -\frac{\partial \psi}{\partial t} = -\frac{\partial \phi_c}{\partial t} = -\frac{\partial}{\partial t} \int_s \vec{B}(t) \cdot d\vec{s} \approx -A_{cross} \frac{\partial}{\partial t} \vec{B}(t) \\
 &= -A_{cross} \frac{\partial}{\partial t} B_0 \sin(\omega t) = -A_{cross} \omega B_0 \cos(\omega t)
 \end{aligned}
 \tag{3.64}$$

Thus, the core flux *emf* is proportional to the peak flux density in the core. From 3.64, the peak flux *emf* can be expressed as

$$|V_{emf}| = \omega B_0 A_{cross} = \kappa B_0
 \tag{3.65}$$

$$\frac{|V_{emf}|}{\kappa} = B_0
 \tag{3.66}$$

Substituting 3.66 back into 3.51 and 3.63, the core loss can be expressed as follows:

$$P_{loss,hysteresis} \approx Vol * f * \eta B_{max}^n = \frac{Vol * f * \eta}{\kappa^n} |V_{emf}|^n
 \tag{3.67}$$

$$\langle P_{loss,eddy} \rangle = \frac{VB_0^2 \omega^2 d^2}{n^2 24 \rho_{core}} = \frac{V |V_{emf}|^2 \omega^2 d^2}{\kappa^2 n^2 24 \rho_{core}} \quad 3.68$$

Recall that  $n$  in the hysteresis loss expression can be from 1.5 and 2.5 and is determined empirically for a material. For this analysis,  $n$  is assumed to be 2 for a first approximation.

$$P_{loss,core} = P_{loss,hysteresis} + P_{loss,eddy} \\ \approx |V_{emf}|^2 \left[ \frac{Vol * f * \eta}{\kappa^2} + \frac{V \omega^2 d^2}{\kappa^2 n^2 24 \rho_{core}} \right] = \beta |V_{emf}|^2 \quad 3.69$$

Note that  $\beta$  is only dependent on frequency and physical parameters. For a constant frequency as in power and mechanical applications,  $\beta$  is constant.

$$P_{loss,core} = \beta |V_{emf}|^2 = \frac{|V_{emf}|^2}{R_e} \quad 3.70$$

and

$$R_e = \frac{|V_{emf}|^2}{P_{loss,core}} = \frac{1}{\beta} \quad 3.71$$

What has been done in equations 3.70 and 3.71 is the replacement of the constant of

proportionality  $\beta$  with an equivalent resistance  $R_e$ , recalling  $P_{resistor} = \frac{V^2}{R}$ . Placing this resistor

properly in the equivalent circuit model in parallel with the mutual inductance is a good

approximation to the real core losses exhibited in the device. The complete circuit diagram is

given below.

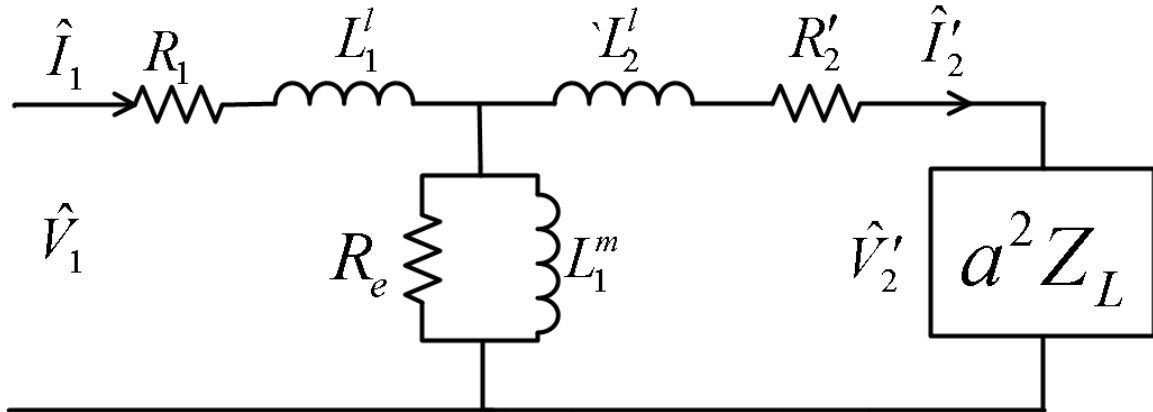


FIG. 3.11. Transformer equivalent circuit with core loss resistor.

In the next section, another conceptual approach to deriving the equivalent circuit model that was discovered as part of this project is presented.

### 3.2.3 Alternate derivation of lumped element transformer model

An alternative technique for the derivation of the lumped element transformer equivalent circuit has been presented [14] as part of this research. The derivation approaches differently in how the coupled circuit equations are first presented. Rather than taking the superposition of self inductance and mutual inductance as contributing to the voltage, this approach takes voltage contributions from leakage flux and core flux. Both approaches account for the total flux.

However, the second approach is more closely related to the physical nature of the device and the mechanism of Faraday's Law emf from flux.

When considering the windings of the transformer, there are two mechanisms for potential to appear across the terminals: ohmic loss and Faraday's law emf. The ohmic potential is from the winding resistance and the current flowing through the wires. The source of the Faraday's law emf is magnetic flux.

Given the two ways voltage can appear across the winding terminals, the coupled circuit equations can be written as follows:

$$v_1(t) = R_1 i_1(t) + V_{1,emf}(t) \quad 3.72$$

$$v_2(t) = R_2 i_2(t) + V_{2,emf}(t) \quad 3.73$$

The magnetic flux that gives rise to the emf exists as both *core flux* that is shared by the primary and secondary and *leakage flux*, which does not link the primary and the secondary.

$$V_{1,emf}(t) = V_{1,emf}^{leakage}(t) + V_{1,emf}^{core}(t) = -\frac{d\phi_1^{leakage}(t)}{dt} - \frac{d\phi_1^{core}(t)}{dt} \quad 3.74$$

$$V_{2,emf}(t) = V_{2,emf}^{leakage}(t) + V_{2,emf}^{core}(t) = -\frac{d\phi_2^{leakage}(t)}{dt} - \frac{d\phi_2^{core}(t)}{dt} \quad 3.75$$

Further analysis of the flux in equations 3.74 and 3.75 gives the following expressions in terms of inductances.

$$V_{1,emf}(t) = -\frac{d\phi_1^{leakage}(t)}{dt} - \frac{d\phi_1^{core}(t)}{dt} = -\frac{d(L_1^l i_1(t))}{dt} - \frac{d(N_1 AB^{core}(t))}{dt} \quad 3.76$$

$$V_{2,emf}(t) = -\frac{d\phi_2^{leakage}(t)}{dt} - \frac{d\phi_2^{core}(t)}{dt} = -\frac{d(L_2^l i_2(t))}{dt} - \frac{d(N_2 AB^{core}(t))}{dt} \quad 3.77$$

In the case of Ethernet transformers, the turns ratio of the primary and secondary windings will be equal. The emf contribution from the core flux will be the same in both the primary and the secondary windings. Thus, equations 3.76 and 3.77 become

$$V_{1,emf}(t) = -\frac{d(L_1^l i_1(t))}{dt} + v_0(t) \quad 3.78$$

and

$$V_{2,emf}(t) = -\frac{d(L_2^l i_2(t))}{dt} + v_0(t) \quad 3.79$$

Evaluating equations 3.78 and 3.79 in AC steady state and using phasor notation, 3.78 and 3.79

become

$$\hat{V}_{1,emf} = j\omega L_1^l \hat{I}_1 + \hat{V}_0 \quad 3.80$$

and

$$\hat{V}_{2,emf}(t) = j\omega L_2^l \hat{I}_2 + \hat{V}_0 \quad 3.81$$

To determine  $\hat{V}_0$ , the core flux must be found using Ampere's law and assuming uniform flux density over the cross section.

$$\begin{aligned} \oint_l \hat{B}_0 \cdot d\vec{l} &= \oint_l \frac{\hat{\phi}_0}{A} \cdot d\vec{l} = \frac{\hat{\phi}_0 l}{A} = \mu(\omega) \hat{I}_{encl} = \mu(\omega)(\hat{I}_1 + \hat{I}_2) \Rightarrow \\ \hat{\phi}_0 &= \frac{\mu(\omega) A (\hat{I}_1 + \hat{I}_2)}{l} \end{aligned} \quad 3.82$$

where  $A$  is the core cross sectional area and it is recognized that the core permeability is complex, dispersive, and linear. ' $l$ ' represents the circumferential path length around the toroid within the cross section. Assuming the permeability is linear is a fair assumption since the material is magnetically soft, the flux magnitude is small and far from saturating the material and the frequencies are sufficiently low such that the magnetization follows the applied field.

$$\mu(\omega) = \mu'(\omega) + j\mu''(\omega) \quad 3.83$$

The emf from the core flux can then be expressed as

$$\begin{aligned} \hat{V}_0 &= -\frac{d\hat{\phi}_0}{dt} = \frac{-j\omega(\mu'(\omega) + j\mu''(\omega))A(\hat{I}_1 + \hat{I}_2)}{l} \quad 3.84 \\ &= \left( \frac{-j\omega\mu'(\omega)A}{l} + \frac{\omega\mu''(\omega)A}{l} \right) (\hat{I}_1 + \hat{I}_2) = Z_0(\omega)(\hat{I}_1 + \hat{I}_2) \end{aligned}$$

Equation 3.84 shows that the emf resulting from the core flux is proportional to the sum of the current of the primary and secondary windings by an effective core impedance,  $Z_0(\omega)$ .

The core impedance is complex, and represents both resistive and reactive components. Thus, the core impedance can be represented as a series resistor and inductor,  $R_0(\omega)$  and

$$X_0(\omega) = \omega L_0(\omega).$$

$$R_0(\omega) = \frac{\omega\mu''(\omega)A}{l} \quad 3.85$$

$$X_0(\omega) = \frac{-\omega\mu'(\omega)A}{l} \quad 3.86$$

The coupled circuit equations now become

$$\hat{V}_1 = R\hat{I}_1 + j\omega L\hat{I}_1 + R_0(\omega)(\hat{I}_1 + \hat{I}_2) - j\omega L_0(\omega)(\hat{I}_1 + \hat{I}_2) \quad 3.87$$

and

$$\hat{V}_2 = R\hat{I}_2 + j\omega L\hat{I}_2 + R_0(\omega)(\hat{I}_1 + \hat{I}_2) - j\omega L_0(\omega)(\hat{I}_1 + \hat{I}_2) \quad 3.88$$

where  $L_1^l \approx L_2^l = L$ .

The equivalent circuit can be intuitively drawn from these equations as shown below.

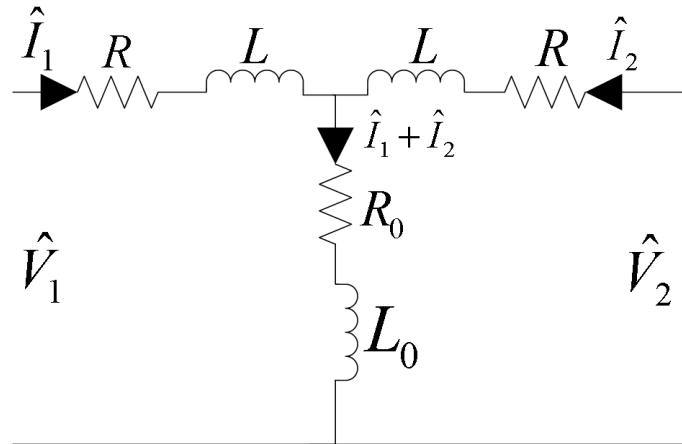


FIG. 3.12. Equivalent circuit derived by alternative method.

The above form of the equivalent circuit has a series R-L core branch. The more familiar equivalent circuit is presented as a parallel R-L core branch. However, the two representations are interchangeable. The same impedance can be represented either way.

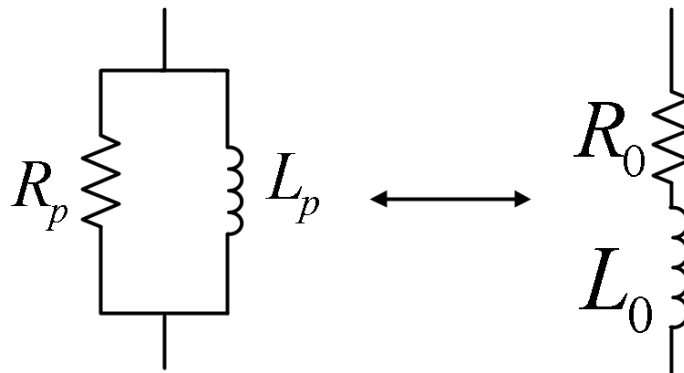


FIG. 3.13. Parallel to Series impedance conversion.

$$\begin{aligned}
Z_s &= R_0 + j\omega L_0 = & 3.89 \\
Z_p &= R_p \parallel j\omega L_p = \frac{j\omega L_p R_p}{j\omega L_p + R_p} = \\
&= \frac{j\omega L_p R_p (-j\omega L_p + R_p)}{\omega^2 L_p^2 + R_p^2} = \frac{\omega^2 L_p^2 R_p + j\omega L_p R_p^2}{\omega^2 L_p^2 + R_p^2}
\end{aligned}$$

By matching the real and imaginary parts of equation 3.89, the two equations can be used to solve for the series element values in terms of the parallel element values and vice versa.

$$R_0 = \frac{\omega^2 L_p^2 R_p}{\omega^2 L_p^2 + R_p^2} \quad 3.90$$

$$L_0 = \frac{L_p R_p^2}{\omega^2 L_p^2 + R_p^2} \quad 3.91$$

$ \begin{aligned} L_0 &= \frac{L_p R_p^2}{\omega^2 L_p^2 + R_p^2} \Rightarrow \\ \omega^2 L_0 L_p^2 + L_0 R_p^2 &= L_p R_p^2 \Rightarrow \\ \omega^2 L_0 L_p^2 + (L_0 - L_p) R_p^2 &= 0 \Rightarrow \\ R_p &= \frac{\sqrt{-4(\omega^2 L_p^2 L_0)(L_0 - L_p)}}{2(L_0 - L_p)} = \sqrt{\frac{-4(\omega^2 L_p^2 L_0)(L_0 - L_p)}{4(L_0 - L_p)^2}} = \omega L_p \sqrt{\frac{L_0}{(L_p - L_0)}} \end{aligned} $	3.92
---	------

$$\begin{aligned}
R_0 &= \frac{\omega^2 L_p^2 R_p}{\omega^2 L_p^2 + R_p^2} \Rightarrow & 3.93 \\
R_0 &= \frac{\omega^2 L_p^2 R_p}{\omega^2 L_p^2 + \frac{\omega^2 L_p^2 L_0}{(L_p - L_0)}} = \frac{R_p}{\frac{L_p - L_0 + L_0}{(L_p - L_0)}} = \frac{R_p (L_p - L_0)}{L_p} \Rightarrow \\
R_0^2 &= \frac{R_p^2 (L_p - L_0)^2}{L_p^2} = \frac{\left( \omega^2 L_p^2 \frac{L_0}{(L_p - L_0)} \right) (L_p - L_0)^2}{L_p^2} = \omega^2 L_0 (L_p - L_0) \Rightarrow \\
L_p &= \frac{R_0^2}{\omega^2 L_0} + L_0
\end{aligned}$$

Plugging equation 3.93 back into equation 3.92 gives the following.

$$\begin{aligned}
R_p &= \omega L_p \sqrt{\frac{L_0}{(L_p - L_0)}} = \omega \left( \frac{R_0^2}{\omega^2 L_0} + L_0 \right) \sqrt{\frac{L_0}{\left( \left( \frac{R_0^2}{\omega^2 L_0} + L_0 \right) - L_0 \right)}} & 3.94 \\
&= \omega \left( \frac{R_0^2}{\omega^2 L_0} + L_0 \right) \frac{\omega L_0}{R_0} = \left( R_0 + \frac{\omega^2 L_0^2}{R_0} \right) \\
R_p &= R_0 + \frac{\omega^2 L_0^2}{R_0}
\end{aligned}$$

Thus, by using equations 3.93 and 3.94, the model can be described in the more familiar form of FIG. 3.11.

### 3.2.4 Capacitances in the transformer lumped equivalent circuit model

The equivalent circuit for the real transformer in FIG. 3.11 shows a number of things that can be improved in order to make the transformer more ideal. In the previous section, improving core loss was thoroughly discussed, including laminating cores and increasing the resistivity of

core materials. Reducing line resistance of the primary and secondary windings can be done by using higher conductivity metals at the trade-off of cost, or increasing winding diameters with the trade-off of fitting more turns around a core.

One of the problems that can be improved by careful design is leakage inductance. By carefully intertwining the primary and secondary, there is a two mechanism improvement in coupling (see FIG. 3.14). First, the bifilar manner of the winding (as shown in FIG. 3.14) reduces leakage flux. Second, the intertwined windings form a capacitive link (cross-winding capacitance) between the primary and secondary windings that supports coupling at high frequencies when core materials lose permeability (see FIG. 3.10). Also, depending on geometry, an intra-winding capacitance (capacitance between the turns of the same winding) can accumulate.



**FIG. 3.14.** Image of bifilar wound Ethernet transformer extracted from package.

Placing the intra-winding and cross-winding capacitances into the lumped equivalent circuit is a topic for debate. FIG. 3.15 shows all of the many places to insert the capacitance into the lumped model. Power transformers have small capacitance values when compared with their large inductances, so power transformer models are generally less sensitive to the capacitor placement. However, the response of bifilar-wound Ethernet transformer models is greatly affected by the chosen placement of the capacitors as mutual inductance decreases.

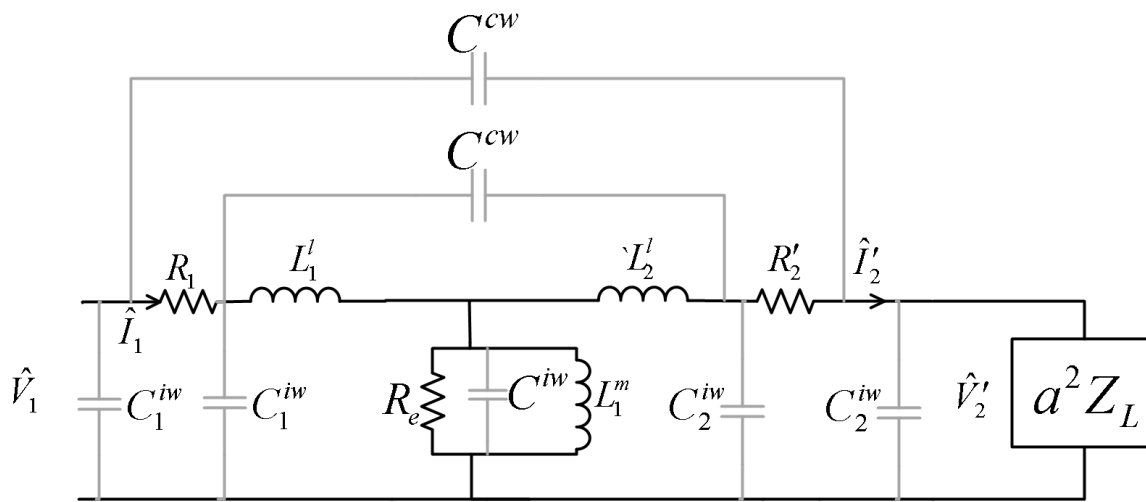


FIG. 3.15. Capacitance placement in the equivalent circuit.

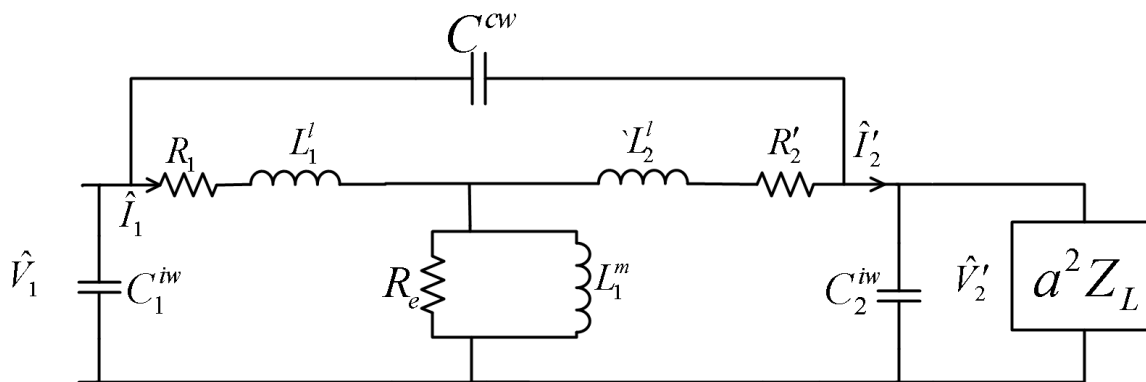


FIG. 3.16. Common transformer equivalent circuit including capacitance.

When considering the physical origin of the capacitances, none of the insertion points are perfectly accurate. The capacitance does not simply exist on one side or the other of the winding resistances. The capacitance is actually infinitesimally distributed along the winding among the resistance and leakage inductance. For this reason, debating which is the accurate model is ultimately fruitless, since all models are inaccurate. Much has been published on analysis of lumped element transformer models for different purposes in different frequency ranges ( [15], [16], [17], [18], [19]). However, for a broad analysis, distributed models are required to properly treat the capacitances. This distributed nature of the model will be analyzed in depth in Chapter 5. However, for transformers with mostly magnetic coupling, the choice of lumped element model is less critical since the effect of the capacitance is smaller. For the remaining discussion of lumped element equivalent circuits, the model of FIG. 3.16 will be used.

This concludes the discussion and derivation of the lumped element transformer equivalent circuit. In the next chapter, the discussion will continue to novel developments in techniques to characterize high frequency transformers with the lumped element model.

## Chapter 4 : Characterization of lumped parameters and ferrites

The previous thorough analysis has delivered an equivalent circuit model that represents a real transformer to a good degree of accuracy. A series of tests have been devised to take a real device and extract the values of the model parameters. In this section, the classic transformer tests will be reviewed and novel high frequency testing techniques will be presented.

### 4.1 Classic transformer tests

The classic transformer tests are designed to characterize power transformers. Power transformers have non-intertwined windings (and negligible cross-winding capacitance) and only operate at a single relatively low frequency. These tests to characterize power transformers require three peak value measurements: voltage, current, and power. In the following sections, these tests will be explained.

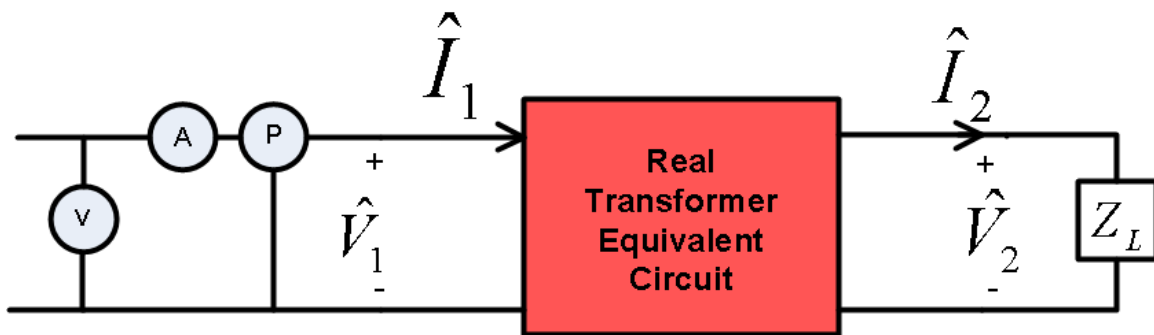


FIG. 4.1. Measurement scheme for classic transformer tests.

#### 4.1.1 Classic short circuit test

In the classic short circuit test, the secondary terminals are shorted. Shorting the secondary terminals allows certain simplifications to be made to the model. First of all, the frequency at which we are testing is sufficiently low such that the capacitances are open circuits;

thus, the capacitors can be removed. Second, with the secondary terminals shorted, the impedance of the load branch is just  $R'_2 + j\omega L'_2$  which is much less than the impedance of the core branch of  $R_e$  and  $L'_1$  in parallel. With the high impedance core branch and the low impedance load branch in parallel, the equivalent impedance is essentially that of the load branch. Thus, the core components can be left out, and the rest of the circuit combined into one resistance and one inductance as shown in FIG. 4.3. The phasor diagram for the circuit is given in FIG. 4.2.

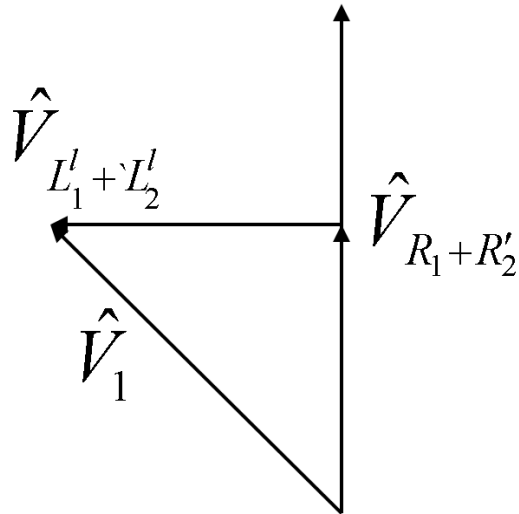


FIG. 4.2. Phasor diagram for SCT approximate equivalent circuit.

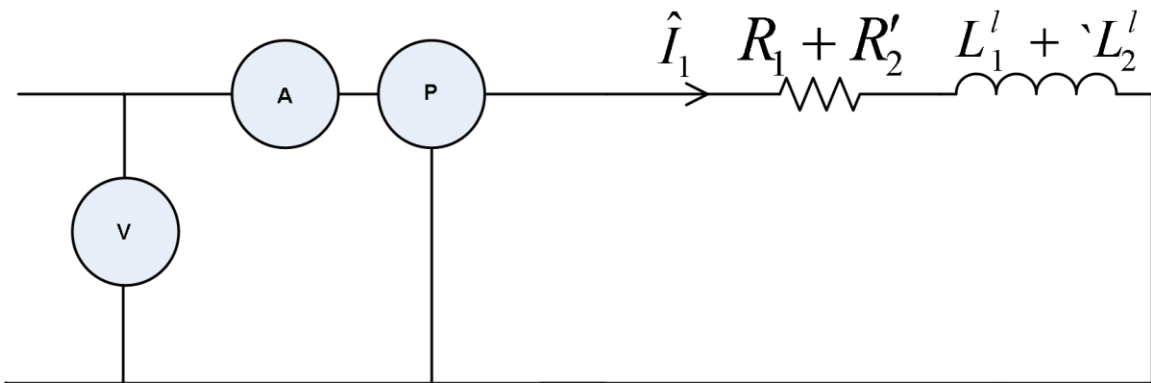


FIG. 4.3. Modified equivalent circuit for the short circuit test.

The procedure for performing the short circuit test is given below.

1. The primary AC voltage peak amplitude is increased until the rated current is reached.
2. The current is measured (or taken as the rated current) as well as the power. The power meter displays only real power consumed. Reactive power that sloshes from the source to the inductor and back again is not displayed on the power meter. The combined resistance can be found as

$$P = I^2 R_{combined} \Rightarrow \frac{|\hat{P}|}{|\hat{I}|^2} = R_1 + R_2' \quad 4.1$$

3. To find the leakage inductances, observe the phasor diagram of FIG. 4.2.

From step 2, resistance is known, and the voltage across the resistance is given by

$$|\hat{V}_{R_1+R_2'}| = |\hat{I}_1| R_{combined} = |\hat{I}_1| (R_1 + R_2') \quad 4.2$$

Multiplying the resistance found in step 2 by the measured current, the resistor voltage can be found.

From the phasor diagram,

$$|\hat{V}_1| = \sqrt{|\hat{V}_{R_1+R_2'}|^2 + |\hat{V}_{L_1'+L_2'}|^2} \quad 4.3$$

Rearranging equation 4.3, the inductance voltage can be isolated.

$$\left| \hat{V}_{L'_1 + L'_2} \right| = \sqrt{\frac{|\hat{V}_1|^2}{\left| \hat{V}_{R_1 + R'_2} \right|^2}} \quad 4.4$$

Then, using the inductance voltage, the inductance value can be found from measured quantities.

$$\left| \hat{V}_{L'_1 + L'_2} \right| = \left| j\omega L_{combined} \hat{I}_1 \right| = \omega L_{combined} \left| \hat{I}_1 \right| \Rightarrow L_{combined} = \frac{\left| \hat{V}_{L'_1 + L'_2} \right|}{\omega \left| \hat{I}_1 \right|} \quad 4.5$$

4. Between steps 2 and 3, both the winding resistance and leakage inductance were found.

#### 4.1.2 Classic open circuit test

In the open circuit test, the terminals on the secondary are left unloaded (open). With no current flowing in the secondary, the secondary winding resistance and leakage inductance become inconsequential. With the core values of main inductance and core loss resistance being very large, the small values of primary resistance and leakage inductance are insignificant. Also, the test is performed at such a low frequency that the capacitances are effectively very large impedances and negligible current paths. The equivalent circuit model becomes as shown in FIG. 4.4.

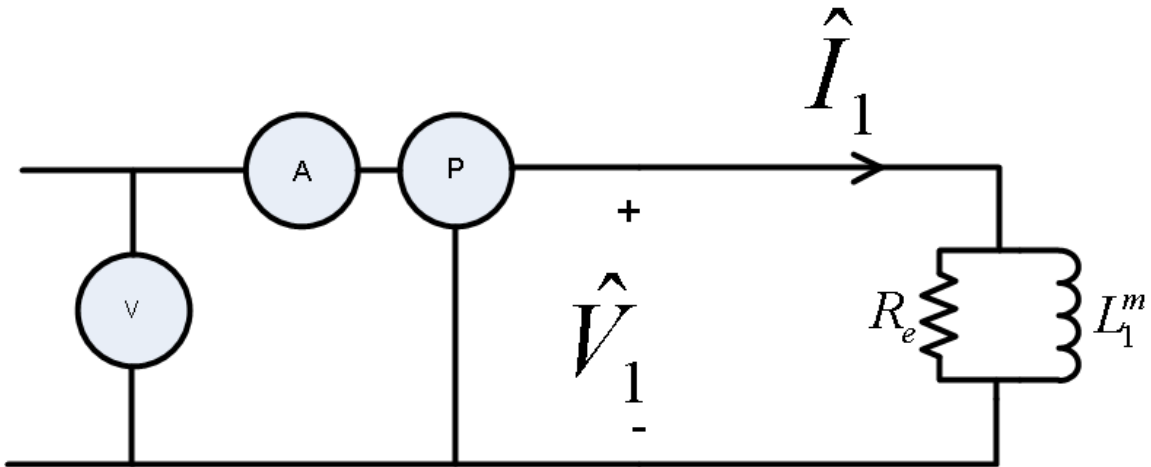


FIG. 4.4. Approximate equivalent circuit for open circuit test.

FIG. 4.5 shows the phasor diagram for the open circuit test equivalent circuit.

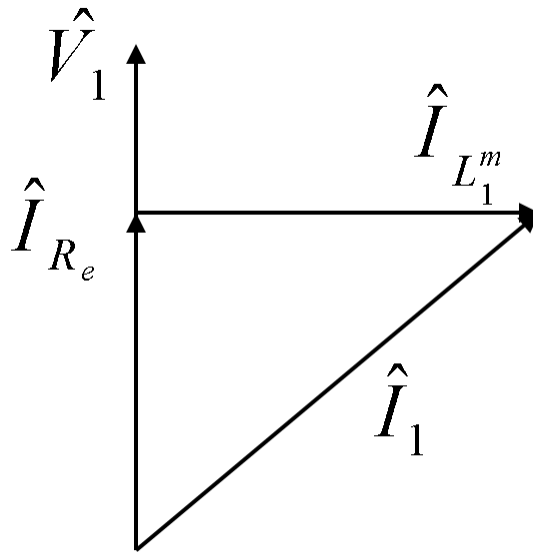


FIG. 4.5. Phasor diagram for OCT equivalent circuit.

The procedure for the open circuit test is as follows:

1. Increase voltage source until the rated voltage or current is reached.

2. Take a measurement from the power meter. Again, the power meter displays only real consumed power, and not reactive power. Thus, the power from the power meter is the power consumed by the model's loss resistor,  $R_e$ .

$$|\hat{P}| = \frac{|\hat{V}_1|^2}{R_e} \Rightarrow R_e = \frac{|\hat{V}_1|^2}{|\hat{P}|} \quad 4.6$$

3. Using the value for  $R_e$  found in step 2, the resistor current can be found.

$$|\hat{I}_{R_e}| = \frac{|\hat{V}_1|}{R_e} \quad 4.7$$

4. From the phasor diagram in FIG. 4.6 and the result of step 3, the main inductance current can be found.

$$|\hat{I}_{L_1^m}| = \sqrt{|\hat{I}_1|^2 - |\hat{I}_{R_e}|^2} \quad 4.8$$

5. Using the main inductance current, the main inductance can be found.

$$|\hat{V}_1| = |\hat{V}_L| = |j\omega L_1^m \hat{I}_{L_1^m}| = \omega L_1^m |\hat{I}_{L_1^m}| \Rightarrow L_1^m = \frac{|\hat{V}_1|}{\omega |\hat{I}_{L_1^m}|} \quad 4.9$$

Steps 2 and 5 give expressions for the core loss resistor and mutual inductance from measureable quantities. Combining the results from the short circuit test will describe all parameters in the classic low frequency transformer equivalent circuit.

### 4.1.3 DC resistance test

Prior to any frequency dependent testing, the winding resistances can be measured using DC voltage and current. The test is a simple one any engineer is familiar with.

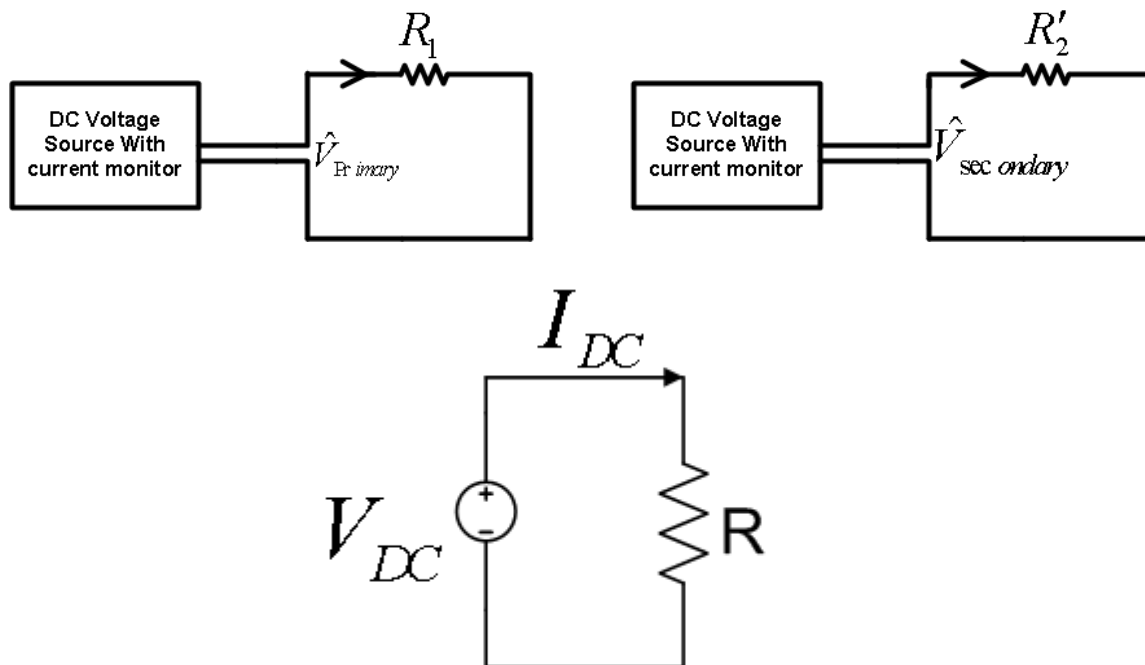


FIG. 4.6. Measurement setup to determine primary and secondary winding resistances.

The procedure to measure the winding resistance is given below.

1. Using a DC voltage source with current monitoring capabilities, adjust the voltage such that the current is below the devices rated current, but also gives the highest possible precision of measurement.
2. Record the voltage and the current output, measure both on the primary and secondary.
3. The winding resistance will be given by

$$R_{winding} = \frac{V_{DC}}{I_{DC}} \quad 4.10$$

Note, however, that the DC resistance is not necessarily the resistance at a given frequency. As frequency increases, the skin effect on the winding conductors will cause the actual resistance to increase from the DC value.

## **4.2 Novel high frequency transformer tests**

The following tests are novel techniques developed for measuring the equivalent circuit parameters of Ethernet transformers. The classic transformer tests may or may not be effective for signal transformers for the following reasons: signal transformers with limited numbers of turns and small core cross section have a main inductance that is limited by design. With a smaller main inductance, the stable flat-band region of the transformers transfer characteristic is shifted to higher frequency. Thus, the tests must be performed at high frequencies. However, the bandwidth of current and power meters is also limited to lower frequencies. Thus, with some simple logic and calculations, an inexpensive measuring technique will deliver all of the necessary information about the particular signal transformer under test. To simplify this presentation, the tests will be described for the case of Ethernet transformers where the device parameters are assumed the same for the primary and secondary windings and the turns ratio is one.

### **4.2.1. Quasi-short circuit test (QSCT)**

The quasi-short circuit test works on the same principle as the classic short circuit test. All of the same model approximations are made with one small difference. Instead of shorting the secondary terminals, a small load is placed on the secondary. This load has a resistance of a

few ohms; approximately the same impedance of the winding resistance and leakage inductances over the measurement frequency range. The test measurement setup is shown in FIG. 4.7. The relatively low frequency validates the assumption that the capacitances are high impedances and negligible. The small load branch will shunt current away from the core branch, making core effects negligible. Thus, the effective experimental circuit is shown in the bottom right of FIG. 4.7.

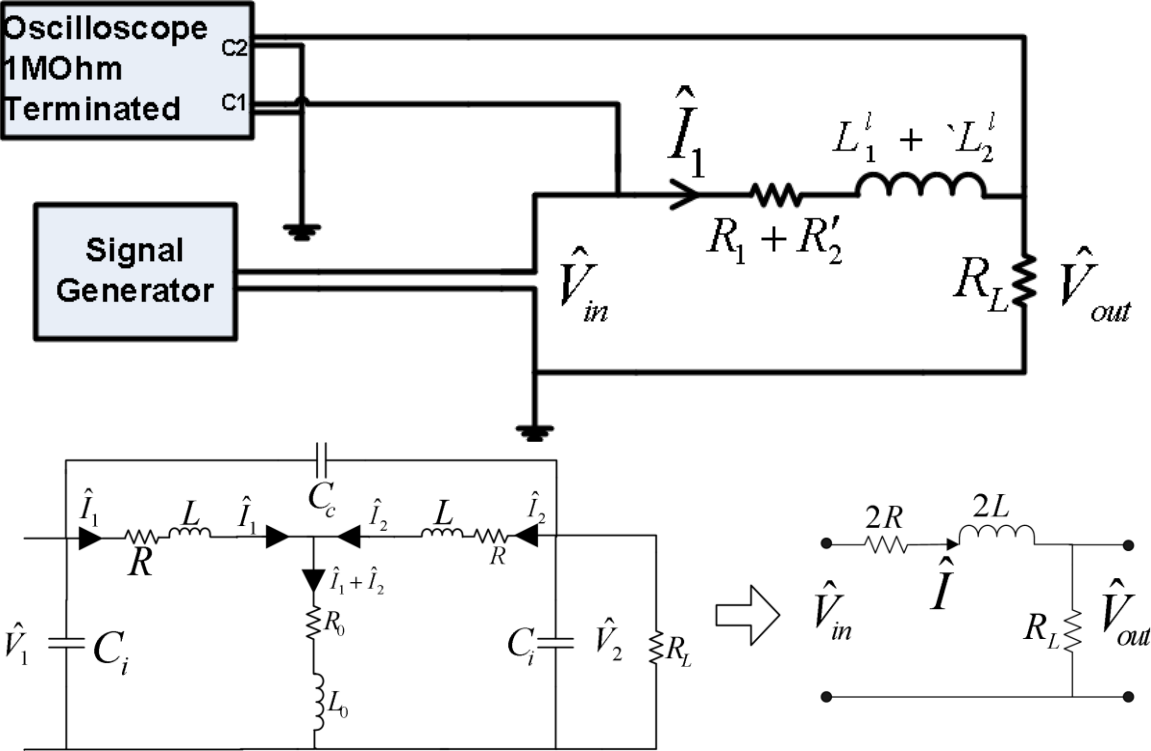


FIG. 4.7. Quasi-short circuit test experimental setup.

Following in FIG. 4.8 is the phasor diagram for the quasi-short circuit test.

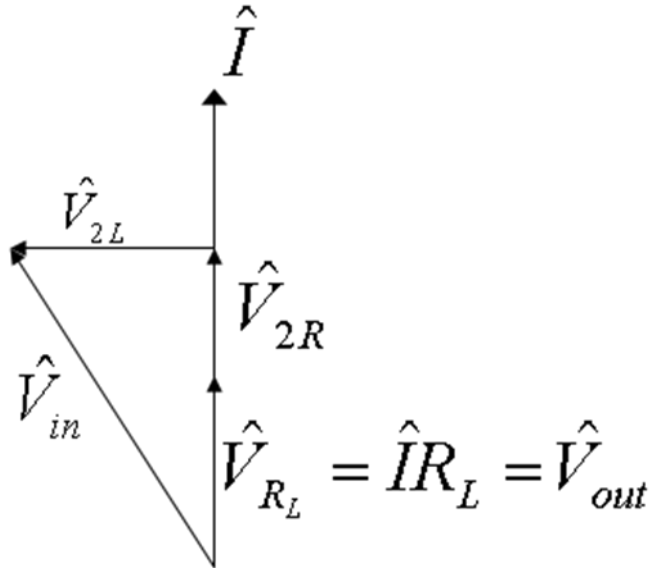


FIG. 4.8. Quasi-short circuit test phasor diagram.

The procedure for the quasi-short circuit test is as follows:

1. Measure the amplitude of  $\hat{V}_{out}$ . Use this amplitude to find the current through the series circuit.

$$|\hat{I}| = \frac{|\hat{V}_{out}|}{R_L} \quad 4.11$$

2. Using the winding resistances determined in the DC circuit test and the current in step 1, the winding resistance voltage can be found.

$$|\hat{V}_{2R}| = 2R|\hat{I}| \quad 4.12$$

3. With both the winding resistance voltage and the load voltage, the inductor voltage can be found from the geometry of the phasor diagram.

$$\begin{aligned} |\hat{V}_{in}|^2 &= (|\hat{V}_{out}| + |\hat{V}_{2R}|)^2 + |\hat{V}_{2L}|^2 \Rightarrow \\ |\hat{V}_{2L}|^2 &= |\hat{V}_{in}|^2 - |\hat{V}_{out}|^2 - 2|\hat{V}_{out}||\hat{V}_{2R}| - |\hat{V}_{2R}|^2 \\ &= |\hat{V}_{in}|^2 - R_L^2|\hat{I}|^2 - 4R_LR|\hat{I}|^2 - 4R^2|\hat{I}|^2 \end{aligned} \quad 4.13$$

4. From the inductance voltage, the inductance can be found.

$$\begin{aligned} |\hat{V}_{2L}| &= |j\omega 2L\hat{I}| = 2\omega L|\hat{I}| \Rightarrow \\ L &= \frac{\sqrt{|\hat{V}_{in}|^2 - R_L^2|\hat{I}|^2 - 4R_LR|\hat{I}|^2 - 4R^2|\hat{I}|^2}}{2\omega|\hat{I}|} \\ &= \frac{R_L \sqrt{|\hat{V}_{in}|^2 - |\hat{V}_{out}|^2 - \frac{4R|\hat{V}_{out}|^2}{R_L} - \frac{4R^2|\hat{V}_{out}|^2}{R_L^2}}}{2\omega|\hat{V}_{out}|} \\ &= \frac{R_L}{2\omega|\hat{V}_{out}|} \sqrt{|\hat{V}_{in}|^2 - |\hat{V}_{out}|^2 \left(1 + \frac{2R}{R_L}\right)} \end{aligned} \quad 4.14$$

### 4.2.2. Quasi-open circuit test (QOCT)

This quasi-open circuit test deviates further from the classic open-circuit test. The measurement setup is given in FIG. 4.9. Since  $R$  and  $L$  are small parameters, they will have a

negligible effect in series with the large core impedance or large oscilloscope channel impedance. The experimental circuit is shown at the bottom right of FIG. 4.9.

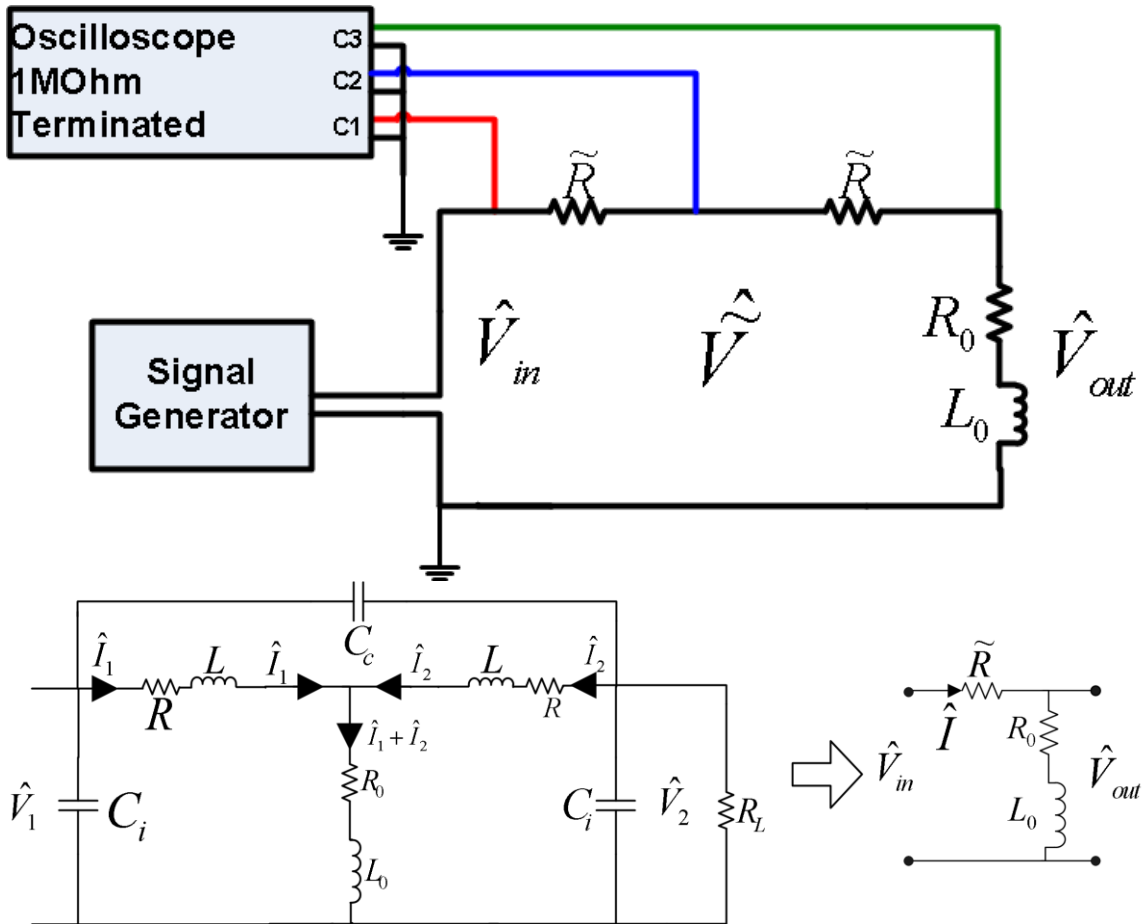
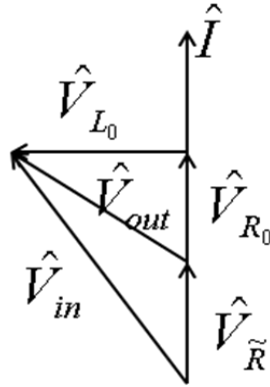


FIG. 4.9. Quasi Open Circuit test measurement setup.

Following is the phasor diagram for the quasi open circuit test.



**FIG. 4.10. Quasi-open circuit test phasor diagram.**

In the above FIG. 4.9, the experimental measurement setup is shown.  $\tilde{R}$  is a discrete added series resistor with a specific value that will be discussed later.  $R_0$  and  $L_0$  are the core loss resistor and mutual inductance as series elements.

Following is the procedure to determine the series elements  $R_0$  and  $L_0$  from the quasi-open circuit test.

1. In this experiment, a resistance was inserted in series with the center conductor of standard RG-58 coaxial cable used for making connections. Small project boxes with two BNC connectors were constructed that allowed resistance to easily be inserted into the scheme and changed but still properly couple to the signal generator, device, and oscilloscope.
2. The device is mounted onto a non-conducting printed circuit board. Small wire runs connect the device input and output ports to BNC connectors. A short BNC cable connects the device output ( $\hat{V}_{out}$ ) directly to a  $1\text{ M}\Omega$  terminated channel of the oscilloscope.

3. The signal generator is connected to the resistance with a T-connector. The second port on the T-connector connects with a short RG-58 cable to a  $1\text{ M}\Omega$  terminated channel on the oscilloscope ( $\hat{V}_{in}$ ).
4. Using math functions on the oscilloscope,  $\hat{V}_{\tilde{R}}$  is calculated as  $\hat{V}_{in} - \hat{V}_{out}$  in time.
5. The signal generator frequency is swept, and the signal amplitudes of  $\hat{V}_{in}$ ,  $\hat{V}_{\tilde{R}}$ , and  $\hat{V}_{out}$  are measured.

The following analysis will describe how the previous amplitude measurements will give values for the series core parameters ( $R_0$  and  $L_0$ ). Consider the phasor diagram from FIG. 4.10. The concept behind the quasi-open circuit test is to use an additional voltage measurement around a known resistance to determine the current flowing in the series circuit.

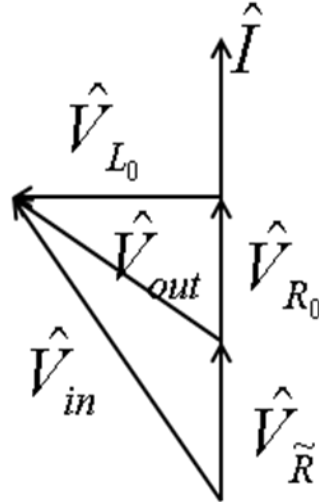


**FIG. 4.11. Phasor Diagram for the quasi-open circuit test.**

The following geometric equations are true about the phasor diagram above.

$$|\hat{I}| = \frac{|\hat{V}_{\tilde{R}}|}{\tilde{R}} \quad 4.15$$

$$|\hat{V}_{in}|^2 = (|\hat{V}_{R_0}| + |\hat{V}_{\tilde{R}}|)^2 + |\hat{V}_{L_0}|^2 \quad 4.16$$

$$|\hat{V}_{out}|^2 = |\hat{V}_{R_0}|^2 + |\hat{V}_{L_0}|^2 \quad 4.17$$

Performing algebraic manipulations on 4.16 and substituting 4.17 will allow  $|\hat{V}_{R_0}|$  to be found.

$$\begin{aligned} |\hat{V}_{in}|^2 &= (|\hat{V}_{R_0}| + |\hat{V}_{\tilde{R}}|)^2 + |\hat{V}_{L_0}|^2 = |\hat{V}_{R_0}|^2 + 2|\hat{V}_{R_0}||\hat{V}_{\tilde{R}}| + |\hat{V}_{\tilde{R}}|^2 + |\hat{V}_{L_0}|^2 = \\ &|\hat{V}_{out}|^2 + 2|\hat{V}_{R_0}||\hat{V}_{\tilde{R}}| + |\hat{V}_{\tilde{R}}|^2 \Rightarrow \\ |\hat{V}_{R_0}| &= \frac{|\hat{V}_{in}|^2 - |\hat{V}_{out}|^2 - |\hat{V}_{\tilde{R}}|^2}{2|\hat{V}_{\tilde{R}}|} \end{aligned} \quad 4.18$$

Using 4.17,  $|\hat{V}_{L_0}|$  can be found.

$$|\hat{V}_{L_0}| = \sqrt{|\hat{V}_{out}|^2 - |\hat{V}_{R_0}|^2} \quad 4.19$$

From the resistance and inductance voltages, the resistance and inductance can be found.

$$\begin{aligned} |\hat{V}_{R_0}| &= \frac{|\hat{V}_{in}|^2 - |\hat{V}_{out}|^2 - |\hat{V}_{\tilde{R}}|^2}{2|\hat{V}_{\tilde{R}}|} = R_0|\hat{I}| \Rightarrow \\ R_0 &= \frac{|\hat{V}_{in}|^2 - |\hat{V}_{out}|^2 - |\hat{V}_{\tilde{R}}|^2}{2|\hat{V}_{\tilde{R}}||\hat{I}|} \end{aligned} \quad 4.20$$

$$|\hat{V}_{L_0}| = \sqrt{|\hat{V}_{out}|^2 - |\hat{V}_{R_0}|^2} = \sqrt{|\hat{V}_{out}|^2 - \frac{|\hat{V}_{in}|^2 - |\hat{V}_{out}|^2 - |\hat{V}_{\tilde{R}}|^2}{2|\hat{V}_{\tilde{R}}|}} = \omega L_0 |\hat{I}| \Rightarrow$$

$$L_0 = \frac{1}{\omega |\hat{I}|} \sqrt{\frac{2|\hat{V}_{\tilde{R}}||\hat{V}_{out}|^2 - |\hat{V}_{in}|^2 + |\hat{V}_{out}|^2 + |\hat{V}_{\tilde{R}}|^2}{2|\hat{V}_{\tilde{R}}|}}$$
4.21

Equations 4.20 and 4.21 express the series loss resistance and the series mutual inductance for a given frequency. Thus, in one measurement at one frequency point, values for resistance and inductance can be acquired. However, as discussed above, the ferrite core materials are dispersive, meaning that their properties are different with different frequency. This means that the lumped equivalent circuit model parameters are different with different frequencies. With this quasi-open circuit test, however, the frequency can be swept and the parameter values found for each frequency in the range of interest. Thus, a frequency dependent model can be constructed with this technique.

Rearranging 3.80 and 3.81, the real and imaginary parts of permeability can be expressed explicitly.

$$\mu''(\omega) = \frac{R_0(\omega)}{\omega N^2 A_{cross}} l$$
4.22

$$\mu'(\omega) = \frac{-L_0(\omega)}{N^2 A_{cross}} l$$
4.23

The important result of equation 4.22 and 4.23 is how this method ultimately results in the measurement of the dispersion relation of the core material. Any isolation transformer can have the core material analyzed *in situ* post production. This allows any device to be calibrated specifically without destructive testing. FIG. 4.12 shows  $R_0$  and  $L_0$  frequency dependence as extracted from an Ethernet transformer by the QOCT technique. From equations 4.22 and 4.23,  $R_0$  and  $L_0$  are proportional to imaginary and real parts of the permeability of the ferrite core. The curves of FIG. 4.12 should have similar features to that of the complex permeability of the ferrite. Published measured permeability data for MnZn ferrites (FIG. 4.13) shows similar behavior to what was measured with the QOCT method.

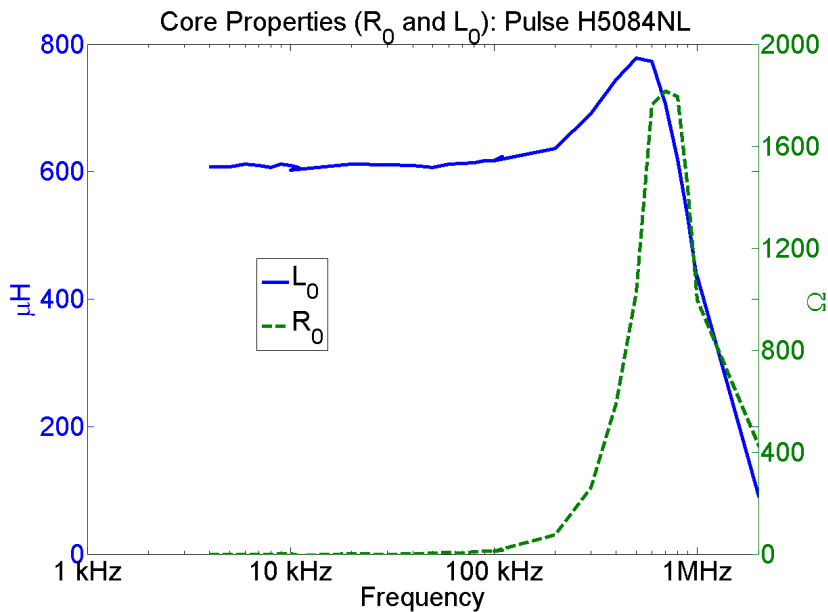
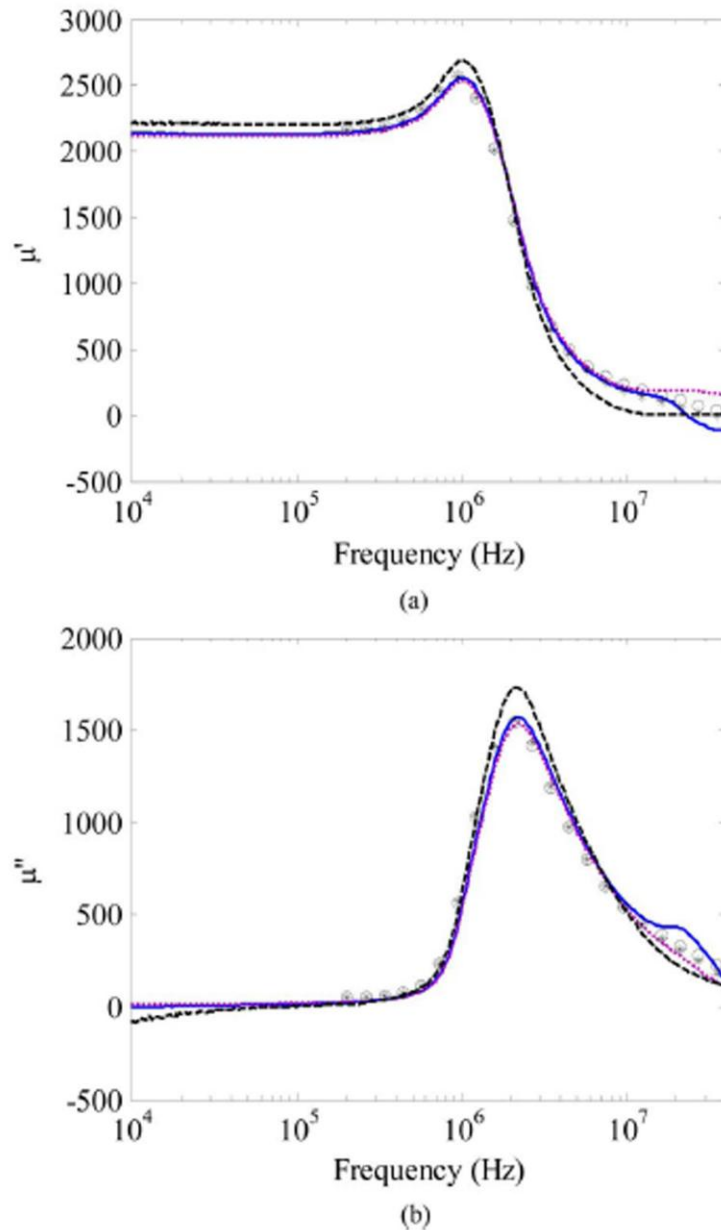


FIG. 4.12. Measured core properties using the quasi open circuit test. [14]



**FIG. 4.13. Complex permeability of Mn-Zn Ferrite (a) Real (b) Imaginary [20]**

The above tests designed for frequency swept measurements on isolation transformers will result in values for the parameters of the lumped equivalent circuit. This equivalent circuit can then be used in circuit simulation software or used for signal analysis and transfer characteristics measurement at frequencies beyond the bandwidth of simple measurement

devices. Other testing schemes for measuring the properties of ferrite materials have been studied and published. However, these techniques require bulk ferrite material and special winding construction and / or expensive measurement equipment ( [21], [13], [20], [22]). The QOCT method is presented as an inexpensive alternative to measuring transformer ferrite properties in-situ.

However, as mentioned above, the lumped element equivalent circuit poses the debate of where to place the cross winding capacitance. This will be discussed in the next chapter as distributed models are analyzed.

### **4.2.3. Measured transfer characteristics**

Using the same measurement technique as was used for the quasi-open circuit test, the transfer function of the device can be measured. An important distinction to make that relates directly to the measurement technique is the specific meaning of the transfer function for this research. Though commercial Ethernet transformers are intended to be coupled to 100  $\Omega$  UTP line, it is the unloaded transfer characteristic that needs to be measured in order to compare the measured data with the analytical model. The model may be correct in the low impedance loading limit, but completely incorrect for the unloaded device. If this were true, then perhaps the physical assumptions on which the model is based are incorrect.

Ultimately, however, comparison of measured data and the analytical model is mostly qualitative. The key frequency regions in which to compare are the regions of non-limited behavior such as the low frequency slope into the flat-band region or the resonance regions. Comparing flat-band regions says little about the accuracy of the model except that both the model and device have reached some limiting case with good coupling.

Presented below is a measured transfer characteristic of a commercial Ethernet transformer for both the differential and common signal modes. By using the extracted parameters from the above tests and the capacitance determination below, the lumped element equivalent circuit behaves similarly to the actual device. The equivalent circuit differential-mode transfer relation matches the resonance location and height and has a low-frequency knee close to the measurement of the commercial device. As will be discussed in the next chapter, some features of the measurement simply cannot be reproduced by a lumped equivalent circuit model. However, a reasonable performance match is demonstrated (See FIG. 4.14).

Also shown below is a measured common mode transfer characteristic. This measurement was performed with the scheme shown in FIG. 4.15. It can be shown that in the lumped model analysis a resonance exists with frequency

$$\omega_{res} = \frac{1}{\sqrt{LC_c}} \quad 4.24$$

where  $L$  represents leakage inductance and  $C_c$  represents cross-winding capacitance.

The resonance frequency depends on parameters that appear in both the differential mode and common mode models. The measured observance of the resonance peak at the same frequency in both differential mode and common mode schemes validates equation 4.24. The flat regions of the measured transfer characteristics indicate a frequency independent coupling. This would be either a ratio of inductances, a ratio of capacitances, or a ratio of resistances. The application of this logic, especially in the case of common mode measurements, will reveal the

values of capacitances. Thus, transfer characteristics complete the necessary measurements to determine model parameters.

Simulated and measured Transfer Relation:  $L=600\mu\text{H}$ ,  $C=15\text{pF}$ ,  $L_1=600\text{nH}$ ,  $R=0.75\Omega$

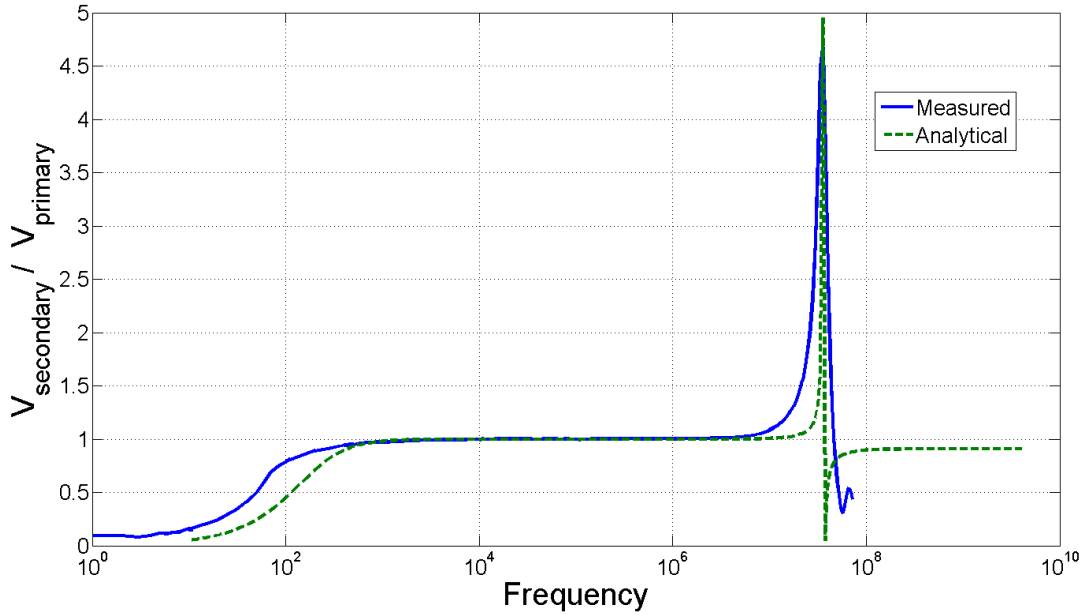


FIG. 4.14. Comparison of measured and calculated transfer characteristics.

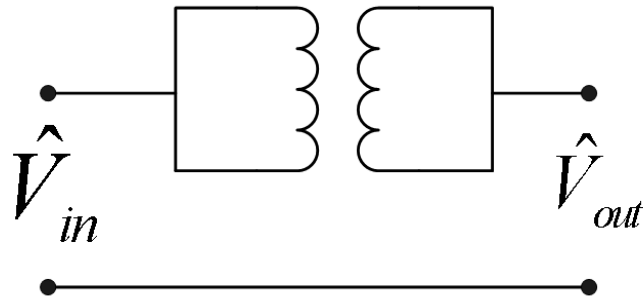


FIG. 4.15. Common-mode transfer characteristic measurement setup.

Measured Common-to-common Mode Transfer Characteristic: Pulse H5084NL

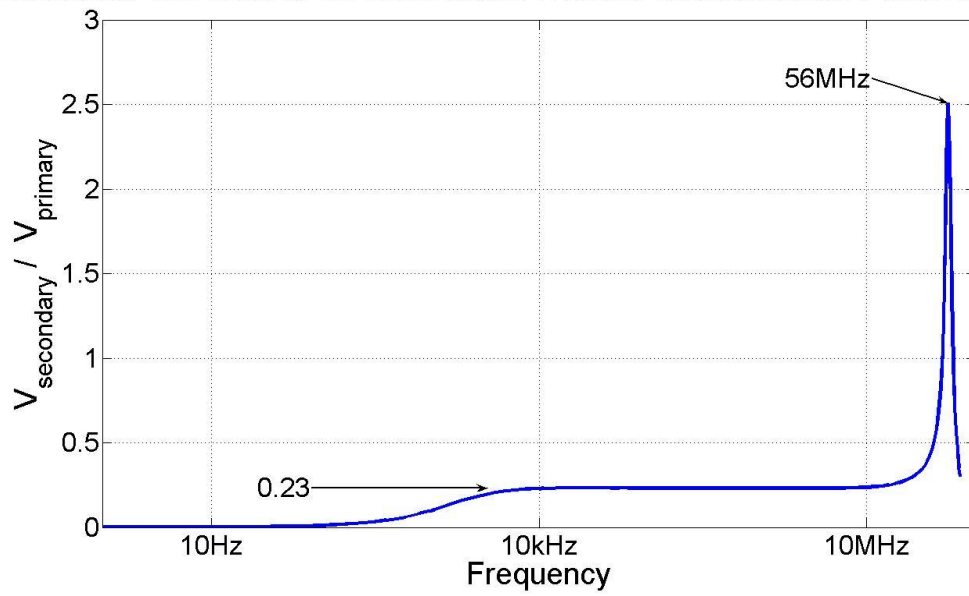


FIG. 4.16. Common-mode transfer characteristic for a 1Gbase-T commercial Ethernet transformer.

## Chapter 5 : Modeling with distributed parameters

### 5.1. Distributed analysis introduction

The capacitance conundrum of the lumped element equivalent circuit forces the consideration of the physical origin of the capacitance. The capacitance comes from the intertwined primary and secondary lines and the tightly packed windings. The close proximity with a varnish dielectric between the conductors forms a capacitor where energy can be stored as the field between two conductors. However, this capacitor is stretched (distributed) along the entire length of the intertwined conductors. The same distribution also applies to the winding resistances and leakage inductance. Thus, all four values incrementally increase with each other. The entire capacitance does not exist anywhere with respect to the entire winding resistance, but infinitesimally increases with an infinitesimal increase in resistance along the winding.

This physical notion of distribution of multiple parameters leads to the development of an infinitesimally distributed circuit model, similar to transmission lines of arbitrary length. These models can be analyzed mathematically or placed into multiple cells of a circuit simulator.

The distributed model analysis will be different for each signal mode, whether common or differential. The signal mode defines the symmetry of the terminal voltages, and thus defines the boundary conditions of the model, and also important model simplifications. Separate models and analyses for differential and common modes will be done in the following sections. The superposition of the two model transfer relations will fully describe the behavior of the device.

## 5.2. Differential mode

As stated above, the differential mode signal implies specific model boundary conditions, as will be discussed below. The problem is formed as a vertically distributed model. Consider FIG. 5.1 which describes the layout and boundary condition for the differential signal model analysis. FIG. 5.1 shows four parallel vertical axes that describe how the primary and secondary voltages as well as the secondary currents coincide with the physical distribution of the windings.

In FIG. 5.1, a purely differential voltage is applied to the primary. The secondary is loaded with an arbitrary load  $Z_L$ . The transformer under analysis is assumed to have a unity turns ratio, implying that the length of winding for both the primary and secondary are equal. In FIG. 5.1, this winding length is  $l$ , and the analysis adopts a coordinate system where either winding center is at  $y=0$ . Thus, the top and bottom of either winding is at  $y = \pm \frac{l}{2}$  respectively.

Given the physical symmetry of the distributed model and the voltage symmetry of the differential mode signal about zero potential, the voltage at  $y=0$  for either the primary or secondary will be zero. A symmetric model will yield the voltage at the physical midpoint to be an equal potential from the top and bottom of the physical device. Since the top and bottom are equal potentials above and below zero volts given the differential signal mode, the midpoint potential is the same for the two windings and equal to zero.

The reference direction of secondary current is into the device at  $y = \frac{l}{2}$ . With the secondary voltage reference polarity positive at  $y = \frac{l}{2}$ , the secondary current at  $y = \frac{l}{2}$  will be

given by the secondary voltage divided by the load impedance, but opposite to the current's

reference direction. Thus,  $\hat{i}_2(\frac{l}{2}) = \frac{-2\hat{V}_2}{Z_L}$ . Following are all of the boundary condition equations

just discussed.

$$\hat{v}_1(\frac{l}{2}) = \hat{V}_1 \quad 5.1$$

$$\hat{v}_2(\frac{l}{2}) = \hat{V}_2 \quad 5.2$$

$$\hat{i}_2(\frac{l}{2}) = \frac{-2\hat{V}_2}{Z_L} \quad 5.3$$

$$\hat{v}_1(0) = \hat{v}_2(0) = 0 \quad 5.4$$

### 5.2.1. Differential-mode distributed model analysis

The synthesis of the actual distributed model must incorporate all of the distributed parameters in each cell (winding resistance, cross-winding capacitance, intra-winding capacitance, leakage inductance, mutual inductance). In general, the cross-winding capacitance will couple between the primary and secondary in each cell. The winding resistance and leakage inductance will appear in series with the primary and secondary respective circuits. The intra-winding capacitance bridges the terminals of either winding. Thus, the intra-winding capacitance will be placed in parallel with the series resistance in each cell noting that the capacitance in each cell will be larger than the lumped value, since capacitors in series divide the value. The mutual inductance is difficult to intuitively place in the circuit model. For this analysis, the mutual inductance floats in the center, meaning that no current can flow through it as an element, but its

presence will affect the differential voltage equations of the distributed analysis. Distributed circuit models have been published which properly treat distributed capacitance, but ignore mutual magnetic coupling and offer no thorough theoretical analysis of the model [23].

In the interest of a more general analysis, the theoretical distributed model analyzed here will consist of generic series elements in each winding, cross-winding elements between the windings, and the floating mutual inductance. The series elements can be expressed as an equivalent impedance and the cross-winding elements can be expressed as an equivalent admittance. Thus, the general cell of the distributed model can be formed as a series impedance, and cross-winding admittance, and a floating mutual inductance (see FIG. 5.2). In the following discussion, the analytical transfer function will be determined by analysis of the cell in FIG. 5.2 and the boundary conditions of FIG. 5.1. Note that the impedances and admittances in the analysis reference FIG. 5.2, and are per length parameter values.

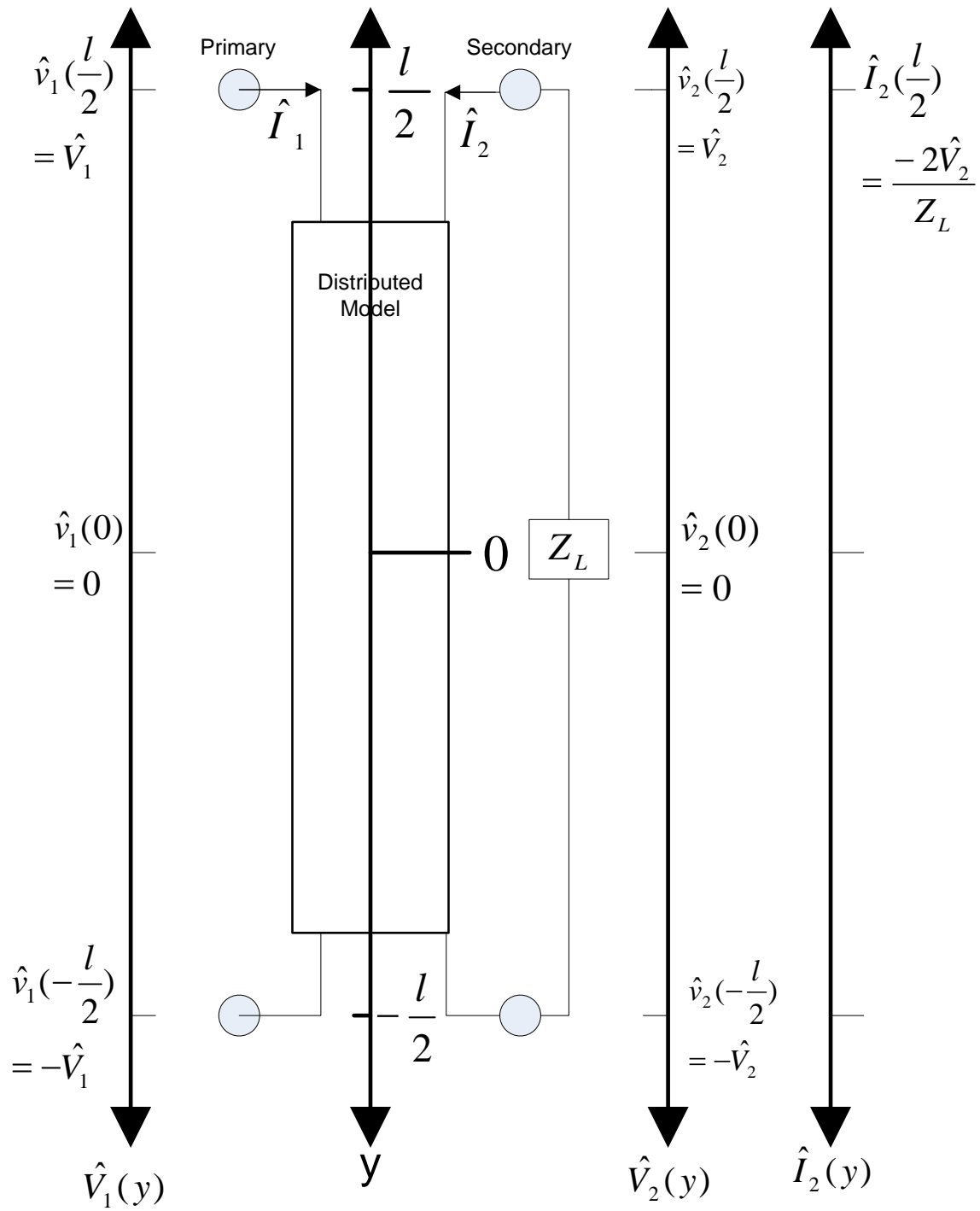


FIG. 5.1. External terminal diagram of differential-mode distributed transformer model with boundary conditions.

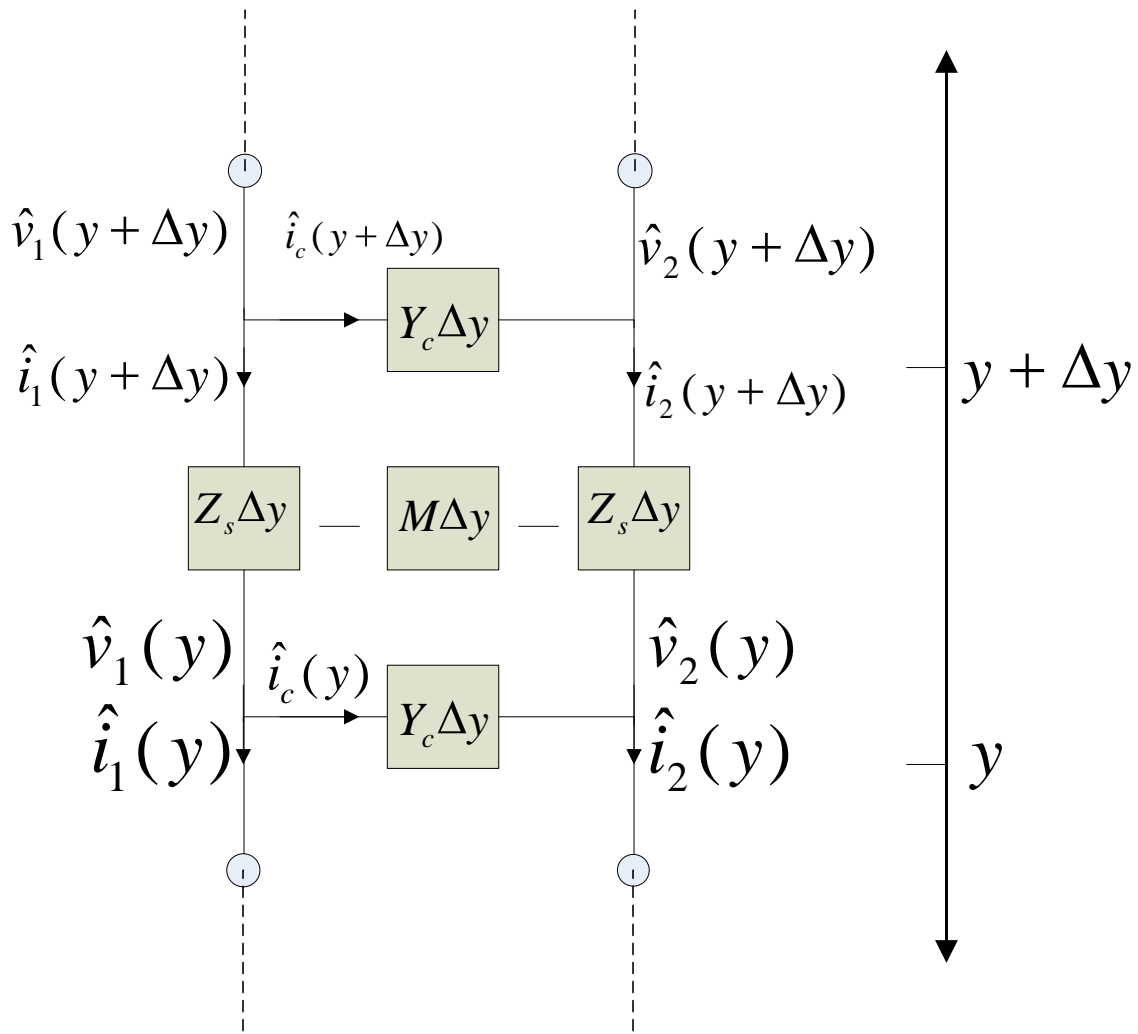


FIG. 5.2. Single cell of differential-mode distributed model.

From the cell in FIG. 5.2, Kirchoff's voltage law (KVL) applied along the series branch yields the following equation.

$$\begin{aligned}\hat{v}_1(y + \Delta y) - \hat{v}_1(y) &= \hat{i}_1(y + \Delta y)Z_s \Delta y + \hat{i}_2(y + \Delta y)M \Delta y \\ \frac{\hat{v}_1(y + \Delta y) - \hat{v}_1(y)}{\Delta y} &= \hat{i}_1(y + \Delta y)Z_s + \hat{i}_2(y + \Delta y)M\end{aligned}$$

$$\lim_{\Delta y \rightarrow 0} \frac{\hat{v}_1(y + \Delta y) - \hat{v}_1(y)}{\Delta y} = \frac{d\hat{v}_1(y)}{dy} = \hat{i}_1(y)Z_s + \hat{i}_2(y)M \quad 5.5$$

Using the same application of KVL to the secondary winding yields the following result.

$$\frac{d\hat{v}_2(y)}{dy} = \hat{i}_2(y)Z_s + \hat{i}_1(y)M \quad 5.6$$

Application of Kirchoff's current law (KCL) to the cross-winding branch gives the following progression of equations:

$$\begin{aligned}\hat{i}_1(y + \Delta y) - \hat{i}_1(y) &= \hat{i}_c(y) = [\hat{v}_1(y) - \hat{v}_2(y)]Y_c \Delta y \\ \frac{\hat{i}_1(y + \Delta y) - \hat{i}_1(y)}{\Delta y} &= \hat{v}_1(y) - \hat{v}_2(y)Y_c\end{aligned}$$

$$\lim_{\Delta y \rightarrow 0} \frac{\hat{i}_1(y + \Delta y) - \hat{i}_1(y)}{\Delta y} = \frac{d\hat{i}_1(y)}{dy} = [\hat{v}_1(y) - \hat{v}_2(y)]Y_c \quad 5.7$$

Performing similar analysis on the secondary winding gives the following equation.

$$\frac{d\hat{i}_2(y)}{dy} = [\hat{v}_2(y) - \hat{v}_1(y)]Y_c = -\frac{d\hat{i}_1(y)}{dy} \quad 5.8$$

The important conclusion that comes from equation 5.7 and 5.8 (which will be used later) is the following:

$$\frac{d\hat{i}_1(y)}{dy} + \frac{d\hat{i}_2(y)}{dy} = \frac{d}{dy}(\hat{i}_1(y) + \hat{i}_2(y)) = \frac{d\hat{i}_1(y)}{dy} - \frac{d\hat{i}_1(y)}{dy} = 0 \quad 5.9$$

Since the derivative with respect to  $y$  of the quantity  $(\hat{i}_1(y) + \hat{i}_2(y))$  is 0, then  $(\hat{i}_1(y) + \hat{i}_2(y))$  must be constant with respect to  $y$ . The sum of the currents can be represented by

$$(\hat{i}_1(y) + \hat{i}_2(y)) = \hat{I} \quad 5.10$$

The following approach attempts and succeeds to find expressions for  $\hat{v}_1(y)$  and  $\hat{v}_2(y)$  explicitly. Adding equations 5.5 and 5.6 gives the following:

$$\frac{d\hat{v}_1(y)}{dy} + \frac{d\hat{v}_2(y)}{dy} = \frac{d}{dy}(\hat{v}_1(y) + \hat{v}_2(y)) =$$

$$\hat{i}_1(y)Z_s + \hat{i}_2(y)M + \hat{i}_2(y)Z_s + \hat{i}_1(y)M = (\hat{i}_1(y) + \hat{i}_2(y))(Z_s + M) = \hat{I}(Z_s + M) \quad 5.11$$

Making the substitution

$$g(y) = \hat{v}_1(y) + \hat{v}_2(y) \quad 5.12$$

and recalling that  $(\hat{i}_1(y) + \hat{i}_2(y)) = \hat{I}$  is constant with respect to  $y$ , equation 5.11 can be integrated.

$$\int \frac{dg(y)}{dy} dy = g(y) = \int \hat{I}(Z_s + M) dy = \hat{I}(Z_s + M)y + C \quad 5.13$$

To determine the constant  $C$ , the boundary condition of equation 5.4 is used.

$$\begin{aligned}
g(0) &= \hat{v}_1(0) + \hat{v}_2(0) = 0 \\
&= \hat{I}(Z_s + M)0 + C = C = 0
\end{aligned}
\tag{5.14}$$

Thus,

$$g(y) = \hat{I}(Z_s + M)y \tag{5.15}$$

Taking the difference of equations 5.5 and 5.6 gives the following:

$$\frac{d}{dy}(\hat{v}_1(y) - \hat{v}_2(y)) = \frac{d}{dy}(f(y)) = (\hat{i}_1(y) - \hat{i}_2(y))(Z_s - M) \tag{5.16}$$

where

$$f(y) = \hat{v}_1(y) - \hat{v}_2(y) \tag{5.17}$$

Taking another derivative of equation 5.16 gives the following:

$$\begin{aligned}
\frac{d^2}{dy^2}(f(y)) &= \left( \frac{d\hat{i}_1(y)}{dy} - \frac{d\hat{i}_2(y)}{dy} \right) (Z_s - M) = \left( \frac{2d\hat{i}_1(y)}{dy} \right) (Z_s - M) \\
&= 2(\hat{v}_1(y) - \hat{v}_2(y))Y_c(Z_s - M) = 2Y_c(Z_s - M)f(y)
\end{aligned}
\tag{5.18}$$

Equation 5.18 delivers the simple differential equation  $\frac{d^2}{dy^2}(f(y)) = 2Y_c(Z_s - M)f(y)$ .

This equation can be solved with exponentials of the following form.

$$f(y) = Ae^{\gamma y} + Be^{-\gamma y} \tag{5.19}$$

Plugging 5.19 into 5.18 and evaluating gives the following:

$$\begin{aligned} \frac{d^2}{dy^2}(f(y)) &= \frac{d^2}{dy^2}(Ae^{\gamma y} + Be^{-\gamma y}) = \gamma^2(Ae^{\gamma y} + Be^{-\gamma y}) \\ &= \gamma^2 f(y) = 2Y_c(Z_s - M)f(y) \end{aligned} \quad 5.20$$

By inspection of equation 5.20,

$$\gamma^2 = 2Y_c(Z_s - M) \quad 5.21$$

Using the boundary condition of equation 5.4, the two constant coefficients of equation 5.19 can be reduced to one.

$$\begin{aligned} f(0) = \hat{v}_1(0) - \hat{v}_2(0) = 0 &= Ae^{\gamma \cdot 0} + Be^{-\gamma \cdot 0} = A + B \Rightarrow \\ &A = -B \end{aligned} \quad 5.22$$

With equation 5.22,  $f(y)$  can be expressed as follows.

$$f(y) = Ae^{\gamma y} - Ae^{-\gamma y} = 2A \sinh(\gamma y) \quad 5.23$$

Recalling equations 5.12 and 5.17, it is apparent that

$$\frac{f(y) + g(y)}{2} = \hat{v}_1(y) \quad 5.24$$

and

$$\frac{g(y) - f(y)}{2} = \hat{v}_2(y) \quad 5.25$$

Plugging equations 5.15 and 5.23 into 5.24 and 5.25 gives the following expressions.

$$\hat{v}_1(y) = \hat{I} \frac{(Z_s + M)}{2} y + A \sinh(\gamma y) = \hat{I} \beta y + A \sinh(\gamma y) \quad 5.26$$

$$\hat{v}_2(y) = \hat{I} \frac{(Z_s + M)}{2} y - A \sinh(\gamma y) = \hat{I} \beta y - A \sinh(\gamma y) \quad 5.27$$

with

$$\beta = \frac{(Z_s + M)}{2} \quad 5.28$$

Now, using the remaining boundary conditions, the constant coefficients  $A$  and  $\hat{I}$  can be solved.

Going back to equation 5.5 and plugging in equation 5.26 evaluated at  $y = \frac{l}{2}$ , the following

expression is obtained.

$$\frac{d\hat{v}_1(\frac{l}{2})}{dy} = \hat{I} \beta + \gamma A \cosh(\gamma \frac{l}{2}) = \hat{i}_1(\frac{l}{2}) Z_s + \hat{i}_2(\frac{l}{2}) M \quad 5.29$$

Using the loaded boundary condition (equation 5.3), substituting  $\gamma' = \frac{\gamma l}{2}$ , and expanding  $\hat{I}$  gives

the following equation.

$$\begin{aligned}
(\hat{i}_1(\frac{l}{2}) + \hat{i}_2(\frac{l}{2}))\beta + \gamma A \cosh(\gamma') &= (\hat{i}_1(\frac{l}{2}) - \frac{2\hat{V}_2}{Z_L})\beta + \gamma A \cosh(\gamma') = \hat{i}_1(\frac{l}{2})Z_s - \frac{2\hat{V}_2}{Z_L}M \Rightarrow \\
\hat{i}_1(\frac{l}{2}) &= \frac{\frac{2\hat{V}_2}{Z_L}(\beta - M) - \gamma A \cosh(\gamma')}{(\beta - Z_s)} \tag{5.30}
\end{aligned}$$

and

$$\begin{aligned}
\hat{I} = \hat{i}_1(\frac{l}{2}) - \frac{2\hat{V}_2}{Z_L} &= \frac{\frac{2\hat{V}_2}{Z_L}(\beta - M) - \gamma A \cosh(\gamma') - \frac{2\hat{V}_2}{Z_L}(\beta - Z_s)}{(\beta - Z_s)} = \\
\hat{I} &= \frac{\frac{2\hat{V}_2}{Z_L}(Z_s - M) - \gamma A \cosh(\gamma')}{(\beta - Z_s)} \tag{5.31}
\end{aligned}$$

Plugging equation 5.31 into the secondary voltage expression (equation 5.27), substituting

$$\beta' = \beta \frac{l}{2} \tag{5.32}$$

and evaluating at  $y = \frac{l}{2}$ , the following is found.

$$\begin{aligned}
\hat{v}_2\left(\frac{l}{2}\right) &= \hat{V}_2 = \left[ \frac{\frac{2\hat{V}_2}{Z_L}(Z_s - M) - \gamma A \cosh(\gamma')}{(\beta - Z_s)} \right] \beta' - A \sinh(\gamma') \\
&= \frac{2\hat{V}_2}{Z_L} \frac{(Z_s - M)}{(\beta - Z_s)} \beta' - \frac{\gamma A \cosh(\gamma') \beta'}{(\beta - Z_s)} - A \sinh(\gamma') \Rightarrow \\
\hat{V}_2 \left( 1 - \frac{2}{Z_L} \frac{(Z_s - M)}{(\beta - Z_s)} \beta' \right) &= - \frac{\gamma A \cosh(\gamma') \beta'}{(\beta - Z_s)} - A \sinh(\gamma') \Rightarrow \\
\hat{V}_2 &= \frac{-A \left( \frac{\gamma \cosh(\gamma') \beta'}{(\beta - Z_s)} + \sinh(\gamma') \right)}{\left( 1 - \frac{2}{Z_L} \frac{(Z_s - M)}{(\beta - Z_s)} \beta' \right)} = \frac{A(\gamma \beta' Z_L \cosh(\gamma') + Z_L(\beta - Z_s) \sinh(\gamma'))}{(2\beta'(Z_s - M) - Z_L(\beta - Z_s))}
\end{aligned}$$

$$\hat{V}_2 = \frac{A(\gamma \beta' Z_L \cosh(\gamma') + Z_L(\beta - Z_s) \sinh(\gamma'))}{(2\beta'(Z_s - M) - Z_L(\beta - Z_s))} \quad 5.33$$

Reevaluating  $\hat{l}$  with equation 5.33 gives the following:

$$\begin{aligned}
\hat{l} &= \frac{\frac{2\hat{V}_2}{Z_L}(Z_s - M) - \gamma A \cosh(\gamma')}{(\beta - Z_s)} \\
&= \frac{2 \left( \frac{A(\gamma \beta' Z_L \cosh(\gamma') + Z_L(\beta - Z_s) \sinh(\gamma'))}{(2\beta'(Z_s - M) - Z_L(\beta - Z_s))} \right)}{Z_L} (Z_s - M) - \gamma A \cosh(\gamma') \\
&= \frac{2 \left( \frac{A(\gamma \beta' \cosh(\gamma') + (\beta - Z_s) \sinh(\gamma'))}{(2\beta'(Z_s - M) - Z_L(\beta - Z_s))} \right) (Z_s - M) - (2\beta'(Z_s - M) - Z_L(\beta - Z_s)) \gamma A \cosh(\gamma')}{(\beta - Z_s)}
\end{aligned} \quad 5.34$$

$$\begin{aligned}
&= A \frac{2(\gamma\beta' \cosh(\gamma') + (\beta - Z_s) \sinh(\gamma'))(Z_s - M) - (2\beta'(Z_s - M) - Z_L(\beta - Z_s))\gamma A \cosh(\gamma')}{(\beta - Z_s)(2\beta'(Z_s - M) - Z_L(\beta - Z_s))} \\
&= A \frac{\cosh(\gamma')(2\gamma\beta'(Z_s - M) - 2\beta'\gamma(Z_s - M) + Z_L\gamma(\beta - Z_s)) + \sinh(\gamma')(2(\beta - Z_s)(Z_s - M))}{(\beta - Z_s)(2\beta'(Z_s - M) - Z_L(\beta - Z_s))}
\end{aligned}$$

$$\hat{I} = A \frac{\cosh(\gamma')(Z_L\gamma) + \sinh(\gamma')(2(Z_s - M))}{(2\beta'(Z_s - M) - Z_L(\beta - Z_s))} \quad 5.35$$

Plugging equation 5.35 into the expression for primary voltage (equation 5.26) and evaluating at

$y = \frac{l}{2}$  gives the following:

$$\begin{aligned}
\hat{v}_1\left(\frac{l}{2}\right) &= \hat{V}_1 = \hat{I}\beta' + A \sinh(\gamma') \\
&= A \frac{\cosh(\gamma')(Z_L\gamma) + \sinh(\gamma')(2(Z_s - M))}{(2\beta'(Z_s - M) - Z_L(\beta - Z_s))} \beta' + A \sinh(\gamma') \\
&= A \frac{\cosh(\gamma')(Z_L\beta'\gamma) + \sinh(\gamma')(2\beta'(Z_s - M)) + (2\beta'(Z_s - M) - Z_L(\beta - Z_s)) \sinh(\gamma')}{(2\beta'(Z_s - M) - Z_L(\beta - Z_s))} \\
&= A \frac{\cosh(\gamma')(Z_L\beta'\gamma) + \sinh(\gamma')(2\beta'(Z_s - M) + 2\beta'(Z_s - M) - Z_L(\beta - Z_s))}{(2\beta'(Z_s - M) - Z_L(\beta - Z_s))} \\
&= A \frac{\cosh(\gamma')(Z_L\beta'\gamma) + \sinh(\gamma')(4\beta'(Z_s - M) - Z_L(\beta - Z_s))}{(2\beta'(Z_s - M) - Z_L(\beta - Z_s))}
\end{aligned}$$

$$\hat{V}_1 = A \frac{\cosh(\gamma')(Z_L\beta'\gamma) + \sinh(\gamma')(4\beta'(Z_s - M) - Z_L(\beta - Z_s))}{(2\beta'(Z_s - M) - Z_L(\beta - Z_s))} \quad 5.36$$

Forming the transfer function from equations 5.33 and 5.36 gives the following:

$$\begin{aligned}
\frac{\hat{V}_2}{\hat{V}_1} &= \frac{A \frac{(\gamma\beta'Z_L \cosh(\gamma') + Z_L(\beta - Z_s) \sinh(\gamma'))}{(2\beta'(Z_s - M) - Z_L(\beta - Z_s))}}{A \frac{\cosh(\gamma')(Z_L\beta'\gamma) + \sinh(\gamma')(4\beta'(Z_s - M) - Z_L(\beta - Z_s))}{(2\beta'(Z_s - M) - Z_L(\beta - Z_s))}} \\
&= \frac{(\gamma\beta'Z_L \cosh(\gamma') + Z_L(\beta - Z_s) \sinh(\gamma'))}{\cosh(\gamma')(Z_L\beta'\gamma) + \sinh(\gamma')(4\beta'(Z_s - M) - Z_L(\beta - Z_s))} \\
\frac{\hat{V}_2}{\hat{V}_1} &= \frac{(\gamma\beta'Z_L \cosh(\gamma') + Z_L(\beta - Z_s) \sinh(\gamma'))}{\cosh(\gamma')(Z_L\beta'\gamma) + \sinh(\gamma')(4\beta'(Z_s - M) - Z_L(\beta - Z_s))} \quad 5.37
\end{aligned}$$

Dividing the numerator and denominator by  $\cosh(\gamma')$  gives the following expression:

$$\begin{aligned}
\frac{\hat{V}_2}{\hat{V}_1} &= \frac{(\gamma\beta'Z_L \cosh(\gamma') + Z_L(\beta - Z_s) \sinh(\gamma'))}{\cosh(\gamma')(Z_L\beta'\gamma) + \sinh(\gamma')(4\beta'(Z_s - M) - Z_L(\beta - Z_s))} \left[ \frac{1}{\cosh(\gamma')} \right] \\
&\quad \left[ \frac{1}{\cosh(\gamma')} \right] \\
\frac{\hat{V}_2}{\hat{V}_1} &= \frac{\gamma\beta'Z_L + Z_L(\beta - Z_s) \tanh(\gamma')}{(Z_L\beta'\gamma) + \tanh(\gamma')(4\beta'(Z_s - M) - Z_L(\beta - Z_s))} \\
&= \frac{\gamma' + \frac{(\beta - Z_s)}{\beta} \tanh(\gamma')}{\gamma' + \tanh(\gamma') \left( \frac{2l(Z_s - M)}{Z_L} - \frac{(\beta - Z_s)}{\beta} \right)} = \frac{\gamma' + \frac{(M - Z_s)}{Z_s + M} \tanh(\gamma')}{\gamma' + \tanh(\gamma') \left( \frac{2l(Z_s - M)}{Z_L} - \frac{(M - Z_s)}{Z_s + M} \right)} \\
\frac{\hat{V}_2}{\hat{V}_1} &= \frac{\gamma' + \frac{(M - Z_s)}{Z_s + M} \tanh(\gamma')}{\gamma' + \tanh(\gamma') \left( \frac{2l(Z_s - M)}{Z_L} - \frac{(M - Z_s)}{Z_s + M} \right)} \quad 5.38
\end{aligned}$$

Equation 5.38 represents the distributed transformer transfer function entirely in terms of physical parameters. To turn equation 5.38 into an expression that offers more intuitive feeling,

consider the transfer function in the case of a low inductance device in which main and leakage inductance can be neglected.

In the limit that  $M \rightarrow 0$ , equation 5.38 now becomes

$$\frac{\hat{V}_2}{\hat{V}_1} = -\frac{\tanh(\gamma') - \gamma'}{\gamma' + \tanh(\gamma') \left(1 + \frac{2Z_s l}{Z_L}\right)}. \quad 5.39$$

When neglecting mutual inductance, equation 5.39 gives a nice and simple transfer function for the distributed transformer circuit model. Equation 5.39 can be simplified further by neglecting leakage inductance and evaluating the model parameters as follows.

$$Z_s = R \parallel \frac{1}{j\omega C_i} = \frac{R}{R + \frac{1}{j\omega C_i}} = \frac{R}{j\omega C_i R + 1} \quad 5.40$$

$$Y_c = \frac{1}{\frac{1}{j\omega C_c}} = j\omega C_c \quad 5.41$$

$$\lim_{M \rightarrow 0} \gamma^2 = 2Y_c(Z_s) = 2(j\omega C_c) \left( \frac{R}{j\omega C_i R + 1} \right) = \frac{j2\omega C_c R}{j\omega C_i R + 1}$$

$$= 2 \left( \frac{j\omega C_c R}{1 + (\omega C_i R)^2} \right) (1 - j\omega C_i R) = 2 \left( \frac{j\omega C_c R + \omega^2 * (RC_c) * (RC_i)}{1 + (\omega C_i R)^2} \right) \quad 5.42$$

$$\lim_{M \rightarrow 0} \gamma' = \frac{l}{2} \sqrt{2} \left( \frac{j\omega C_c R + \omega^2 * (RC_c) * (RC_i)}{1 + (\omega C_i R)^2} \right)^{1/2} = \frac{\sqrt{2}}{2} \left( \frac{j\omega C_c R l^2 + \omega^2 * (RC_c l^2) * (RC_i)}{1 + (\omega C_i R)^2} \right)^{1/2}$$

$$= \frac{\sqrt{2}}{2} \left( \frac{j\omega\tilde{C}_c\tilde{R} + \omega^2 * (\tilde{R}\tilde{C}_c) * (RC_i)}{1 + (\omega C_i R)^2} \right)^{1/2} = \frac{\sqrt{2}}{2} \left( \frac{j\omega\alpha + \omega^2 \alpha\alpha'}{1 + (\omega\alpha')^2} \right)^{1/2} \quad 5.43$$

where  $C_c$  is the per length cross-winding capacitance,  $C_i$  is the per length intra-winding capacitance,  $R$  is the per length series winding resistance and the following substitutions have been made.

$$\tilde{R} = Rl \quad 5.44$$

$$\tilde{C}_c = C_c l \quad 5.45$$

$$\alpha = \tilde{R}\tilde{C}_c \quad 5.46$$

$$\alpha' = RC_i \quad 5.47$$

Plugging 5.42 and 5.40 into 5.39 will give the transfer function of the  $R - C_i - C_c$  distributed model of the transformer [24].

$$\begin{aligned}
\frac{\hat{V}_2}{\hat{V}_1} &= -\frac{(\tanh(\gamma') - \gamma')}{\left[ \left( 1 + \frac{2Z_s l}{Z_L} \right) \tanh(\gamma') + \gamma' \right]} \\
&\quad \left( \tanh\left( \frac{\sqrt{2}}{2} \left( \frac{j\omega\alpha + \omega^2\alpha\alpha'}{1 + (\omega\alpha')^2} \right)^{1/2} \right) - \frac{\sqrt{2}}{2} \left( \frac{j\omega\alpha + \omega^2\alpha\alpha'}{1 + (\omega\alpha')^2} \right)^{1/2} \right) \\
&= -\frac{\left[ \left( 1 + \frac{2 \left( \frac{R}{j\omega C_i R + 1} \right) l}{Z_L} \right) \tanh\left( \frac{\sqrt{2}}{2} \left( \frac{j\omega\alpha + \omega^2\alpha\alpha'}{1 + (\omega\alpha')^2} \right)^{1/2} \right) + \frac{\sqrt{2}}{2} \left( \frac{j\omega\alpha + \omega^2\alpha\alpha'}{1 + (\omega\alpha')^2} \right)^{1/2} \right]}{\left( \tanh\left( \frac{\sqrt{2}}{2} \left( \frac{j\omega\alpha + \omega^2\alpha\alpha'}{1 + (\omega\alpha')^2} \right)^{1/2} \right) - \frac{\sqrt{2}}{2} \left( \frac{j\omega\alpha + \omega^2\alpha\alpha'}{1 + (\omega\alpha')^2} \right)^{1/2} \right)} \\
&= -\frac{\left[ \left( 1 + \frac{2\tilde{R}}{Z_L} \left( \frac{1}{j\omega\alpha' + 1} \right) \right) \tanh\left( \frac{\sqrt{2}}{2} \left( \frac{j\omega\alpha + \omega^2\alpha\alpha'}{1 + (\omega\alpha')^2} \right)^{1/2} \right) + \frac{\sqrt{2}}{2} \left( \frac{j\omega\alpha + \omega^2\alpha\alpha'}{1 + (\omega\alpha')^2} \right)^{1/2} \right]}{\left( \tanh\left( \frac{\sqrt{2}}{2} \left( \frac{j\omega\alpha + \omega^2\alpha\alpha'}{1 + (\omega\alpha')^2} \right)^{1/2} \right) - \frac{\sqrt{2}}{2} \left( \frac{j\omega\alpha + \omega^2\alpha\alpha'}{1 + (\omega\alpha')^2} \right)^{1/2} \right)} \tag{5.48} \\
&= -\frac{\left[ \left( 1 + 2\lambda \left( \frac{1}{j\omega\alpha' + 1} \right) \right) \tanh\left( \frac{\sqrt{2}}{2} \left( \frac{j\omega\alpha + \omega^2\alpha\alpha'}{1 + (\omega\alpha')^2} \right)^{1/2} \right) + \frac{\sqrt{2}}{2} \left( \frac{j\omega\alpha + \omega^2\alpha\alpha'}{1 + (\omega\alpha')^2} \right)^{1/2} \right]}{\left( \tanh\left( \frac{\sqrt{2}}{2} \left( \frac{j\omega\alpha + \omega^2\alpha\alpha'}{1 + (\omega\alpha')^2} \right)^{1/2} \right) - \frac{\sqrt{2}}{2} \left( \frac{j\omega\alpha + \omega^2\alpha\alpha'}{1 + (\omega\alpha')^2} \right)^{1/2} \right)} \tag{5.49}
\end{aligned}$$

The following substitutions have been made in equation 5.48.

$$\lambda = \frac{\tilde{R}}{Z_L} \tag{5.49}$$

Equation 5.48 reveals that for the distributed transformer model conceived above, the transfer function depends on only three parameters:  $\alpha$ ,  $\alpha'$ , and  $\lambda$ . FIG. 5.3 and FIG. 5.4 show how the transfer function behaves when changing these parameters.

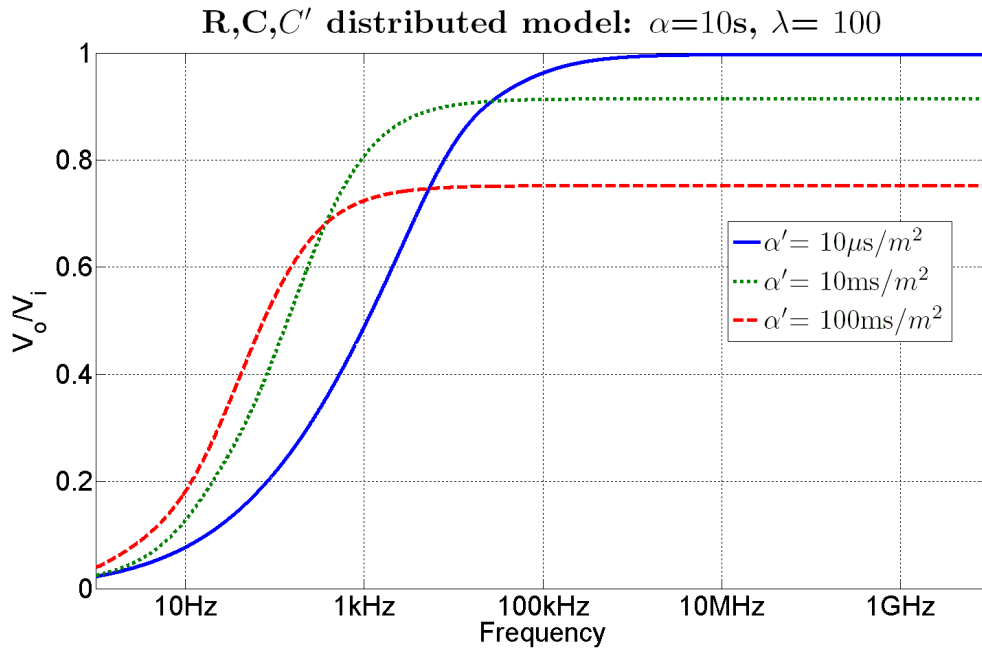


**FIG. 5.3. Distributed model without inductance transfer characteristic (varying alpha prime).**

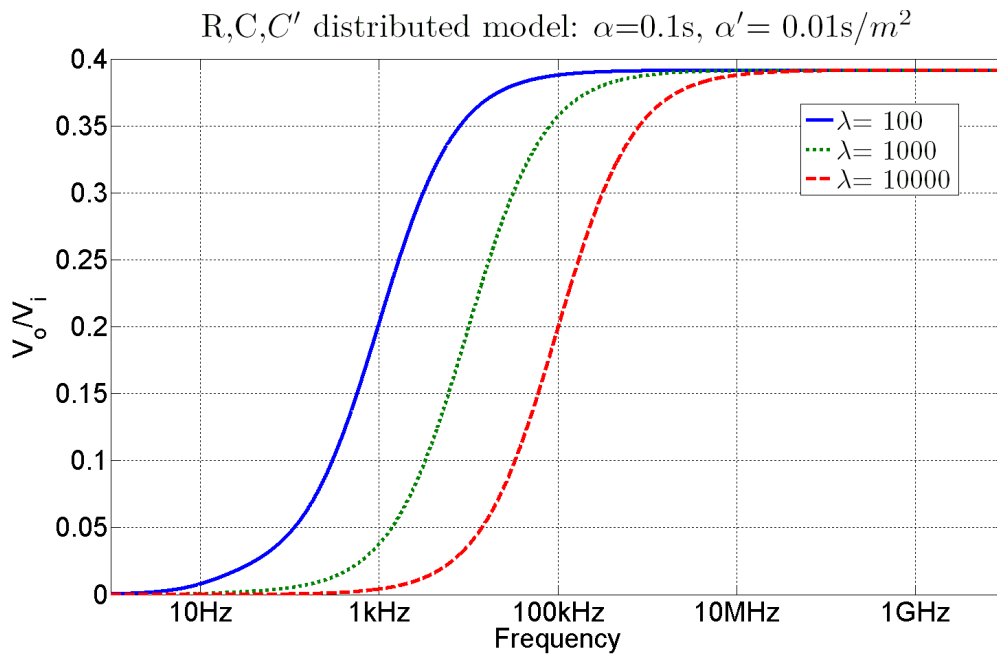


**FIG. 5.4. Distributed model without inductance transfer characteristic (varying Lambda).**

Another important expression that can be derived from the above distributed model is the primary input impedance, which is the ratio of the differential mode winding terminal voltage ( $2\hat{V}_1$ ) and the winding current.

$$Z_1 = \frac{2\hat{V}_1}{\hat{I}_1} \quad 5.50$$

Using equations 5.30 and 5.36, the input primary impedance is given by the following equation. An example impedance plot using the distributed analytical expression is given in FIG. 5.5.

$$\begin{aligned}
Z_1 &= \frac{2A \frac{\cosh(\gamma')(Z_L\beta'\gamma) + \sinh(\gamma')(4\beta'(Z_s - M) - Z_L(\beta - Z_s))}{(2\beta'(Z_s - M) - Z_L(\beta - Z_s))}}{2 \left[ \frac{A(\gamma\beta'Z_L \cosh(\gamma') + Z_L(\beta - Z_s) \sinh(\gamma'))}{(2\beta'(Z_s - M) - Z_L(\beta - Z_s))} \right] \frac{(\beta - M) - \gamma A \cosh(\gamma')}{Z_L}} \\
&= 2 \frac{\frac{\cosh(\gamma')(Z_L\beta'\gamma) + \sinh(\gamma')(4\beta'(Z_s - M) - Z_L(\beta - Z_s))}{(2\beta'(Z_s - M) - Z_L(\beta - Z_s))}}{\left[ \frac{(\gamma\beta'Z_L \cosh(\gamma') + Z_L(\beta - Z_s) \sinh(\gamma'))}{(2\beta'(Z_s - M) - Z_L(\beta - Z_s))} \right] \frac{(\beta - M) - \gamma Z_L \cosh(\gamma')}{Z_L(\beta - Z_s)}} \\
&= 2 \frac{\cosh(\gamma')(Z_L\beta'\gamma) + \sinh(\gamma')(4\beta'(Z_s - M) - Z_L(\beta - Z_s))}{2(\gamma\beta' \cosh(\gamma') + (\beta - Z_s) \sinh(\gamma'))(\beta - M) - \gamma \cosh(\gamma')(2\beta'(Z_s - M) - Z_L(\beta - Z_s))} \\
&= 2 \frac{\cosh(\gamma')(Z_L\beta'\gamma) + \sinh(\gamma')(4\beta'(Z_s - M) - Z_L(\beta - Z_s))}{2\gamma\beta' \cosh(\gamma') + 2(\beta - M) \sinh(\gamma') + Z_L\gamma \cosh(\gamma')} \\
&= \frac{(Z_L\beta'\gamma) + \tanh(\gamma')(4\beta'(Z_s - M) - Z_L(\beta - Z_s))}{\gamma(\beta' + \frac{Z_L}{2}) + (\beta - M) \tanh(\gamma')}
\end{aligned} \quad 5.51$$

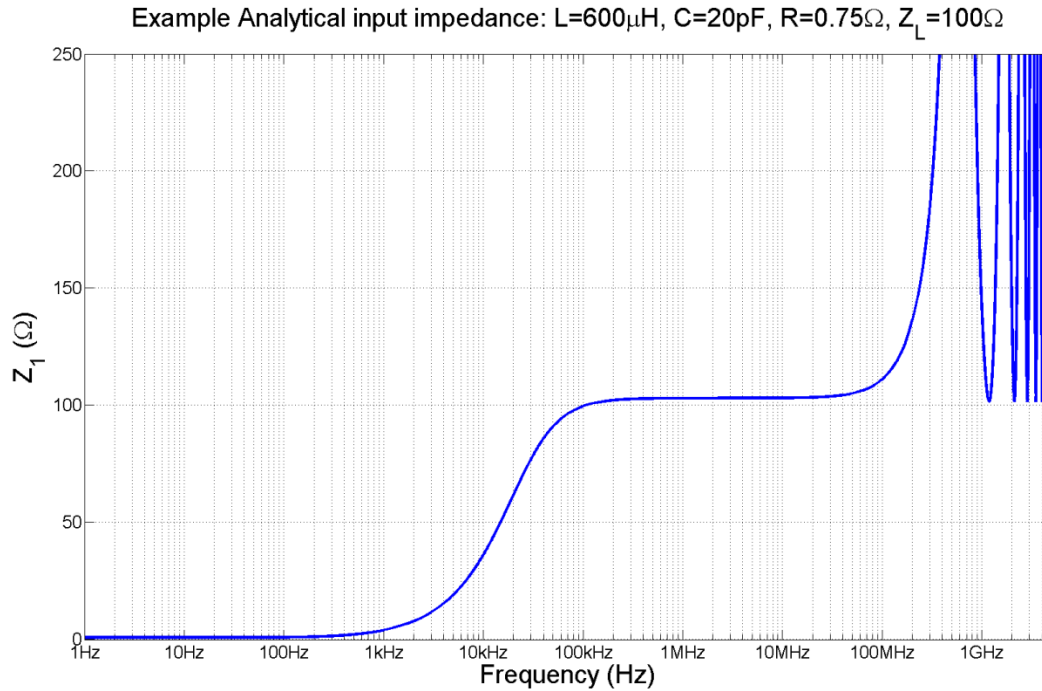


**FIG. 5.5.** Plot of transformer input impedance calculated by the analytical distributed model equations.

The above analysis results in analytical expression for the transfer relation and input impedance using the distributed model of a transformer regarding differential-mode signals. Similar to the analysis of the lumped element equivalent circuit, in certain frequency regions (depending on the impedance topology and values) the distributed model collapses into a simpler form. In chapter 6, these simplifications are used to analyze commercial device measurements to extract their model parameters.

### **5.3. Common-mode model**

Similar to the differential mode analysis, the common mode signal implies specific boundary conditions and simplifications to the distributed model. Consider FIG. 5.7 showing the boundary conditions. For this analysis, the midpoint of the winding will be connected through an arbitrary impedance to ground, equal on both windings. This is commonly done in practice to

shunt common-mode currents and reduce common mode interference coupling to the secondary winding. Also, with common-mode signals, the signal voltage on either terminal is equal. With the physical symmetry of the winding, the upper half and lower half of the distributed model are identical. Thus, the analysis can be performed on a half-model, with the careful boundary modification that the current at the  $y=0$  node is twice that of the half-winding alone.

The placement of the load is a final consideration. Placing the load between the secondary terminals will have no effect, since the signal mode is evenly symmetric. With even symmetry (same voltage on both terminals) no current will flow through the load and the issue is moot. However, the load can and is considered to be between each terminal and ground, and is equal for the upper and lower half-windings. Following is the full mathematical analysis of the common-mode distributed model, resulting in an analytical expression for the common-mode transfer relation.

**5.3.1. Common mode distributed model analysis**

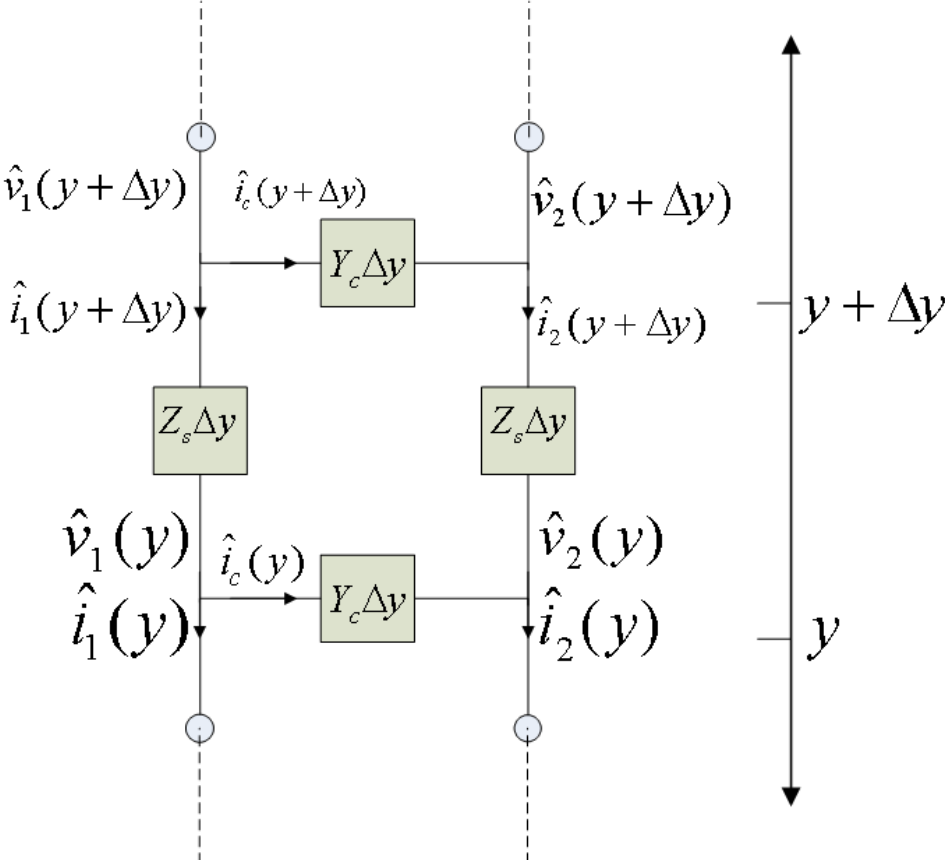


**FIG. 5.6. Single cell of common-mode distributed model.**

Similar to the analysis of the differential-mode model, the following differential equations can be derived from the infinitesimally small circuit cell shown above in FIG. 5.6.

$$\hat{i}_1(y + \Delta y) - \hat{i}_1(y) = (\hat{v}_1(y) - \hat{v}_2(y))Y_C \Delta y \quad 5.52$$

$$\frac{\hat{i}_1(y + \Delta y) - \hat{i}_1(y)}{\Delta y} = (\hat{v}_1(y) - \hat{v}_2(y))Y_C \quad 5.53$$

$$\lim_{\Delta y \rightarrow 0} \frac{\hat{i}_1(y + \Delta y) - \hat{i}_1(y)}{\Delta y} = \frac{d\hat{i}_1(y)}{dy} = (\hat{v}_1(y) - \hat{v}_2(y))Y_C \quad 5.54$$

$$\frac{d\hat{i}_2(y)}{dy} = -\frac{d\hat{i}_1(y)}{dy} = -(\hat{v}_1(y) - \hat{v}_2(y))Y_C \quad 5.55$$

Note:

$$\frac{d\hat{i}_1(y)}{dy} + \frac{d\hat{i}_2(y)}{dy} = 0 = \frac{d}{dy}(\hat{i}_1(y) + \hat{i}_2(y)) = \frac{d}{dy}(\hat{I}) \quad 5.56$$

thus implying  $\hat{I}$  is a constant. KVL on the series branch gives the following differential voltage equations.

$$\frac{d\hat{v}_1(y)}{dy} = Z_s \hat{i}_1(y) \Rightarrow \hat{i}_1(y) = \frac{1}{Z_s} \frac{d\hat{v}_1(y)}{dy} \quad 5.57$$

$$\frac{d\hat{v}_2(y)}{dy} = Z_s \hat{i}_2(y) \Rightarrow \hat{i}_2(y) = \frac{1}{Z_s} \frac{d\hat{v}_2(y)}{dy} \quad 5.58$$

Thus,  $\hat{I}$  can be written in terms of the first derivative of the voltages.

$$\hat{I} = \hat{i}_1(y) + \hat{i}_2(y) = \frac{1}{Z_s} \left( \frac{d\hat{v}_1(y)}{dy} + \frac{d\hat{v}_2(y)}{dy} \right) (\text{constant}) \quad 5.59$$

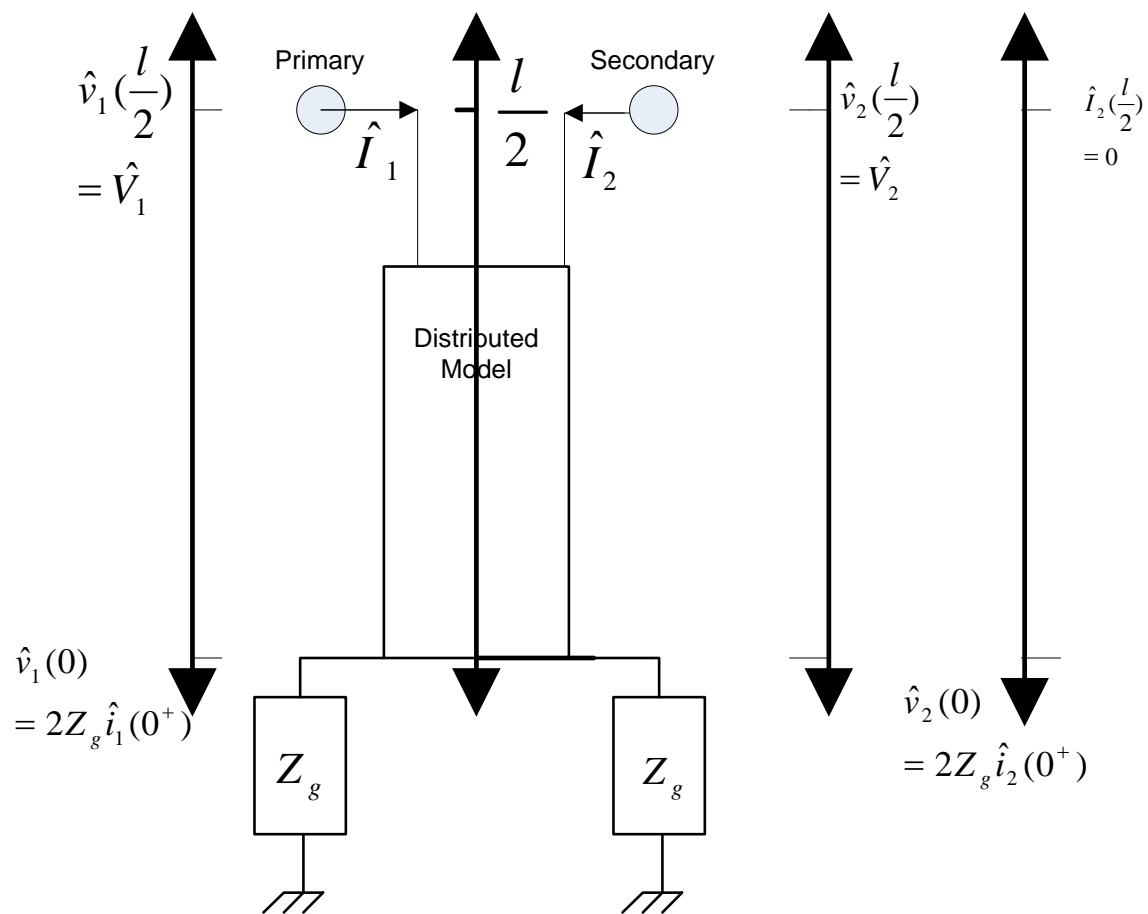


FIG. 5.7. External terminal diagram of common-mode distributed transformer half-model with boundary conditions.

The boundary conditions on the total model are as follows. Equations 5.57 and 5.58 have been used to express the boundary conditions using voltages only.

BCs:

$$\hat{v}_1(0) = 2Z_g \hat{i}_1(0^+) = \frac{2Z_g}{Z_s} \frac{d\hat{v}_1(0)}{dy} \quad 5.60$$

(Primary Center Node Voltage)

$$\hat{v}_2(0) = 2Z_g \hat{i}_2(0^+) = \frac{2Z_g}{Z_s} \frac{d\hat{v}_2(0)}{dy} \quad 5.61$$

(Secondary Center Node Voltage)

$$\hat{i}_2\left(\frac{l}{2}\right) = -\frac{\hat{V}_2}{Z_L} = \frac{1}{Z_s} \frac{d\hat{v}_2\left(\frac{l}{2}\right)}{dy} \Rightarrow \hat{V}_2 + \frac{Z_L}{Z_s} \frac{d\hat{v}_2\left(\frac{l}{2}\right)}{dy} = 0 \quad 5.62$$

(Secondary Loading)

The following expressions are defined and substituted as functions  $f(y)$  and  $g(y)$ .

$$f(y) = \hat{v}_1(y) + \hat{v}_2(y) \quad 5.63$$

$$g(y) = \hat{v}_1(y) - \hat{v}_2(y) \quad 5.64$$

Using equations 5.57 and 5.58,  $\frac{df(y)}{dy}$  can be integrated with respect to  $y$ .

$$\int \frac{df(y)}{dy} dy = f(y) = \int Z_s (\hat{i}_1(y) + \hat{i}_2(y)) dy = \int Z_s (\hat{I}) dy = Z_s (\hat{I}) y + C \quad 5.65$$

$$f(y) = Z_s (\hat{I}) y + C$$

Using boundary conditions 5.60 and 5.61,  $C$  can be found.

$$f(0) = 2Z_g \hat{I} = C \quad 5.66$$

$f(y)$  can then be written as follows.

$$f(y) = Z_s \hat{I} y + 2Z_g \hat{I} \quad 5.67$$

Differentiating  $g(y)$  and using 5.57 and 5.58 gives the following:

$$\frac{dg(y)}{dy} = Z_s (\hat{i}_1(y) - \hat{i}_2(y)) \quad 5.68$$

Differentiating 5.68 and using 5.55 gives the following:

$$\frac{d^2g(y)}{dy^2} = Z_s \left( \frac{d\hat{i}_1(y)}{dy} - \frac{d\hat{i}_2(y)}{dy} \right) = 2Z_s \left( \frac{d\hat{i}_1(y)}{dy} \right) = 2Z_s Y_c (g(y)) \quad 5.69$$

Solutions for  $g(y)$  in 5.69 are of the form

$$g(y) = Ae^{\gamma y} + Be^{-\gamma y} \quad 5.70$$

where

$$\gamma^2 = 2Z_s Y_c \quad 5.71$$

Using the boundary conditions 5.60 and 5.61 and equation 5.70,  $B$  can be found in terms of  $A$ .

$$\begin{aligned} g(0) = A + B &= \frac{2Z_g}{Z_s} \left( \frac{d\hat{v}_1(0)}{dy} - \frac{d\hat{v}_2(0)}{dy} \right) = \frac{2Z_g}{Z_s} \frac{dg}{dy}(0) = \frac{2Z_g}{Z_s} (\gamma(A - B)) = \frac{2Z_g \gamma A}{Z_s} - \frac{2Z_g \gamma B}{Z_s} \Rightarrow \\ B \left( 1 + \frac{2Z_g \gamma}{Z_s} \right) &= \left( \frac{2Z_g \gamma}{Z_s} - 1 \right) A \Rightarrow \\ B &= A \left( \frac{2Z_g \gamma - Z_s}{2Z_g \gamma + Z_s} \right) \end{aligned} \quad 5.72$$

and

$$\begin{aligned}
g(y) &= Ae^{\gamma y} + A\left(\frac{2Z_g\gamma - Z_s}{2Z_g\gamma + Z_s}\right)e^{-\gamma y} = \frac{A(2Z_g\gamma + Z_s)e^{\gamma y} + A(2Z_g\gamma - Z_s)e^{-\gamma y}}{2Z_g\gamma + Z_s} & 5.73 \\
&= \frac{A(2Z_g\gamma)(e^{\gamma y} + e^{-\gamma y}) + A(Z_s)(e^{\gamma y} - e^{-\gamma y})}{2Z_g\gamma + Z_s} = \frac{A(4Z_g\gamma)\cosh(\gamma y) + A(2Z_s)\sinh(\gamma y)}{2Z_g\gamma + Z_s}
\end{aligned}$$

From 5.63 and 5.64, the following equations for the position dependent voltage are found.

$$\hat{v}_1(y) = \frac{f(y) + g(y)}{2} \quad 5.74$$

$$\hat{v}_2(y) = \frac{f(y) - g(y)}{2} \quad 5.75$$

Plugging equations 5.67 and 5.73 into equations 5.74 and 5.75 gives the explicit forms of the position dependent primary and secondary voltage as shown below.

$$\begin{aligned}
\hat{v}_1(y) &= \frac{Z_s\hat{I}y + 2Z_g\hat{I} + \frac{A(4Z_g\gamma)\cosh(\gamma y) + A(2Z_s)\sinh(\gamma y)}{2Z_g\gamma + Z_s}}{2} & 5.76 \\
&= \frac{\hat{I}}{2}(Z_s y + 2Z_g) + \frac{A(2Z_g\gamma)\cosh(\gamma y) + A(Z_s)\sinh(\gamma y)}{2Z_g\gamma + Z_s}
\end{aligned}$$

$$\hat{v}_2(y) = \frac{\hat{I}}{2}(Z_s y + 2Z_g) - \frac{A(2Z_g\gamma)\cosh(\gamma y) + A(Z_s)\sinh(\gamma y)}{2Z_g\gamma + Z_s} \quad 5.77$$

To find  $\hat{I}$ , the first derivative of 5.77 can be used as well as equation 5.58.

$$\frac{d\hat{v}_2(y)}{dy} = Z_s\hat{i}_2(y) = \frac{\hat{I}}{2}Z_s - \frac{1}{2}\frac{dg(y)}{dy} \quad 5.78$$

Evaluating 5.78 at  $\frac{l}{2}$  and using boundary condition 5.62 yields the following. Also, the

argument of  $g$  is changed from  $y$  to  $\gamma y$  ( $g(\gamma y)$ ).

$$\frac{d\hat{v}_2(\frac{l}{2})}{dy} = -\frac{Z_s \hat{V}_2}{Z_L} = \frac{\hat{I}}{2} Z_s - \frac{1}{2} \frac{dg(\gamma')}{dy} = \frac{\hat{i}_1(l/2)}{2} Z_s - \frac{Z_s \hat{V}_2}{2Z_L} - \frac{1}{2} \frac{dg(\gamma')}{dy} \Rightarrow$$

$$\hat{i}_1(l/2) = -\frac{\hat{V}_2}{Z_L} + \frac{1}{Z_s} \frac{dg(\gamma')}{dy} \Rightarrow \hat{I} = -\frac{2\hat{V}_2}{Z_L} + \frac{1}{Z_s} \frac{dg(\gamma')}{dy} \quad 5.79$$

where

$$\gamma' = \gamma \frac{l}{2} \quad 5.80$$

Evaluating 5.77 at  $\frac{l}{2}$  and inserting the expression for  $\hat{I}$  from 5.79 yields the following equation

$$\hat{V}_2 = \left( -\frac{\hat{V}_2}{Z_L} + \frac{1}{2Z_s} \frac{dg(\gamma')}{dy} \right) \left( \frac{Z_s l}{2} + 2Z_g \right) - \frac{g(\gamma')}{2} \quad 5.81$$

$$= -\frac{Z_s \hat{V}_2 l}{2Z_L} - \frac{2\hat{V}_2 Z_g}{Z_L} + \frac{l}{4} \frac{dg(\gamma')}{dy} + \frac{Z_g}{Z_s} \frac{dg(\gamma')}{dy} - \frac{g(\gamma')}{2} \Rightarrow$$

$$\hat{V}_2 \left( 1 + \frac{Z_s l}{2Z_L} + \frac{2Z_g}{Z_L} \right) = \frac{l}{4} \frac{dg(\gamma')}{dy} + \frac{Z_g}{Z_s} \frac{dg(\gamma')}{dy} - \frac{g(\gamma')}{2} \Rightarrow$$

$$\hat{V}_2 = \frac{\left( \frac{l}{4} \frac{dg(\gamma')}{dy} + \frac{Z_g}{Z_s} \frac{dg(\gamma')}{dy} - \frac{g(\gamma')}{2} \right)}{\left( 1 + \frac{Z_s l}{2Z_L} + \frac{2Z_g}{Z_L} \right)}$$

$\hat{I}$  can now be expressed as follows:

$$\begin{aligned}
\hat{I} &= \frac{-2Z_s \left( \frac{l}{4} \frac{dg(\gamma')}{dy} + \frac{Z_g}{Z_s} \frac{dg(\gamma')}{dy} - \frac{g(\gamma')}{2} \right) + \left( Z_L + \frac{Z_s l}{2} + 2Z_g \right) \frac{dg(\gamma')}{dy}}{Z_s \left( Z_L + \frac{Z_s l}{2} + 2Z_g \right)} \\
&= \frac{Z_s g(\gamma') + Z_L \frac{dg(\gamma')}{dy}}{Z_s \left( Z_L + \frac{Z_s l}{2} + 2Z_g \right)}
\end{aligned} \tag{5.82}$$

The expression for  $\hat{v}_1(\frac{l}{2})$  in terms of  $g$  is as follows:

$$\begin{aligned}
\hat{V}_1 &= \frac{\hat{I}}{2} \left( Z_s \frac{l}{2} + 2Z_g \right) + \frac{g(\gamma')}{2} \\
&= \frac{\left( \frac{Z_s g(\gamma') + Z_L \frac{dg(\gamma')}{dy}}{2Z_s \left( Z_L + \frac{Z_s l}{2} + 2Z_g \right)} \right) \left( \frac{Z_s l}{2} + 2Z_g \right) + \frac{g(\gamma')}{2}}{2 \left( Z_s g(\gamma') + Z_L \frac{dg(\gamma')}{dy} \right) \left( \frac{Z_s l}{2} + 2Z_g \right) + 2Z_s \left( Z_L + \frac{Z_s l}{2} + 2Z_g \right) g(\gamma')} \\
&= \frac{2 \left( Z_s g(\gamma') + Z_L \frac{dg(\gamma')}{dy} \right) \left( \frac{Z_s l}{2} + 2Z_g \right) + 2Z_s \left( Z_L + \frac{Z_s l}{2} + 2Z_g \right) g(\gamma')}{4Z_s \left( Z_L + \frac{Z_s l}{2} + 2Z_g \right)} \\
&= \frac{2 \left( Z_L \frac{dg(\gamma')}{dy} \right) \left( \frac{Z_s l}{2} + 2Z_g \right) + 2Z_s \left( Z_L + Z_s l + 4Z_g \right) g(\gamma')}{4Z_s \left( Z_L + \frac{Z_s l}{2} + 2Z_g \right)}
\end{aligned} \tag{5.83}$$

$\hat{V}_2$  (equation 5.81) can be written to have the same denominator as  $\hat{V}_1$ .

$$\hat{V}_2 = \frac{4Z_s Z_L \left( \frac{l}{4} \frac{dg(\gamma')}{dy} + \frac{Z_g}{Z_s} \frac{dg(\gamma')}{dy} - \frac{g(\gamma')}{2} \right)}{4Z_s \left( Z_L + \frac{Z_s l}{2} + 2Z_g \right)} \quad 5.84$$

The transfer function for the entire device is given by the following expression:

$$\frac{\hat{V}_2}{\hat{V}_1} = \frac{2Z_s Z_L \left( \left( \frac{l}{4} + \frac{Z_g}{Z_s} \right) \frac{dg(\gamma')}{dy} - \frac{g(\gamma')}{2} \right)}{\left( \frac{dg(\gamma')}{dy} \right) \left( \frac{Z_s Z_L l}{2} + 2Z_L Z_g \right) + Z_s (Z_L + Z_s l + 4Z_g) g(\gamma')} \quad 5.85$$

Substituting in for  $g$  (equation 5.73) and its derivatives gives the following.

$$\begin{aligned}
\frac{\hat{V}_2}{\hat{V}_1} &= \left[ \frac{\frac{I}{4} + \frac{Z_g}{Z_s} \left( \frac{A(4Z_g\gamma^2) \sinh(\gamma') + A(2Z_s\gamma) \cosh(\gamma')}{2Z_g\gamma + Z_s} \right)}{2Z_s Z_1} - \frac{\left( \frac{A(4Z_g\gamma) \cosh(\gamma') + A(2Z_s) \sinh(\gamma')}{2Z_g\gamma + Z_s} \right)}{2} \right] \\
&= \left( \frac{A(4Z_g\gamma^2) \sinh(\gamma') + A(2Z_s\gamma) \cosh(\gamma')}{2Z_g\gamma + Z_s} \right) \left( \frac{Z_s Z_1 I}{2} + 2Z_1 Z_g \right) + Z_s (Z_1 + Z_3) \left( \frac{A(4Z_g\gamma) \cosh(\gamma') + A(2Z_s) \sinh(\gamma')}{2Z_g\gamma + Z_s} \right) \\
&= \frac{2Z_s Z_1 \left( \frac{I}{4} + \frac{Z_g}{Z_s} \right) (4Z_g\gamma^2 \sinh(\gamma') + 2Z_s\gamma \cosh(\gamma')) - (2Z_g\gamma) \cosh(\gamma') - (Z_s) \sinh(\gamma')}{(4Z_g\gamma^2 \sinh(\gamma') + 2Z_s\gamma \cosh(\gamma')) \left( \frac{Z_s Z_1 I}{2} + 2Z_1 Z_g \right) + Z_s (Z_1 + Z_3) (A(4Z_g\gamma) \cosh(\gamma') + (2Z_s) \sinh(\gamma'))}
\end{aligned}$$

5.86

Grouping *cosh* and *sinh* terms gives the following:

$$\begin{aligned}
\frac{\hat{V}_2}{\hat{V}_1} &= \frac{2Z_s Z_I \left( \frac{l}{4} + \frac{Z_\epsilon}{Z_s} \right) (4Z_\epsilon \gamma^2 \sinh(\gamma') + 2Z_s \gamma \cosh(\gamma')) - (2Z_\epsilon \gamma) \cosh(\gamma') - (Z_s) \sinh(\gamma')}{(4Z_\epsilon \gamma^2 \sinh(\gamma') + 2Z_s \gamma \cosh(\gamma')) \left( \frac{Z_s Z_I l}{2} + 2Z_s (Z_I + Z_s) (4Z_\epsilon \gamma) \cosh(\gamma') + (2Z_s) \sinh(\gamma') \right)} \\
&= \frac{2Z_s Z_I \sinh(\gamma') (Z_\epsilon l \gamma^2 + \frac{4Z_\epsilon^2 \gamma^2}{Z_s}) + 2Z_s Z_I \cosh(\gamma') (Z_s \gamma')}{\sinh(\gamma') (2Z_\epsilon \gamma^2 Z_s Z_I l + 8Z_\epsilon^2 \gamma^2 Z_I + 2Z_s^2 Z_I + 2Z_s^2 l + 8Z_s^2 Z_\epsilon) + \cosh(\gamma') (Z_s^2 Z_I l \gamma + 4Z_s Z_I Z_s \gamma + 4Z_\epsilon Z_I Z_s \gamma + 4Z_\epsilon Z_s^2 l \gamma + 16Z_\epsilon^2 Z_s \gamma)} \\
&= \frac{Z_I \sinh(\gamma') (2Z_s Z_\epsilon l \gamma^2 + 8Z_\epsilon^2 \gamma^2 - 2Z_s^2) + Z_I \cosh(\gamma') (2Z_s^2 \gamma')}{\sinh(\gamma') (2Z_\epsilon \gamma^2 Z_s Z_I l + 8Z_\epsilon^2 \gamma^2 Z_I + 2Z_s^2 Z_I + 2Z_s^2 l + 8Z_s^2 Z_\epsilon) + \cosh(\gamma') (Z_s^2 Z_I l \gamma + 4Z_s Z_I Z_s \gamma + 4Z_\epsilon Z_I Z_s \gamma + 4Z_\epsilon Z_s^2 l \gamma + 16Z_\epsilon^2 Z_s \gamma)} \\
&= \frac{\sinh(\gamma') (2Z_s Z_\epsilon l \gamma^2 + 8Z_\epsilon^2 \gamma^2 - 2Z_s^2) + \cosh(\gamma') (2Z_s^2 \gamma')}{\sinh(\gamma') (2Z_\epsilon \gamma^2 Z_s l + 8Z_\epsilon^2 \gamma^2 + 2Z_s^2 + \frac{2Z_s^2 l + 8Z_s^2 Z_\epsilon}{Z_I}) + \cosh(\gamma') (Z_s^2 l \gamma + 4Z_s Z_s \gamma + 4Z_\epsilon Z_s \gamma + \frac{4Z_\epsilon Z_s^2 l \gamma + 16Z_\epsilon^2 Z_s \gamma}{Z_I})} \\
&= \frac{\sinh(\gamma') (Z_s Z_\epsilon l \gamma^2 + 4Z_\epsilon^2 \gamma^2 - Z_s^2) + \cosh(\gamma') (Z_s^2 \gamma')}{\sinh(\gamma') (Z_s Z_\epsilon \gamma^2 l + 4Z_\epsilon^2 \gamma^2 + Z_s^2 + \frac{Z_s^2 l + 4Z_s^2 Z_\epsilon}{Z_I}) + \cosh(\gamma') (Z_s^2 \gamma' + 4Z_s Z_s \gamma + \frac{2Z_\epsilon Z_s^2 l \gamma + 8Z_\epsilon^2 Z_s \gamma}{Z_I})}
\end{aligned}$$

5.87

Multiplying the numerator and denominator by  $\frac{1}{\cosh(\gamma')}$  yields the following final result for the transfer function.

$$\frac{\hat{V}_2}{\hat{V}_1} = \frac{\tanh(\gamma')(Z_s Z_g l \gamma^2 + 4Z_g^2 \gamma^2 - Z_s^2) + (Z_s^2 \gamma')}{\tanh(\gamma')(Z_s Z_g \gamma^2 l + 4Z_g^2 \gamma^2 + Z_s^2 + \frac{Z_s^3 l + 4Z_s^2 Z_g}{Z_L}) + (Z_s^2 \gamma' + 4Z_g Z_s \gamma + \frac{2Z_g Z_s^2 l \gamma + 8Z_g^2 Z_s \gamma}{Z_L})}$$

5.88

**5.1.**

## 5.4. Summary

This chapter has concluded in the full analysis of the distributed model of unity turns ratio Ethernet transformers for both differential-mode and common-mode signals. Transfer functions for both modes have been derived (equations 5.38 and 5.88), the superposition of which will result in the complete transfer characteristic of the device. Both transfer functions were derived in terms of arbitrary impedances. Though the components of the per-length impedances and admittances are intuitive from the physical nature of the device, the topology of the impedance is something that will be validated empirically in the following chapter.

## Chapter 6 : Testing of commercial Ethernet transformers

### 6.1. Introduction

There are many reasons to fully characterize current commercial state of the art Ethernet transformers. To fully understand the function and behavior of Ethernet transformers, they must be characterized in terms of isolation ability, common-mode rejection, differential-mode transparency, and model parameters. These results will be used to compare against the distributed model results from chapter 5. Precise characterization will also benefit the design of novel isolation devices.

Commercial Ethernet transformers are designed around Ethernet standards (IEEE 802.3) published by the IEEE [25]. Ethernet transformer use is necessary for an Ethernet device to comply with the isolation requirement in the standard (reproduced below [25]).

#### **55.5.1 Isolation requirement**

The PHY shall provide electrical isolation between the port device circuits, including frame ground (if any) and all MDI leads. This electrical isolation shall withstand at least one of the following electrical strength tests:

- a) 1500 V rms at 50 Hz to 60 Hz for 60 s, applied as specified in Section 5.2.2 of IEC 60950-1:2001.
- b) 2250 V dc for 60 s, applied as specified in Section 5.2.2 of IEC 60950-1:2001.
- c) A sequence of ten 2400 V impulses of alternating polarity, applied at intervals of not less than 1 s. The shape of the impulses is 1.2/50  $\mu$ s (1.2  $\mu$ s virtual front time, 50  $\mu$ s virtual time or half value), as defined in Annex N of IEC 60950-1:2001.

There shall be no insulation breakdown, as defined in Section 5.2.2 of IEC 60950-1:2001, during the test. The resistance after the test shall be at least 2 M $\Omega$ , measured at 500 V dc.

**FIG. 6.1. Isolation clause in IEEE 802.3 Base-T Ethernet standard. [25]**

In addition to requiring isolation, the IEEE 802.3 standard outlines bandwidth requirements and testing schemes for differential-mode operation and common-mode suppression for the

entire Ethernet physical layer. It is assumed that the Ethernet transformer (only a small part of the physical layer) should be maximally transparent to the differential-mode and maximally suppressive to the common-mode within the outlined frequency ranges. For reference, the frequency ranges are reproduced in Table 6.1 below ([25], [26]).

Knowing that the Ethernet transformers satisfy these bandwidth requirements reasonably well does not offer much information about the real behavior of the devices in the following respects: flat band heights, low knee frequency, resonance behavior, and loading behavior. For some example Ethernet transformer devices (one or two devices out of the entire product line), detailed white papers are published [27]. However, this information is not detailed enough to be useful for model comparisons.

To illuminate as much as possible the true behavior of these devices, precise measurements of the devices were performed. Ethernet transformers designed for 1GBase-T and 10GBase-T Ethernet data rates were characterized in both the differential and common modes. These results were then compared with distributed model fits and found to be in good agreement. The testing methods and results are given in the following sections. Low frequency measurements were previously shown in chapter 4 for the extraction of core parameters for 1GBase-T Ethernet transformers. The following measurements were designed to extend the frequency range and improve the quality of impedance extraction using higher precision (and higher cost) tools.

**Table 6.1. Bandwidths for DM and CM signals for different Ethernet standards [25], [26]**

<b>Ethernet Standard</b>	<b>DM Pass band</b>	<b>CM Suppression Band</b>
100Base-T2	1 MHz – 100 MHz	1 MHz – 250 MHz
1GBase-T	1 MHz – 100 MHz	1 MHz – 250 MHz
10GBase-T	1 MHz – 500 MHz	80 MHz – 1 GHz

## 6.2. Differential-mode Ethernet transformer testing

To perform differential-mode testing on Ethernet transformers, the transformer is thought of as a 2-port device: primary port and secondary port. With this in mind, the general testing concept and procedure was as follows.

A 2-port vector network analyzer (VNA) was used to measure the scattering parameters of the device under test (DUT) in the frequency range from 10kHz to 2 GHz. The VNA port lines were connected as shown in FIG. 6.2. The Ethernet transformers were tested in their commercial packages and mounted to custom designed printed circuit boards outfitted with subminiature version A (SMA) female connectors (see FIG. 6.3).

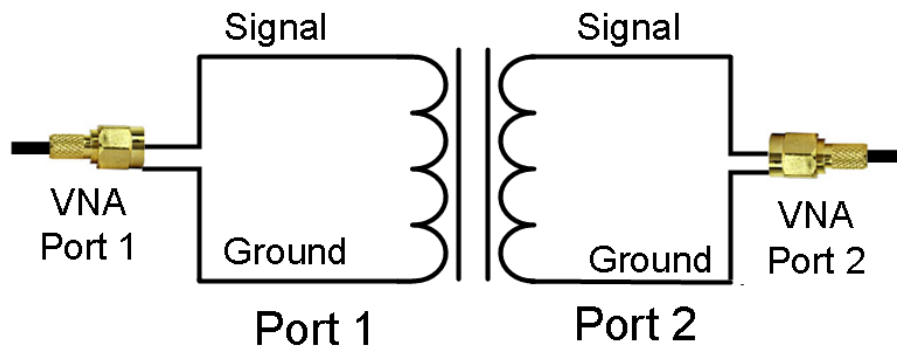


FIG. 6.2. Differential mode VNA testing scheme.

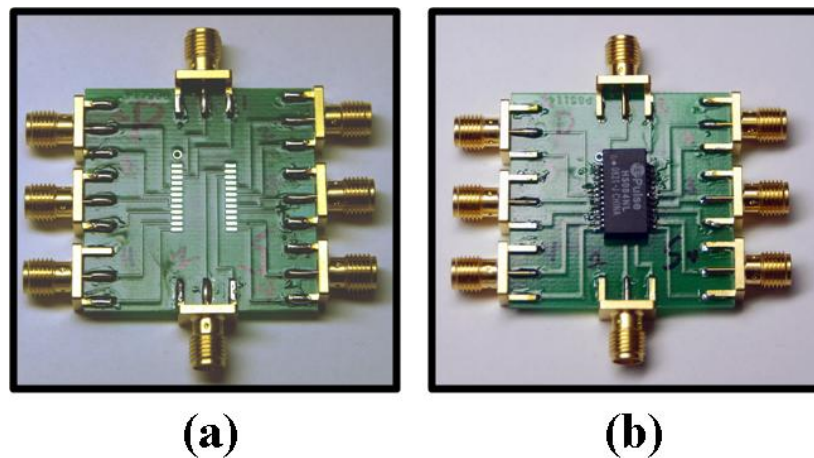


FIG. 6.3. 1GBase-T differential-mode VNA testing custom circuit boards (a) without device (b) with device

Precise testing, especially at high frequencies, requires accounting of all connecting cables, adapters, and PCB lines. To accomplish this, a set of identical circuit boards were used to build a custom set of VNA calibration standards: short, open, load, and through (SOLT). Calibrating the VNA with the standard set characterizes the scattering parameters of all connectors up to the input pins of the transformer package. The effects of the connection hardware can then be factored out of the measurement of the DUT by cascaded 2-port network matrix manipulation (See Appendix A for the procedure). This is all done automatically within the analyzer.

Though the device and calibration set are different for the two types of transformers, the calibration procedure and measurement procedure are identical. The vector network analyzer (VNA) measures scattering parameters where port voltages are defined as either incident ( $V_{portX}^+$ ) or reflected ( $V_{portX}^-$ ) on a specific port. The voltage at the device terminals is given by the following equation, stating that the terminal voltage is the sum of the incident and reflected voltages.

$$V_{portX} = V_{portX}^- + V_{portX}^+ \quad 6.1$$

Though network theory is a familiar topic to many, it is important to rehash the concept here because network matrices will need to be manipulated for analysis of the transformer measurements.

An electrical network with  $N$  defined ports of signal entrance and exit can be fully described with an  $N \times N$  matrix of complex frequency-dependent parameters. Common parameters used for microwave devices are scattering parameters, impedance parameters, and admittance parameters. In the special case of 2-port networks,  $ABCD$  parameters (*Transmission matrix*) can be used with the important ability to be cascaded mathematically. With  $ABCD$  parameters, the matrix

describing a cascade of 2-port devices will be the product of each device's *ABCD* matrix. See Appendix B for an example validating the cascade ability. The definitions of the different parameter types are given in the table below.

**Table 6.2. Network parameter descriptions [28].**

<i>Parameter type</i>	<i>Symbol</i>	<i>Definition</i>	<i>Conditions</i>	<i>Matrix equation form (2x2 example)</i>
Scattering	$S$	$S_{ij} = \frac{V_i^-}{V_i^+}$	$V_k^+ = 0, k \neq j$	$\begin{bmatrix} V_1^- \\ V_2^- \end{bmatrix} = \begin{bmatrix} S_{11} & S_{12} \\ S_{21} & S_{22} \end{bmatrix} \begin{bmatrix} V_1^+ \\ V_2^+ \end{bmatrix}$
Impedance	$Z$	$Z_{ij} = \frac{V_i}{I_j}$	$I_k = 0, k \neq j$	$\begin{bmatrix} V_1 \\ V_2 \end{bmatrix} = \begin{bmatrix} Z_{11} & Z_{12} \\ Z_{21} & Z_{22} \end{bmatrix} \begin{bmatrix} I_1 \\ I_2 \end{bmatrix}$
Admittance	$Y$	$Y_{ij} = \frac{I_i}{V_j}$	$V_k = 0, k \neq j$	$\begin{bmatrix} I_1 \\ I_2 \end{bmatrix} = \begin{bmatrix} Y_{11} & Y_{12} \\ Y_{21} & Y_{22} \end{bmatrix} \begin{bmatrix} V_1 \\ V_2 \end{bmatrix}$
<i>ABCD</i>	$A, B, C, D$	$A = \frac{V_1}{V_2}, I_2 = 0$ $B = \frac{V_1}{I_2}, V_2 = 0$ $C = \frac{I_1}{V_2}, I_2 = 0$ $D = \frac{V_1}{I_2}, V_2 = 0$		$\begin{bmatrix} V_1 \\ I_1 \end{bmatrix} = \begin{bmatrix} A & B \\ C & D \end{bmatrix} \begin{bmatrix} V_2 \\ I_2 \end{bmatrix}$

In the upcoming data analysis, all forms of network parameters will be used. The raw data from the VNA will be in scattering parameters, while the model analyses will use impedance and admittance parameters. *ABCD* parameters will be used in Appendix A to describe VNA calibration, but also in the next chapter for measurement de-embedding. Knowing only the system impedance, all parameter types can be converted into any other parameter type. Here, the conversion formulas will be used without explanation. For insight into the conversion formulas, see **Appendix C**. It is important to note, however, that the admittance parameters are not simply

the element by element reciprocal of the impedance parameters; see the conversion formulas in Appendix C for more information.

It is the interest of the upcoming data analysis to evaluate the devices performance for changing loads. However, scattering parameter measurement is precisely designed to be performed in a matched system with a broadband system impedance (usually  $Z_0 = 50\Omega$ ). To be able to change the load and evaluate the device performance, an equivalent circuit is required. Though similar in appearance, this is not the equivalent transformer circuit discussed in chapters 3 and 4. The equivalent circuits used for these analyses have frequency-dependent measured parameters. There is no need to describe the circuit as resistance, capacitance, and inductance, but only complex impedance or admittance. The following paragraphs describe how the equivalent circuit is formed from the raw scattering data.

The VNA will measure the 2-port scattering matrix over a specified range of frequencies. This implies the data set consists of a  $2 \times 2$  matrix of complex scattering values for each frequency measured. At each frequency, the measured scattering matrix can be converted to an impedance matrix using the conversion formulas given below.

$$Z_{11} = Z_0 \frac{(1 + S_{11})(1 - S_{22}) + S_{12}S_{21}}{(1 - S_{11})(1 - S_{22}) - S_{12}S_{21}} \quad 6.2$$

$$Z_{12} = Z_0 \frac{2S_{12}}{(1 - S_{11})(1 - S_{22}) - S_{12}S_{21}} \quad 6.3$$

$$Z_{21} = Z_0 \frac{2S_{21}}{(1 - S_{11})(1 - S_{22}) - S_{12}S_{21}} \quad 6.4$$

$$Z_{22} = Z_0 \frac{(1 - S_{11})(1 + S_{22}) + S_{12}S_{21}}{(1 - S_{11})(1 - S_{22}) - S_{12}S_{21}} \quad 6.5$$

The formation of the equivalent circuit from impedance parameters can be found in Appendix E. To characterize a device with a passive component equivalent circuit, the device must be *reciprocal*, meaning that the signal measured on port  $Y$  caused by the signal on port  $X$  is identical to the signal measured on port  $X$  caused by the signal on port  $Y$ . This also means that the cross-port parameter terms are equal:  $Z_{21} = Z_{12}$ . All passive circuits must be reciprocal, so if it is possible to equate a device's behavior to the behavior of a passive circuit, the device must be reciprocal. However, the device need not be assumed reciprocal; the reciprocity can be validated by comparing the measured values of the cross-port parameters to see if they are equal ( $Z_{21} \approx Z_{12}$ ).

It is interesting to note that the transformer is a well-known non-reciprocal device. However, referencing the analyses of chapter 3, the transformer becomes reciprocal when the turns ratio is unity. In the equivalent circuit of chapter 3, the issue of reciprocity was avoided by using scaled quantities for both the parameter values and voltages. Given that Ethernet transformers have a unity turns ratio, they can be treated as reciprocal. The reciprocity was also verified experimentally.

Knowing that the device being measured is reciprocal, the equivalent circuit can be represented in either of two ways: T-type circuit topology and  $\Pi$  - type circuit topology (See FIG. 6.4 and FIG. 6.5).

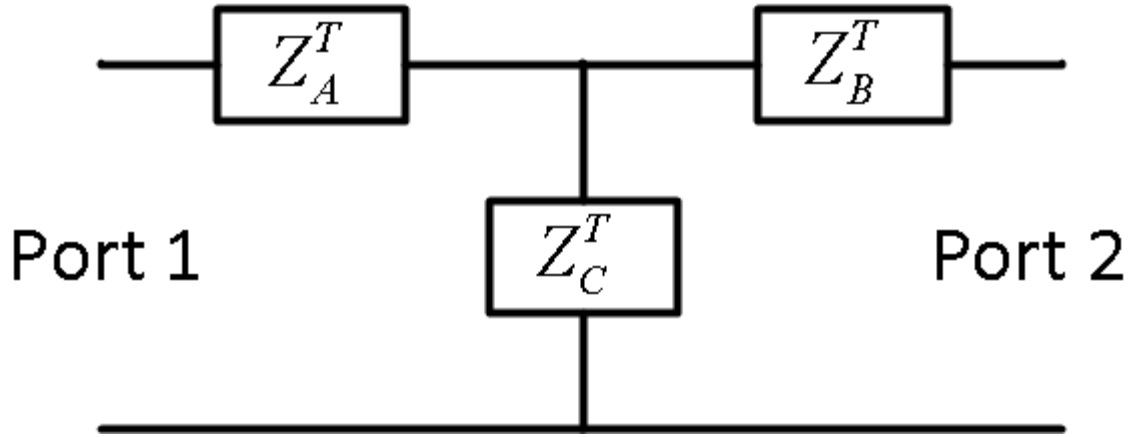


FIG. 6.4. T-Type equivalent circuit

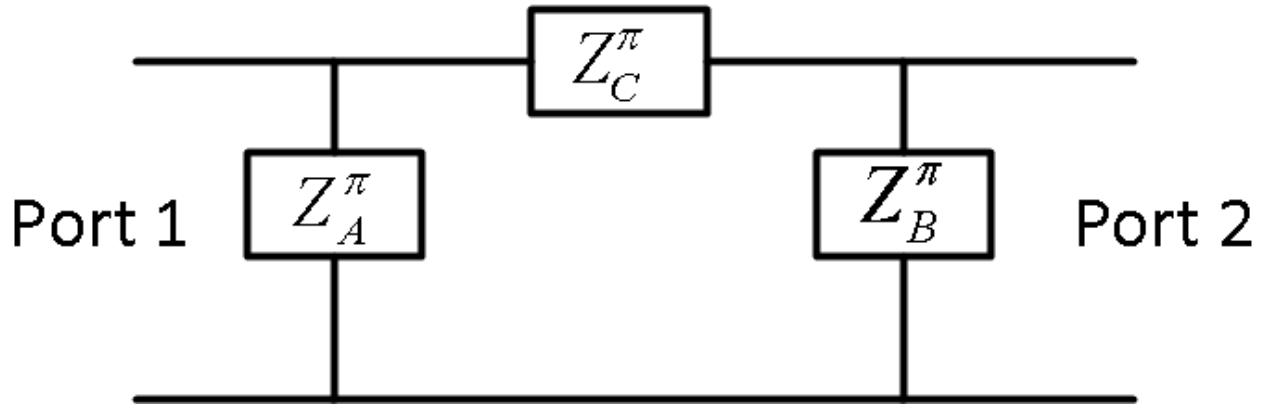


FIG. 6.5. Pi-type equivalent circuit

From the derivation in Appendix E, the following equations relate the model impedances of FIG. 6.4 and FIG. 6.5 to the measured 2-port impedances.

$$Z_A^T = Z_{11} - Z_{12} \quad 6.6$$

$$Z_B^T = Z_{22} - Z_{21} = Z_{22} - Z_{12} \quad 6.7$$

$$Z_C^T = Z_{12} = Z_{21} \quad 6.8$$

$$Z_A^\pi = \frac{1}{Y_{11} + Y_{12}} \quad 6.9$$

$$Z_B^\pi = \frac{1}{Y_{22} + Y_{21}} = \frac{1}{Y_{22} + Y_{12}} \quad 6.10$$

$$Z_C^T = \frac{1}{-Y_{12}} = \frac{1}{-Y_{21}} \quad 6.11$$

Using the T-type equivalent circuit from FIG. 6.4, the loaded transfer relation can be found using voltage division across complex impedances. The load impedance ( $Z_L$ ) is assumed to be placed across the secondary terminals, and the differential port voltages for the primary and secondary are  $\hat{V}_1$  and  $\hat{V}_2$ , respectively. The transfer function is given as follows.

$$\begin{aligned} \hat{V}_2 &= \left( \frac{Z_L}{Z_L + Z_B^T} \right) \hat{V}_{Z_C^T} = \left( \frac{Z_L}{Z_L + Z_B^T} \right) \left( \frac{\left( \frac{(Z_L + Z_B^T)Z_C^T}{Z_L + Z_B^T + Z_C^T} \right)}{\left( \frac{(Z_L + Z_B^T)Z_C^T}{Z_L + Z_B^T + Z_C^T} \right) + Z_A^T} \right) \hat{V}_1 \\ &= \left( \frac{Z_L}{Z_L + Z_B^T} \right) \left( \frac{(Z_L + Z_B^T)Z_C^T}{(Z_L + Z_B^T)Z_C^T + Z_A^T(Z_L + Z_B^T + Z_C^T)} \right) \hat{V}_1 \\ &= \left( \frac{Z_L Z_C^T}{(Z_L + Z_B^T + Z_A^T)Z_C^T + Z_A^T(Z_L + Z_B^T)} \right) \hat{V}_1 \rightarrow \\ &\frac{\hat{V}_2}{\hat{V}_1} = \left( \frac{Z_L Z_C^T}{(Z_L + Z_B^T + Z_A^T)Z_C^T + Z_A^T(Z_L + Z_B^T)} \right) \end{aligned} \quad 6.12$$

Thus, equation 6.12 gives the transfer relation in terms of measurable quantities of the T-type equivalent circuit. The II-type equivalent circuit will be used later for impedance analysis. With the measured equivalent circuit and an equation to determine the transfer relation from the

equivalent circuit, it is now possible to thoroughly analyze the Ethernet transformers. This will be done in the following sections.

### 6.2.1. 1GBase-T Ethernet transformer

Through the analysis of the measured equivalent circuit in the differential-mode signal configuration, it is possible to extract important values that describe the Ethernet transformer. In this section, the following will be extracted with explanation from the measured data regarding the 1Gbase-T Ethernet transformer: differential mode transfer relation, mutual inductance, leakage inductance, line resistance, and core resistance. For reference, the physical dimensions of the 1GBase-T Ethernet transformer are given in Table 6.3 below.

**Table 6.3. 1GBase-T Ethernet transformer physical dimensions.**

<i>Device</i>	<i>Total turns (N)</i>	<i>Outside diameter</i>	<i>Inside diameter</i>	<i>Height</i>	<i>A<sub>cross-section</sub></i>	<i>~ Line Length</i>
1GBase-T XFMR	13	3.5mm	1.5mm	2.5mm	2.5 $\mu\text{m}^2$	~9.1cm

#### 6.2.1.1. Transfer relation

The differential mode transfer relation is given in FIG. 6.6 with different loads. Recalling Table 6.1, the differential mode bandwidth should extend up to 100MHz. The measured transfer relation shows a resonance at about 65MHz, which is too low to be from a transmission line effect with only 9.1cm of line length. Thus, the resonance is more likely due to device inductance and capacitance. Ignoring the potential signal distortion from the resonance, the 100 $\Omega$  loaded transfer relation has a 3dB bandwidth of about 120MHz.

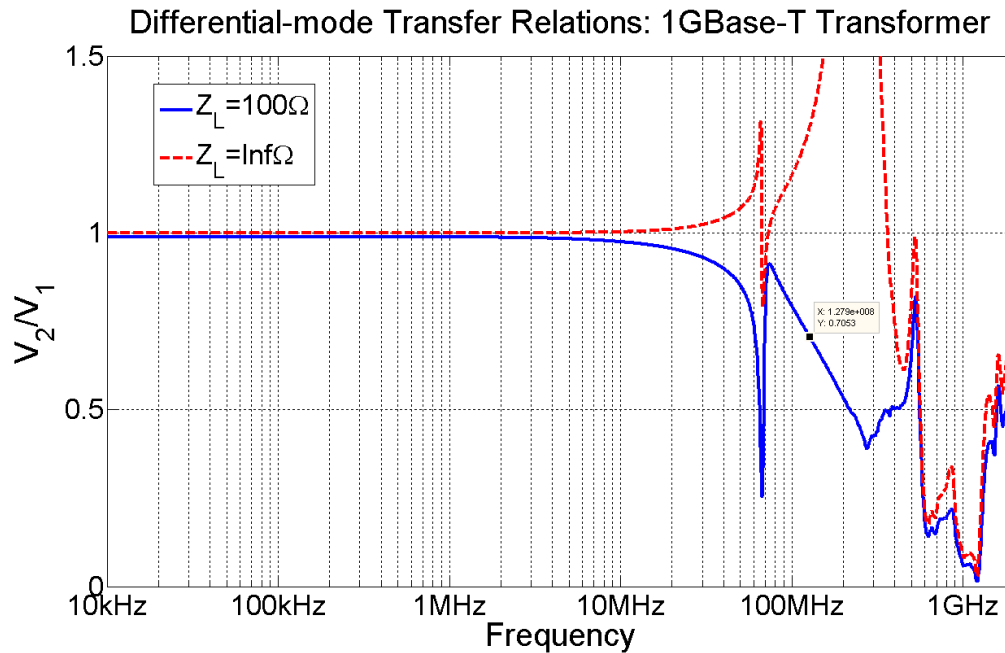


**FIG. 6.6. 1GBase-T Ethernet Transformer transfer relation.**

The frequency range of the precision VNA does not extend low enough to see the low frequency roll off. However, using an automated in-house built measuring system, the scalar transfer relation can be measured (in a less precise manner) from 1Hz up to 80 MHz. The scheme limits the measurement to infinite loads, and is purely a measurement of signal magnitude. The description of the in-house measurement system can be found in Appendix D. This data has been added to the infinite load VNA data and is shown in FIG. 6.7. From the in-house data in FIG. 6.7, the low frequency 3dB point is around 75Hz.

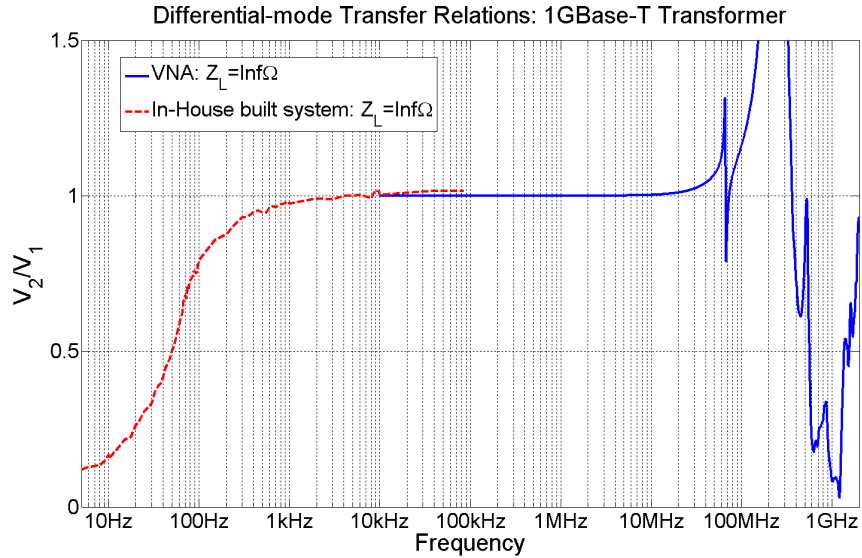


FIG. 6.7. 1GBase-T infinite loaded transfer relation with in-house system supplemental data.

### 6.2.1.2. Mutual inductance

By comparing the T-type equivalent circuit to the equivalent circuit of chapter 3, it is clear that the mutual inductance is part of  $Z_C^T$  from the T-type circuit. By taking the imaginary part of  $Z_C^T$  and looking at a frequency region where the inductance will dominate the impedance, the mutual inductance can be extracted (See FIG. 6.8). This is done by first taking the series inductance from the measured data and converting it to the equivalent and more familiar parallel inductance, **using equations 3.88 and 3.89 from chapter 3**. From the figure, it is clear that in the low frequency range, where the core impedance is approximately the mutual inductance impedance, the transformer has a stable inductance of approximately 600 $\mu$ H - 650  $\mu$ H.

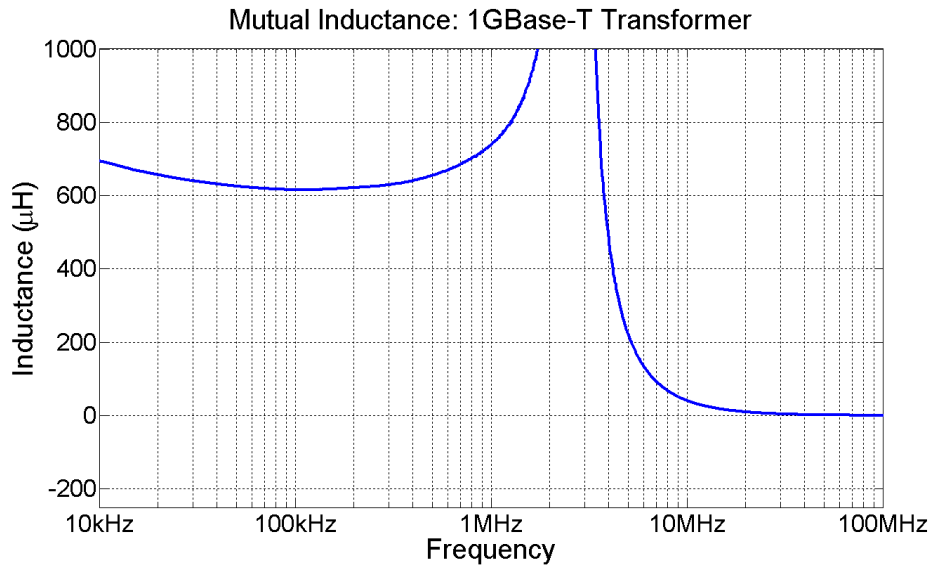


FIG. 6.8. 1GBase-T Ethernet transformer mutual inductance extraction.

### 6.2.1.3. Leakage inductance

Again, by comparing the T-type equivalent circuit to the equivalent circuit of chapter 3, it is clear that the leakage inductance is part of  $Z_A^T$  and  $Z_B^T$  from the T-type circuit. By taking the imaginary parts of  $Z_A^T$  and  $Z_B^T$  and looking at a frequency region where the inductance will dominate the impedance, the leakage inductance can be extracted (See FIG. 6.9). From the figure, it is apparent that the leakage inductance is stable from about 10MHz to about 40MHz. In this range the leakage inductances are about 110nH and 90nH for the primary and secondary, respectively.

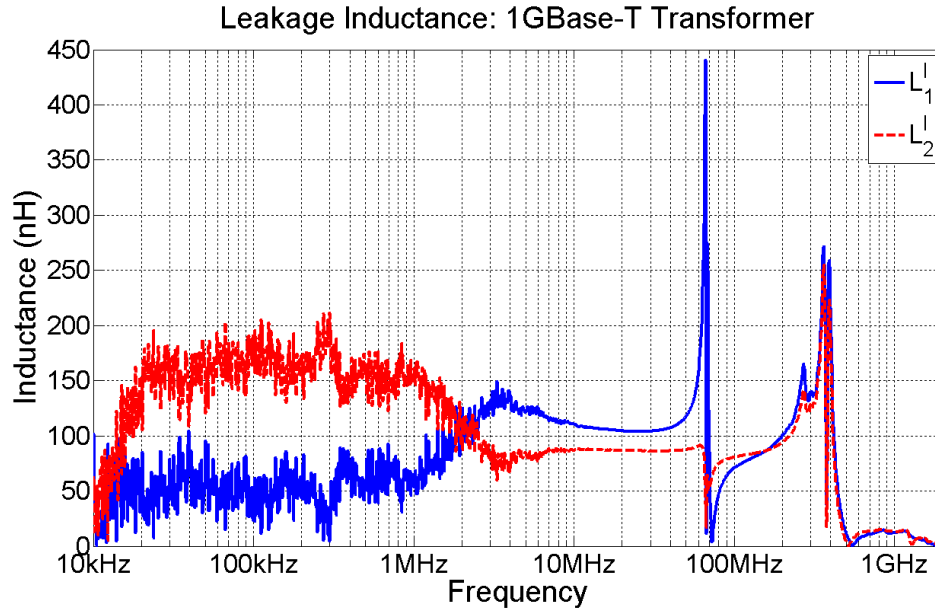


FIG. 6.9. 1GBase-T Ethernet transformer leakage inductance extraction.

#### 6.2.1.4. Line resistance

By taking the real part of  $Z_A^T$  and  $Z_B^T$ , the line resistance can be found (See FIG. 6.10). It isn't necessary to do this measurement with a VNA; DC resistance measurement would suffice. However, this information reinforces the validity of the treatment of the real and imaginary parts of the equivalent circuit impedances. The resistance at low frequency was found to be about  $0.6\Omega$ , which is in agreement with DC measurements of  $0.65\Omega$  [29].

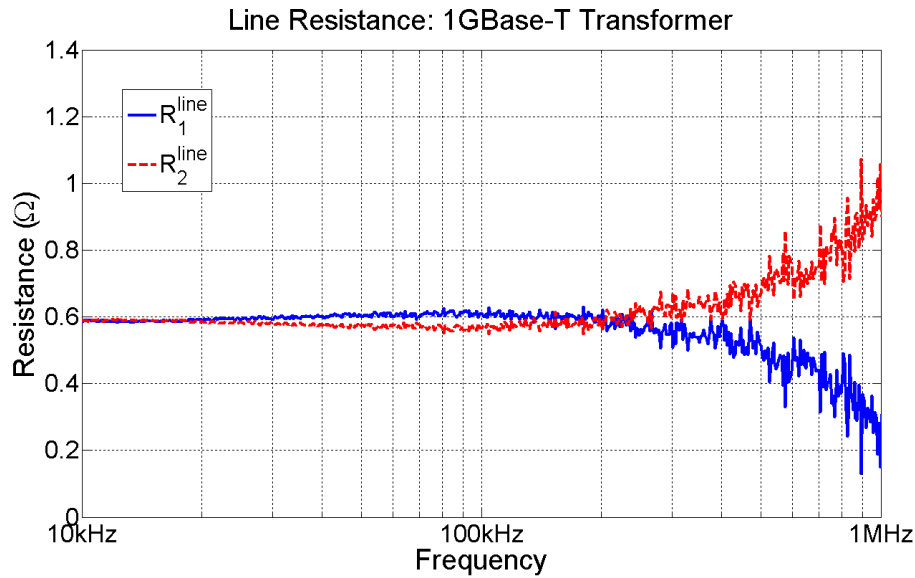
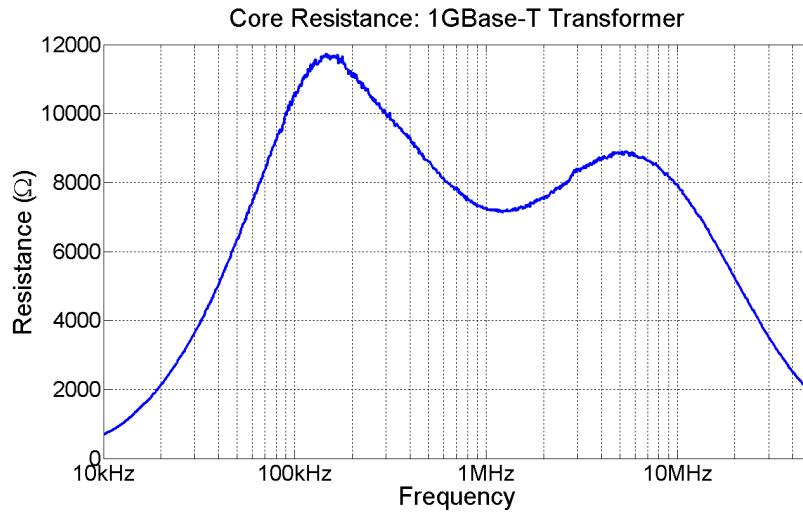


FIG. 6.10. 1GBase-T transformer line resistance.

#### 6.2.1.5. Core loss resistance

As was discussed in chapter 3, the resistance that represents core losses relies on complicated mechanisms and only loosely fits the approximation of a lumped resistance. By taking the real part of  $Z_C^T$  and converting the series resistance to an equivalent parallel resistance using the conversion **equations 3.89 and 3.88 from chapter 3**, insight can be gained into the behavior of the actual resistance. Ideally, this resistance (in parallel form) should be as large as possible, implying low losses. FIG. 6.11 shows the behavior of the core resistance, which is above  $2\text{k}\Omega$  from 20kHz up to 50MHz, and above  $6\text{k}\Omega$  from about 50kHz to about 20MHz.



**FIG. 6.11. 1GBase-T Ethernet transformer core loss resistance.**

### 6.2.2. 10GBase-T Ethernet transformer

Using the same analysis as for the 1GBase-T transformers above, the same parameters can be extracted for the 10GBase-T transformers: differential mode transfer relation, mutual inductance, leakage inductance, line resistance, and core resistance. Given the process is the same as for the 1GBase-T transformers, this section will just comment on the features of the data. The physical dimensions of the 10GBase-T Ethernet transformer are given in the table below.

**Table 6.4. 10GBase-T Ethernet transformer physical dimensions.**

<i>Device</i>	<i>Total turns (N)</i>	<i>Outside diameter</i>	<i>Inside diameter</i>	<i>Height</i>	<i>A<sub>cross-section</sub></i>	<i>~ Line Length</i>
10GBase-T XFMR	6	3.1mm	1.0mm	2.0mm	2.1μm <sup>2</sup>	~3.7cm

### 6.2.2.1. Differential-mode transfer relation

As can be seen in FIG. 6.12, the transfer relation has resonance behavior around 200-300MHz. This appears as a spike in the unloaded transfer relation. This resonance frequency is slightly too low to be a transmission line resonance with only 3.7cm of wire. Transmission line effects would require at least 10cm of wire at 300MHz to be detectable. This leads to the belief that the resonance mechanism is device inductance and capacitance. The 100Ω loaded transfer relation is well behaved, having a 3dB bandwidth of about 475 MHz. From the in-house data in FIG. 6.13, the low frequency 3dB point is around 200Hz.

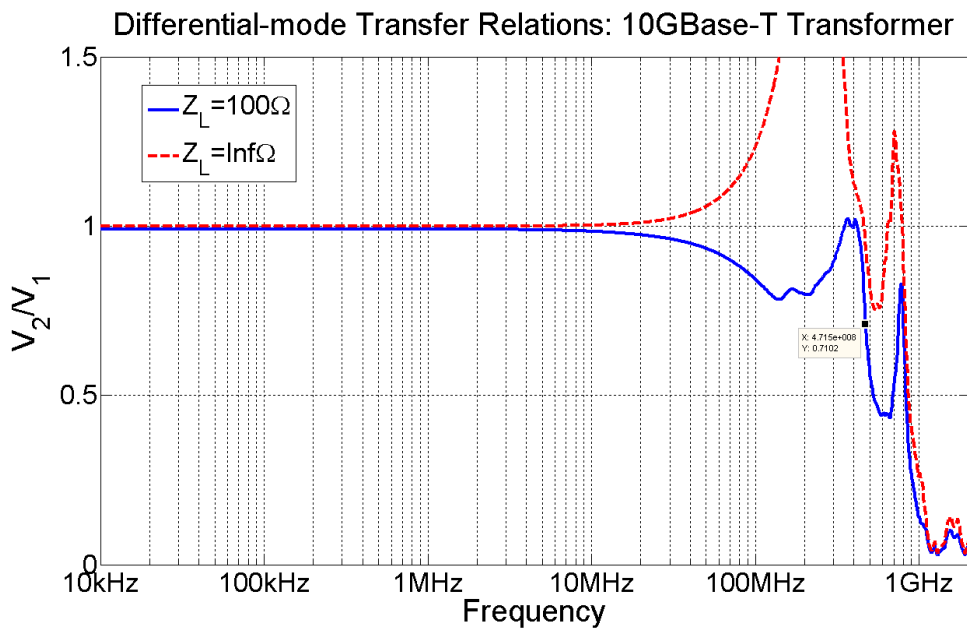


FIG. 6.12. 10GBase-T Ethernet transformer measured transfer relation with different loads.

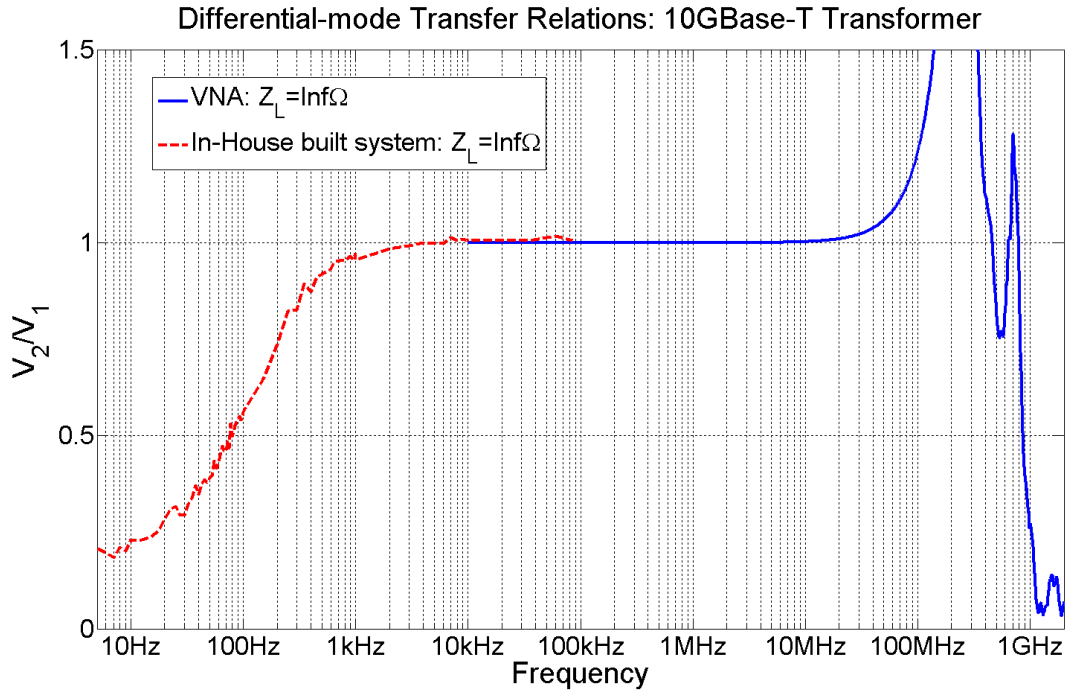


FIG. 6.13. 10GBase-T Ethernet transformer measured transfer relation with in-house system low frequency data.

### 6.2.2.2. Mutual inductance

FIG. 6.14 shows the extracted mutual inductance. In the low frequency region, the inductance value is found to be approximately 150 – 175  $\mu\text{H}$ .

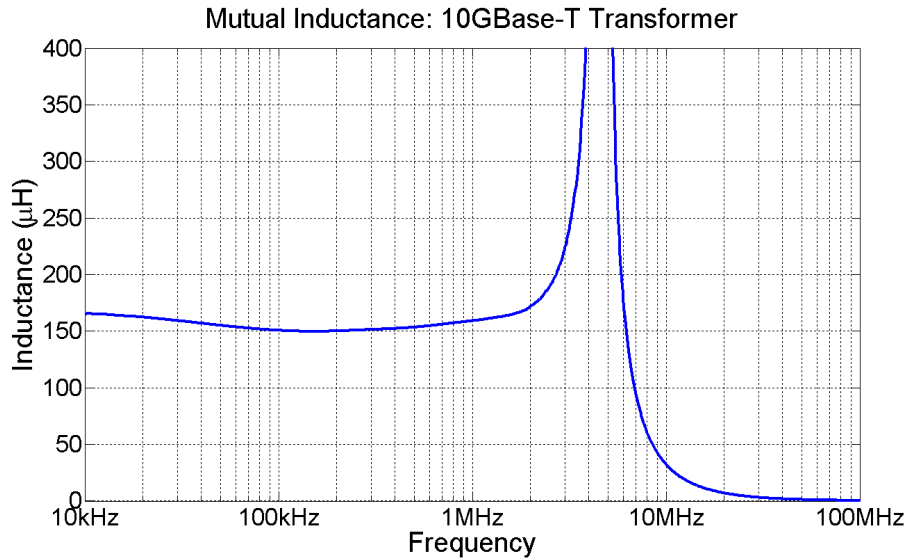


FIG. 6.14. 10GBase-T Ethernet transformer extracted mutual inductance.

### 6.2.2.3. Leakage inductance

Looking at the leakage inductance in the frequency range from about 10MHz to about 150MHz, FIG. 6.15 shows values of about 65nH and 80 nH for the primary and secondary windings, respectively.

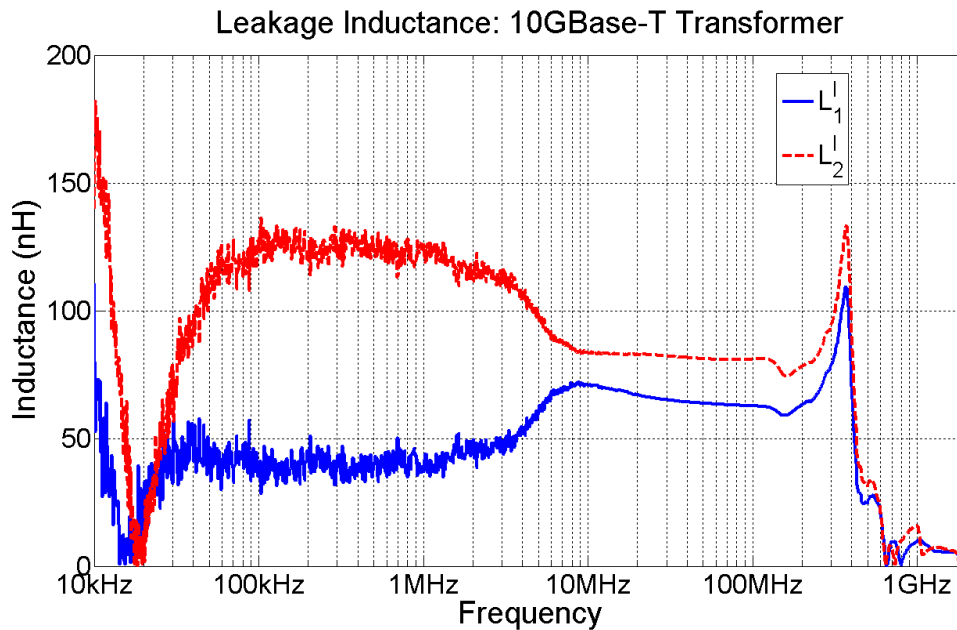


FIG. 6.15. 10GBase-T Ethernet transformer extracted leakage inductance.

### 6.2.2.4. Line resistance

FIG. 6.16 shows an obvious difference between the primary and secondary line resistance, in contrast to the 1GBase-T transformer measurement where the two values were identical. However, this is to be expected due to the inclusion of a common mode choke on the secondary side within the device package for 10GBase-T transformers. Though the choke shouldn't affect any other parameter values, the added wire wrapping around the choke unavoidably increases the line resistance. Thus, the secondary line resistance as measured by the VNA will be higher. The VNA data shows about 0.25Ω and 0.63Ω for the primary and

secondary, respectively. These values agree roughly with the DC measured values of  $0.30\Omega$  and  $0.71\Omega$  for the primary and secondary, respectively.

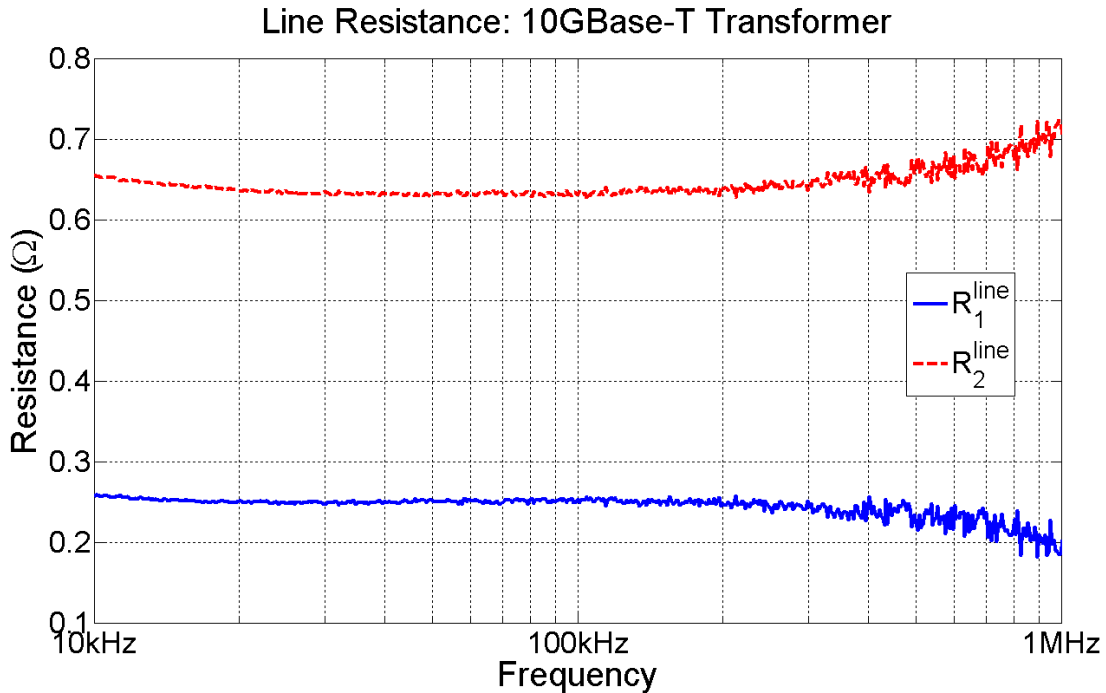


FIG. 6.16. 10GBase-T Ethernet transformer line resistance.

### 6.2.2.5. Core loss resistance

FIG. 6.17 shows the core loss resistance for the 10GBase-T transformer exhibiting the same shape as the 1GBase-T transformers, but with less magnitude (higher loss). This leads to the consideration of the underlying physical factors that affect the resistance value. FIG. 6.18 compares the series core resistance and the series mutual inductance of the 1GBase-T and 10GBase-T Ethernet transformers. From **equations 3.80 and 3.81 in chapter 3**, the values of both the series mutual inductance and series core resistance depend on the square of the number of turns and the cross-sectional area ( $N^2 A_{cross}$ ). Using the data from **Table 6.4 and Table 6.3**, the factor relating the 1GBase-T and 10GBase-T transformer core values is given by the following.

$$\frac{N_{1G}^2 A_{Cross}^{1G}}{N_{10G}^2 A_{Cross}^{10G}} = \frac{(13)^2 * 2.5 \times 10^{-6}}{(6)^2 * 2.1 \times 10^{-6}} = 5.5886 \quad 6.13$$

The ratio of 1GBase-T and 10GBase-T values from FIG. 6.18 is less than the predicted 5.59, and actually closer to 4, the squared turn number ratio by itself. However, qualitatively the 10GBase-T does have smaller core values which are to be expected theoretically from a device with fewer turns and smaller cross-sectional area.

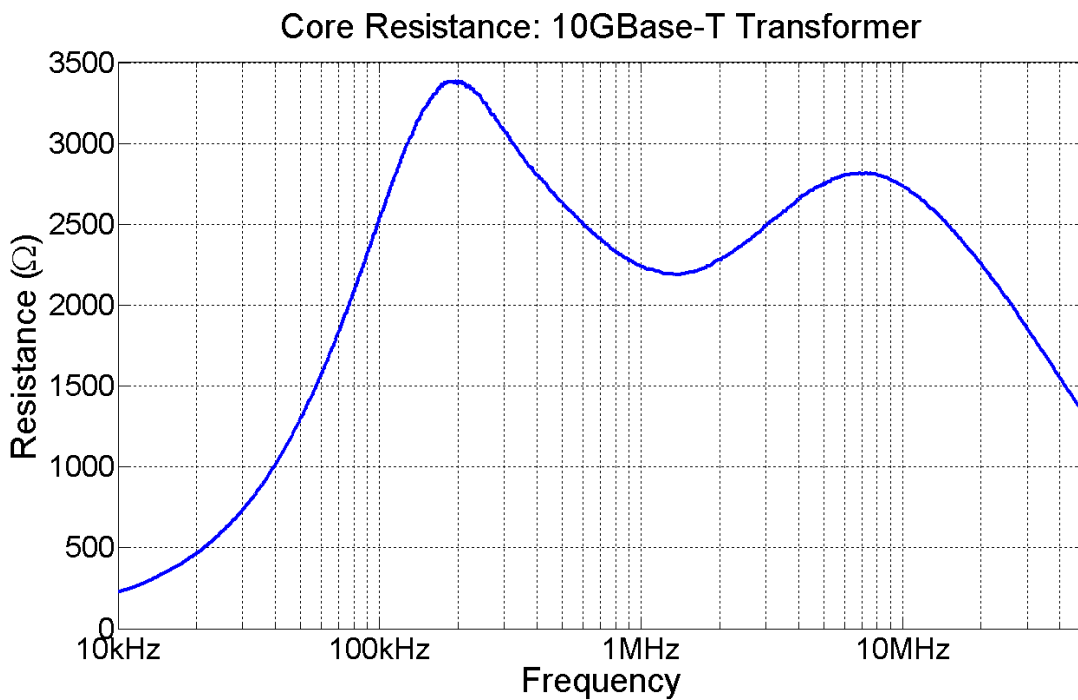
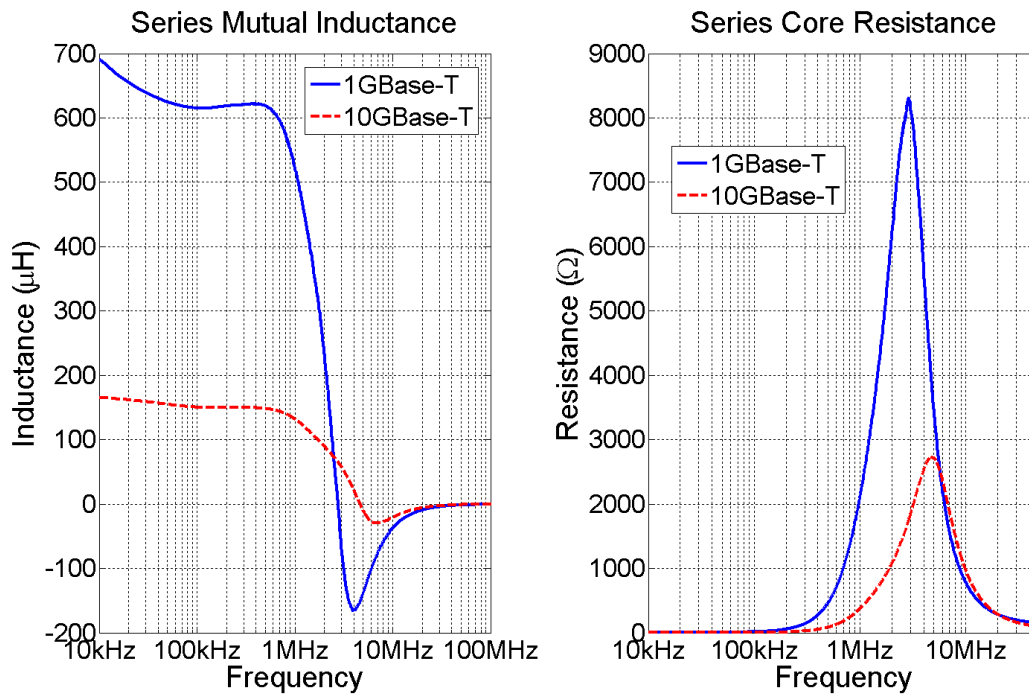


FIG. 6.17. 10GBase-T Ethernet transformer core loss resistance.



**FIG. 6.18.** Comparison of series core parameters for 1GBase-T and 10GBase-T transformers.

### 6.2.3. Large PVC-core transformer

In chapter 7, the fabrication of dielectric-core transformers is discussed. To further explore the behavior of dielectric-core, bifilar-wound, rectangular cross-section toroidal transformers, such a transformer was constructed on a larger scale. This transformer is about the size of a roll of duct tape and constructed around a piece of polyvinyl chloride (PVC) (see FIG. 6.19 and FIG. 6.20). By constructing the transformer on a larger scale, it is thought that the inductance will be significantly increased (with respect to other non-magnetic core devices) and thus, more accurately measured. The precise physical dimensions for the PVC-core transformer are given in Table 6.5 below. Following is the analysis and parameter extraction for the large PVC-core bifilar wound toroidal transformer.

**Table 6.5. PVC-core transformer physical dimensions.**

<i>Device</i>	<i>Total turns (N)</i>	<i>Outside diameter</i>	<i>Inside diameter</i>	<i>Height</i>	<i>A<sub>cross-section</sub></i>	<i>~Line Length</i>
PVC-core XFMR	50	11.491cm	3.94cm	4.905cm	18.52cm <sup>2</sup>	~8.68m

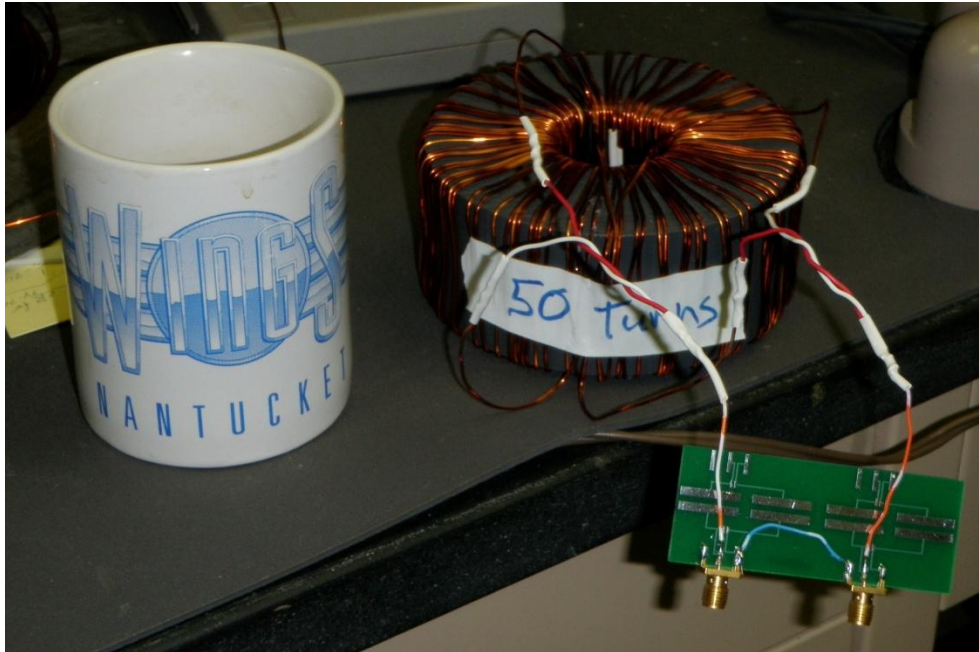


**FIG. 6.19. PVC-core transformer with coffee cup to present scale.**

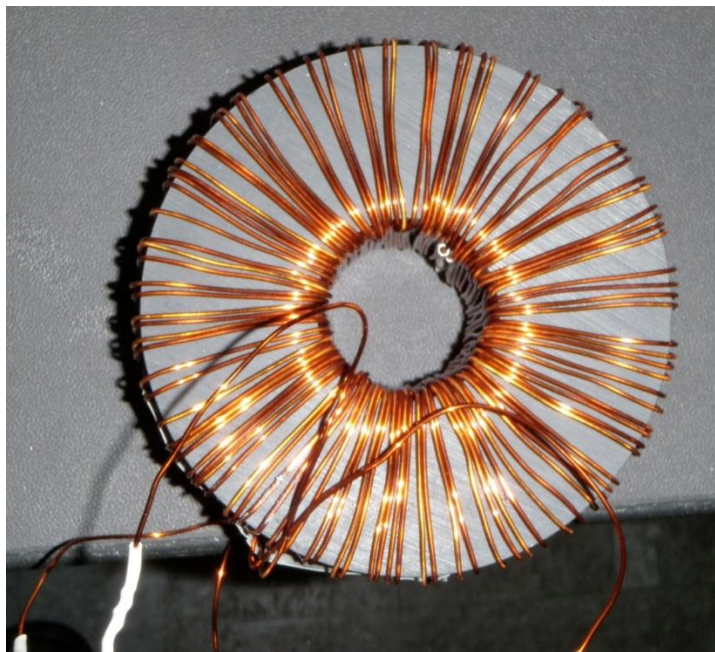


**FIG. 6.20. PVC-core transformer top view.**

### 6.2.3.1. Differential-mode transfer relation

FIG. 6.21 and FIG. 6.22 show the differential-mode transfer relation for the VNA and in-house measurement system, respectively. The VNA data (FIG. 6.21) shows greater detail in the high frequency resonances. However, both figures show a high frequency resonance at approximately 4MHz. With over 8.5 meters of wire wrapped around the transformer, 4MHz is approximately where transmission line effects would appear (8.5m is slightly greater than one tenth the free space wavelength at 4MHz). Even though this device has a dielectric core, while the previously discussed Ethernet transformers had magnetic cores, one cannot deny the trend of decreasing resonance frequency with increasing line length – a characteristic of transmission line effects. Using the rule-of-thumb for transmission line effects to be line lengths at least one tenth the free-space wavelength of the signal frequencies, the Ethernet transformers resonant frequencies are still below where they are expected to be. However, the resonance frequencies still appear to decrease with increasing line length, implying some transmission-line type effects.

The low frequency 3dB point is at about 1kHz, where the high frequency 3dB point is at approximately 2.5MHz. In between these frequencies, the flat band is very well behaved and would pass signals without distortion.

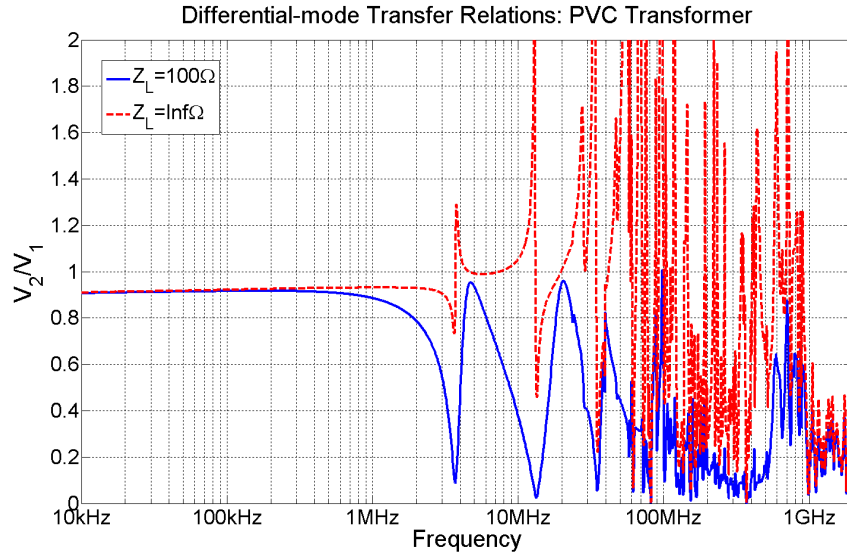


FIG. 6.21. PVC-core transformer VNA measured differential-mode transfer relation for different loads.

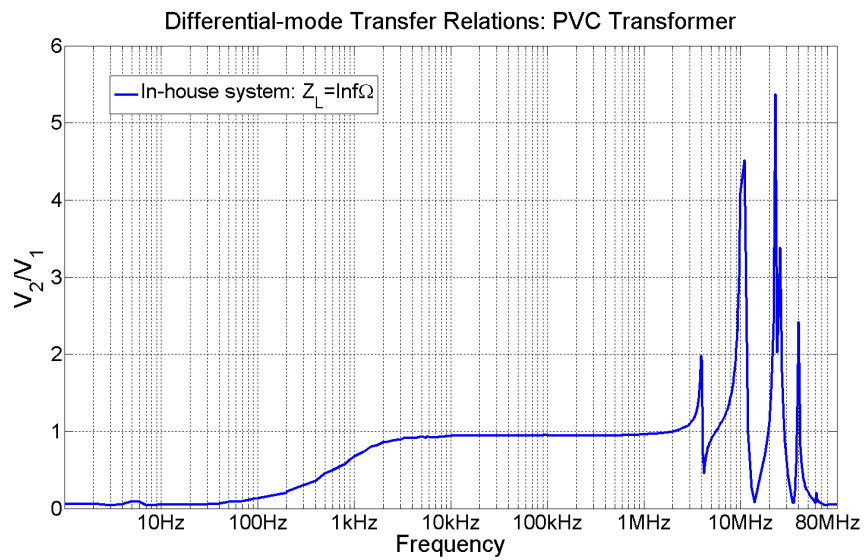
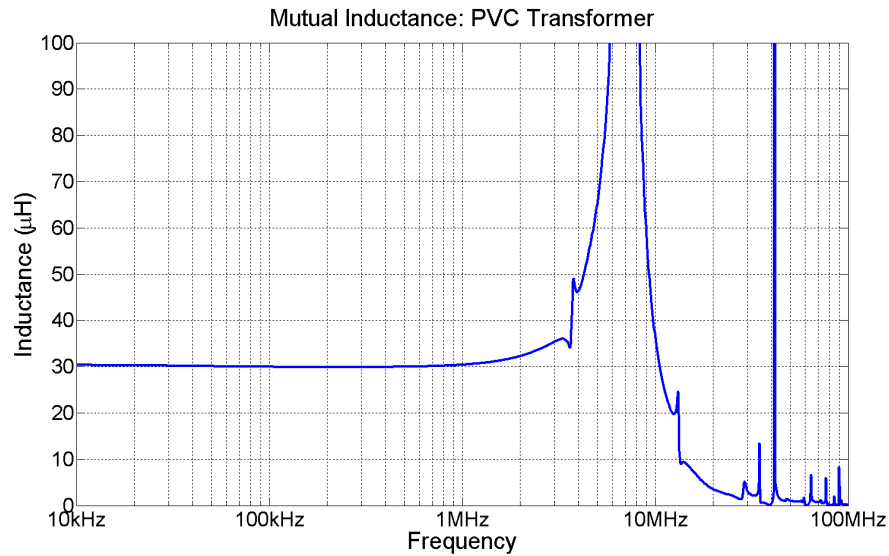


FIG. 6.22. PVC-core transformer in-house system measure differential-mode transfer relation.

### 6.2.3.2. Mutual inductance

FIG. 6.23 shows the low frequency region of extractable mutual inductance as about  $30\mu\text{H}$ . This is considerably lower than the much smaller Ethernet transformers, but this is expected. Due to the dielectric-core, the flux density which couples the windings is considerably less in the

PVC with  $\mu_0$  magnetic permeability as opposed to the ferrite core Ethernet transformers with a permeability that is hundreds to thousands of times  $\mu_0$ .



**FIG. 6.23. PVC-core transformer extracted mutual inductance.**

### 6.2.3.3. Leakage inductance

The leakage inductance of the PVC transformer is also expected to be greater without a low-reluctance core to guide flux. That is indeed what is seen in FIG. 6.24, which shows a leakage inductance in the stable region of about  $2\mu\text{H}$  and  $2.5\mu\text{H}$  for the primary and secondary, respectively. Recall the Ethernet transformers had leakage inductances on the order of 100 nH.

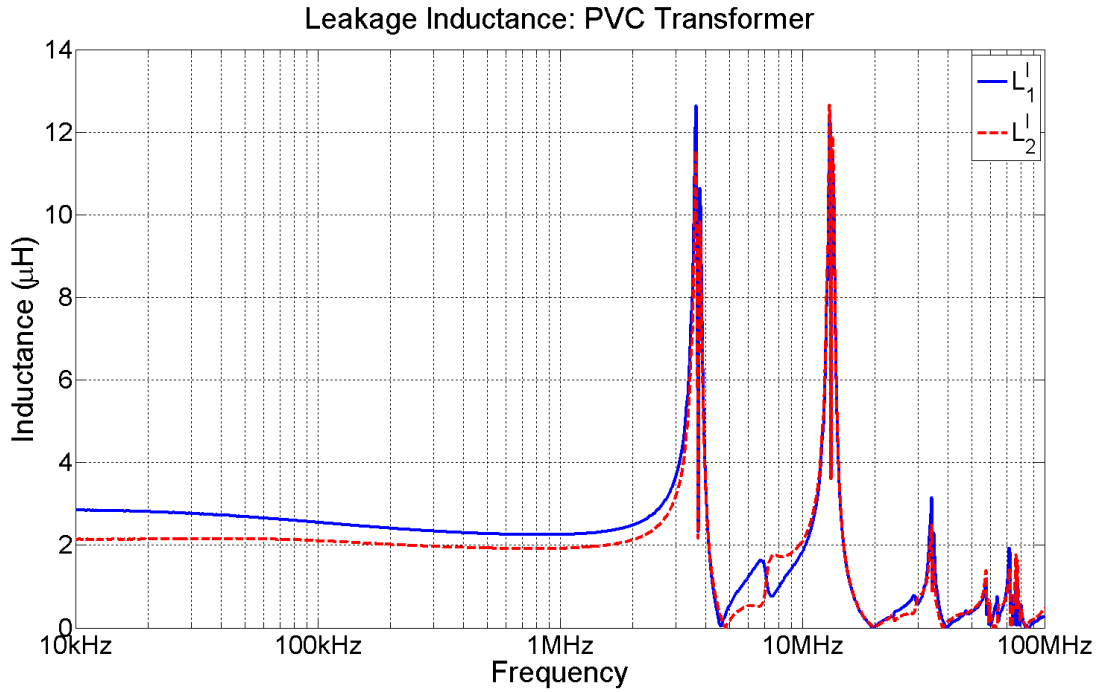


FIG. 6.24. PVC-core transformer extracted leakage inductance.

#### 6.2.3.4. Line resistance

FIG. 6.25 shows the line resistance of PVC transformer. Notice how with the larger leakage inductance and the smaller resistance, the stable region to extract line resistance becomes smaller and shifts to lower frequencies. The low frequency limit of line resistance is shown in FIG. 6.25 to be about  $0.21\Omega$  and  $0.17\Omega$  for the primary and secondary, respectively. The DC measurements, for comparison, were  $0.28\Omega$ .

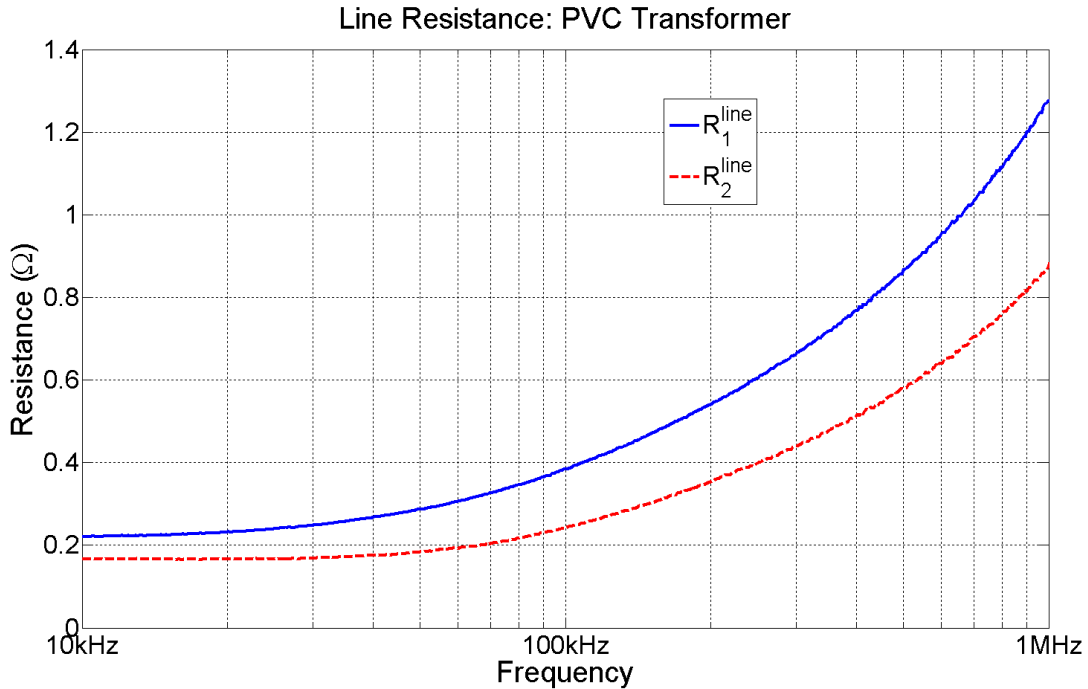


FIG. 6.25. PVC-core transformer extracted line resistance.

### 6.2.3.5. Core loss resistance

With a dielectric core material which is non-magnetic with low conductivity, the core loss resistance is expected to be quite large. From FIG. 6.26, the core resistance peaks at about 70k $\Omega$ , compared to 12k $\Omega$  for the 1GBase-T transformer and 3.5k $\Omega$  for the 10GBase-T transformer. However, the shape of the core loss resistance dispersion curve for the PVC-core transformer is single peaked and at a higher frequency. Recall that the parallel resistance depends on the series resistance (which depends on frequency) and the inductance-frequency product. With a smaller value for mutual inductance, the effect of the frequency dependent series resistance will dominate, resulting in the steeply sloping dispersive loss resistance of FIG. 6.26.

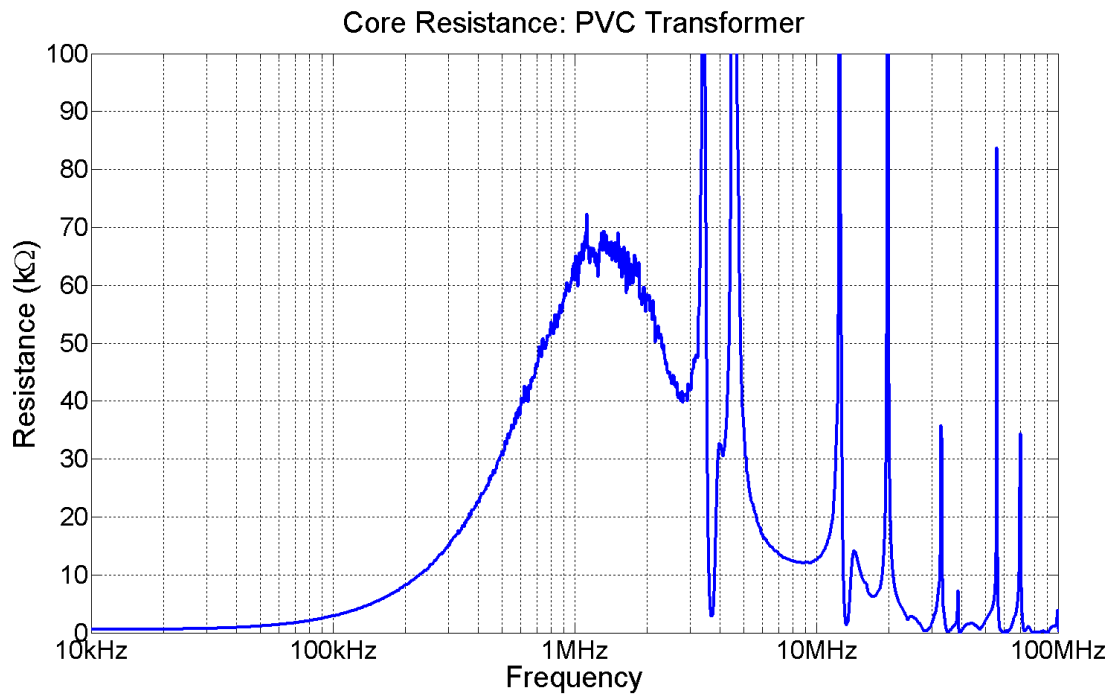


FIG. 6.26. PVC-core transformer extracted core loss resistance.

### 6.3. Common-mode Ethernet transformer testing

To measure the behavior of Ethernet transformers with common-mode signals, an identical approach is used to the differential-mode measurements. The key difference is the way the connections are routed on the custom built circuit boards.

To make the applied and measured signals purely common-mode signals, the terminals of the windings are connected together (See FIG. 6.27). The signal is applied to the connected terminals (now one node) and the ground is connected to the winding center tap. The grounding of the center tap is a common technique used in practice to minimize the coupling of common-mode signals. The custom built circuit boards for common mode measurements are shown in FIG. 6.28.

In chapter 2, the equations for the decomposition of line voltage into differential and common modes were given. By connecting the terminals of a winding or port together, the two line voltage equations become equal. Manipulation of the equation shows that in this configuration, the differential mode voltage is forced to 0, and the measurement is purely of common-mode signals. The algebra is shown below in equation 6.14.

Since the network analysis theory is identical to the case of differential-mode signals, it need not be repeated here. Scattering parameters were measured and converted to impedance parameters, from which an equivalent circuit was formed. Using the equivalent circuit, the common-mode transfer relation can be examined. The results for 1GBase-T and 10GBase-T Ethernet transformers as well as a modified experiment on the PVC-core transformer are presented in the following sections.

$$\begin{aligned}
 V^+ &= \frac{V_{dm}}{2} + V_{cm} = V^- = -\frac{V_{dm}}{2} + V_{cm} & 6.14 \\
 \frac{V_{dm}}{2} + V_{cm} &= -\frac{V_{dm}}{2} + V_{cm} \\
 \frac{V_{dm}}{2} &= -\frac{V_{dm}}{2} \Rightarrow \frac{V_{dm}}{2} = -\frac{V_{dm}}{2} = 0
 \end{aligned}$$

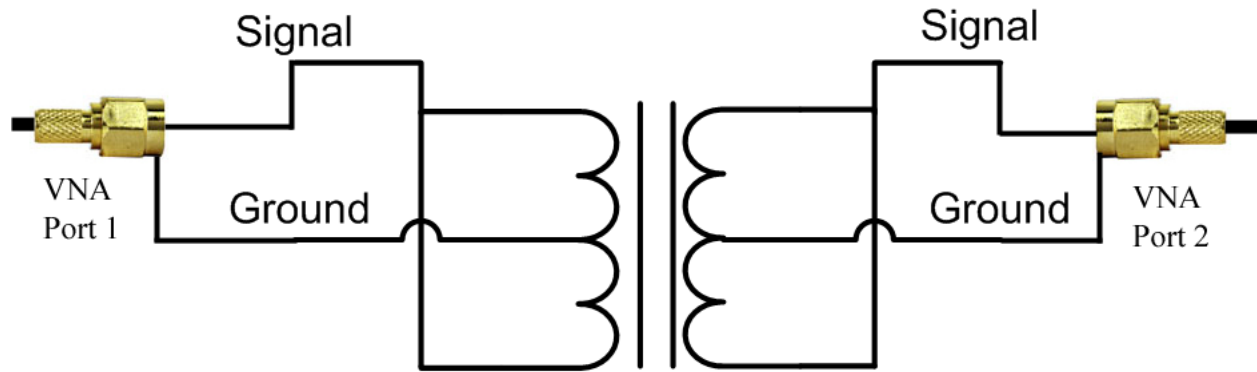


FIG. 6.27. Common-mode measurement scheme.

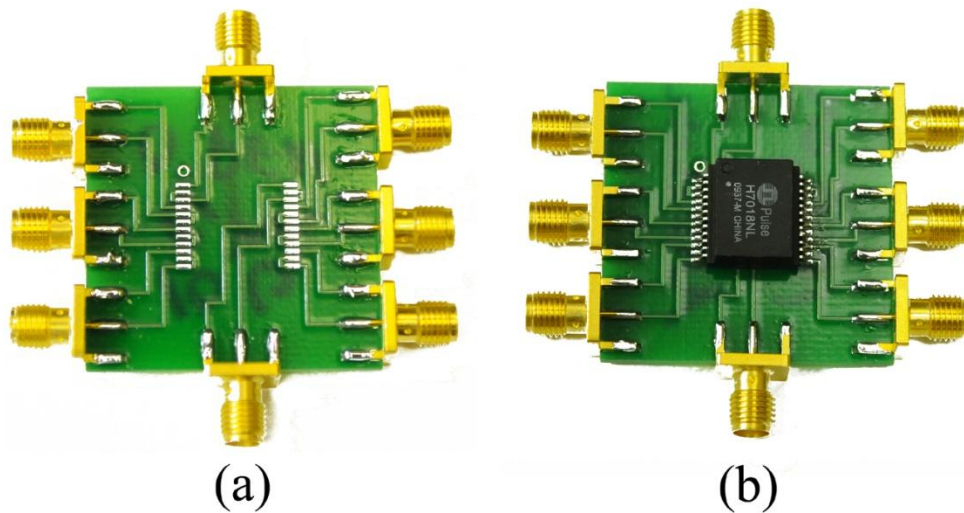


FIG. 6.28. Custom circuit boards for common-mode measurements (a) without device package (b) with device package.

### 6.3.1. Common-mode signal suppression

As discussed in chapter 3, the bifilar wound transformer works well to reduce leakage inductance but gives rise to an appreciable cross-winding capacitance. This cross-winding capacitance is a channel for common-mode interference signals to couple from the primary to the secondary. Common-mode signals are further suppressed in practice by grounding the winding center tap or using a common-mode choke. Both of these methods are discussed in the following sections.

### 6.3.1.1. Common-mode signal suppression by grounding the winding center tap

Common-mode voltages (referenced to ground) appear on the winding terminals from the unshielded twisted pair cable which couples interference power from the environment. In a traditional ungrounded configuration, the only impedance paths from the windings to ground are through the cross-winding capacitance to the secondary winding and whatever circuits are connected to the secondary (See FIG. 6.30). If the cross-winding capacitance is large, the impedance will be low, making common-mode currents larger. From FIG. 6.30, the common mode current will flow through the load and common-mode voltage will appear on the secondary.

FIG. 6.31 shows what happens when the winding center taps are grounded. The initial common-mode current is shown to split off in fractions denoted  $a$ ,  $b$ ,  $c$ , and  $d$ . The purpose of grounding the winding center tap is to provide a path to common-mode currents that has much lower impedance than the path through the cross-winding capacitance [30]. Thus, the goal is to have the ' $a$ ' current much larger than the ' $b$ ' current, and also to have the ' $c$ ' current much larger than the ' $d$ ' current.

The key issue that may or not be obvious is that it may appear that the common-mode current flowing through the winding and out the center tap would flow through the large winding inductance, making the impedance of this path just as large as through the cross-winding capacitance. However, the subtlety is that the currents in the top half of the winding will now be flowing in the opposite direction to the currents in the bottom half of the winding (See FIG. 6.31). This creates opposing magnetic fields in the core, thus canceling the excitation of any core flux by common mode currents (See FIG. 6.29). Without the excitation of flux, the winding

structure is just a wire and is non-inductive. Thus, the only impedance along the center tap path are the small winding resistances.

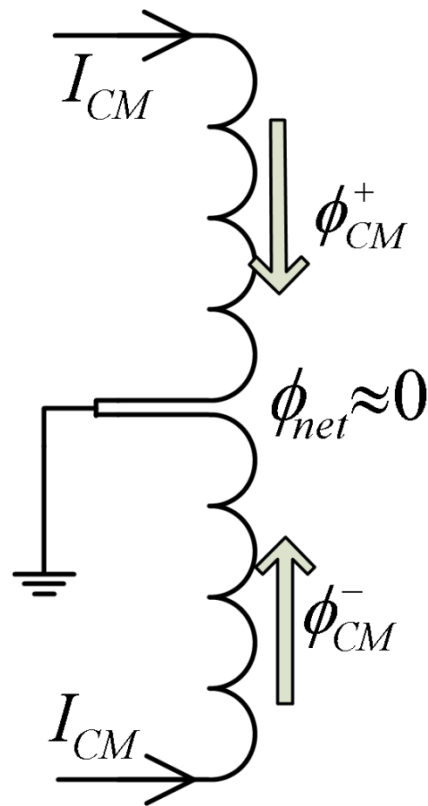


**FIG. 6.29. Diagram of common-mode flux cancellation in a transformer winding with a grounded center tap.**

From chapter 4, recall that by definition of the oddly symmetric differential-mode voltages, the differential mode voltage will be zero at the center of the winding, regardless of the center tap connection. Thus, the center tap can be freely used to short common-mode currents to ground without affecting the differential-mode signals.

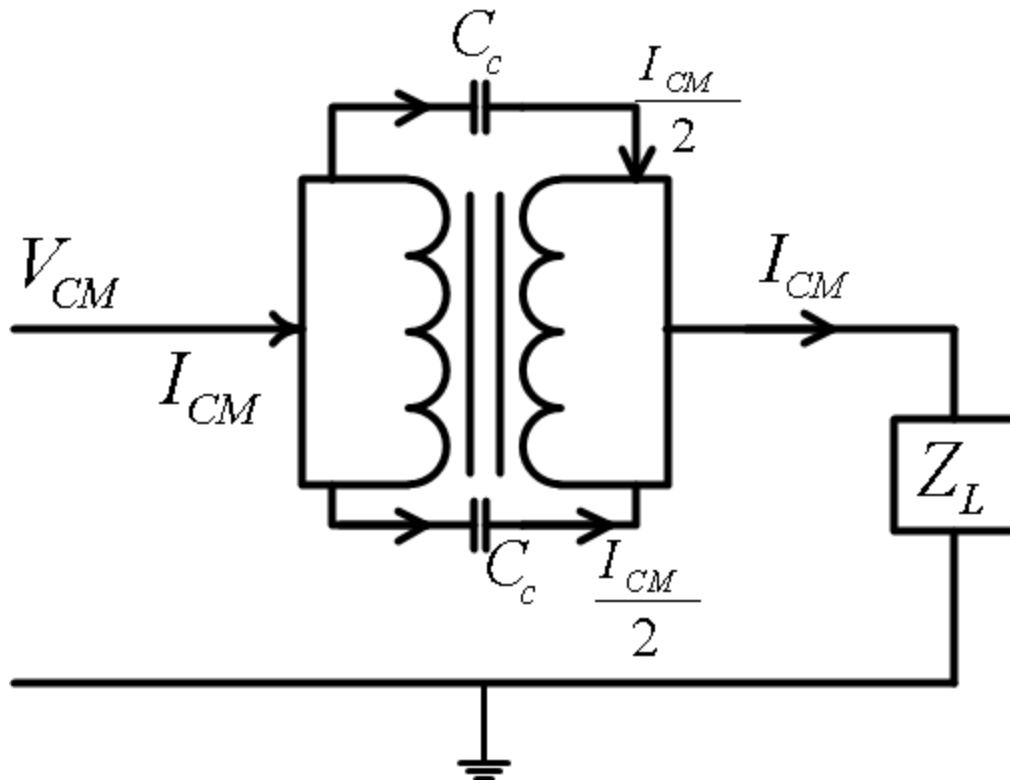


FIG. 6.30. Common-mode currents on a traditional transformer with load.

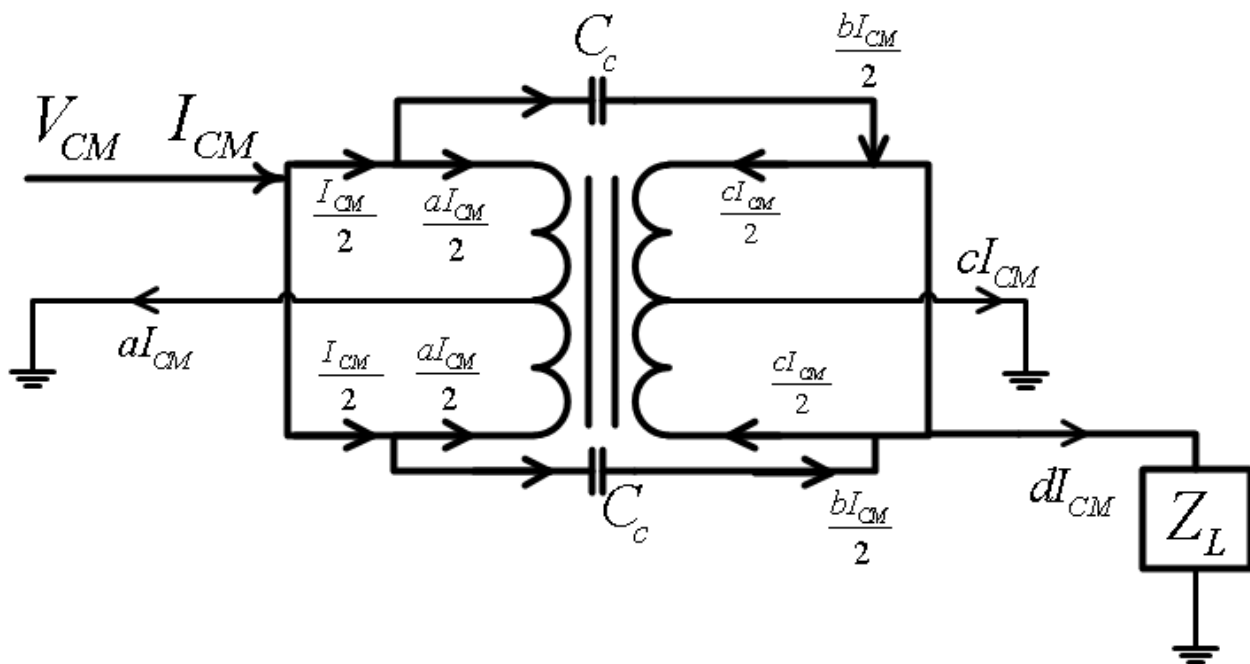


FIG. 6.31. Common-mode currents on a transformer with a grounded center tap.

### 6.3.1.2. Common-mode signal suppression by choke

Grounding the winding center tap is a useful secondary suppression technique. However, as frequencies increase, the assumption that the path through the center tap has lower impedance than the path through the cross-winding capacitance may no longer be true. Also, if the center tap is not perfectly in the center, the center tap path will possess some inductance that causes the center tap path impedance to increase with frequency, while the cross-winding capacitance path impedance decreases. To further cinch off common-mode currents, a common mode choke can be used after the secondary winding terminals.

A common-mode choke is constructed the same way as a transformer, except that the signal lines are connected to different windings (See FIG. 6.32). Similar to how oppositely flowing currents cancelled inductance when using the grounded center tap, the two modes of current will experience different impedances through the common-mode choke. The differential mode will have current flowing in opposite directions in the two windings (refer to them as *top* and *bottom* as seen in FIG. 6.32). The oppositely flowing differential-mode currents will cancel flux in the core, so the differential-mode current will not be impeded by inductance in either winding. However, the common-mode current flows in the same direction in both windings. Thus, the common-mode current is impeded by the expected large choke inductance (See FIG. 6.33). The large series inductive impedance for the common-mode currents makes the grounded center tap impedance on the secondary side comparably small for high frequencies.

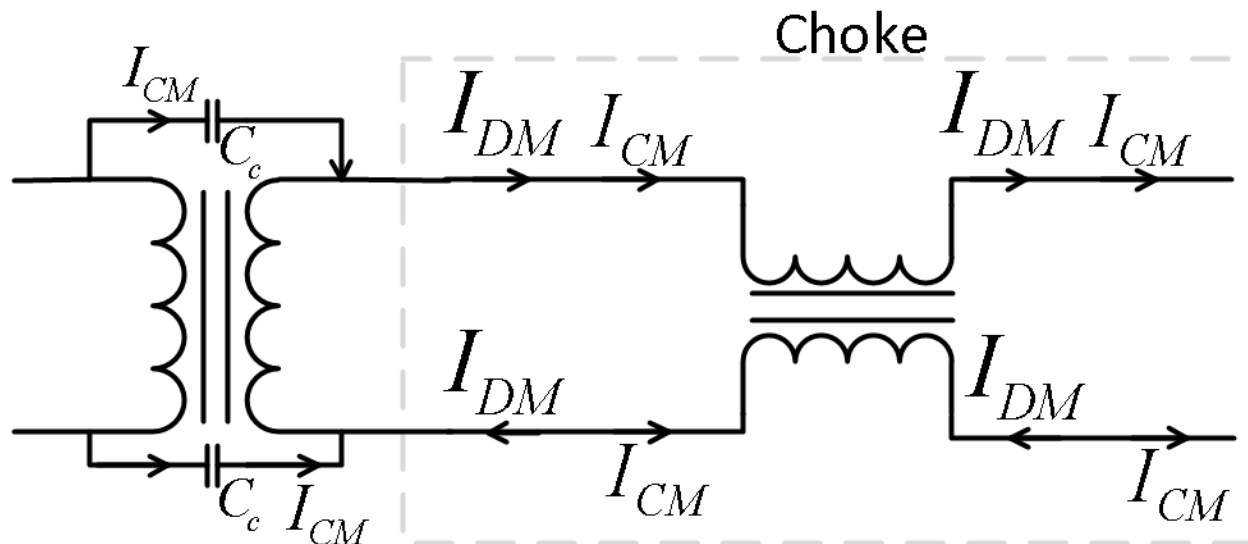


FIG. 6.32. Description of currents in common-mode chokes.

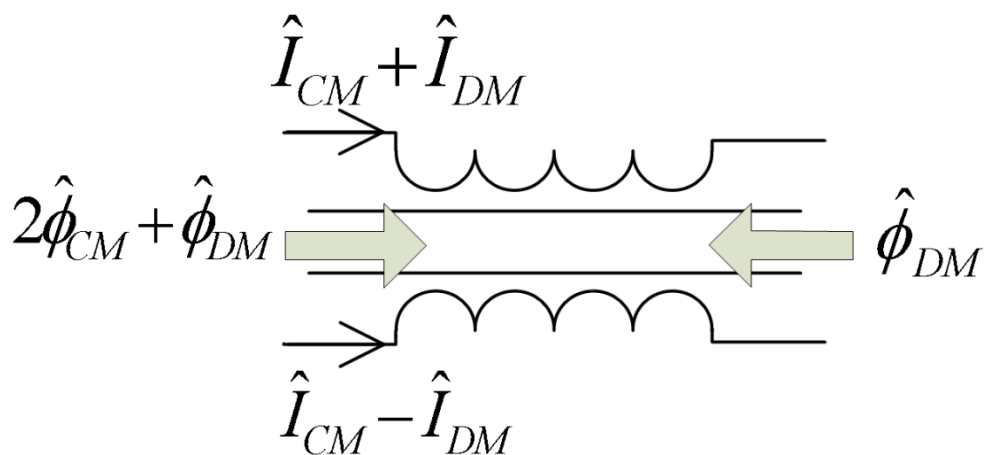


FIG. 6.33. Diagram of flux cancellation and common-mode current suppression using a common-mode choke.

### 6.3.2. 1GBase-T Ethernet transformer

FIG. 6.34 shows the common mode transfer relation for the 1GBase-T Ethernet transformer. The major features include the nonexistent low frequency coupling, the 1MHz low frequency rolloff, the flatband from about 1MHz to 30MHz, and the sharp resonance at about 65MHz. These features and their causes will be discussed more later in this chapter under the “Modeling” section.

In the common-mode measurement scheme, device inductance is minimized to only leakage inductance. This allows a more precise measurement of capacitances within the transformers. However, even with minimal inductances, the imaginary parts of impedance in the  $\Pi$ -type equivalent circuit are still inductive. The capacitance will not simply appear as the reactance of a circuit branch. So, to extract the capacitance, the principal resonance frequency of the impedance is used with the extracted inductance to determine the capacitance using a parallel LC circuit topology for the impedance.

Comparing the  $\Pi$ -type equivalent circuit with the equivalent circuit of chapter 3, it is apparent that an effective cross-winding capacitance can be extracted from  $Z_C^\Pi$ , while the effective intra-winding capacitances can be extracted from  $Z_A^\Pi$  and  $Z_B^\Pi$ . This is done for the 1GBase-T and the 10GBase-T transformers in the following sections.

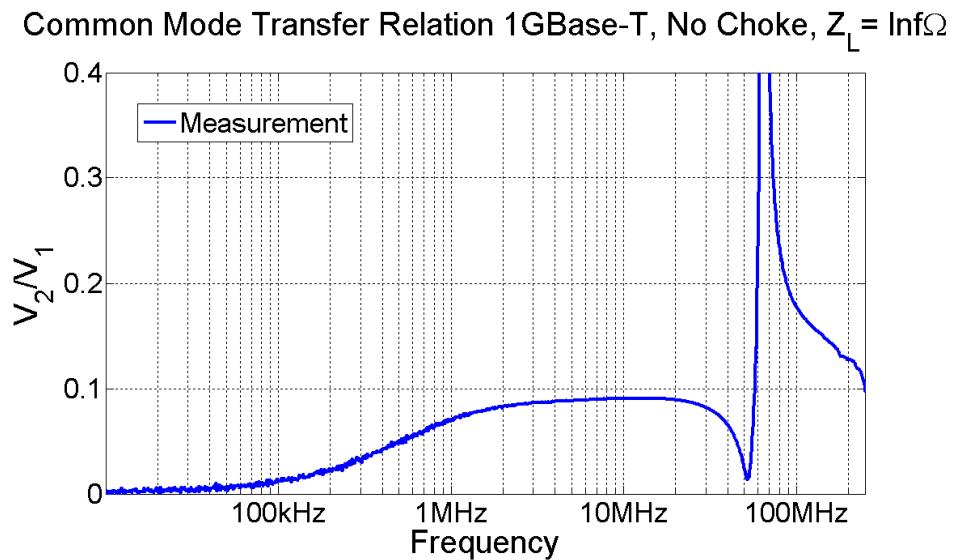


FIG. 6.34. 1GBase-T Ethernet transformer common-mode transfer relation [31].

### 6.3.2.1. Cross-winding capacitance

FIG. 6.35 shows the extracted impedance and inductance from the measured  $Z_C^\Pi$ .

Making the approximation that the resonance in impedance is from a parallel LC-type circuit, the cross-winding capacitance can be extracted as follows.

$$\omega_R^2 = \frac{1}{LC} \Rightarrow \tag{6.15}$$

$$C = \frac{1}{L\omega_R^2}$$

Taking the resonance frequency and the inductance from FIG. 6.35, the capacitance is found to be 39pF.

$$C_C = \frac{1}{L\omega_R^2} = \frac{1}{(235nH)(2\pi * 52.4MHz)^2} = 39.1pF \tag{6.16}$$

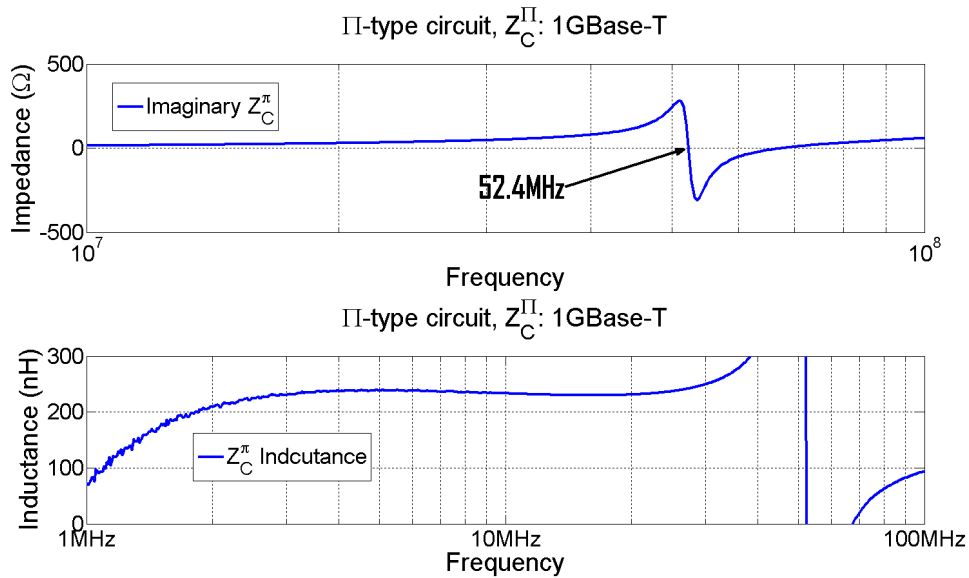


FIG. 6.35. 1GBase-T Ethernet transformer cross-winding capacitance analysis.

### 6.3.2.2. Intra-winding capacitance

Performing the same analysis as on the cross-winding capacitance, the effective intra-winding capacitances can be extracted. Taking resonance frequency and inductance values from FIG. 6.36, the intra-winding capacitances are determined as follows.

$$C_A = \frac{1}{L_A \omega_{R,A}^2} = \frac{1}{(33nH)(2\pi * 752MHz)^2} = 1.36pF \quad 6.17$$

$$C_B = \frac{1}{L_B \omega_{R,B}^2} = \frac{1}{(27nH)(2\pi * 794MHz)^2} = 1.49pF \quad 6.18$$

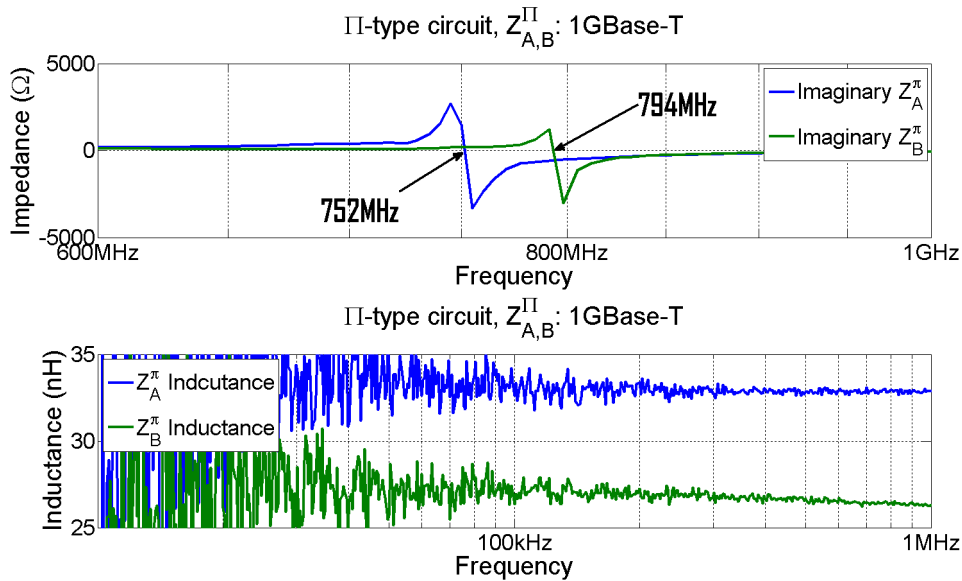


FIG. 6.36. 1GBase-T Ethernet transformer intra-winding capacitance analysis.

### 6.3.3. 10GBase-T Ethernet transformer

FIG. 6.37 shows the common mode transfer relation for the 10GBase-T Ethernet transformer. The major features include the small low frequency coupling, the 1MHz low frequency roll-off, the flatband from about 1MHz to about 20MHz, and the sharp resonance at about 70MHz. These features and their causes will be discussed more later in this chapter under the “Modeling” section.

Similar to the 1GBase-T transformer section above, extraction of cross-winding and intra-winding effective capacitances will be done in the following sections.

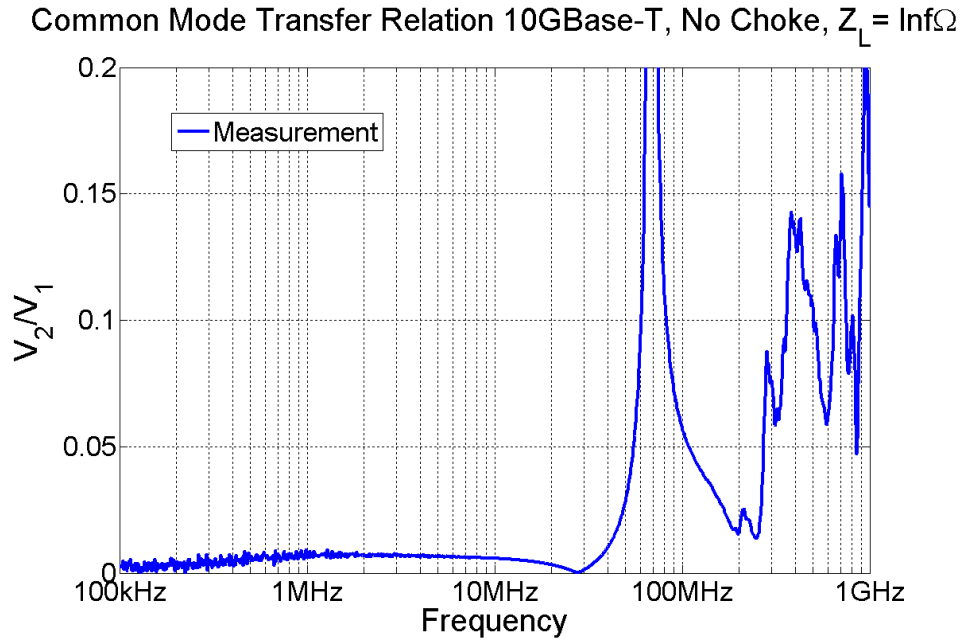


FIG. 6.37. 10GBase-T Ethernet transformer common-mode transfer relation [31].

### 6.3.3.1. Cross-winding capacitance

Proceeding as before with the 1GBase-T Ethernet transformers, the 10GBase-T Ethernet transformer data is presented in FIG. 6.38 and FIG. 6.39 followed by the calculations of the capacitances.

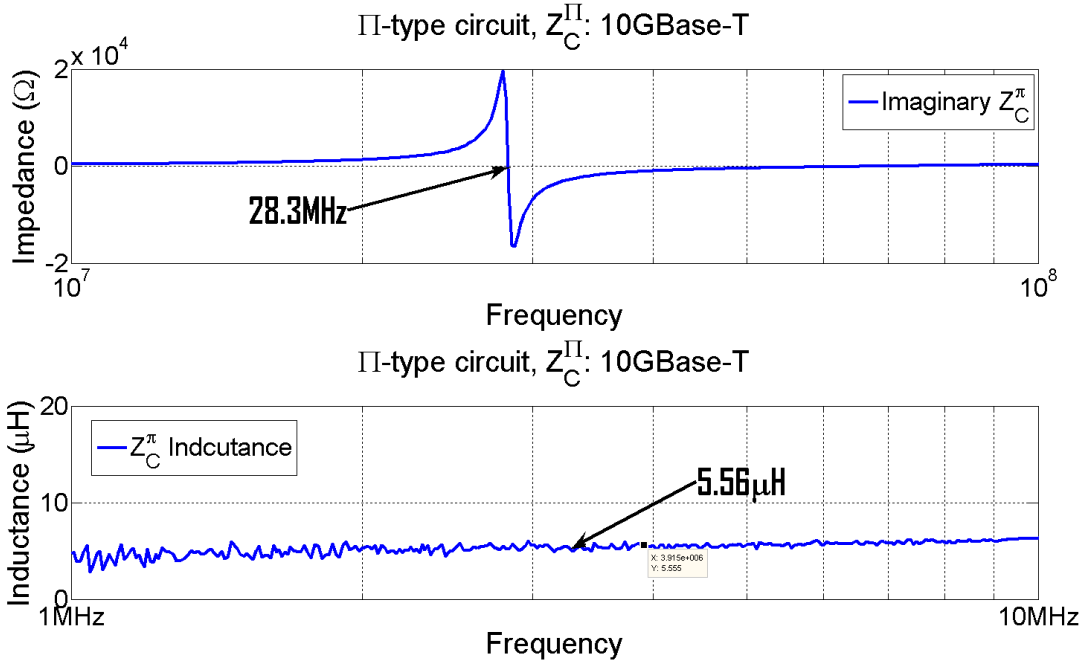


FIG. 6.38. 10GBase-T Ethernet transformer cross-winding capacitance analysis.

$$C_C = \frac{1}{L\omega_R^2} = \frac{1}{(5.56\mu\text{H})(2\pi * 28.3\text{MHz})^2} = 5.69\text{pF} \quad 6.19$$

### 6.3.3.2. Intra-winding capacitance

Performing the same analysis on  $Z_A^{\text{II}}$  and  $Z_B^{\text{II}}$  as on  $Z_C^{\text{II}}$  for the cross-winding capacitance, the effective intra-winding capacitances can be extracted. Taking resonance frequency and inductance values from FIG. 6.39, the intra-winding capacitances are determined from the following equations.

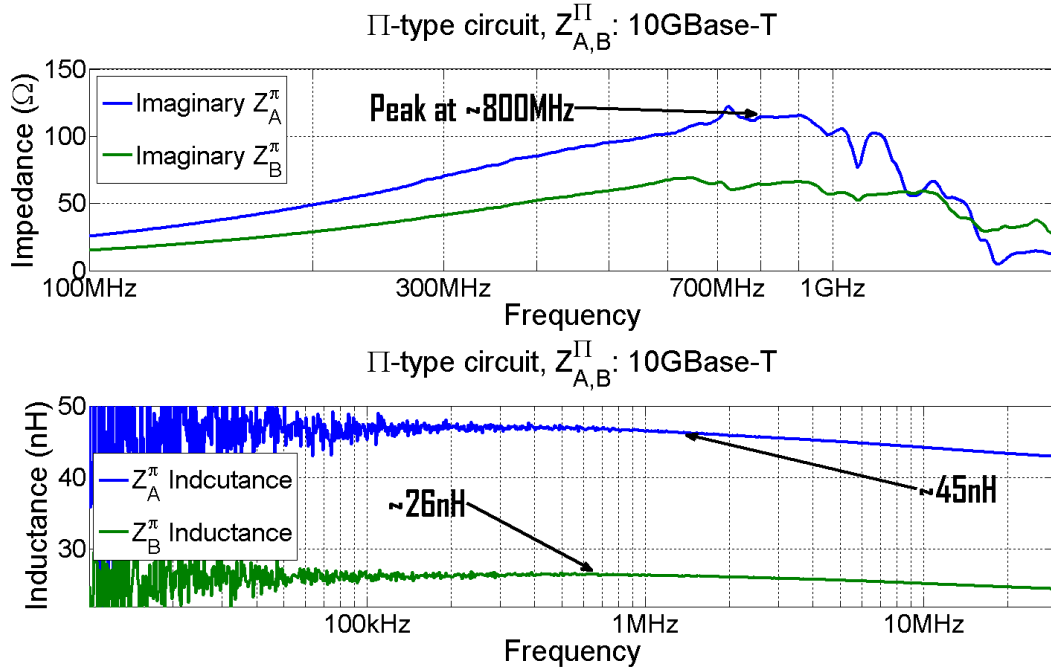


FIG. 6.39. 10GBase-T Ethernet transformer intra-winding capacitance analysis.

$$C_A = \frac{1}{L_A \omega_{R,A}^2} = \frac{1}{(45nH)(2\pi * 800MHz)^2} = 0.88 pF \quad 6.20$$

$$C_B = \frac{1}{L_B \omega_{R,B}^2} = \frac{1}{(26nH)(2\pi * 800MHz)^2} = 1.52 pF \quad 6.21$$

### 6.3.3.3. Effectiveness of choke on common-mode suppression

Recalling Table 6.1, manufacturers of Ethernet transformer packages have to satisfy a certain bandwidth of common-mode suppression. To this end, the inclusion of a common-mode choke in the Ethernet transformer package is not uncommon. Such is the case with the 10GBase-T transformer package. A common mode choke is included in series, connected to the secondary winding terminals.

However, it was the purpose of the measurement to evaluate the suppression of common-mode signals by the transformer alone. Thus, for all of the above measurements, the choke was removed from the transformer package. For a final comparison, however, the common-mode transfer relation was measured with the choke in place. Both transfer relations are plotted in FIG.

6.40. With the choke in place and an infinite load on the secondary, the sharp common-mode resonance at about 70MHz is suppressed, but a broad resonance appears between 400 and 500MHz. However, when the transformer is loaded with  $100\Omega$  (the impedance of the twisted pair cable), the broad resonance is found to be suppressed to an acceptable level. Thus, FIG. 6.40 shows that with proper loading, the addition of common-mode chokes greatly improves common-mode suppression.

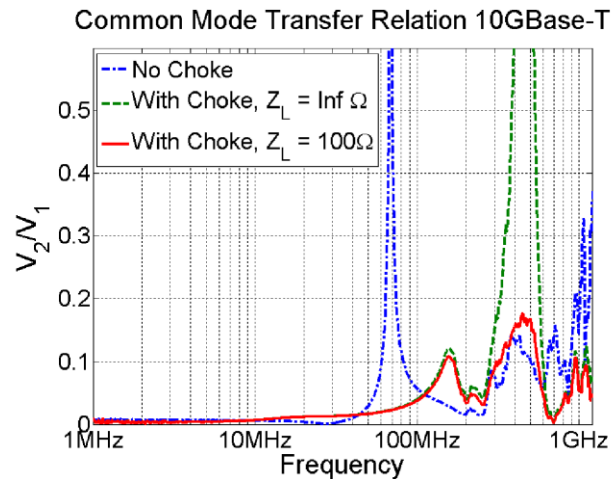
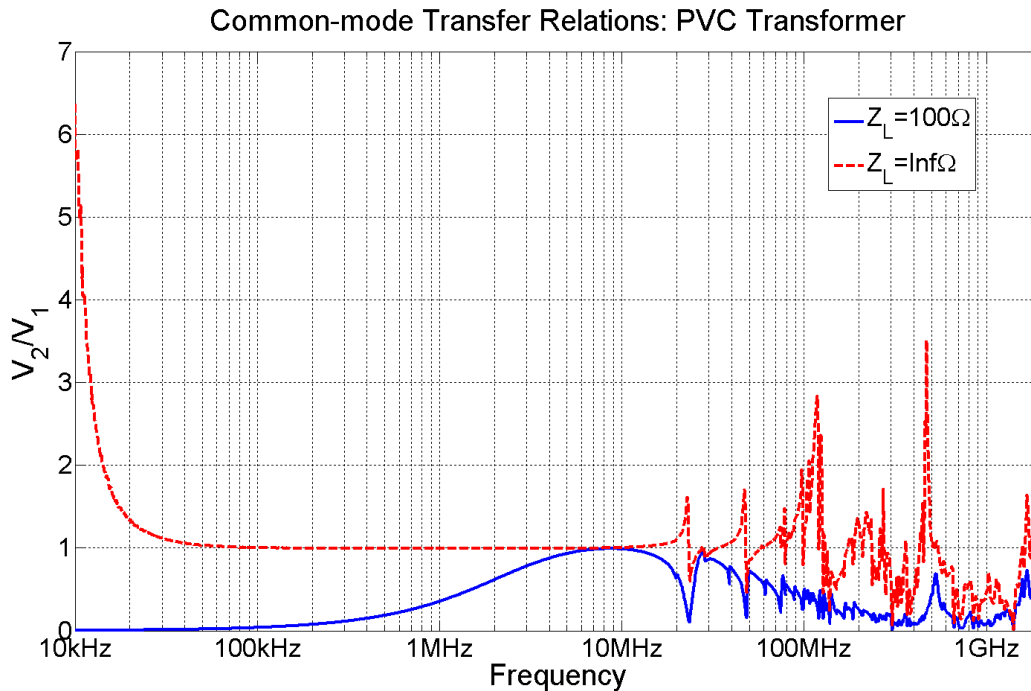


FIG. 6.40. 10GBase-T Ethernet transformer common-mode transfer relation with and without common-mode chokes [31].

### 6.3.4. Large PVC-core transformer

In contrast to the measurement scheme for the Ethernet transformers, the large PVC-core transformer was measured in the manner of FIG. 6.30. The ground of VNA port 1 was connected to the ground of VNA port 2, and the signal of port 1 (port 2) was applied to the connected terminals of the primary (secondary). In this manner, it should be straight forward to extract the cross-winding capacitance which is the purpose of the large scale dielectric core transformer. However, given the different measurement scheme, the common-mode transfer relation for this PVC-core transformer looks significantly different from that of the Ethernet transformers, but behaves as expected (See FIG. 6.37). Since the measurement has now become the measurement of a series impedance, as the load becomes large, the transfer relation amplitude increases. As the

load decreases, the transfer relation takes on a low frequency roll-off due to the changing proportion with the series capacitance impedance.



**FIG. 6.41. PVC-core transformer common-mode transfer relation.**

By creating a  $\Pi$ -type equivalent circuit, the cross-winding capacitance can be clearly extracted. By using **equations 6.9, 6.10, and 6.11** while referencing FIG. 6.5, the  $\Pi$ -type equivalent circuit is formed. Then, by taking the imaginary part of  $Z_C^\pi$ , the cross-winding capacitance can be extracted. From FIG. 6.42, the cross-winding capacitance is approximately 600pF. Similar analyses of  $Z_A^\pi$  and  $Z_B^\pi$  shows that these impedances are swamped by inductance, making the extraction of intra-winding capacitance impossible. The same applies to the large PVC-core transformer is, however, expected to have low intra-winding capacitance due to the widely spaced turns around the toroid.

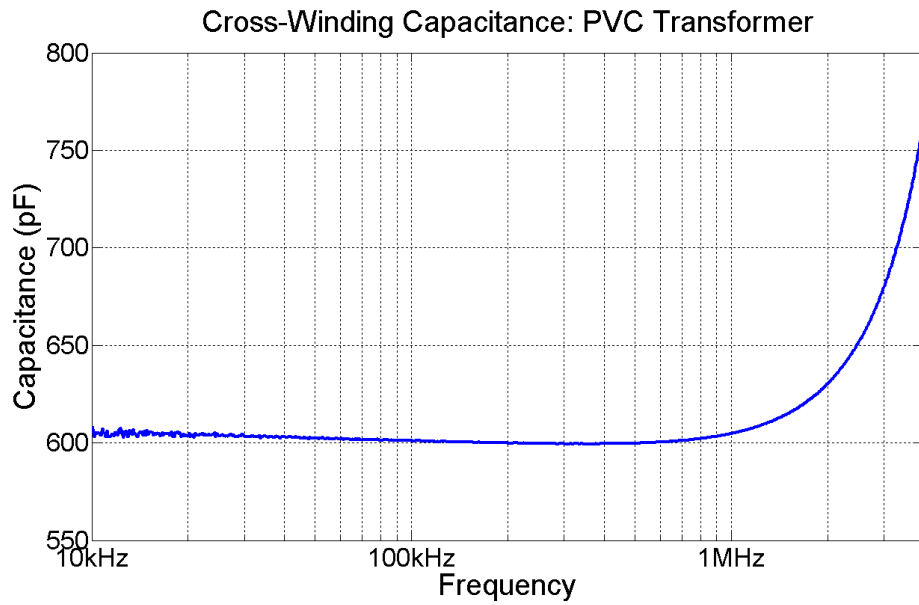


**FIG. 6.42. PVC-core transformer extracted cross-winding capacitance.**

#### **6.4. Summary of extracted values**

Sections 6.2 and 6.3 showed the analysis of network analyzer data for the purpose of parameter extractions. In most cases, the measured equivalent circuit was compared with the analytical equivalent circuit in order to extract certain lumped parameter values. However, as was asserted in chapter 4, these values as lumped parameters do not perfectly describe transformers due to the distributed nature of the capacitance. None-the-less, using the extracted effective lumped parameter values, the behavior of magnetic core transformers can be replicated with a good degree of accuracy. A table summarizing the extracted values is given below (Table 6.6).

**Table 6.6. Summary of all transformers extracted parameters.**

<i>Device</i>	<i>Mutual inductance</i>	<i>Leakage inductance</i>	<i>Line Resistance VNA (DC)</i>	<i>Core-loss resistance</i>	<i>Cross-winding capacitance</i>	<i>Intra-winding capacitance</i>
1GBase-T Ethernet Transformer	~610 $\mu$ H	110nH	0.6 $\Omega$ (0.65 $\Omega$ )	~7k $\Omega$ -11.5k $\Omega$	39.1pF	1.36pF
		90nH	0.6 $\Omega$ (0.65 $\Omega$ )			1.49pF
10GBase-T Ethernet Transformer	~160 $\mu$ H	65nH	0.25 $\Omega$ (0.3 $\Omega$ )	~2.25k $\Omega$ - 3.4k $\Omega$	5.69pF	0.88pF
		80nH	0.63 $\Omega$ (0.71 $\Omega$ )			1.52pF
PVC-core Transformer	30 $\mu$ H	2 $\mu$ H	0.21 $\Omega$ (0.28 $\Omega$ )	~70k $\Omega$	600pF	-
		2.5 $\mu$ H	0.17 $\Omega$ (0.28 $\Omega$ )			-

## 6.5. Model comparison

### 6.5.1. Introduction

In the preceding sections, differential-mode and common-mode transfer relations were presented for two types of Ethernet transformers and a PVC-core transformer. Chapter 3 presented lumped element circuit models for differential mode signals, while chapter 5 presented distributed models for Ethernet transformers in differential-mode and common-mode schemes. In this section, models formed with the previously extracted parameters will be compared with the measured data.

### 6.5.2. Differential-mode lumped element models

At the end of chapter 3, it was stated that the placement of the capacitance in the lumped element circuit model was a topic for debate, since the capacitances are actually distributed throughout the windings. However, the lumped element model should be valid in certain situations. For the sake of a complete set of comparisons, the lumped element equivalent circuits

from chapter 3 (of the specific form of FIG. 6.43) will be evaluated with the extracted parameter values in the following section.

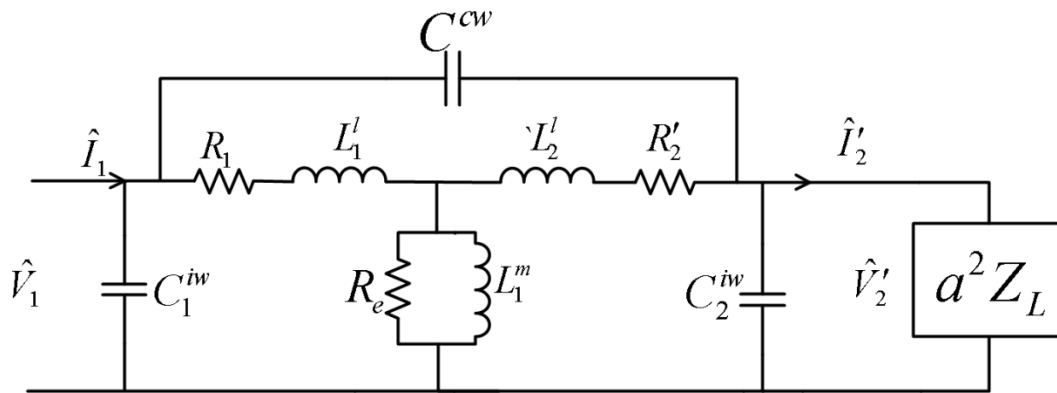


FIG. 6.43. Lumped element equivalent circuit used for comparison to measured transfer relations.

### 6.5.2.1. 1GBase-T transformer lumped equivalent circuit comparison

FIG. 6.44 shows the transfer relation for the lumped element equivalent circuit both loaded and unloaded compared with the measured transfer relation of the 1GBase-T Ethernet transformer. The equivalent circuit parameter values are equal to the extracted values from Table 6.6.

As can be seen from the figures, some of the main features are reproduced by the lumped circuit, such as the low frequency behavior and a single high frequency resonance. However, the frequencies of the features do not precisely match, and some major high frequency resonance behavior is missing. The missing resonance behavior at high frequency can be attributed to the distributed nature of the windings. This will be discussed more in the distributed model comparison section.

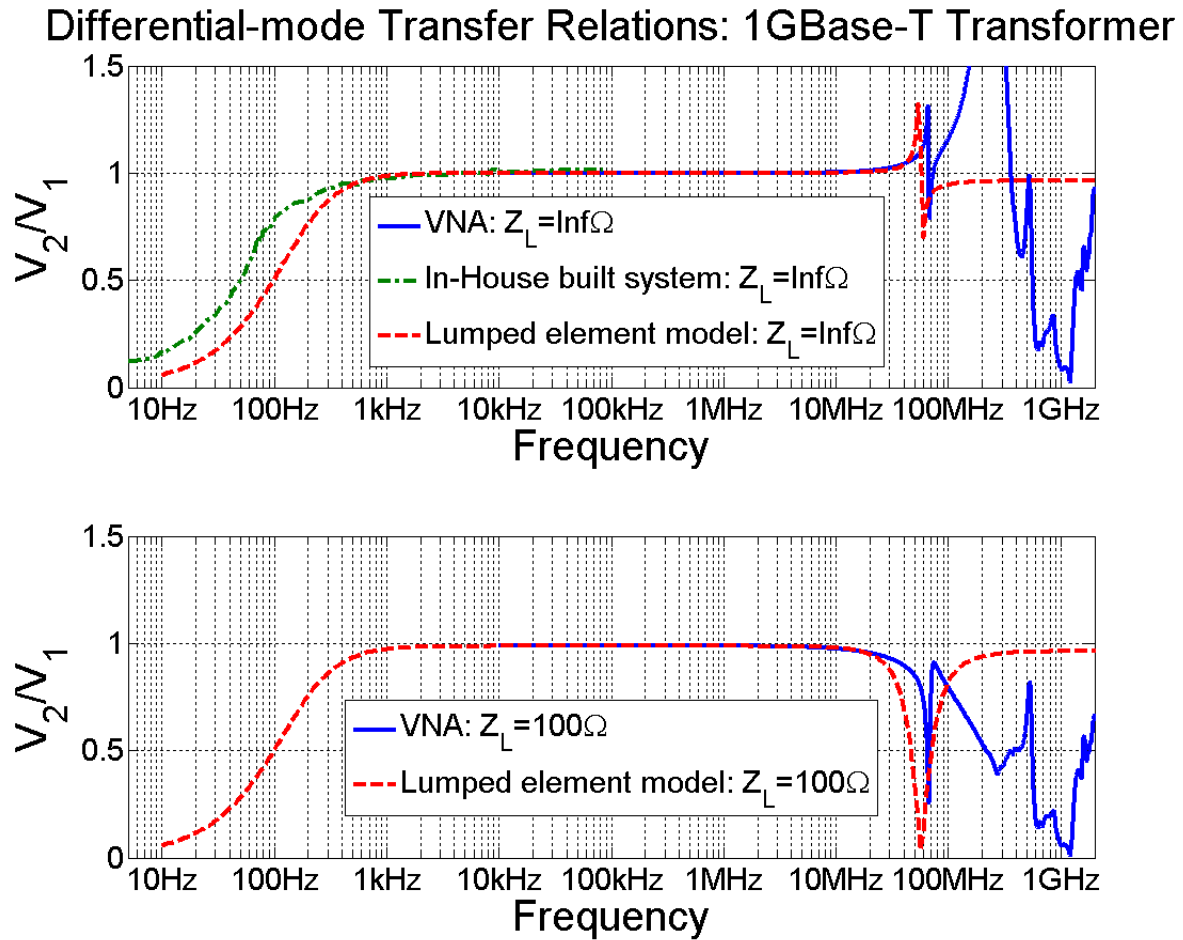


FIG. 6.44. 1GBase-T Ethernet Transformer lumped equivalent circuit transfer relation comparison.

### 6.5.2.2. 10GBase-T transformer lumped equivalent circuit comparison

FIG. 6.45 shows the transfer relation for the lumped element equivalent circuit both loaded and unloaded compared with the measured transfer relation of the PVC-core transformer. The equivalent circuit parameter values are equal to the extracted values from Table 6.6.

Similar to the comparison of the 1GBase-T transformer, the low frequency behavior is reproduced but at the wrong frequency, and a single high frequency resonance is reproduced. In this case, the resonance behavior is similar, but also at the wrong frequency.

## Differential-mode Transfer Relations: 10GBase-T Transformer

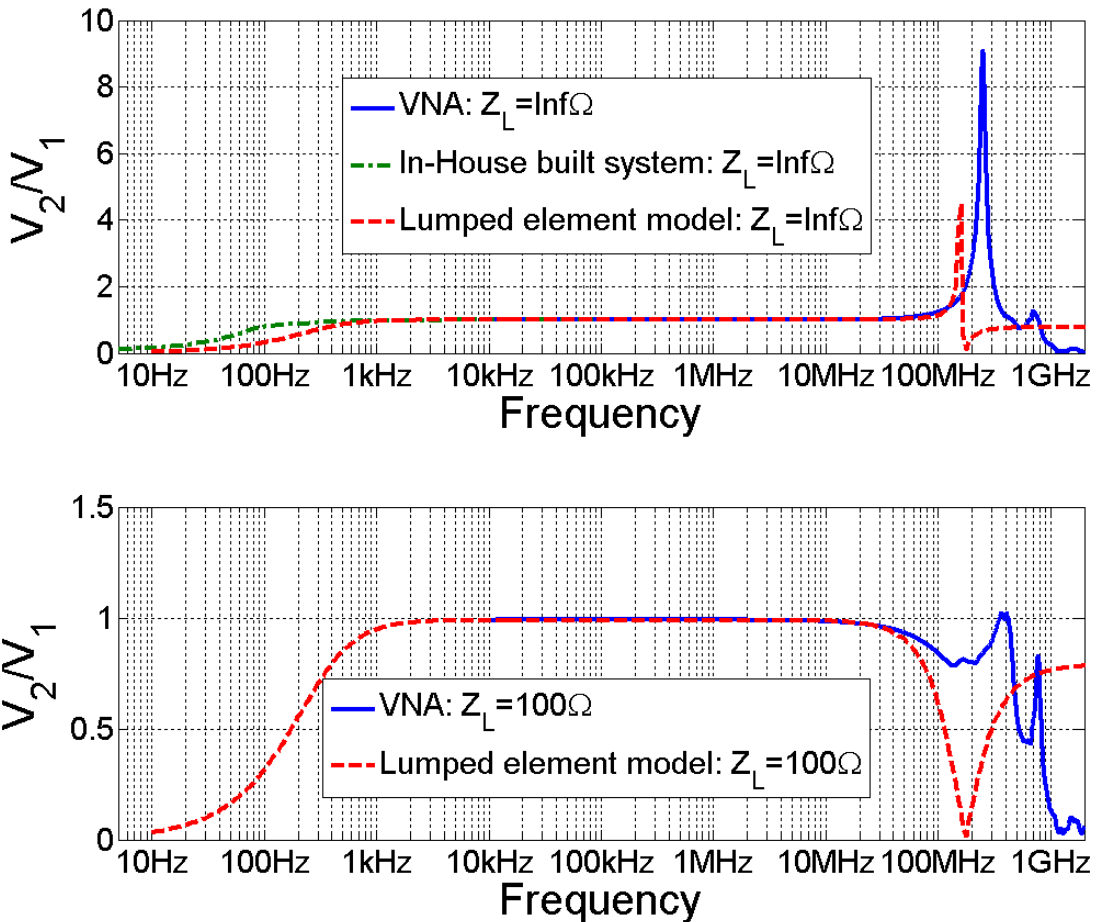


FIG. 6.45. 10GBase-T Ethernet Transformer lumped equivalent circuit transfer relation comparison.

### 6.5.2.3. PVC-core transformer lumped equivalent circuit comparison

FIG. 6.46 shows the transfer relation for the lumped element equivalent circuit both loaded and unloaded compared with the measured transfer relation of the 10GBase-T Ethernet transformer. The equivalent circuit parameter values are equal to the extracted values from Table 6.6.

In this case, the lumped circuit produced very similar behavior, even with slightly detuned resonance frequencies. The low frequency behavior was close to matching, and the high frequency behavior was very similar with slightly different resonance frequency and slightly

different amplitudes. A better match was found for the unloaded circuit than the loaded circuit behavior.

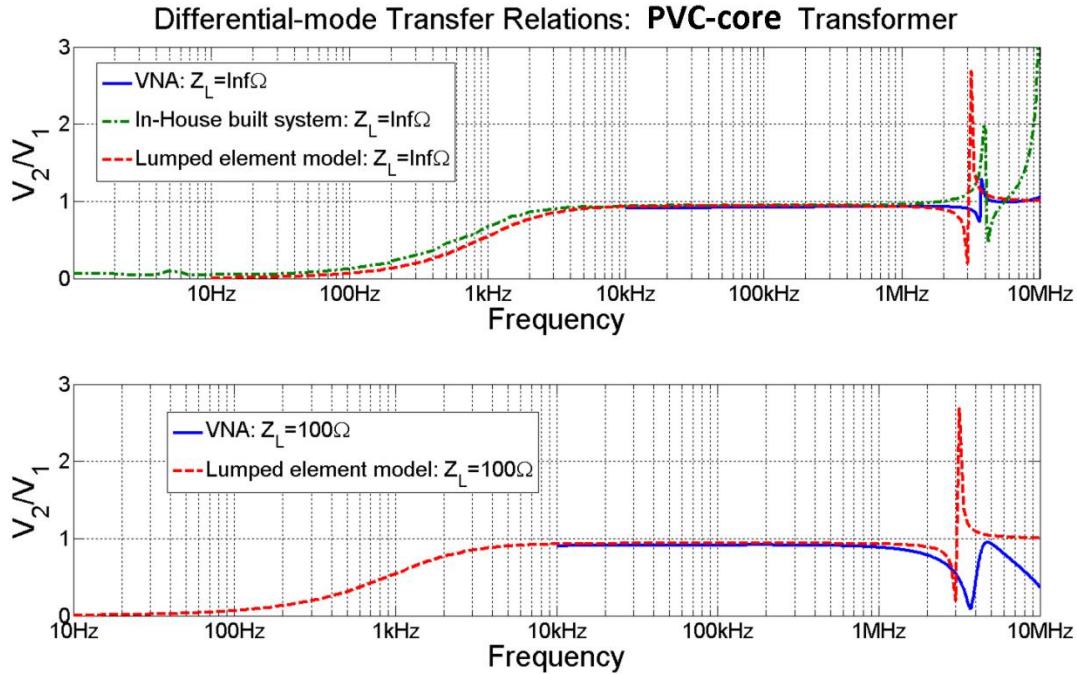


FIG. 6.46. PVC-core Transformer lumped equivalent circuit transfer relation comparison.

### 6.5.3. Differential-mode distributed models

In the distributed differential-mode model of chapter 5, infinitesimal circuit cells (reproduced in FIG. 6.47) were used to derive an expression for the differential-mode transfer relations (equation 6.22). However, the specific topologies for the per-length impedance and admittances are left to be defined. For the differential-mode model, the intuitive definitions of series impedance, cross-winding admittance, and mutual impedance were used. See FIG. 6.48, FIG. 6.49, and FIG. 6.50 for the chosen circuit topologies.

In the following sections, the extracted parameter values from the previous section will be used with the differential-mode transfer function (equation 6.22) and the per-length topologies to produce transfer relation plots and compare them with the measured transfer relations.

6.22

$$\frac{\hat{V}_2}{\hat{V}_1} = \frac{\gamma' + \left( \frac{M - Z_s}{Z_s + M} \right) \tanh(\gamma')}{\gamma' + \left( \frac{2l(Z_s - M)}{Z_L} - \left( \frac{M - Z_s}{Z_s + M} \right) \right) \tanh(\gamma')}$$

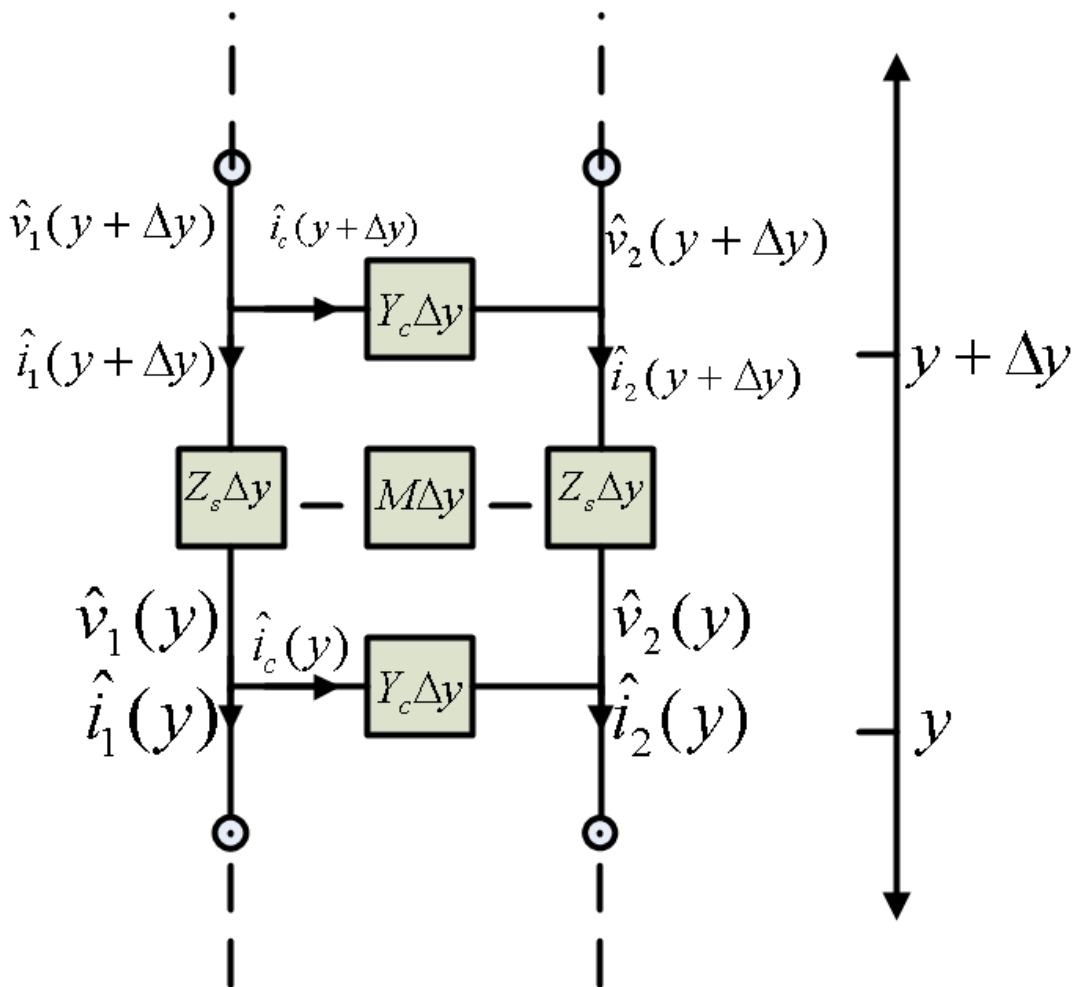


FIG. 6.47. Differential-mode distributed circuit cell.

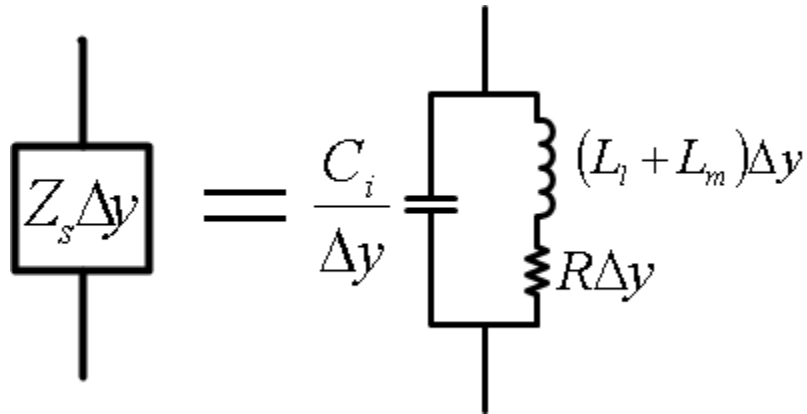


FIG. 6.48. Chosen differential-mode per-length impedance topology.

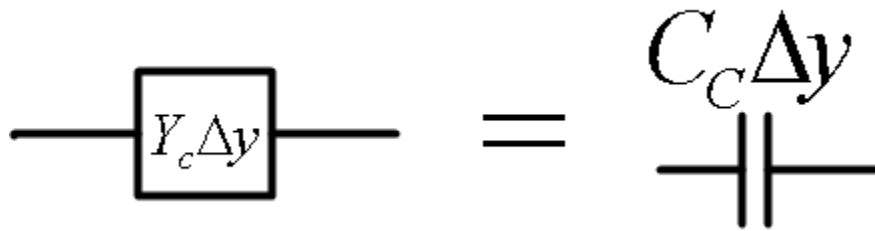


FIG. 6.49. Chosen differential-mode per-length admittance topology.

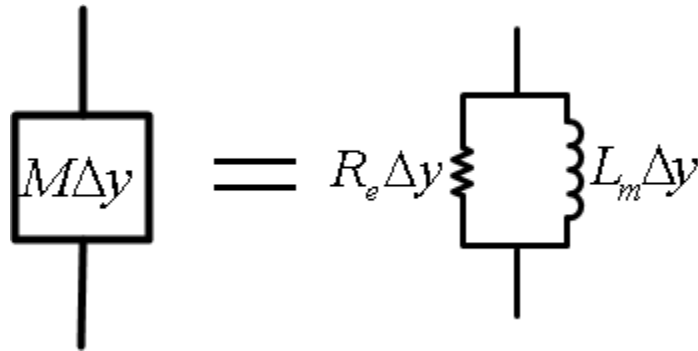


FIG. 6.50. Chosen differential-mode per-length mutual impedance topology.

### 6.5.3.1 1GBase-T differential-mode model comparisons

FIG. 6.51 and FIG. 6.52 show the distributed differential-mode model plotted over the measured differential-mode transfer relation for the 1GBase-T Ethernet transformer. FIG. 6.51 shows the model transfer function when the exact extracted values are used. It is apparent that both the low frequency and high frequency behavior are shifted in frequency. The high frequency resonances also have different behavior from the measured resonances.

To exhibit that the model is capable of reproducing the behavior of the measured transformer, the initial model parameter values were tuned to create a better match. FIG. 6.52 shows the tuned model plotted over the measured transformer transfer relation. Though the tuned model is also not a perfect match, it does match the major features well enough to call it a qualitative match. It is a topic for future research to relate in a more intelligent manner the extracted parameters to the distributed model parameters.

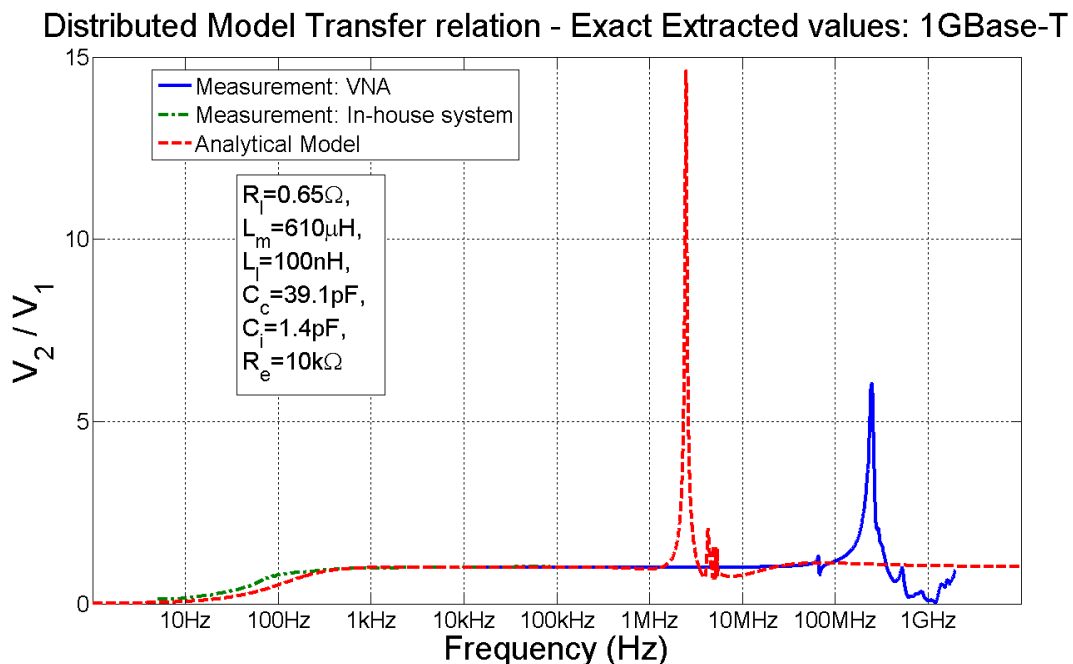
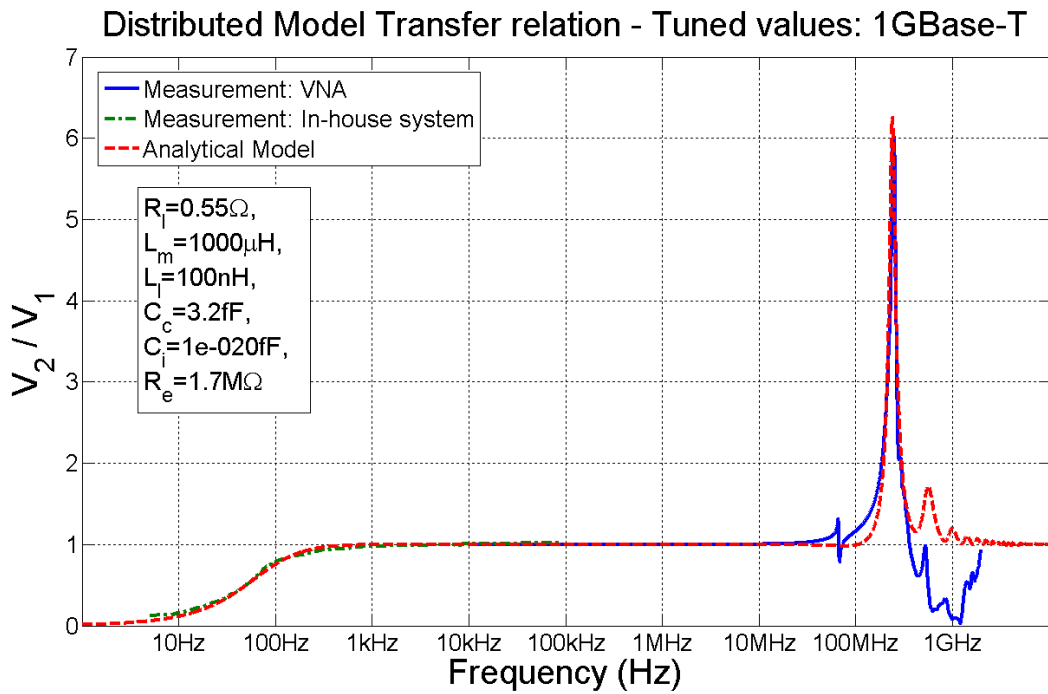


FIG. 6.51. 1GBase-T Ethernet transformer differential-mode model comparison - exact extracted values.



**FIG. 6.52. 1GBase-T Ethernet transformer differential-mode model comparison - Tuned values.**

### **6.5.3.2 10GBase-T transformer differential-mode model comparisons**

FIG. 6.53 and FIG. 6.54 show the distributed differential-mode model transfer function with extracted and tuned parameter values, respectively, for the 10GBase-T Ethernet transformer. For a discussion of the differences in the plots and their relevance, see the beginning of section 6.5.3.1.

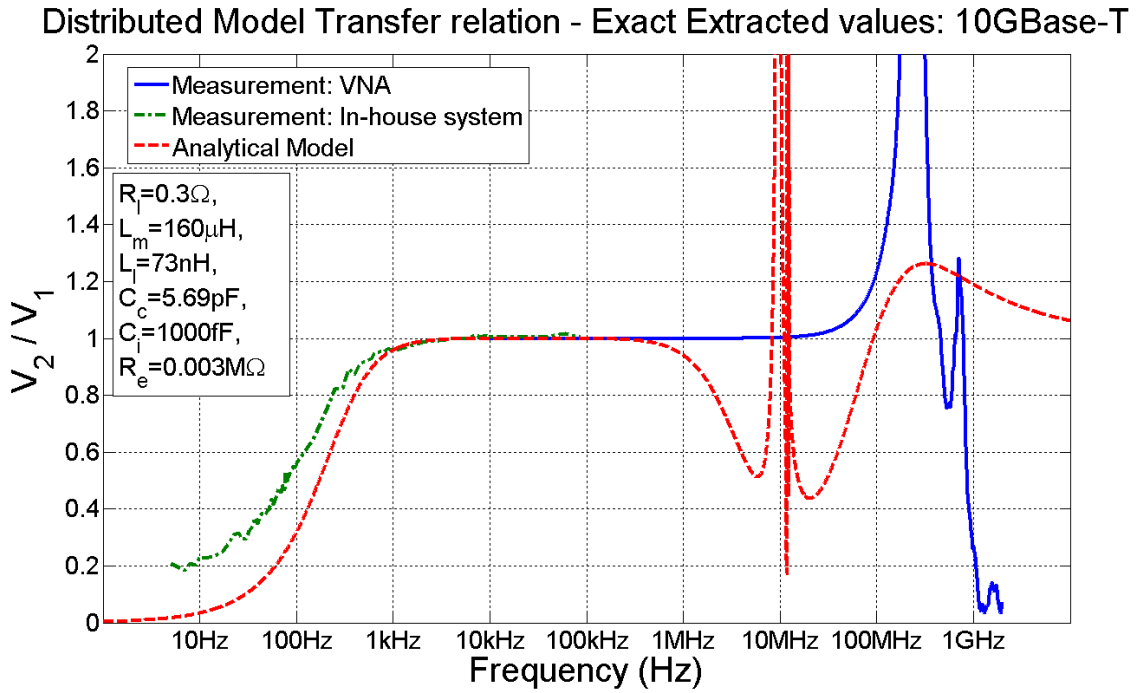


FIG. 6.53 10GBase-T Ethernet transformer differential-mode model comparison - exact extracted values.

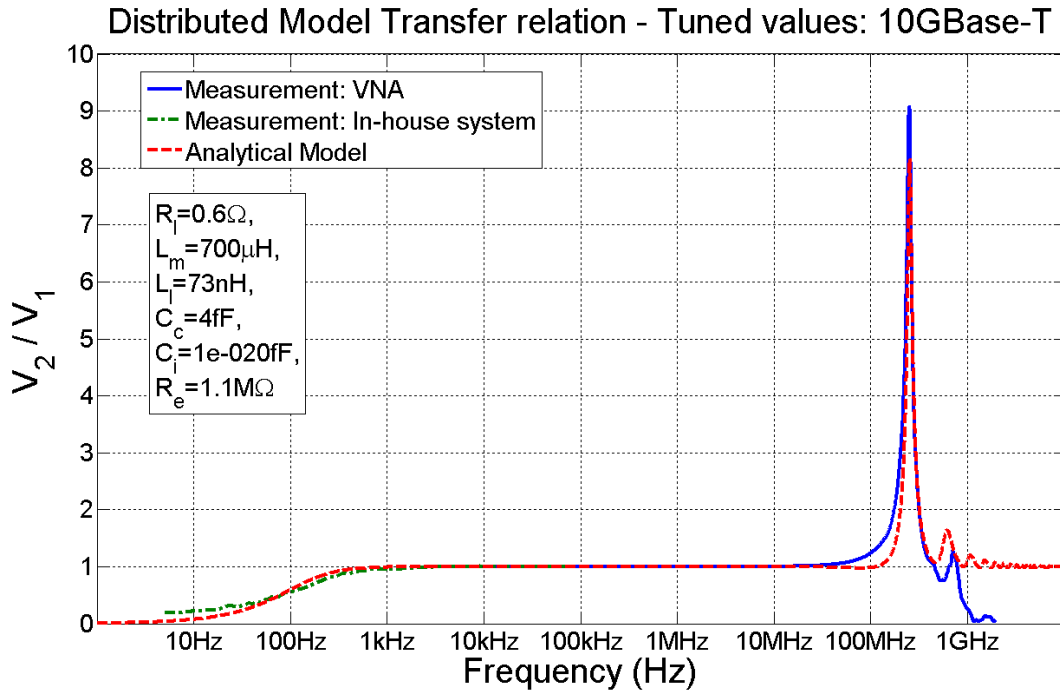


FIG. 6.54. 10GBase-T Ethernet transformer differential-mode model comparison - Tuned values.

### 6.5.3.3 PVC-core transformer differential-mode model comparison

FIG. 6.55 and FIG. 6.56 show the distributed differential-mode model transfer function with extracted and tuned parameter values, respectively, for the PVC-core transformer. For a discussion of the differences in the plots and their relevance, see the beginning of section 6.5.3.1.

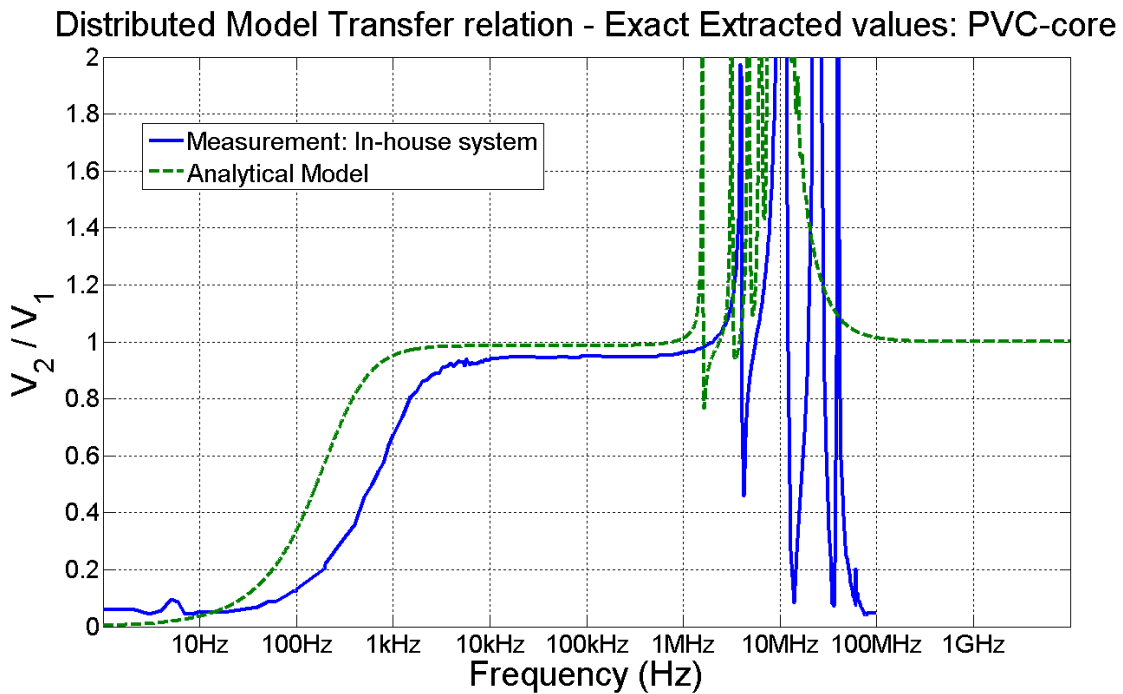


FIG. 6.55. PVC-core transformer differential-mode model comparison - exact extracted values.

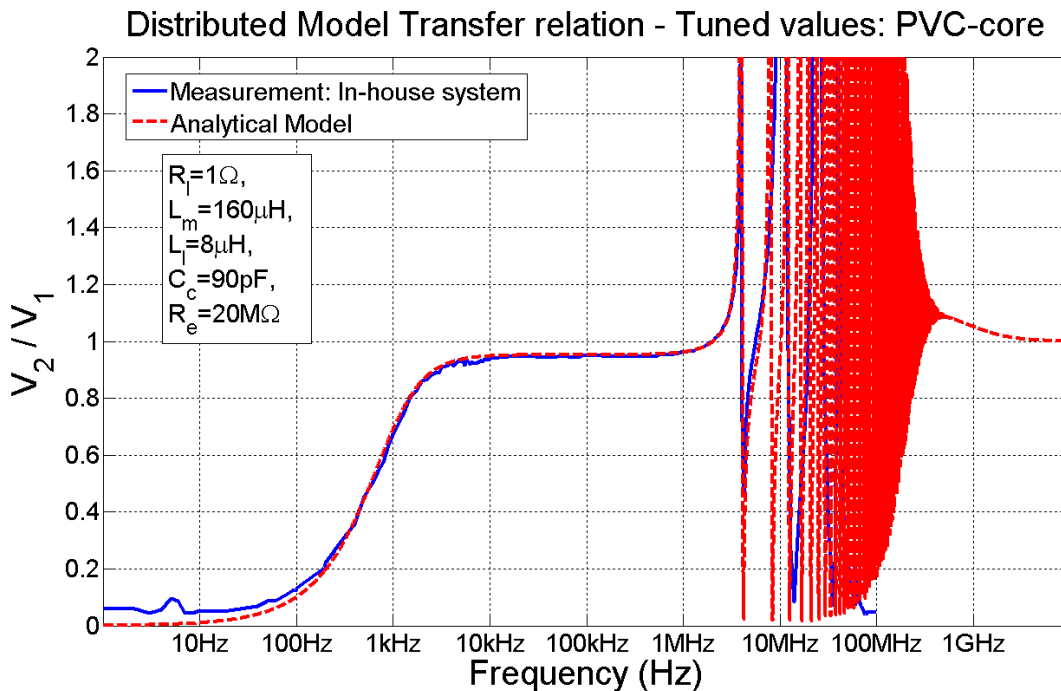


FIG. 6.56. PVC-core transformer differential-mode model comparison - Tuned values.

#### 6.5.4. Differential-mode model comparison summary

Distributed differential-mode model transfer functions were compared with measured transfer relations for the 1GBase-T and 10GBase-T Ethernet transformer as well as the large PVC-core transformer. The comparisons showed that using the extracted parameter values directly produced model transfer relations that were poor matches to the measured transfer relations. Tuning of the values significantly improved the transfer functions match to the measured transfer relation, and exhibits high frequency resonance behavior that cannot be produced with a lumped element model. This shows that the differential-mode distributed model transfer function is capable of matching the measured transfer functions, but the distributed model parameters are not the parameters extracted in Table 6.6. Relating the measured parameters to the distributed model parameters is a topic for future research.

### 6.5.5. Common-mode distributed models

The common-mode transfer function (equation 6.23) was derived using the common-mode infinitesimal distributed circuit cell (see FIG. 6.57). Just as with the differential-mode model, the specific circuit topology of the impedance and admittance are open to definition. In the case of the common-mode transfer relation, choosing the proper per-length impedance and admittance circuit topologies will be part of the tuning process. First, however, for comparison with the common-mode measurements with zero ground impedance, equation 6.23 can be simplified as shown in equation 6.24. Thus, equation 6.24 will be used for plotting the model transfer relations.

Unlike the differential-mode model, tuning the common-mode model will require a change in circuit topology. However, for comparison, the common-mode model transfer relation will be first plotted using a similar topology as in the differential mode modeling, shown in FIG. 6.58 and FIG. 6.59. For tuning the model, the topology shown in FIG. 6.60 gives the best results and will be used for the per-length series impedance.

In the following sections, the distributed common-mode model transfer function will be compared with the measured transfer relation (extracted values and tuned values) for 1GBase-T and 10GBase-T Ethernet transformers.

$$\frac{\hat{V}_2}{\hat{V}_1} = \frac{\tanh(\gamma')(Z_s Z_g l \gamma^2 + 4Z_g^2 \gamma^2 - Z_s^2) + (Z_s^2 \gamma')}{\tanh(\gamma')(Z_s Z_g \gamma^2 l + 4Z_g^2 \gamma^2 + Z_s^2 + \frac{Z_s^3 l + 4Z_s^2 Z_g}{Z_L}) + (Z_s^2 \gamma' + 4Z_g Z_s \gamma + \frac{2Z_g Z_s^2 l \gamma + 8Z_g^2 Z_s \gamma}{Z_L})}$$

6.23

$$\frac{\hat{V}_2}{\hat{V}_1} = \frac{\tanh(\gamma')(-Z_s^2) + (Z_s^2\gamma')}{\tanh(\gamma')(Z_s^2 + \frac{Z_s^3 l}{Z_L}) + (Z_s^2\gamma')} = \frac{\gamma' - \tanh(\gamma')}{\gamma' + (1 + \frac{Z_s l}{Z_L})\tanh(\gamma')}$$

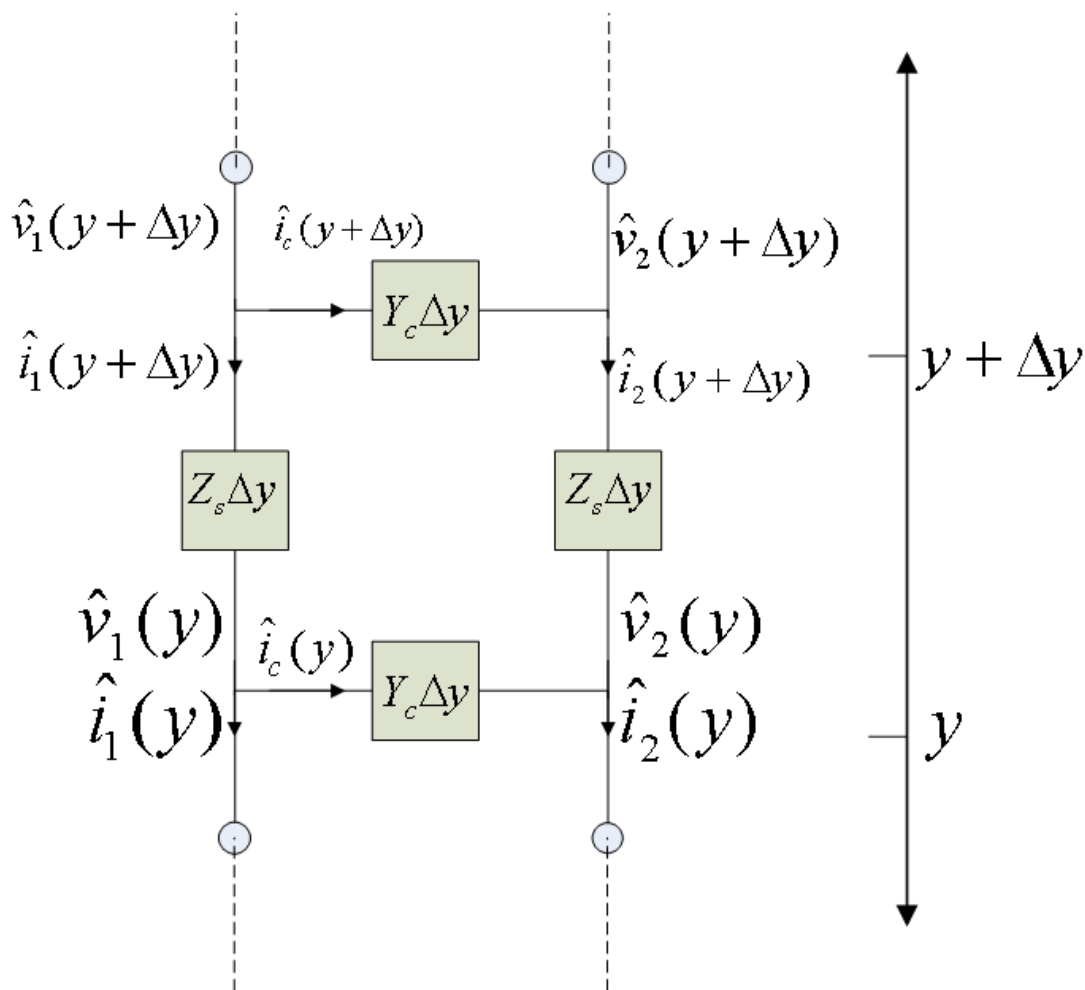


FIG. 6.57. Distributed infinitesimal circuit cell for the common-mode model.

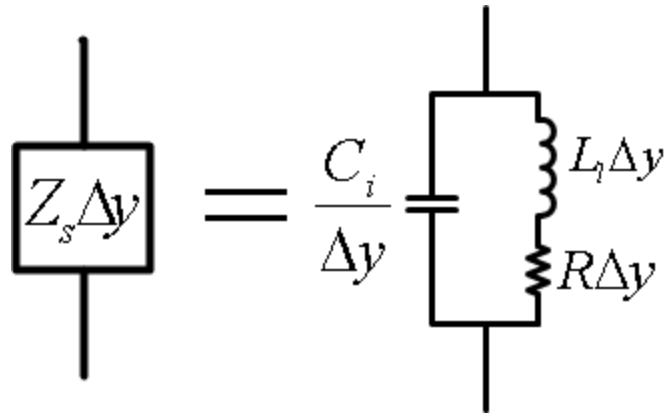


FIG. 6.58. Circuit topology for the distributed common-mode model per-length series impedance .

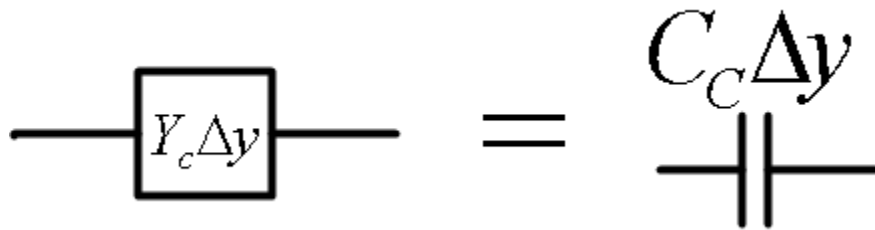


FIG. 6.59. Circuit topology for the distributed common-mode model per-length cross-winding admittance.

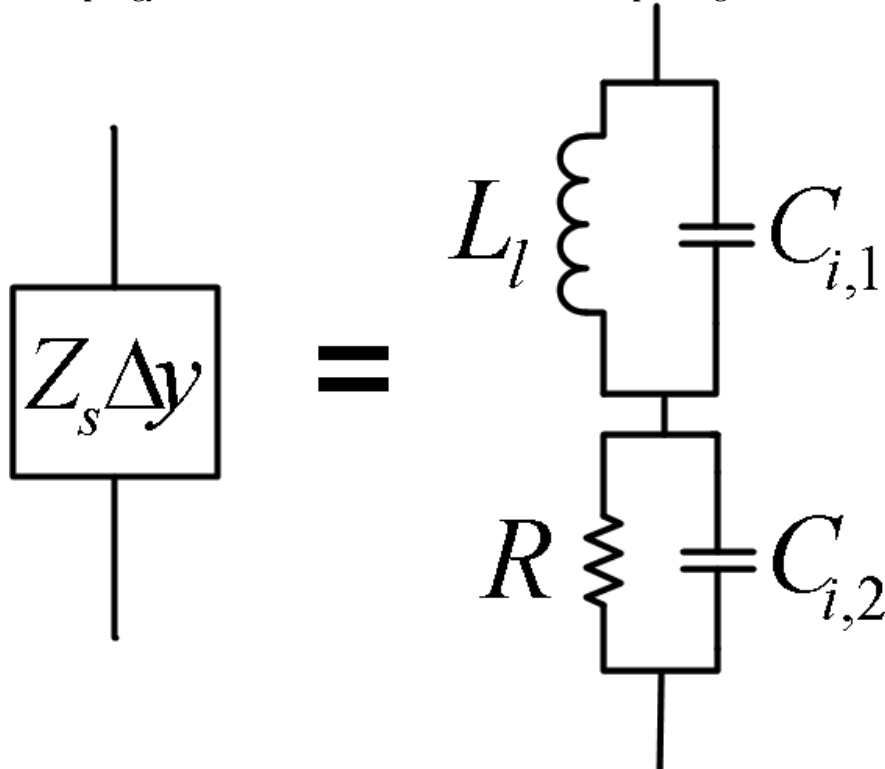


FIG. 6.60. Tuning topology for the per-length impedance of the common-mode distributed model.

### 6.5.5.1. 1GBase-T common-mode model transfer function comparison

FIG. 6.61 shows the pure mismatch of the model transfer function plotted over the measured data for the 1GBase-T Ethernet transformer. With tuning, however, an excellent match was achieved as seen in FIG. 6.62. Tuning, in the common-mode case, involves both changing the impedance topology and adjusting parameter values. As was the case with the differential-mode model, such a match supports the validity of the model transfer equation but also requires further research into relating the extracted parameter values to model parameter values.

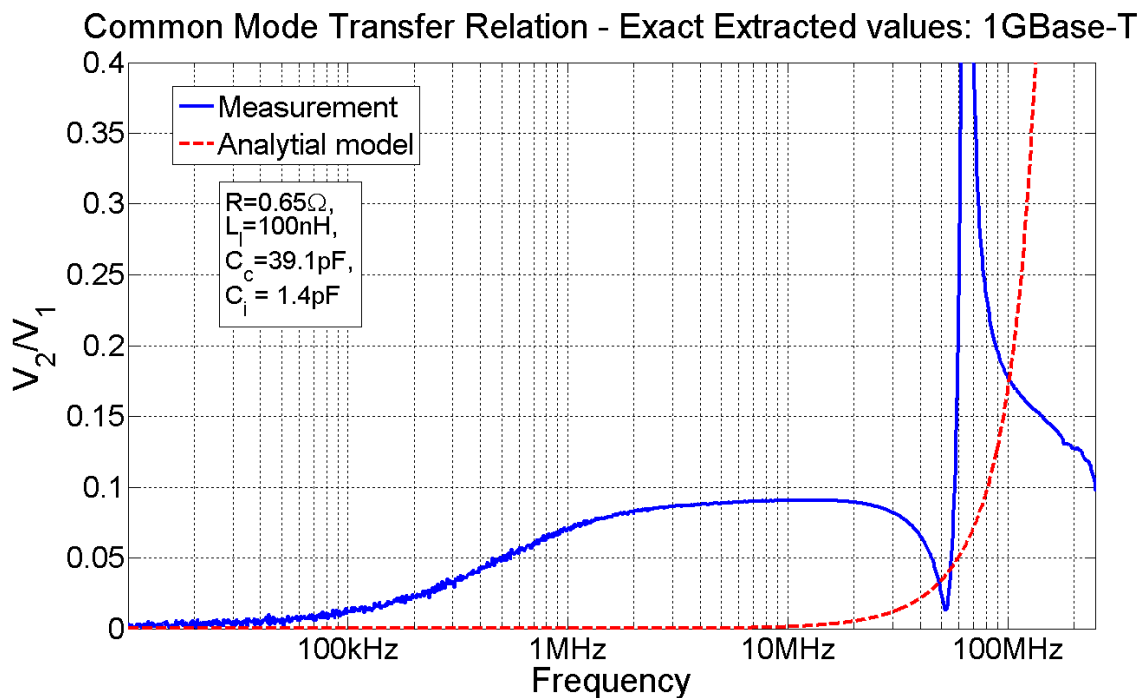
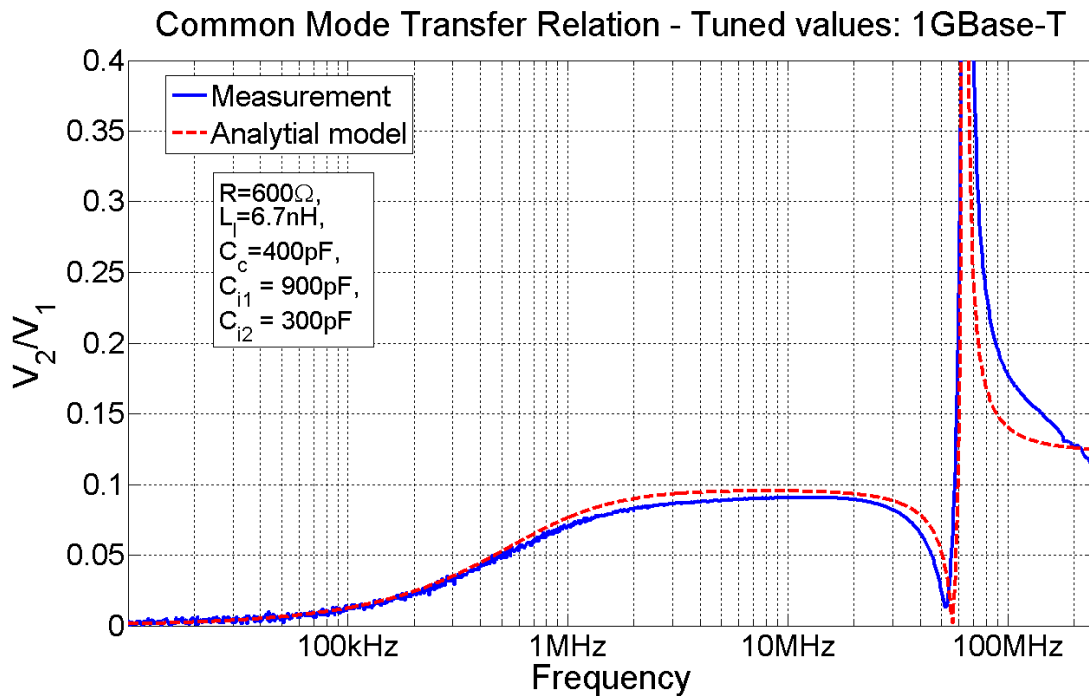


FIG. 6.61. 1GBase-T transformer: Common-mode distributed model transfer relation with extracted parameter values.



**FIG. 6.62. 1GBase-T transformer: Common-mode distributed model transfer relation with tuned parameter values [31].**

#### **6.5.5.2. 10GBase-T transformer distributed common-mode transfer function comparison**

FIG. 6.63 shows the pure mismatch of the model transfer function plotted over the measured data for the 10GBase-T Ethernet transformer. With tuning, however, an excellent match was achieved as seen in FIG. 6.64. As was the case with the differential-mode model, such a match supports the validity of the model transfer equation but also requires further research into relating the extracted parameter values to model parameter values.

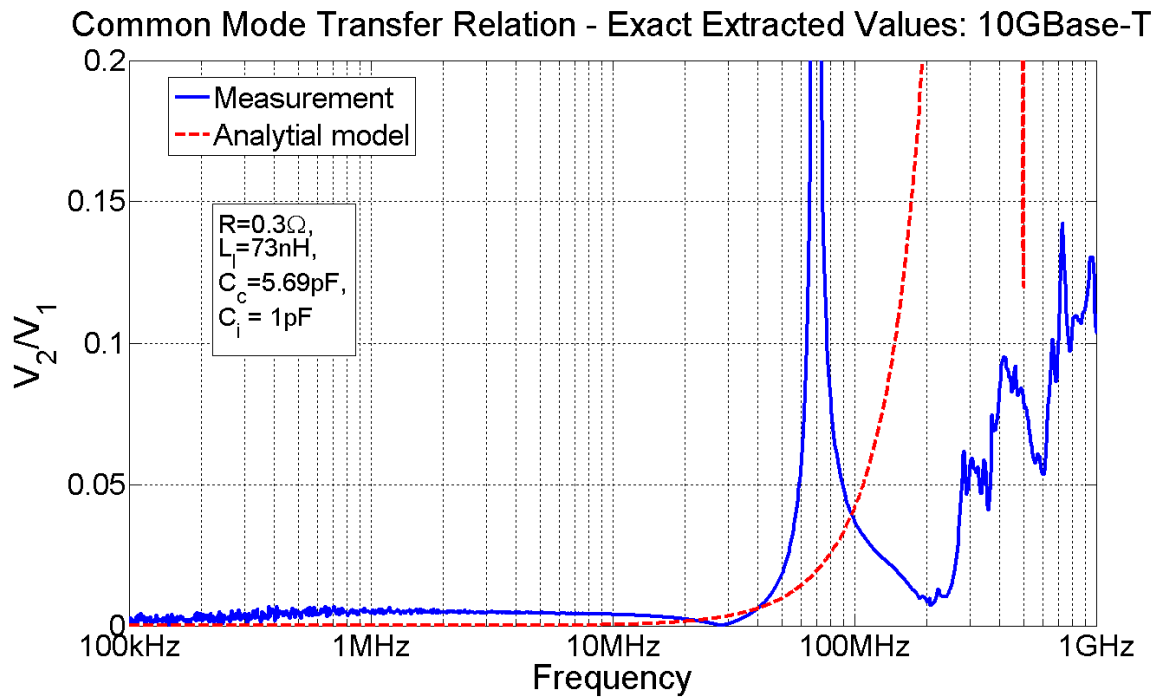


FIG. 6.63. 10GBase-T transformer: Common-mode distributed model transfer relation with extracted parameter values.

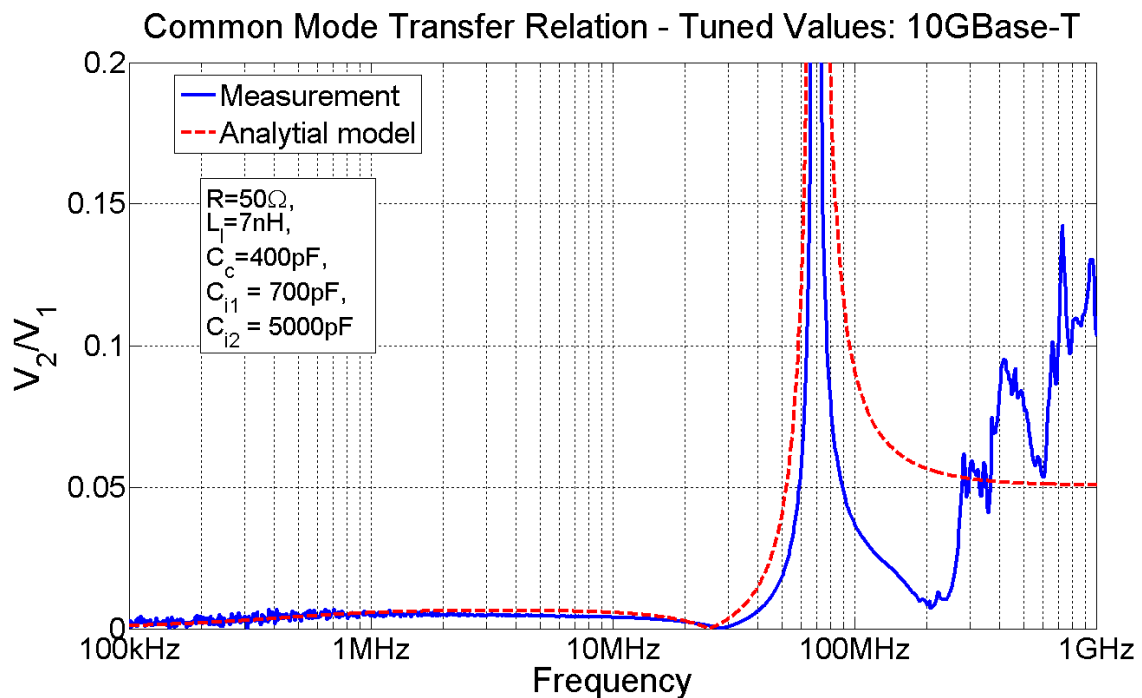


FIG. 6.64. 10GBase-T transformer: Common-mode distributed model transfer relation with tuned parameter values [31].

### **6.5.6. Testing of commercial Ethernet transformers summary**

This chapter presented how 1GBase-T and 10GBase-T Ethernet transformers were tested using both an in-house built scalar system as well as a vector network analyzer. The measurement results were decomposed and translated to form an equivalent network, from which transfer relations were plotted and equivalent circuit parameters were extracted (see chapter 3, Table 6.6). In addition to the commercial Ethernet transformers, a lab-built large toroidal PVC-core bifilar-wound transformer was also tested and analyzed.

After the transformers were thoroughly analyzed, the equivalent circuit from chapter 3 as well as the distributed models from chapter 5 (both differential-mode and common-mode) were compared to the measured transfer relations. It was found that when using the exact values of the extracted parameters, the lumped equivalent circuits delivered the best match to the measured data. However, tuning the distributed model values resulted in the distributed model transfer relations giving superior matches to the measured data. It was found that the distributed models could recreate complicated resonance behavior that would not be possible with the lumped-element equivalent circuit. The relation of the extracted parameter values to the distributed model parameter values so the models would no longer require tuning is a topic for future research.

## Chapter 7 : Dielectric-core toroid transformer: Fabrication and analysis

### 7.1. Introduction and background

For most designs of transformers with soft magnetic cores, the geometry does not need to be critically precise. As long as magnetic flux from the primary winding has a low reluctance closed path through which it can return (North to South pole) and this path is shared with the secondary winding, the device will behave as expected. Many microfabricated transformer designs have non-critical geometries because they use magnetic core materials ([32], [33], [34], [35], [36]), but also have complicated fabrication processes to reduce losses. However, as the frequency of the flux increases, the permeability of ferrites will become unstable and approach the permeability of vacuum (see FIG. 4.12). As the permeability of the core approaches that of the ambient air, the core will no longer act as a flux guide. The reluctance of the core path will be the same as the path through the air, so flux will circulate through the air path and not link the primary to the secondary winding. This air path flux was discussed previously and is referred to as *leakage flux* – flux that does not link the primary and the secondary windings. Increasing leakage flux decreases coupling from the primary to the secondary and degrades the flat band region of the transformer transfer relation.

In addition to the declining permeability, ferrites exhibit other deleterious high-frequency behavior. Ferromagnetic resonance (FMR) is a phenomena related to magneto-dynamics in which the signal frequency applied to the magnetic material is the same as the precession frequency of the magnetic moment. FMR can be used to characterize crystalline magnetic materials by applying a strong magnetic field along a specific crystallographic direction of the sample. FMR can be observed in a less predictable way by the simple application of microwave

fields to magnetic materials, causing valleys of absorption. These core material FMR absorption valleys distort the transformer transfer relation at high frequencies, in turn distorting signals.

It is apparent that Mn-Zn ferrite cores will not effectively guide flux for frequencies up to 1GHz. As the permeability deteriorates with frequency, the leakage flux will increase and the coupling will decrease. Above 1GHz, ferromagnetic resonances will occur distorting the flat band region of the transformer. At high frequencies, the core materials flux guiding benefits are lost, and FMR, eddy current losses, and hysteresis losses become a detriment to signal coupling [37]. A forward thinking design would need to avoid ferrite core materials.

Ferrites, however, cannot easily be replaced. Ferrite materials themselves solved many of the core loss problems of larger metal alloy transformers. Ferrites are currently the best designed core materials for broadband signal transformers. The only way to avoid the remaining magnetic problems with ferrites is to switch to a non-magnetic core material. Creating a coreless (air-core) transformer would remove the high frequency difficulties, but also the lower frequency flux guiding benefits. The following section considers low frequency flux guiding without a flux guiding magnetic core.

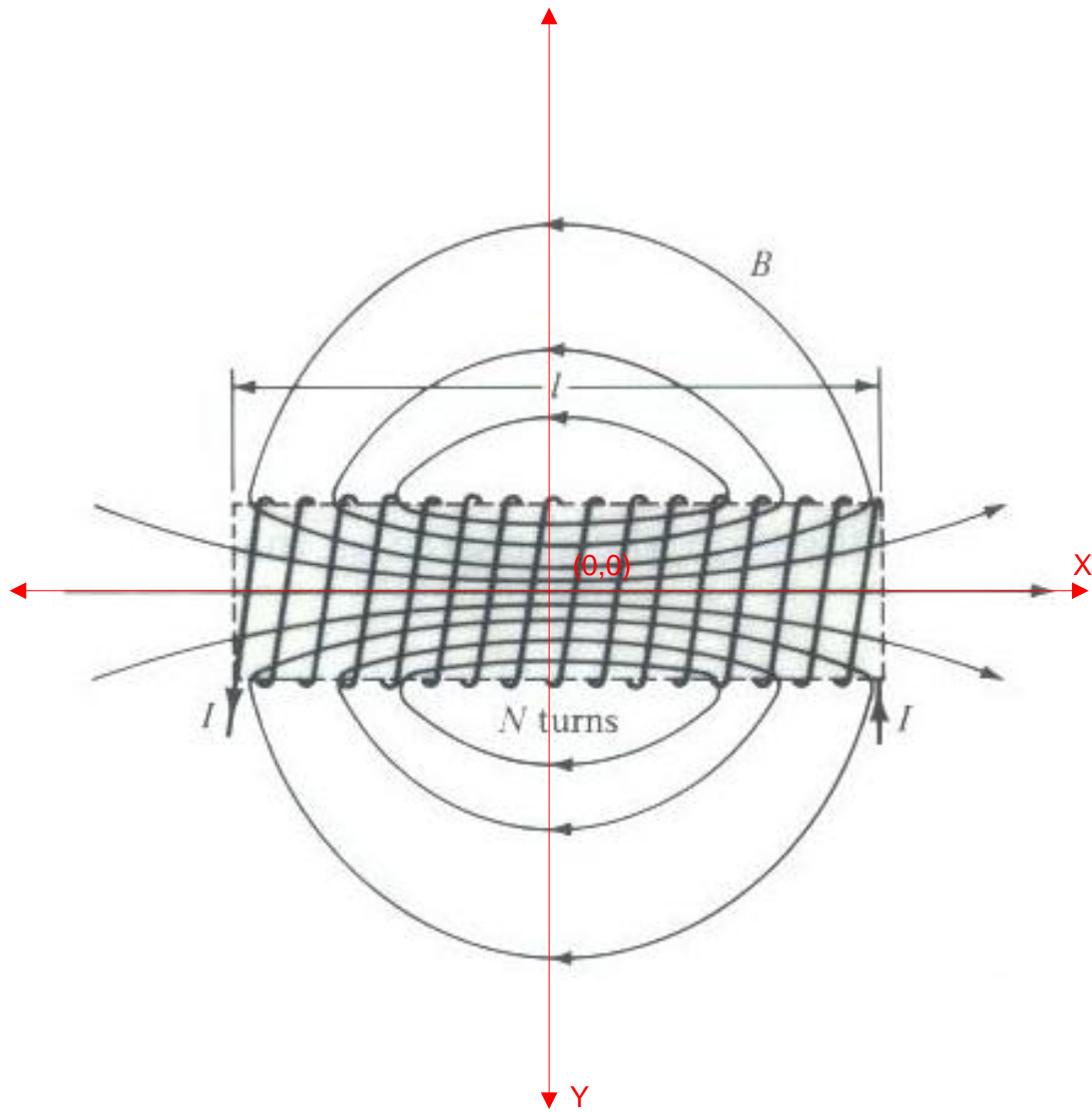


**FIG. 7.1. Magnetic fields of a long solenoid. (Plonus, M. Applied Electromagnetics. McGraw Hill, 1978. Reproduced with permission of The McGraw-Hill Companies) [38]**

The simple solenoid is a good example to understand the magnetic fields of an air-core winding. Given a cylindrical winding as shown in FIG. 7.1, the current in each turn of the winding will be going the same direction. Consider, first, a single current-carrying loop as shown in FIG. 7.2. FIG. 7.2 shows a cross section of a single loop (or parallel wires), such that the left conductor carries current out of the plane of the page, and the right conductor carries current into the plane of the page. Recalling that the field away from a current carrying wire depends on

radial distance from the wire, then on the equidistant line between the conductors, the field contribution from both will be equal in magnitude. The components perpendicular to the plane of the loop will be in the same direction, but the components parallel to the plane of the loop will be in opposite directions. Thus, along the equidistant line from both wires, the parallel planar components sum to zero and the perpendicular component is doubled. As the observation point moves away from this equidistant line, the parallel planar components are still opposite, but no longer equal in magnitude. As the observer moves closer to the edge of the loop the parallel planar components of magnetic field will increase as shown in FIG. 7.2.

The magnetic fields of a single wire loop support the somewhat qualitative assumption about the field (and thus the flux density) outside the wire loops is much less than within the loops as flux lines have an infinite volume through which to return.

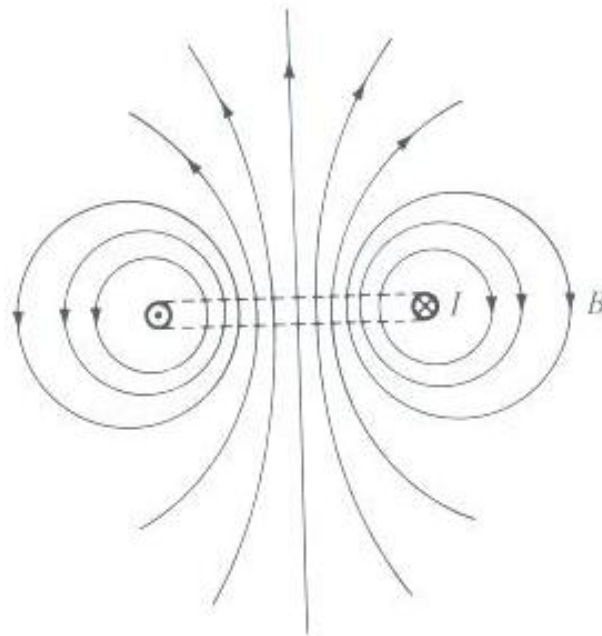


**FIG. 7.2. Magnetic field depiction of a single current carrying loop cross-section. (Plonus, M. Applied Electromagnetics. McGraw Hill, 1978. Reproduced with permission of The McGraw-Hill Companies) [38]**

FIG. 7.5 illustrates how the magnetic field around each turn of a cylindrical winding would behave. The  $\hat{y}$  component of field will cancel with the  $\hat{y}$  component of field of adjacent windings. Of course, fields from a current source are actually immutable. When the fields are said to cancel, this simply indicates that the superposition of fields from two or more sources result in zero or reduced field to be observed at a point. A winding turn will immutably have a  $\hat{y}$  and an  $\hat{x}$  component of field out to an infinite radial direction. However, given the orientation of adjacent turns, the  $\hat{x}$  field components will constructively superimpose while the  $\hat{y}$  field components will destructively superimpose among turns, giving the resultant observed field as shown in the figures. It is this observed field (or net field) which is felt by the media through which it passes, and it is on this field that flux depends.

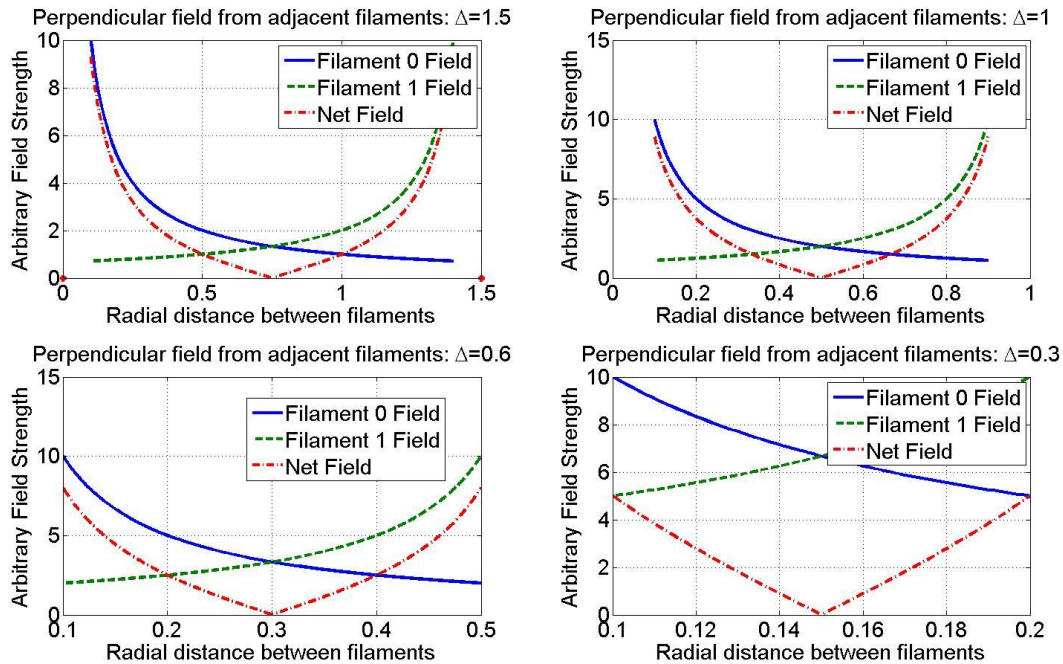
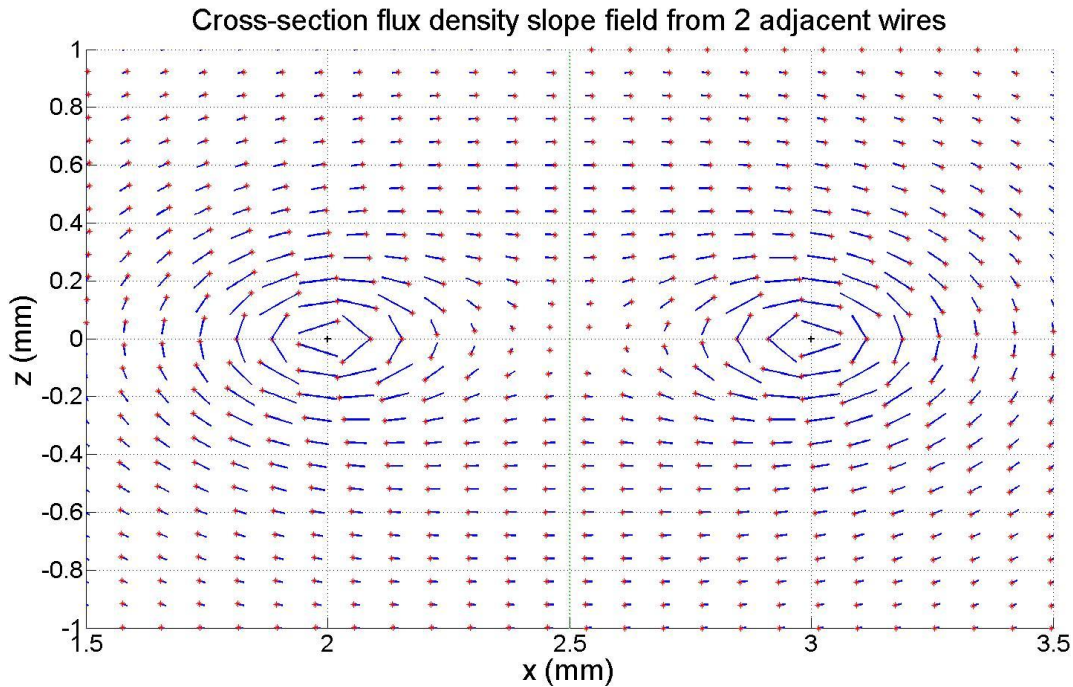


FIG. 7.3. Net field perpendicular to the cross-section between two filaments carrying identical current in the same direction. ( $\Delta$  is the distance between filament centers)

Notice that FIG. 7.5 shows the fields canceling with the nearest neighbor. Consider briefly the concept of two adjacent infinitely thin current filaments carrying the same DC current. The field magnitude predictably decays radially away from the filament centers. If the current in both filaments is traveling in the same direction, then the field in the cross-section between the filaments will be going in opposite directions. For the field in the cross section to perfectly cancel, the field from one filament at one point in the cross-section must have equal magnitude to the field from the other filament at that point. This perfect cancelation only occurs along the equidistant line between the filaments, so it is impossible to perfectly cancel the fields everywhere in the cross-section (See FIG. 7.3 and FIG. 7.4). FIG. 7.4 shows a flux density slope field around two adjacent wires. The equidistant line is marked on the plot, and it is clear that at the equidistant point in the plane of the wires, all flux density drops to zero as the magnitudes and directions are perfectly matched but opposite. Away from the equidistant point in the plane, however, perpendicular-to-the-plane flux density increases. However, it can be seen in FIG. 7.3 that by tightly packing the filaments, both the net field magnitude as well as the area in which it is non-zero is decreased. FIG. 7.5 shows the cut view of turn wires around a core and how the field lines cancel spatially regarding the structure. This assumption of tightly packed windings is often used in textbook derivations to idealize the flux confinement.



**FIG. 7.4. Cross-section flux density slope field for adjacent wires at  $x=2\text{mm}$  and  $x=3\text{mm}$  with current flowing into the page. Line lengths indicate flux magnitude.**

Beyond the cross section between nearest neighbor turns, there is field that remains but decays out to infinite distance (as  $1/r$ ). Another assumption that is often used is to assume the cylindrical winding is infinitely long, so any turn considered will have equal numbers of turns to either side of it in the positive and negative  $\hat{x}$  directions. This implies an infinite winding symmetry. Thus, there is also long range cancelation of the  $\hat{y}$  component of field (interaction of fields of winding turns out to infinity). In practice, long range cancelation is only valid for the turn at the winding midpoint. If the turn location is closer to the end of the solenoid, where the symmetry of long range cancelation is destroyed, the field lines will circulate through the sides of the solenoid as shown in as shown in FIG. 7.1.

With the assumptions in the ideal solenoid of nearest-neighbor and long-range field cancelation, the only field remaining within the solenoid will be perpendicular to the turn planes

in the  $\hat{x}$  direction. Outside the solenoid, the external field (and flux) lines start at one end and return to the opposite end of the solenoid through what is assumed an infinite volume. Since the volume is infinite and the flux is finite, it is inferred that the flux density is zero a small distance outside of the solenoid. Though this analysis considers non-magnetic core winding structures, it is important to highlight a difference between the long solenoid and the toroid. If the core material of the long solenoid were magnetic, the maximum flux density would be limited due to the large air gap through which the flux returns. By forming a toroid where the ends of a solenoid are wrapped around such that the core is continuous, the air-gap is eliminated and the total reluctance of the flux path is significantly reduced.

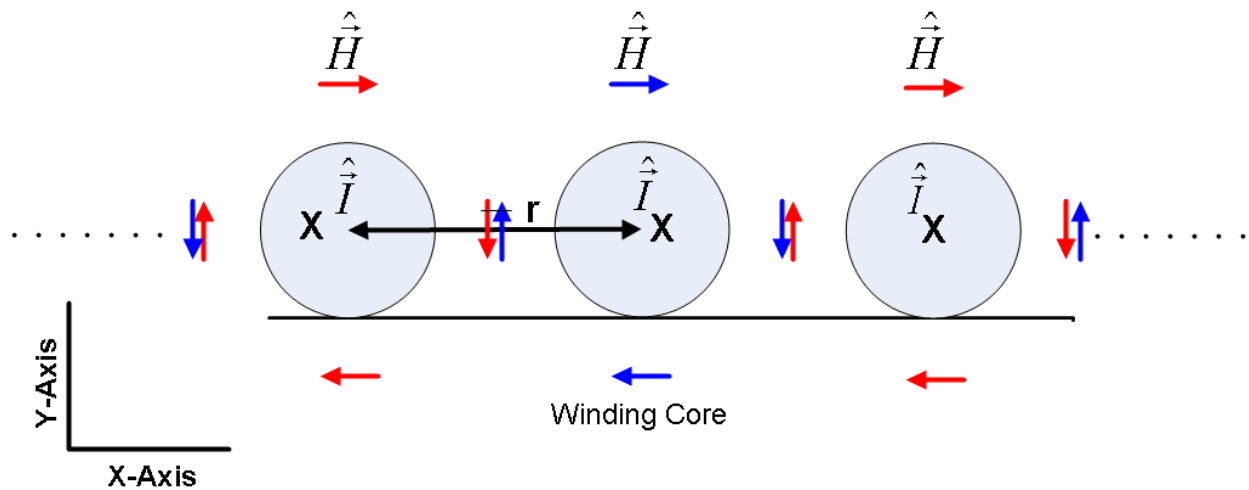
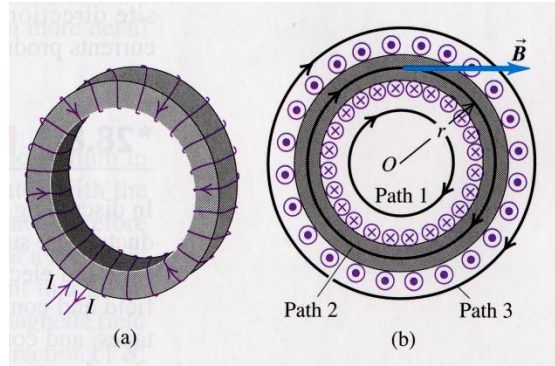


FIG. 7.5. Adjacent winding turns field interaction.

Though the long solenoid has many advantages, the return flux is still flux that is unguided. If the long solenoid were split into two windings to be used as a transformer, very little of the return flux would link the primary winding to the secondary. A bifilar wound design of transformer as a long solenoid would do well, but it would still contaminate the surrounding circuits with magnetic flux. This leads to the toroidal geometry where a long solenoid is curled into a loop, the ends are brought together, and the return flux path has no air gap (see FIG. 7.6).



**FIG. 7.6. Flux diagram of rectangular cross-section toroid inductor.** (Young,/ Freedman/Sandin/Ford. Sear's and Zemansky's University Physics, 10<sup>th</sup> ed., (c)2000, Reprinted by permission of Pearson Education, Inc., Upper Saddle River, New Jersey) [10]

The torus return flux is guided back to the core by geometry rather than magnetic materials. However, curling the long solenoid destroys the radial symmetry, and makes the field along the cross-section non-uniform. This is due to how the turns (which are the same number on the inner and outer radii of the toroid) are more widely spaced on the outer radius than on the inner radius of the toroid. This field non-uniformity decreases, however, as the inner radius of the toroid and the outer radius of the toroid differ from each other by a smaller fraction of the average radius. If the toroid is assumed to be of proper dimensions such that the field is approximately uniform over the cross section, the inductance can be calculated from Ampere's law. Though the derivation can appear in different texts in slightly different ways, the more sophisticated way finds the core flux density as dependent on radius. However, it assumes that there is no flux variation in the azimuthal (theta) direction. The validity of this assumption is discussed in section 7.3.2.

The following sections will discuss the general torus and then extend the general analysis to specific geometry of thin film fabricated designs.

## 7.2. Thin-film dielectric-core transformers: Fabrication and analysis

### 7.2.1. Introduction

As discussed above, without a high permeability magnetic material core, using a toroid geometry will best contain magnetic flux to the volume within the winding structure. In this section, the volume within the windings will be referred to as the *core*, whether or not the core is a separate material structure. Maximum confinement of the magnetic field has both the advantage of boosting magnetic coupling between the windings and minimizing flux contamination of nearby circuits.

With the use of any transformer, all factors must be considered. In a finished device, minimum functional criteria must be satisfied, such as bandwidth and power handling in ideal conditions. Beyond ideal conditions, the transformer will have to satisfy isolation safety tests and maintain operation in severely non-ideal (noisy) environments. For a first generation of fabricated transformers, minimum operational requirements under ideal conditions are the main concern.

To determine the operation performance of the device, the models of chapters 3 and 5 can be used to predict performance. To use these models, however, the device parameter values such as main and leakage inductance, cross- and intra-winding capacitance, and line resistance must be known. Thus, the design of the transformer must be analyzed to extract the model parameters theoretically. This remains a topic for future research. However, significant progress has been made in parameter prediction and will be discussed in this chapter.

Out of all the parameters considered, the two most significant are the mutual inductance and line resistance. For the toroid inductor with a rectangular cross-section, a well-known theoretical calculation of the inductance can be used and is presented in the following section.

Though the calculation is for the self inductance, the approximation can be used that the bifilar windings will share the flux and the self-inductance is approximately equal to the mutual inductance. A more sophisticated method for calculating the inductance will be given in a later section. However, for choosing initial design physical parameters, the following method for inductance calculation will suffice.

### 7.2.1.1 Rectangular cross-section toroid theoretical inductance calculation

This calculation can be found in most electromagnetics text books. What is important to note and will be discussed later in this chapter is the assumption that the windings are tightly packed. This is an important assumption, because it means that leakage flux is essentially zero. This implies that the flux contributed by one excited turn of a winding contributes to the flux through all other turns equally, because no flux leaks around the outside of the core.

To calculate inductance of the toroid, recall first equation 3.18,  $L = \frac{\hat{\psi}}{\hat{I}}$ , which is the definition of inductance. Using Ampere's law,  $\oint_l \hat{H} \cdot d\vec{l} = \hat{I}_{encl}$ , and path 2 from the above toroid in FIG. 7.6, the field within a toroid can be found. Consider FIG. 7.7 and FIG. 7.8 below and the following analysis.

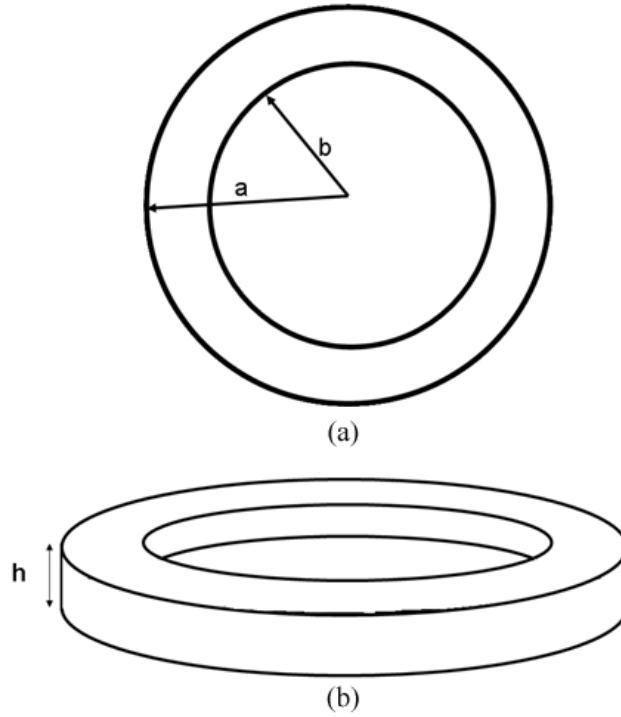


FIG. 7.7. Square cross-section torus with labeled dimensions. (a) top view (b) side view

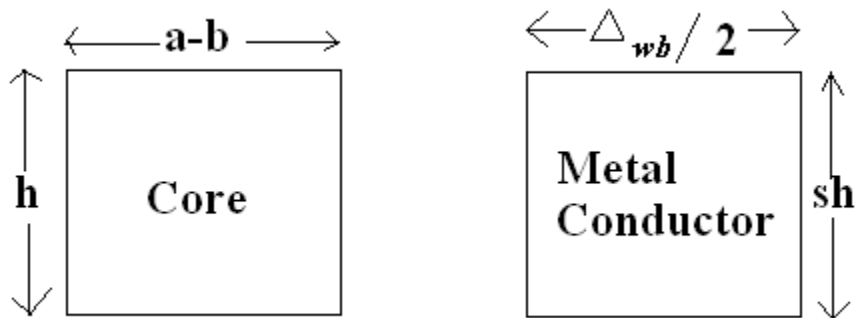


FIG. 7.8. Torus core and metal conductor cross section labeled dimensions.

Ampere's law states the following.

$$\oint_l \hat{H} \cdot d\vec{l} = \hat{I}_{encl} = N\hat{I} \tag{7.1}$$

$$d\vec{l} = r \cdot d\vec{\theta} \tag{7.2}$$

$$\oint_l \hat{H} \cdot d\vec{l} = \int_0^{2\pi} \hat{H}_\theta r \cdot d\vec{\theta} = 2\pi r \hat{H}_\theta = N\hat{I} \Rightarrow \hat{H} \approx \hat{H}_\theta = \frac{N\hat{I}}{2\pi r} \quad 7.3$$

To find the inductance, the flux density is found from the field, and then the total flux through the torus is found from the flux density.

$$\hat{B}_{torus} = \mu(\omega)\hat{H}_{torus} = \frac{\mu(\omega)N\hat{I}}{2\pi r} \quad 7.4$$

Integrating the flux density over the core cross section gives the total flux.

$$\begin{aligned} \phi_{torus} &= \int_{A_{cs}} \hat{B}_{torus} \cdot d\vec{A} = \frac{\mu(\omega)N\hat{I}}{2\pi} \int_0^h dh' \int_b^a \frac{1}{r} d\vec{r} = \frac{\mu(\omega)Nh\hat{I}}{2\pi} \ln\left(\frac{a}{b}\right) \\ \phi_{torus} &= \frac{\mu(\omega)Nh\hat{I}}{2\pi} \ln\left(\frac{a}{b}\right) \end{aligned} \quad 7.5$$

The flux linkages are given by  $N\phi_{torus}$ , and the inductance by  $\frac{N\phi_{torus}}{\hat{I}}$ .

$$\psi_{torus} = N\phi_{torus} = \frac{\mu(\omega)N^2h\hat{I}}{2\pi} \ln\left(\frac{a}{b}\right) \quad 7.6$$

$$L_{torus} = \frac{\psi_{torus}}{\hat{I}} = \frac{\mu(\omega)N^2h}{2\pi} \ln\left(\frac{a}{b}\right) \quad 7.7$$

The important conclusion from equation 7.7 is that to boost the inductance, two things can be done: the number of turns can be increased which would increase the inductance by an N-

squared factor, or the height and/or difference in diameters can be increased, essentially increasing the cross-sectional area. With this in mind, it is in the interests of inductive performance to maximize device turns and height.

### 7.2.1.2 Winding geometry considerations

As mentioned above, besides inductance, winding line resistance is of paramount concern. The conclusion from the inductance calculation was that to boost inductance, the number of turns (and thus, line length) would need to be maximized. This, of course, will increase line resistance and ultimately hurt performance.

Choosing the proper line geometry to minimize resistance is important. In the following sections, transformers with straight rectangular lines as well as transformers with wedge shaped lines will be analyzed, fabricated, and tested. However, regardless of winding shape, the start and end coordinates of the connection lines will be the same. Consider these start and end points as a winding lattice, around which the basis 3D line will be placed.

To find these start and end points, cylindrical coordinates are used. The points will either lie on the inside circle or the outside circle, and the angular separation between adjacent turns will be constant.

With an N-turn transformer, the  $d\theta$  (in cylindrical coordinates) between inner circle points or outer circle points is given by the following equation.

$$d\theta = \frac{2\pi}{N} \quad 7.8$$

The angular distance between an inner circle point and an outer circle point would be half this value, as the outside circle points are at the angular midpoint between inner circle points.

$$d\theta_{io} = \frac{\pi}{N} \quad 7.9$$

The fabrication will occur as sequential layers, so each winding must be defined with respect to a given layer. The winding will not be continuous in a single layer, but rather a set of lines between the inner circle and the outer circle. These lines will not be parallel to the radial direction, but will have a pitch proportional to the number of turns. The bottom layer lines will thus have a complementary pitch to connect the adjacent top layer lines. Considering the top layer primary winding, the features in that layer will be defined by a vector of start and end coordinates, which will be considered to start on the inner circle and end on the outer circle, though the labeling is arbitrary. The top layer primary start and end points are defined by equations 7.10 and 7.11, respectively. The bottom layer primary start and end points are given by equations 7.12 and 7.13, respectively. The bottom layer is considered to start on the outer circle and end on the inner circle.

$$(\theta_k, r_k)_{\text{Primary,Top}}^{\text{Start}} = (k * d\theta, b) \quad 7.10$$

$$(\theta_k, r_k)_{\text{Primary,Top}}^{\text{End}} = (k * d\theta + d\theta_{io}, a) = ((k + \frac{1}{2}) * d\theta, a) \quad 7.11$$

$$(\theta_k, r_k)_{\text{Primary,Bottom}}^{\text{Start}} = ((k + \frac{1}{2}) * d\theta, a) \quad 7.12$$

$$(\theta_k, r_k)_{\text{Primary,Bottom}}^{\text{End}} = ((k + 1) * d\theta, b) \quad 7.13$$

for  $k = [0, N - 1]$ .

Up to this point, only a single winding has been considered. However, the transformer will have two windings. The secondary coordinates will be calculated the same way as above, except offset by  $d\theta_{io}$ . The set of eight equations defining the points for the primary and secondary windings are given below.

$$(\theta_k, r_k)_{Secondary, Top}^{Start} = (k * d\theta + d\theta_{io}, b) = ((k + \frac{1}{2}) * d\theta, b) \quad 7.14$$

$$(\theta_k, r_k)_{Secondary, Top}^{End} = ((k + 1) * d\theta, a) \quad 7.15$$

$$(\theta_k, r_k)_{Secondary, Bottom}^{Start} = ((k + 1) * d\theta, a) \quad 7.16$$

$$(\theta_k, r_k)_{Secondary, Bottom}^{End} = ((k + \frac{3}{2}) * d\theta, b) \quad 7.17$$

for  $k = [0, N - 1]$ .

The coordinate lattice defined above is a set of points lying on the circles defining the toroidal winding. In reality, when the 3D lines are built around the lattice points, they will necessarily extend beyond the lattice points over the toroid core edge. Also, a turn will necessarily be omitted to make winding terminals in the final structure.

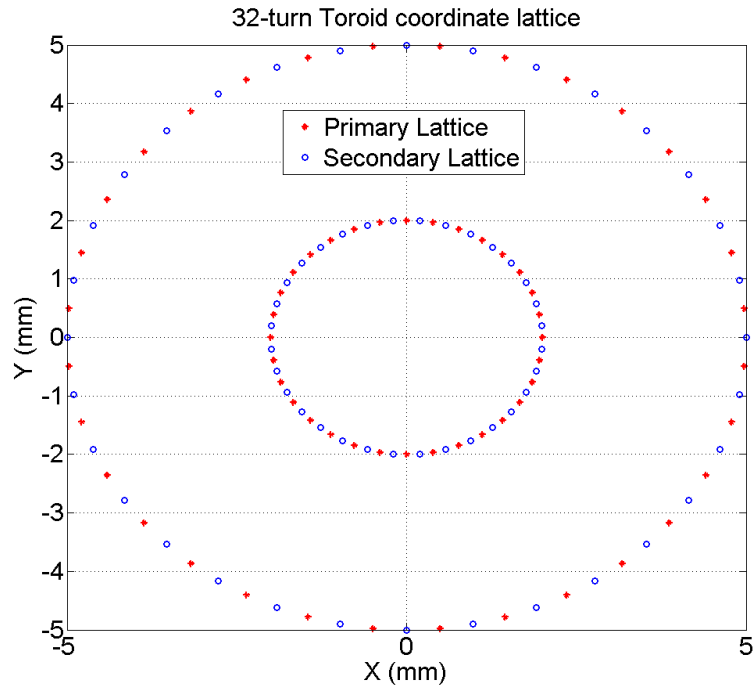


**FIG. 7.9. 32-turn toroid transformer coordinate lattice.**

An important analytical number for future analyses is the winding length. Knowing the coordinate lattice for the turns of the winding, the length can be analytically found. To find the length, the distance between an inner circle point and an outer circle point must be calculated.

Two test point coordinates are given in equations 7.18 and 7.19.

$$P_{inner}^{cylindrical} = (b_r, 0) \tag{7.18}$$

$$P_{outer}^{cylindrical} = (b_r, d\theta_{io}) = (b_r, \frac{\pi}{N}) \tag{7.19}$$

where  $b_r$  and  $a_r$  are the toroid inner and outer radii, respectively. Converting these points to rectangular coordinates gives the following.

$$P_{inner}^{rectangular} = (b_r, 0) \quad 7.20$$

$$P_{outer}^{rectangular} = (a_r \cos(d\theta_{io}), a_r \sin(d\theta_{io})) = \left( a_r \cos\left(\frac{\pi}{N}\right), a_r \sin\left(\frac{\pi}{N}\right) \right) \quad 7.21$$

The distance between the points is given as follows.

$$l_c = \sqrt{\left(a_r \cos\left(\frac{\pi}{N}\right) - b_r\right)^2 + \left(a_r \sin\left(\frac{\pi}{N}\right)\right)^2} = \sqrt{a_r^2 + b_r^2 - 2a_r b_r \cos\left(\frac{\pi}{N}\right)} \quad 7.22$$

### 7.2.1.3 Fabrication limitations

As discussed above, the two principle parameters that will affect the transformer performance are inductance and line resistance. Inductance needs to be maximized while resistance needs to be minimized.

One of the main limitations to silicon sample processing is height. Effective lithographic processing of sample features requires photoresists at least as thick as the features. Photoresists designed for thick depositions are, themselves, quite viscous and difficult to work with.

Taller features also require thicker metal depositions. Metal deposition systems such as RF sputtering or E-beam evaporator deposit at a slow rate (4 – 10 Å /sec). Though thick metal

depositions are possible, they would require much time and attention and multiple deposition runs, making process development and trouble-shooting difficult.

For these reasons, prototype samples need to be carefully considered. Though it is clear that thick devices with large core cross-sections are desirable, as well as thick metals with low resistance, it is not practical to push these limits early in device fabrication. At the early stages, it is more beneficial to produce thinner samples at a faster rate with a higher probability of functionality to develop the processing steps. In the future, after the process has been established and proven to work, the devices can be made thicker.

## **7.2.2. Rectangular line design**

### **7.2.2.1 Design and mask drawing**

The rectangular line winding design is the straight forward choice, and the most similar to an actual wound transformer. The lines are of constant width and bifilar wound as seen in FIG. 7.10 and FIG. 7.11. The mask and model drawing procedure was entirely scripted. MATLAB was used to calculate the necessary start points and rotation angles and compile the drawing procedure into an AutoCad script.

Using the vector of lattice coordinates defined in equations 7.10 through 7.17, the rectangular lines were drawn using a start point, length, area, and angle of rotation in an AutoCad command (See FIG. 7.10 and FIG. 7.11). Square caps and square vias were placed over the top-bottom line overlaps at an angle parallel to the  $\hat{\theta}$  direction.

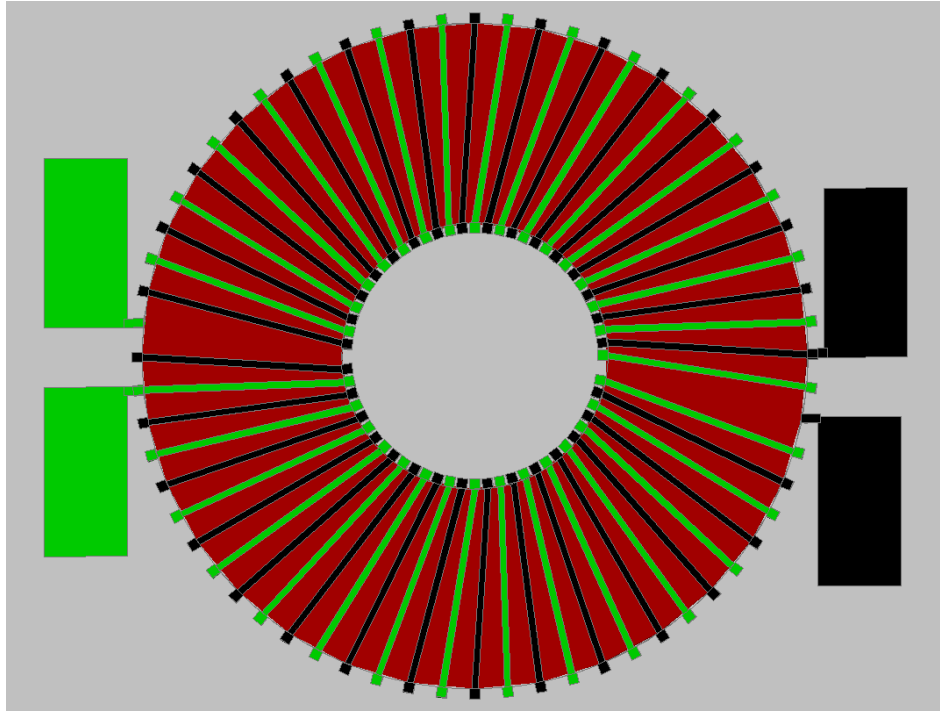


FIG. 7.10. Top view of 3D rendering of bifilar wound toroidal transformer with core structure.

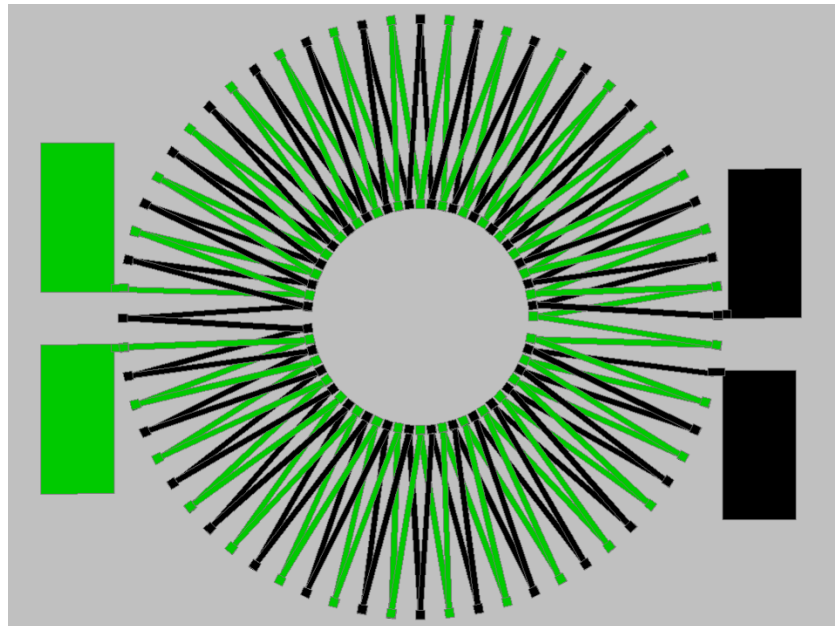
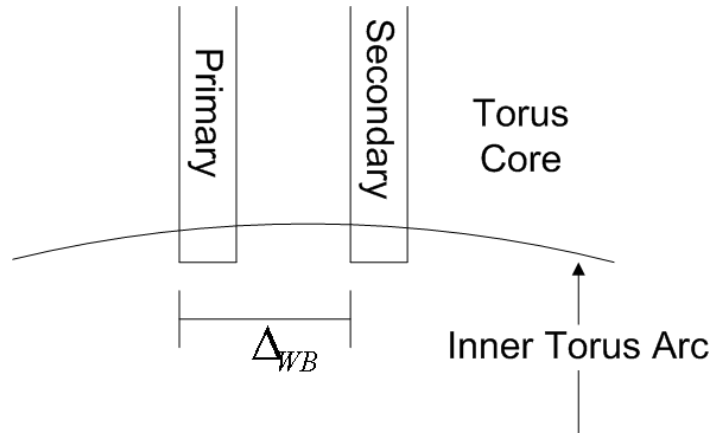


FIG. 7.11. Top view of 3D rendering of bifilar wound toroidal transformer without core structure.

Since the coordinate lattice points do not take up two dimensional width, the choice of line width remains open. The maximum width that the metal lines can be, however, is the distance between lattice points on the inner circle (See FIG. 7.12). This distance is referred to as

the *width budget* ( $\Delta_{wb}$ ). Out of the width budget must come the metal line width and the line gap. The gap must be sufficiently wide to accommodate the limits on contact photolithography and structural stresses during processing. The width budget is determined by the lattice coordinates, which are determined by the number of turns and the inner circle radius. The width budget can be calculated from the number of turns and the inner circle radius directly, as shown in equation 7.23.



**FIG. 7.12. Width Budget of torus geometry.**

$$\Delta_{wb} = \frac{b - \text{Circumference}}{\text{totalTurns}} = \frac{2\pi b}{2N} = \frac{\pi b}{N} \tag{7.23}$$

For this particular design, the metal line width was chosen to be equal to the line gap, as defined in equation 7.24.

$$w_m = w_g = \frac{\Delta_{wb}}{2} = \frac{\pi b}{2N} \tag{7.24}$$

With the coordinate lattice and the metal line width determined, the AutoCad script can be compiled and the masks can be drawn. In the following sections, parameter values such as resistance, capacitance, and inductance for this design are considered.

### 7.2.2.2 Resistance

The following analysis calculates the resistance of an N-turn toroid transformer that has rectangular shaped lines on the top and bottom metal layers.

Consider a rectangular cross section toroid transformer with inner radius  $b$ , outer radius  $a$ , and height  $h_c$ . Wound around the transformer are flat metal lines with square vertical vias that comprise the windings. The geometry of the windings is azimuthally repeating such that the resistance of the entire winding is N times the resistance of a single turn. The general expression for resistance along the length of a metal structure is given by equation 7.25 below.

$$R = \rho \frac{L}{A} \tag{7.25}$$

where  $\rho$  is the metal resistivity,  $L$  is the length of the structure, and  $A$  is the cross-sectional area of the structure. Consider the transformer in FIG. 7.13. Each turn has 4 regions: vertical inside via, top metal line, vertical outside via, and bottom metal line. In the following sections, the resistance of each of the four regions is calculated.

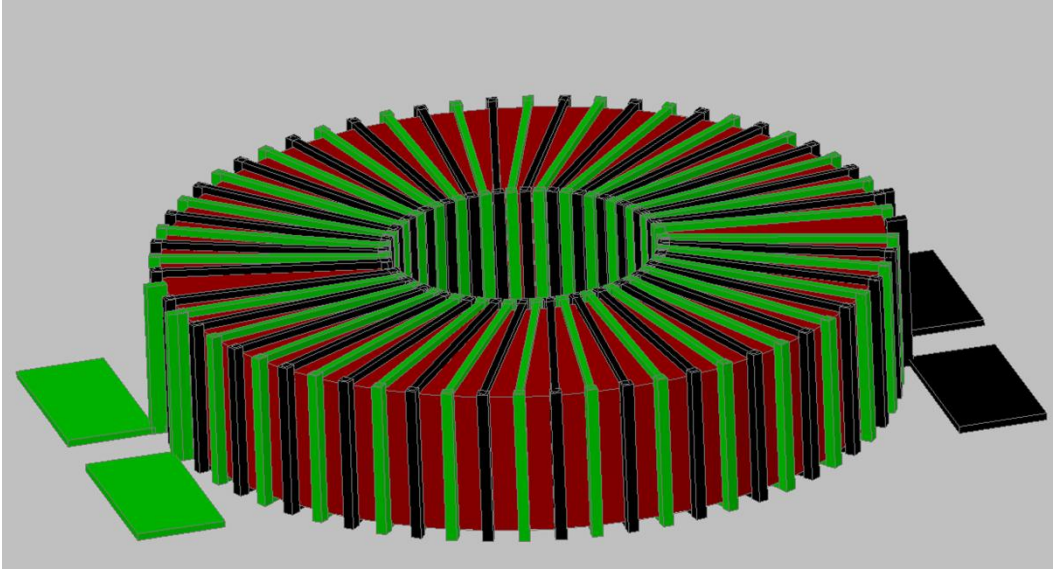


FIG. 7.13. Oblique view of 3D model of rectangular lined 32-turn bifilar-wound transformer.

Before breaking up the resistance into the four regions, there are dimensions common to all regions that can be identified:

$w_m$  : Metal line width

$h_{m,T}$  : Top metal layer thickness

$h_{m,B}$  : Bottom metal layer thickness

$\rho_T$  : Top metal resistivity

$\rho_B$  : Bottom metal resistivity

## 1. Vertical vias

Since the geometry of the via is constant along the length, and the same on the inside and outside radii, the calculation of the resistance is straightforward.

$$R_{vias} = \rho_T \frac{h_c}{(w_i)^2} \quad 7.26$$

## 2. Top and bottom layer metal lines

With the constant cross-sectional geometry of the metal lines, calculating the resistance is straightforward. The length of a line segment was calculated in equation 7.22 above.

$$R_{Top} = \rho_T \frac{l_c}{h_{m,T} w_m} = \frac{\rho_T \sqrt{a_r^2 + b_r^2 - 2a_r b_r \cos\left(\frac{\pi}{N}\right)}}{h_{m,T} w_m} \quad 7.27$$

$$R_{Bottom} = \rho_B \frac{l_c}{h_{m,B} w_m} = \frac{\rho_B \sqrt{a_r^2 + b_r^2 - 2a_r b_r \cos\left(\frac{\pi}{N}\right)}}{h_{m,B} w_m} \quad 7.28$$

## 3. Total resistance

The total resistance will now be the sum of all four segment resistances, times the number of turns,  $N$ .

$$R_{Total} = N(2R_{vias} + R_T + R_B) = N \left( 2\rho_T \frac{h_c}{(w_i)^2} + \rho_T \frac{l_c}{h_{m,T} w_m} + \rho_B \frac{l_c}{h_{m,B} w_m} \right) \quad 7.29$$

### 7.2.2.3 Calculation of total capacitance of straight lined toroid transformer

To evaluate the cross winding capacitance of the bifilar wound toroid transformer, an analysis of coplanar stripline capacitance that employs conformal mapping is taken from the literature [39]. Without presenting details of the derivation, the paper [39] uses conformal mapping to form a parallel-plate geometry from the coplanar geometry. The parallel-plate capacitance equation with the conformed parameters is used to calculate the coplanar capacitance in vacuum and with a substrate. The vacuum and substrate capacitances are then combined to reflect the capacitance of the finite-height substrate geometry. The calculation of twin-line capacitance in the presence of a half-infinite substrate has been considered in textbooks [40], but this paper considers the coplanar line on a finite-height substrate. The toroid transformer is defined by inner radius  $b_r$  and outer radius  $a_r$ . The capacitance calculation is based on cross sectional dimensions as shown in FIG. 7.14.

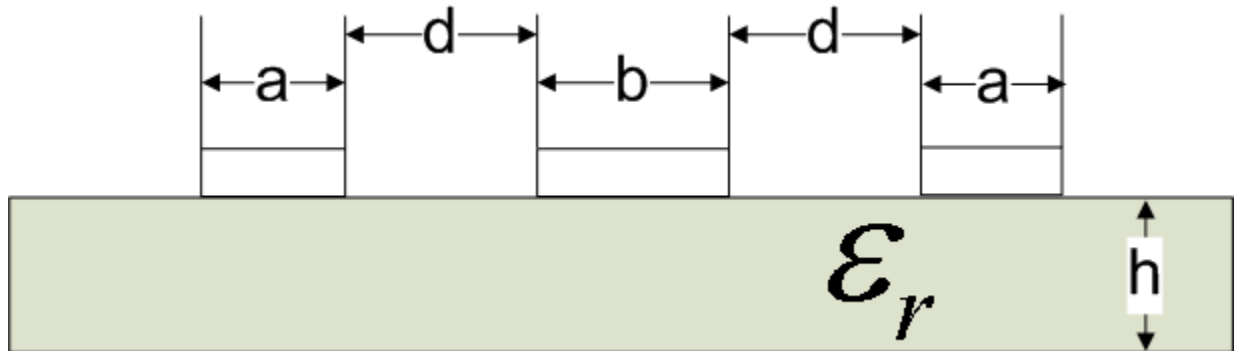


FIG. 7.14. Coplanar stripline cross sectional dimensions.

FIG. 7.14 shows the primary line with width  $b$ , the adjacent secondary lines with width  $a$ , the separation between them as width  $d$ , and the substrate with height  $h$ .

The analysis of the capacitance considers the superposition of two cases: with the metal lines in air ( $C_1$ ) and with the metal lines on a substrate with relative permittivity  $\epsilon_r$  ( $C_2$ ). The expressions for the two capacitances (calculated as per length) are described below. Applying this analysis to the transformer windings requires a calculation of the capacitance of one turn. The total capacitance is  $N$  times the one-turn calculation because of the azimuthally repeating structure.

1.  $\underline{C_1}$

$$C_1 = 4\epsilon_0 \frac{K(k_1')}{K(k_1)} \quad 7.30$$

where  $K$  represents the complete elliptical integral of the first kind and  $k_1$  and  $k_1'$  are as defined below.

$$k_1 = \left(1 + \frac{2a}{2d+b}\right) \sqrt{\frac{(1 + \frac{b}{d})}{(1 + \frac{a}{d} + \frac{b}{d})(1 + \frac{a}{d})}} \quad 7.31$$

$$k_1' = \sqrt{1 - (k_1)^2} \quad 7.32$$

2.  $\underline{C_2}$

$$C_2 = 2\epsilon_0(\epsilon_r - 1) \frac{K(k_2')}{K(k_2)} \quad 7.33$$

$$k_2' = \left( \frac{\sinh\left(\frac{\pi b}{4h}\right)}{\sinh\left(\frac{\pi}{2h}\left(\frac{b}{2} + d\right)\right)} \right) \sqrt{\frac{\sinh^2\left(\frac{\pi}{2h}\left(\frac{b}{2} + d + a\right)\right) - \sinh^2\left(\frac{\pi}{2h}\left(\frac{b}{2} + d\right)\right)}{\sinh^2\left(\frac{\pi}{2h}\left(\frac{b}{2} + d + a\right)\right) - \sinh^2\left(\frac{\pi b}{4h}\right)}} \quad 7.34$$

$$k_2 = \sqrt{1 - (k_2')^2} \quad 7.35$$

The capacitance calculation can be broken into four geometric regions per turn: inside vertical via, outside vertical via, bottom horizontal metal line, and top horizontal metal line. The first case to consider is the case of rectangular shaped horizontal metal lines, where the gap between them changes over the run from the inside radius to the outside radius. The four regions can be considered as capacitances in parallel so that they can be calculated separately and summed to find the total capacitance per turn.

Before breaking up the resistance into the four regions, there are dimensions common to all regions that can be discussed: the metal line width ( $w$ ), the inside gap width ( $w_{g,i}$ ) and the outside gap width ( $w_{g,o}$ ). For the case of constant width metal lines,  $a$  and  $b$  dimensions in FIG. 7.14 are both equal to  $w$ . These values can be related to the radii and turn number values, but ultimately they must be assigned for a specific geometry. Thus, this analysis considers the general case with widths  $w$ ,  $w_{g,i}$  and  $w_{g,o}$ .

## 1. Vertical inside via

Since the geometry of the via is constant along the length, the calculation of the capacitance is straightforward and is given by the sum of **equation** 7.30 and 7.33 times  $h$ , taking  $d$  in FIG. 7.14 as  $w_{g,i}$ .

$$k_{1,i} = \left(1 + \frac{2w}{2w_{g,i} + w}\right) \sqrt{\frac{\left(1 + \frac{w}{w_{g,i}}\right)}{\left(1 + \frac{w}{w_{g,i}} + \frac{w}{w_{g,i}}\right)\left(1 + \frac{w}{w_{g,i}}\right)}} \quad 7.36$$

$$C_{1,i} = 4h\epsilon_0 \frac{K(k_1')}{K(k_1)} \quad 7.37$$

$$k_{2,i}' = \left(\frac{\sinh\left(\frac{\pi w}{4h}\right)}{\sinh\left(\frac{\pi}{2h}\left(\frac{w}{2} + w_{g,i}\right)\right)}\right) \sqrt{\frac{\sinh^2\left(\frac{\pi}{2h}\left(\frac{w}{2} + w_{g,i} + w\right)\right) - \sinh^2\left(\frac{\pi}{2h}\left(\frac{w}{2} + w_{g,i}\right)\right)}{\sinh^2\left(\frac{\pi}{2h}\left(\frac{w}{2} + w_{g,i} + w\right)\right) - \sinh^2\left(\frac{\pi w}{4h}\right)}} \quad 7.38$$

$$C_{2,i} = 2h\epsilon_0(\epsilon_r - 1) \frac{K(k_2')}{K(k_2)} \quad 7.39$$

## 2. Vertical Outside Via

This is identical to the calculation of the vertical inside via, except taking  $d$  in FIG. 7.14 as  $w_{g,o}$ .

$$k_{1,o} = \left(1 + \frac{2w}{2w_{g,o} + w}\right) \sqrt{\frac{\left(1 + \frac{w}{w_{g,o}}\right)}{\left(1 + \frac{w}{w_{g,o}} + \frac{w}{w_{g,o}}\right)\left(1 + \frac{w}{w_{g,o}}\right)}} \quad 7.40$$

$$C_{1,o} = 4h\epsilon_0 \frac{K(k_1')}{K(k_1)} \quad 7.41$$

$$k_{2,o}' = \left(\frac{\sinh\left(\frac{\pi w}{4h}\right)}{\sinh\left(\frac{\pi}{2h}\left(\frac{w}{2} + w_{g,o}\right)\right)}\right) \sqrt{\frac{\sinh^2\left(\frac{\pi}{2h}\left(\frac{w}{2} + w_{g,o} + w\right)\right) - \sinh^2\left(\frac{\pi}{2h}\left(\frac{w}{2} + w_{g,o}\right)\right)}{\sinh^2\left(\frac{\pi}{2h}\left(\frac{w}{2} + w_{g,o} + w\right)\right) - \sinh^2\left(\frac{\pi w}{4h}\right)}} \quad 7.42$$

$$C_{2,o} = 2h\epsilon_0(\epsilon_r - 1) \frac{K(k_2')}{K(k_2)} \quad 7.43$$

### 3. Top metal line

With constant width metal lines, the line gap will change linearly over the run from the inside radius to the outside radius on the top and bottom layers of the transformer windings. The gap has the following linear dependence.

$$w_g(x) = w_{g,i} + \left(\frac{w_{g,o} - w_{g,i}}{l_c}\right)x \quad 7.44$$

where  $x$  is the distance along the line between the inner and outer cylinders, and  $l_c$  is the line length as defined in equation 7.22.

Substituting equation 7.44 into equations 7.31 and 7.34 for  $d$  gives the following  $x$  dependent equations for capacitance.

$$k_{1,T}(x) = \left( 1 + \frac{2w}{2 \left( w_{g,i} + \left( \frac{w_{g,o} - w_{g,i}}{l_c} \right) x \right) + w} \right) * \sqrt[3]{ \frac{ \left( 1 + \frac{w}{ \left( w_{g,i} + \left( \frac{w_{g,o} - w_{g,i}}{l_c} \right) x \right) } \right) }{ \left( 1 + \frac{w}{ \left( w_{g,i} + \left( \frac{w_{g,o} - w_{g,i}}{l_c} \right) x \right) } + \frac{w}{ \left( w_{g,i} + \left( \frac{w_{g,o} - w_{g,i}}{l_c} \right) x \right) } \right) * \left( 1 + \frac{w}{ \left( w_{g,i} + \left( \frac{w_{g,o} - w_{g,i}}{l_c} \right) x \right) } \right) } \right)} \quad 7.45$$

$$k_{2,T}'(x) = \left( \frac{ \sinh \left( \frac{\pi w}{4h} \right) }{ \sinh \left( \frac{\pi}{2h} \left( \frac{w}{2} + \left( w_{g,i} + \left( \frac{w_{g,o} - w_{g,i}}{l_c} \right) x \right) \right) \right) } \right) * \sqrt[3]{ \frac{ \sinh^2 \left( \frac{\pi}{2h} \left( \frac{3w}{2} + \left( w_{g,i} + \left( \frac{w_{g,o} - w_{g,i}}{l_c} \right) x \right) \right) \right) - \sinh^2 \left( \frac{\pi}{2h} \left( \frac{w}{2} + \left( w_{g,i} + \left( \frac{w_{g,o} - w_{g,i}}{l_c} \right) x \right) \right) \right) }{ \sinh^2 \left( \frac{\pi}{2h} \left( \frac{3w}{2} + \left( w_{g,i} + \left( \frac{w_{g,o} - w_{g,i}}{l_c} \right) x \right) \right) \right) - \sinh^2 \left( \frac{\pi w}{4h} \right) } \right)} \quad 7.46$$

To find the capacitance of the top metal line over the entire run, the capacitance expression (equations 7.30 and 7.33) must be integrated with respect to  $x$  from 0 to  $l_c$ . Given the complexity of the equations involving both hyperbolic trigonometry as well as elliptical integrals, these integrals can be evaluated numerically using MATLAB.

$$C_{1,T} = 4\varepsilon_0 \int_0^{l_c} \left( \frac{K(\sqrt{1-(k_{1,T}(x))^2})}{K(k_{1,T}(x))} \right) dx \quad 7.47$$

$$C_{2,T} = 4\varepsilon_0 \int_0^{l_c} \left( \frac{K(k'_{2,T}(x))}{K(\sqrt{1-(k'_{2,T}(x))^2})} \right) dx \quad 7.48$$

#### 4. Bottom Metal Line

The capacitance of the horizontal bottom metal line run will be identical to the capacitance of the top metal horizontal line run. This calculation does not need to be repeated.

$$C_{1,B} = 4\varepsilon_0 \int_0^{l_c} \left( \frac{K(\sqrt{1-(k_{1,B}(x))^2})}{K(k_{1,B}(x))} \right) dx = 4\varepsilon_0 \int_0^{l_c} \left( \frac{K(\sqrt{1-(k_{1,T}(x))^2})}{K(k_{1,T}(x))} \right) dx \quad 7.49$$

$$C_{2,B} = 4\varepsilon_0 \int_0^{l_c} \left( \frac{K(k'_{2,B}(x))}{K(\sqrt{1-(k'_{2,B}(x))^2})} \right) dx = 4\varepsilon_0 \int_0^{l_c} \left( \frac{K(k'_{2,T}(x))}{K(\sqrt{1-(k'_{2,T}(x))^2})} \right) dx \quad 7.50$$

## 5. Total Capacitance

The total capacitance for a single turn is given by the following equation.

$$\begin{aligned} C_T^{1\text{-turn}} &= (C_{1,i} + C_{2,i}) + (C_{1,o} + C_{2,o}) + (C_{1,T} + C_{2,T}) + (C_{1,B} + C_{2,B}) \\ &= (C_{1,i} + C_{2,i}) + (C_{1,o} + C_{2,o}) + 2(C_{1,T} + C_{2,T}) \end{aligned} \quad 7.51$$

The total capacitance between the primary and secondary windings is given by  $N$  times the 1-turn capacitance.

$$C_T^{Winding} = N * ((C_{1,i} + C_{2,i}) + (C_{1,o} + C_{2,o}) + 2(C_{1,T} + C_{2,T})) \quad 7.52$$

### 7.2.2.4 Inductance

Recall the theoretical inductance equation 7.7.

$$L_{torus} = \frac{\psi_{torus}}{\hat{I}} = \frac{\mu(\omega)N^2h}{2\pi} \ln\left(\frac{a}{b}\right)$$

The inductance equation does not depend on line geometry, only core geometry and turn number. Thus, the expression will be the same for all transformers.

## **7.2.2.5 Fabrication**

### **7.2.2.5.1 Initial process outline and problems**

It was known from the beginning of the process design that a large core cross-section was needed for higher inductance. To this end, a thick photoresist material (Su-8) was going to be used for the core. Su-8 is a negative photoresist made by MicroChem, and is capable of being made quite thick (40 to 100 microns and above). However, Su-8 comes in multiple viscosities, all the way down to thin Su-8 of only a micron or less. The initial process was as follows:

- 1) Deposit 500 nm of aluminum by E-beam evaporator.
- 2) Apply bottom metal pattern via contact lithography and Fuji 906-10 positive photoresist and wet etch with aluminum etchant.
- 3) Deposit and pattern 40 microns of Su-8 as donut shapes over bottom metal layer lines
- 4) Deposit 1 micron of aluminum with E-beam evaporator and planetary sample rotation.
- 5) Apply top metal pattern via contact lithography and Fuji 908-35 positive photoresist and wet etch with aluminum etchant.

Difficulties working with the thicker Su-8 and problems patterning the thick Su-8 with thinner photoresists forced the process back to a thinner Su-8 photoresist. The process was continually modified over the course of many months. The bottom aluminum layer was switched with gold and lift-off was used rather than etching. This assured an oxide free bottom metal layer to which the top metal could connect.

Though this process was explored for many months, a continuous low-resistance winding was never achieved. Scanning electron microscope (SEM) images showed some cracking at the

sidewall connections. It was concluded that the thinnest part of the metal line connections occurred over the edge of the core. At this edge, aluminum etchant would get in between the Su-8 and the aluminum, trapping the etchant which would eventually dissolve the sidewall connection. Though this did not occur on every connection, it was determined empirically that it occurred for about 20% - 25% of the interconnections. With 64 interconnections making up the lowest density winding, the chance for an entire continuous winding was about  $(0.8)^{64} = 6.2771e-007$ .

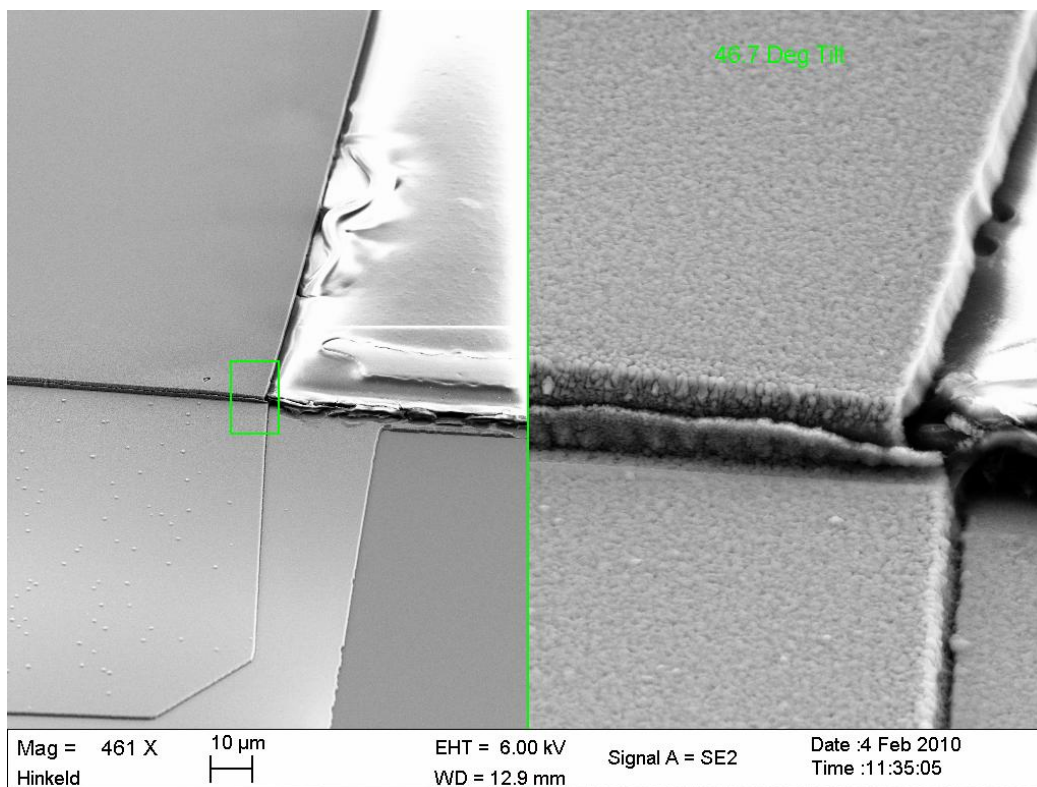


**FIG. 7.15. Image of aluminum sidewall cracking over Su-8.**

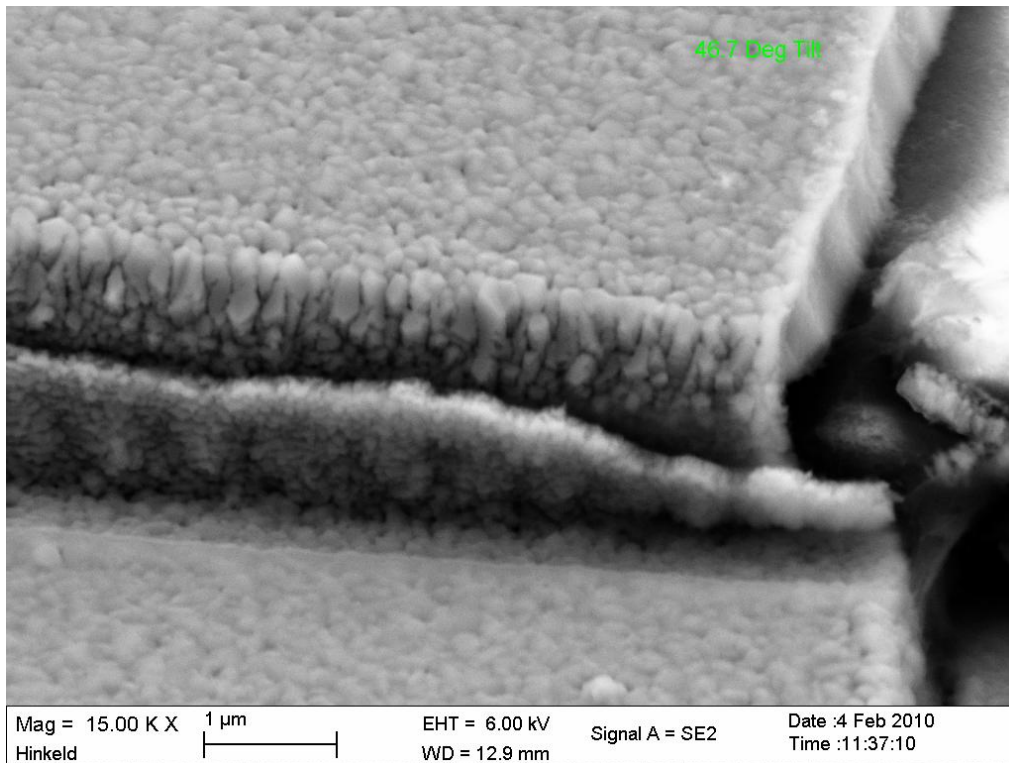


**FIG. 7.16. Enhanced image of aluminum sidewall cracking over Su-8.**

#### **7.2.2.5.2 Successful Process**

To avoid the problem of trapping etchant in unwanted places, The process could be revised to use entirely lift-off patterning. However, lift-off patterning requires the entire sample to be bathed in strong resist removers for a long period of time. Though the intention was to dissolve the top metal pattern lift-off resist, the Su-8 would inevitably deform or dissolve in the process.

To get away from metal etching to lift-off, another non-photoresist dielectric would have to be used. Thus, silicon dioxide was selected as the new core material and the process was once again changed to incorporate via holes rather than an air-encompassed dielectric core-structure. The new process uses a new thick photoresist to improve lift-offs: NR-71 3000PY made by

Futterex (~3 microns thick). Also, the lift-off solvent becomes RR-41 made by Futterex. The new process is as follows.

- 1) Spin Futterex NR-71 3000 PY negative photoresist and expose/develop with bottom metal layer pattern by contact photolithography.
- 2) Deposit 200 Å Ti / 2000Å Au / 100Å Ti by E-beam evaporator.
- 3) Lift-off in hot RR-41 for ~45 minutes
- 4) Deposit 500nm of SiO<sub>2</sub> by ICP-CVD.
- 5) Spin Fuji 908-35 positive photoresist and expose/develop with via mask pattern.
- 6) Reactive ion etch (RIE) vias in SiO<sub>2</sub>. RIE vias in top Ti layer.
- 7) Remove remnant 908-35 and descum. Spin/expose/develop NR-71 3000PY with top metal layer pattern.
- 8) Deposit 200Å Ti/ 750nm Au by E-beam evaporator
- 9) Lift-off top metal pattern in hot RR-41 for ~45 mintues.

The above process is abridged to some degree. Those familiar with contact lithography know that every step listed above incorporates multiple bakes, RIE descums, or acetone air-brushings. Note, in step 6 the top Ti layer is etched away. This is to solve a problem found with both Al and Ti of native oxide formation increasing the resistance of the windings. The Ti must be there for the SiO<sub>2</sub> to adhere to the metal lines, but the Ti must be etched away where via contact will be made to the top metal lines.

With this process, 32 and 64-turn continuous winding transformers were fabricated. In the next section, the nominal device parameters will be summarized and some theoretical values will be calculated.

### 7.2.2.5.3 Final device parameters and theoretical values

**Table 7.1. Fabricated rectangular line transformer physical dimensions.**

$N$	$a_r$ (mm)	$b_r$ (mm)	$w_m$ ( $\mu\text{m}$ )	$h_{m,t}$ (nm)	$h_{m,b}$ (nm)	$h_c$ (nm)
32	5	2	98.2	750	200	500
64	5	2	49.1	750	200	500
128	5	2	24.5	750	200	500
256	5	2	12.3	750	200	500

Samples with 32, 64, 128, and 256-turn transformers were completed (See FIG. 7.17 and FIG. 7.18). However, the only devices with both windings electrically continuous were the 32 and 64-turn transformers. Table 7.1 summarizes the final physical parameters of the fabricated transformers. Using the above analysis of resistance, inductance, and capacitance, those values can be calculated from the physical parameters and are given in Table 7.2 below. In the next section, high frequency and DC measurements will be discussed and results will be presented and compared with the theoretical values.

**Table 7.2. Fabricated transformer theoretically predicted resistance, inductance, and cross-winding capacitance.**

$N$	$R$ ( $\Omega$ ) theory	$L$ (pH) theory	$C$ (pF) theory
32	137.87	93.8	35.0
64	549.3	375.3	70.0
128	2194.9	1501.3	140.0
256	8777.5	6005.0	280.0

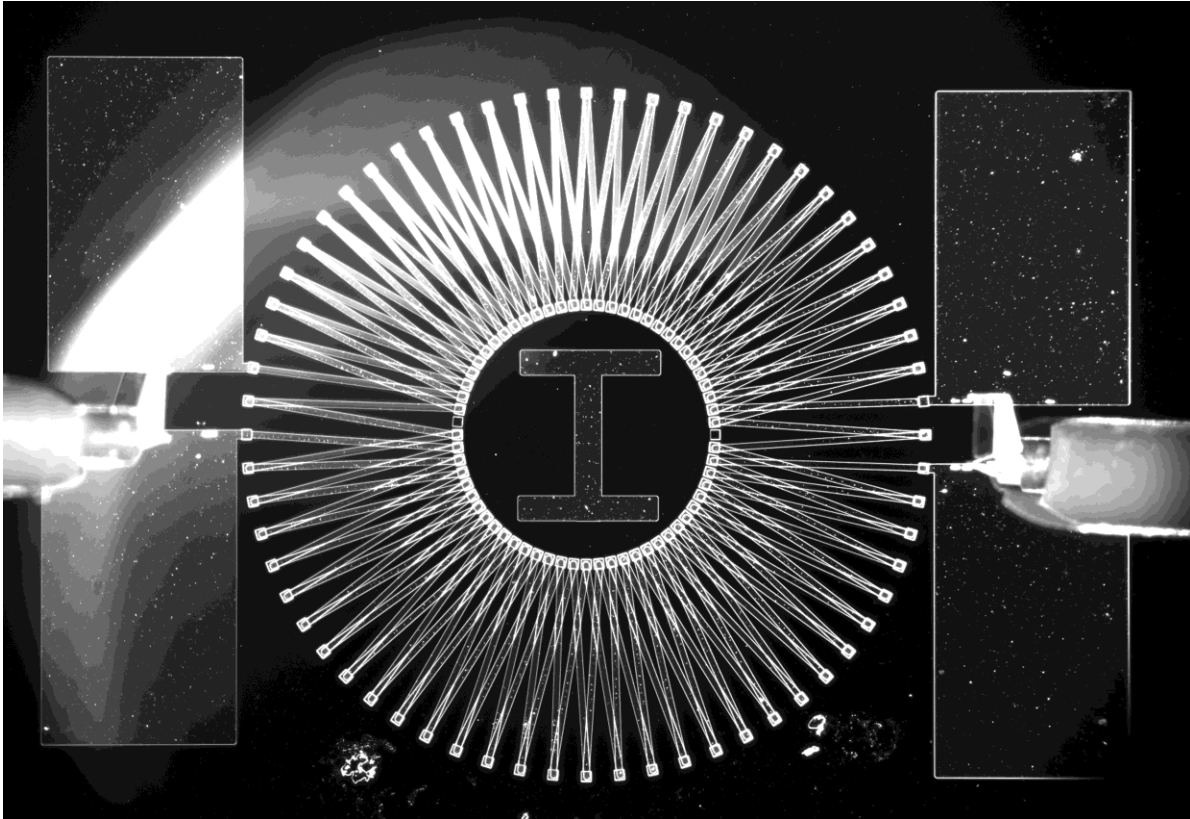


**FIG. 7.17.** Probe station micrograph of a 32-turn fabricated silicon dioxide core transformer with probe contacts.

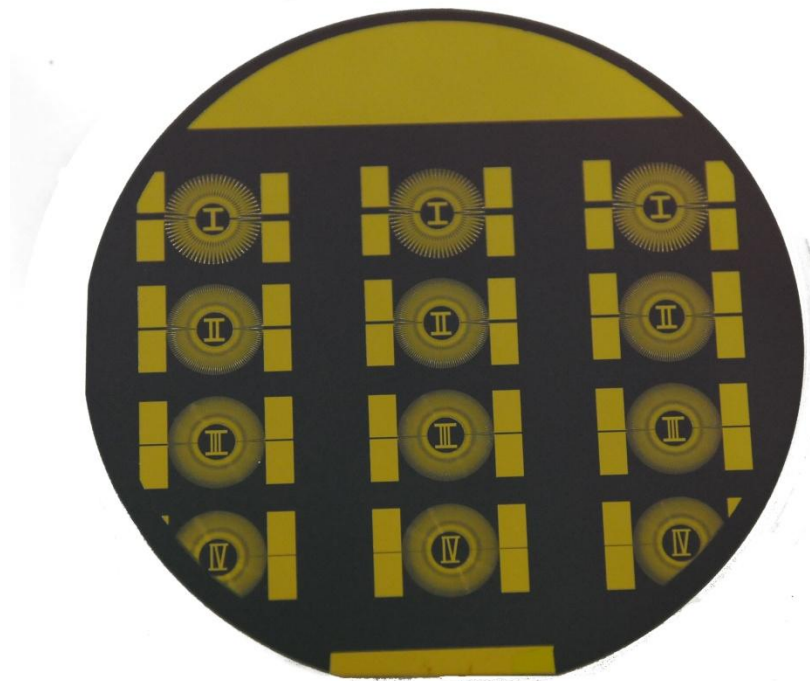


**FIG. 7.18.** 3-inch silicon wafer with 32, 64, 128, and 256-turn rectangular line devices.

### 7.2.2.6 Measurement scheme and results

To measure the performance of the fabricated transformers, a Cascade Microtech M150 RF microprobe station was used (See FIG. 7.19 and FIG. 7.20). The probe station uses a vacuum chuck to fix the sample in place, while RF probe tips can be positioned over the sample contact pads using micrometers. A binocular microscope with a video camera is positioned over the stage to aid in planting the probes on the sample. The RF probes couple through SMA connectors to either a VNA or precision DC multimeter.

When using the probe station with the VNA, Cascade Microtech supplies an impedance standard substrate (ISS) that allows manual analyzer calibration down to the tips of the probes. Both the DC measurements and VNA measurements are discussed in the following sections.

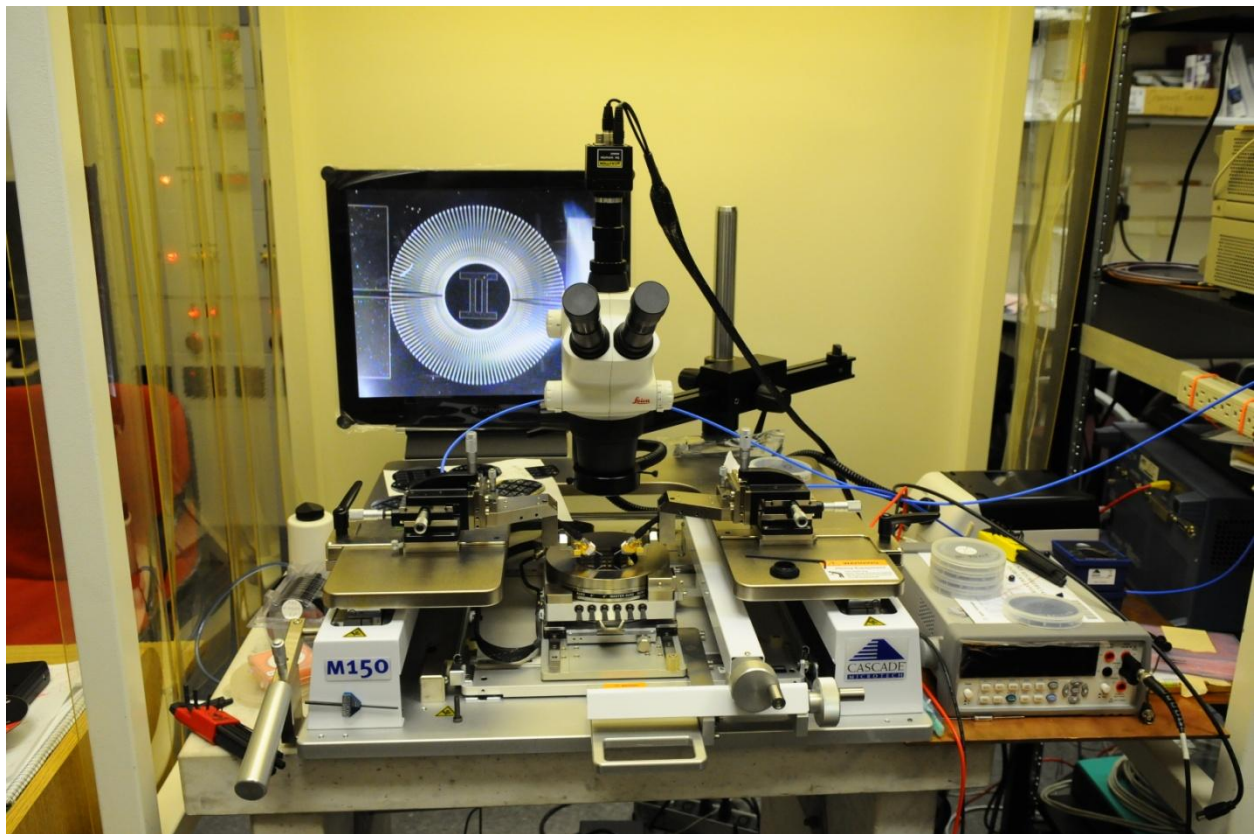


**FIG. 7.19. Cascade Microtech M150 probe station used to characterize fabricated transformers.**

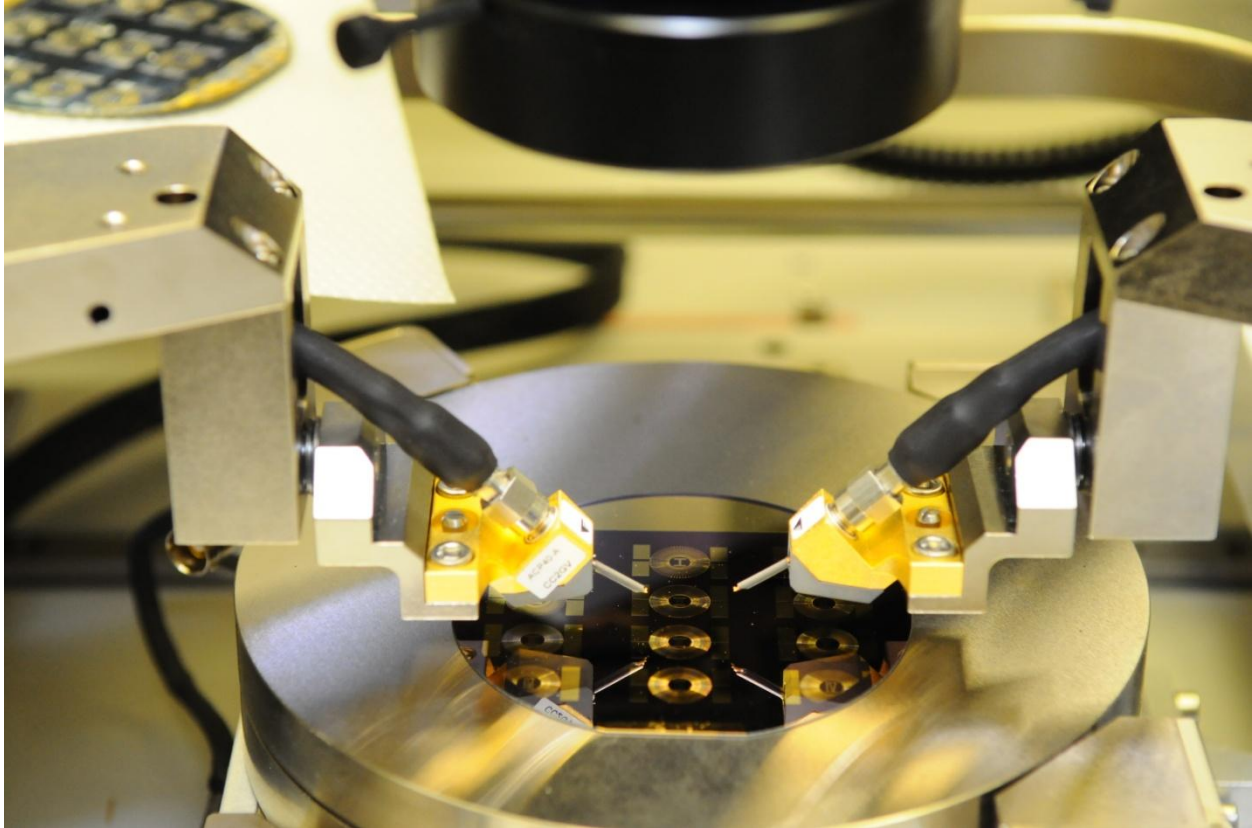


**FIG. 7.20. Close-up photo of probe station RF probes over sample.**

**Table 7.3. DC resistance measurements of fabricated transformers.**

Sample	N	Device	Primary DC Res ( $\Omega$ )	Secondary DC Res ( $\Omega$ )
S22	32	H1B	306.94	307.23
S22	32	H1C	309.7	309.1
S22	64	H2B	1279.3	1279.8
S22	64	H2C	1252.5	1251.6
HX24	32	H1A	258.25	258.48
HX24	32	H1B	259.7	259.66
HX24	32	H1C	264.07	263.7
HX24	64	H2A	1068	1067.7
HX24	64	H2B	1094.7	1094.4
HX24	64	H2C	1079.4	1079.1

### 7.2.2.6.1 DC resistance measurements

By probing the sample on the probe station while the probes were connected to a precision multimeter, precise resistances can be extracted. The extracted resistances are shown in Table 7.3. The data in the table shows that devices with the same number of turns on the same sample have consistent resistances, but the resistances change significantly from one sample to another. This suggests that subtle process variations, such as changes in metal thicknesses or the quality of layer interconnects, can significantly change the device performance.

Comparing the measured resistance of Table 7.3 to the theoretically predicted resistances of Table 7.2 reveals that the actual resistances are much higher than what was predicted. This is not a surprising fact for the following reason. The theoretical predictions use a resistivity value of bulk material in the calculations. However, metal grains of evaporated thin films are quite different from metal grains of bulk metal, resulting in a different resistivity [41].

Going back to the resistance formula shows how the resistance should change with changing  $N$ . Consider the example of the resistance of two different turn number transformers shown below.

$$R_0 = \rho \frac{L_0}{A_0} = \rho \frac{L_0}{w_0 h_{m,0}} \quad 7.53$$

$$R_1 = \rho \frac{L_1}{A_1} = \rho \frac{\left(\frac{N_1}{N_0}\right) L_0}{w_1 h_{m,0}} = \rho \frac{\left(\frac{N_1}{N_0}\right) L_0}{\left(\frac{\pi b}{N_1}\right) h_{m,0}} = \rho \frac{\left(\frac{N_1}{N_0}\right) L_0}{\left(\frac{N_0}{N_1}\right) \left(\frac{\pi b}{N_0}\right) h_{m,0}} = \rho \frac{\left(\frac{N_1}{N_0}\right) L_0}{\left(\frac{N_0}{N_1}\right) w_0 h_{m,0}} = \left(\frac{N_1}{N_0}\right)^2 R_0 \quad 7.54$$

$$\frac{R_1}{R_0} = \left(\frac{N_1}{N_0}\right)^2 \quad 7.55$$

The resistances in Table 7.3 exhibit approximately the dependence of equation 7.55. This supports the reasoning that the measured resistance values differ from the theoretical values by a resistivity factor. Small deviations in the measured resistance behavior from equation 7.55 could be explained by increased layer interconnect resistance that was not properly accounted for.

#### **7.2.2.6.2 VNA measurements**

After calibrating the VNA using the ISS, another calibration procedure must be performed to more accurately characterize the behavior of the transformer windings. FIG. 7.17 shows a picture of a completed device with large contact pads on which the probes connect. However, these contact pads are not truly part of the device, but will contribute shunt impedance to the measurement. To de-embed the windings from the contact pads, the following procedure is used.

- 1) A test sample is made that omits the bottom metal layer such that the contact pads are disconnected and floating over silicon dioxide. Test pad structures were also placed on second generation mask designs.
- 2) A one-port measurement is performed on each pair of contact pads to extract the shunt impedance.
- 3) Using the measured pad impedance, a two-port ABCD network is formed to represent the shunt impedance in a cascaded system as shown in equation 7.56 (See also FIG. 7.21).
- 4) By multiplying the measured ABCD matrix (front and back) by the inverse of the pad impedances (equation 7.57, 7.58, 7.59), the resulting ABCD matrix will represent only the performance of the winding structure.

$$\begin{bmatrix} A & B \\ C & D \end{bmatrix}_{Shunt} = \begin{bmatrix} 1 & 0 \\ \frac{1}{Z_{Pad1}} & 1 \end{bmatrix} \quad 7.56$$

$$\begin{bmatrix} A & B \\ C & D \end{bmatrix}_{Shunt}^{-1} = \begin{bmatrix} 1 & 0 \\ -\frac{1}{Z_{Pad1}} & 1 \end{bmatrix} \quad 7.57$$

$$\begin{bmatrix} A & B \\ C & D \end{bmatrix}_{Measured} = \begin{bmatrix} A & B \\ C & D \end{bmatrix}_{Pad1} \begin{bmatrix} A & B \\ C & D \end{bmatrix}_{Dut} \begin{bmatrix} A & B \\ C & D \end{bmatrix}_{Pad2} \quad 7.58$$

$$\begin{bmatrix} A & B \\ C & D \end{bmatrix}_{Pad1}^{-1} \begin{bmatrix} A & B \\ C & D \end{bmatrix}_{Measured} \begin{bmatrix} A & B \\ C & D \end{bmatrix}_{Pad2}^{-1} = \quad 7.59$$

$$\begin{bmatrix} A & B \\ C & D \end{bmatrix}_{Pad1}^{-1} \begin{bmatrix} A & B \\ C & D \end{bmatrix}_{Pad1} \begin{bmatrix} A & B \\ C & D \end{bmatrix}_{Dut} \begin{bmatrix} A & B \\ C & D \end{bmatrix}_{Pad2} \begin{bmatrix} A & B \\ C & D \end{bmatrix}_{Pad2}^{-1} = \begin{bmatrix} A & B \\ C & D \end{bmatrix}_{Dut}$$

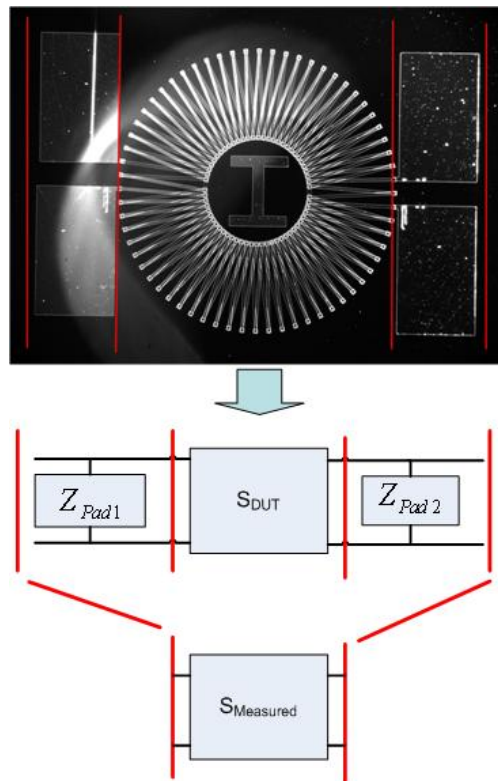


**FIG. 7.21. Decomposition of the measured scattering parameters into pad impedance and winding performance.**

After de-embedding, the transformer transfer relation results are given in FIG. 7.22 and FIG. 7.23 below. As the transfer relations show, the unloaded 32-turn transformer has a distinguishable flat-band, but also a broad resonance at about 40MHz. By loading the transformer with  $100\Omega$ , the resonance is suppressed and the transformer has a flat-band from about 10 MHz to 40MHz.

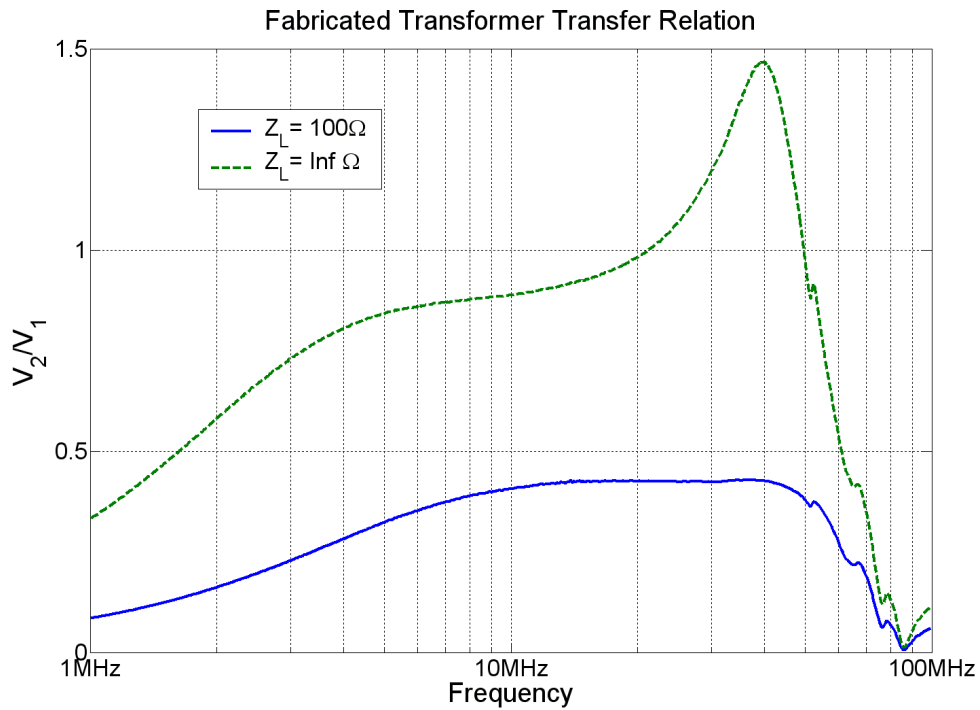


**FIG. 7.22. 32-turn fabricated transformer transfer relation for various loads.**

The measured transfer relation of the 64-turn fabricated transformer is shown in FIG. 7.23. The unloaded device has a flatband from about 5 MHz to 20 MHz, but is contaminated by a large, broad resonance. When loaded with  $100\Omega$ , it is clear that the resonance is suppressed, but at the cost of a discernable flatband.

## Fabricated Transformer Transfer Relation

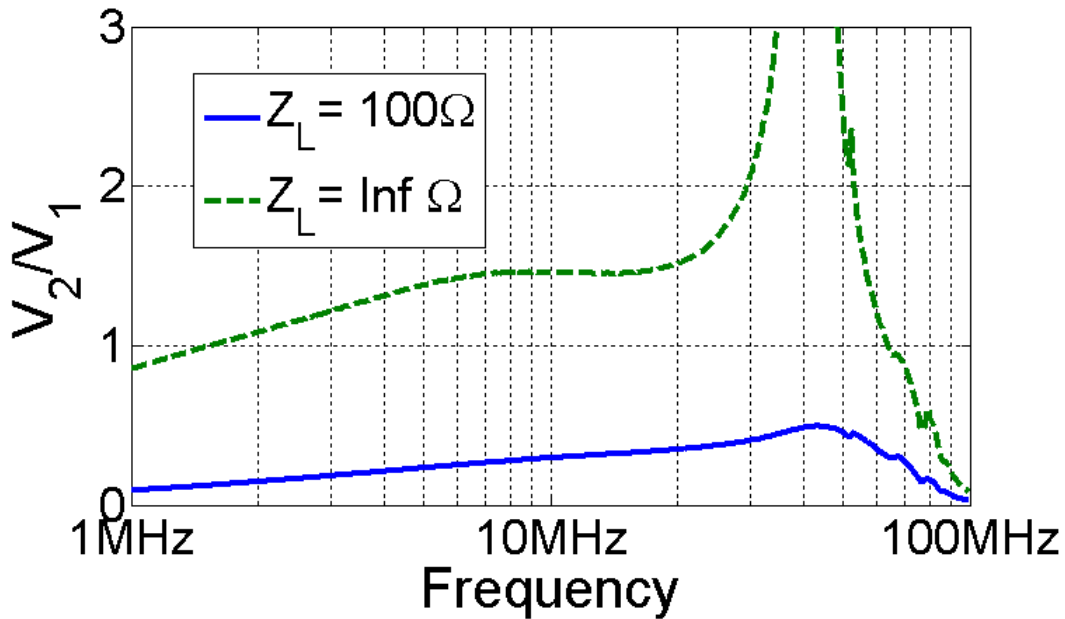


FIG. 7.23. 64-turn fabricated transformer transfer relation for various loads.

Attempts at analyzing the measurement results in the same manner as the commercial Ethernet transformers to extract parameters showed no frequency regions where an element could be said to dominate. Thus, it was not possible to extract model parameters from these devices with any degree of confidence.

In summary, the transfer relation results show that the current best performance is found for a 32-turn transformer loaded with  $100\Omega$ . The table below summarizes the performance metrics of the fabricated transformers along with the commercial Ethernet transformers.

**Table 7.4. Summary of performance metrics for fabricated and commercial Ethernet transformers.**

Sample	N	Primary DC Res ( $\Omega$ )	Sec DC Res ( $\Omega$ )	Vol ( $\text{mm}^3$ )	Frequency Range (MHz)
1	32	307	307	0.0928	10-40
1	32	310	309	0.0928	10-40
1	64	1279	1280	0.0928	5-20
1	64	1253	1252	0.0928	5-20
2	32	258	258	0.0928	10-40
2	32	260	260	0.0928	10-40
2	32	264	264	0.0928	10-40
2	64	1068	1068	0.0928	5-20
2	64	1095	1094	0.0928	5-20
2	64	1079	1079	0.0928	5-20
Commercial 1GBase-T	13	0.65	0.65	64	0.001-150
Commercial 10GBase-T	6	0.30	0.30	68	0.001-480

### 7.2.3. Wedge shaped line design

The wedge line scheme for reducing resistance in fabricated thin-film transformers has been explored before, but for the purpose of power transformation at only one frequency [42]. It is the purpose of these fabricated transformers to be flat-banded over a wide bandwidth, and to be so without magnetic core materials. Following is a discussion of the design, fabrication, and testing of wedge-lined transformers.

#### 7.2.3.1 Design and mask drawing

The use of wedge shaped lines has the advantage of boosting cross-winding capacitance and reducing resistance. Designing and drawing the masks begins with the same coordinate lattice as for the rectangular lines. However, rather than compiling into an AutoCAD script that draws rectangles, the new script draws closed polylines of a user defined number of points. Consider a

lattice coordinate point  $(a, \theta_i)$  on the outer circle and the lattice coordinate point  $(b, \theta_i)$  on the inner circle. The coordinates of the polyline can be defined by taking an equal angle to either side of the lattice coordinate. The points on the outer and inner circle are defined by equations 7.60 through 7.65.

$$(a, \theta_{k, \text{polyline}}) = (a, \theta_k \pm \frac{d\theta_{w,o}}{2}) \quad 7.60$$

$$(b, \theta_{k, \text{polyline}}) = (b, \theta_k \pm \frac{d\theta_{w,i}}{2}) \quad 7.61$$

$$d\theta_{w,o} = \frac{\pi}{N} - d\theta_{g,o} \quad 7.62$$

$$d\theta_{w,i} = \frac{\pi}{N} - d\theta_{g,i} \quad 7.63$$

$$d\theta_{g,o} = \frac{w_g}{a} \quad 7.64$$

$$d\theta_{g,i} = \frac{w_g}{b} \quad 7.65$$

where  $w_g$  is the desired gap arc length between adjacent lines.

By extending the wedge lines in the radial direction, top and bottom layer overlap is achieved over which vias can be placed (See FIG. 7.24 and FIG. 7.25). Given the superior performance of the low resistance rectangular-line 32-turn transformer, 8 and 16-turn wedge masks were made and devices were fabricated. In the following sections, as was done in the previous section, the theoretical resistance, cross-winding capacitance, and inductance are analyzed.

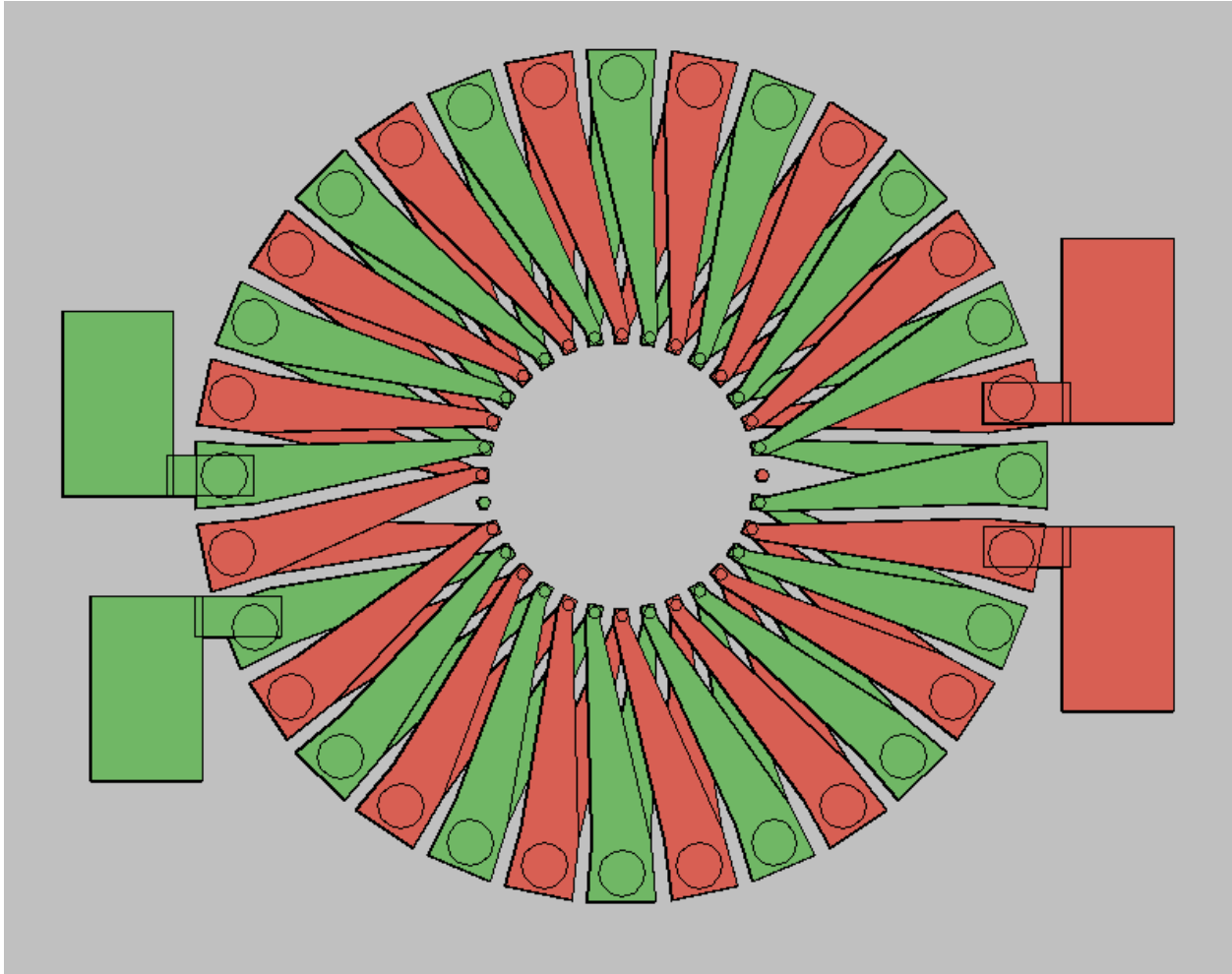


**FIG. 7.24. Top view: 3D model of 16-turn wedge shaped transformer**

### 7.2.3.2 Wedge line resistance calculation

The following analysis calculates the resistance of an  $N$ -turn toroid transformer that has wedge shaped lines on the top and bottom metal layers.

Consider a rectangular cross section toroid transformer with inner radius  $b$ , outer radius  $a$ , and height  $h_c$ . Wound around the transformer are flat metal lines with vertical vias that comprise the windings. The geometry of the windings is azimuthally repeating such that the

resistance of the entire winding is  $N$  times the resistance of a single turn. The general expression for resistance along the length of a metal structure is given by equation 7.66 below.

$$R = \rho \frac{L}{A} \quad 7.66$$

Where  $\rho$  is the metal resistivity,  $L$  is the length of the structure, and  $A$  is the cross-sectional area of the structure. Consider the transformer in FIG. 7.25. Each turn has 4 regions: vertical inside via, top metal line, vertical outside via, and bottom metal line. In the following sections, the resistance of each of the four regions is calculated.

Before breaking up the resistance into the four regions, there are dimensions common to all regions that can be identified: the inside radius metal line width ( $w_i$ ) and the outside radius metal line width ( $w_o$ ). These values can be related to the radii and turn number values, but ultimately they must be assigned for a specific geometry. Thus, this analysis considers the general case with line widths  $w_i$  and  $w_o$ . Also, there is the possibility of using different metals with different thickness in the top and bottom layers. Thus, we introduce multiple variables as follows:

$h_{m,T}$  : Top metal thickness

$h_{m,B}$  : Bottom metal thickness

$\rho_T$  : Top metal resistivity

$\rho_B$  : Bottom metal resistivity

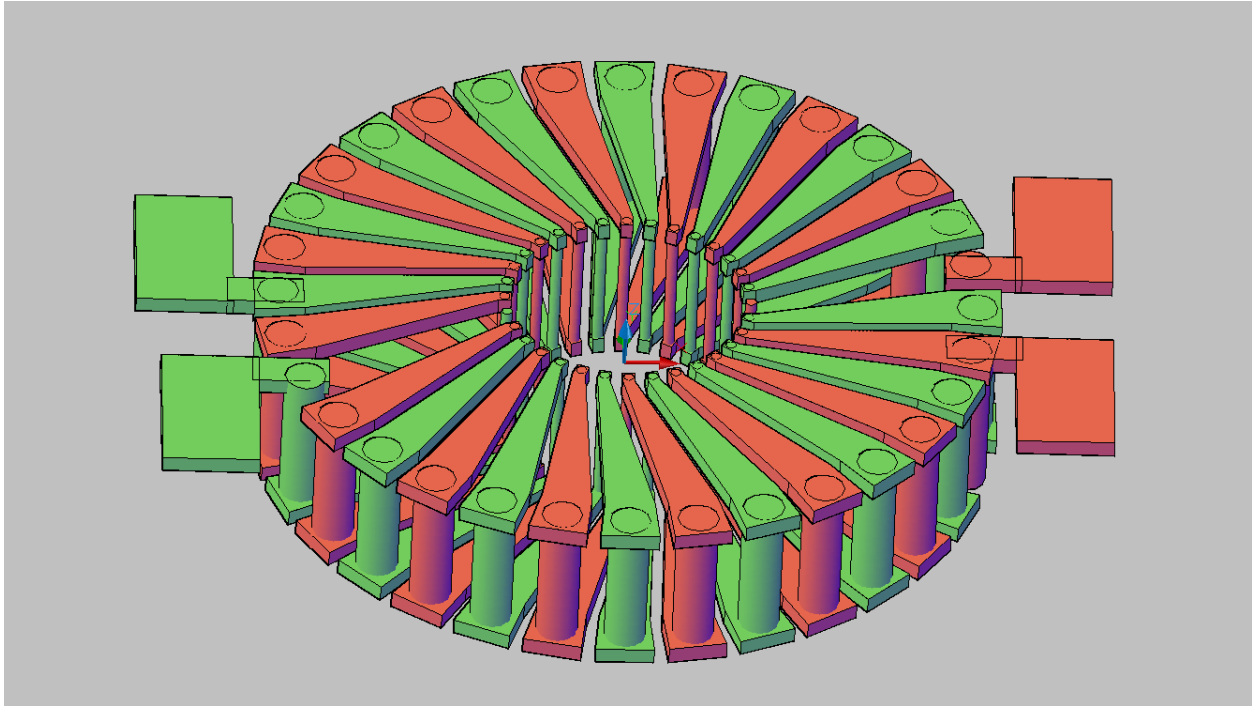


FIG. 7.25. 3D model of toroid transformer with wedge shaped lines.

### 1. Vertical inside via

Since the geometry of the via is constant along the length, the calculation of the resistance is straightforward. However, the geometry of the via may either be a square with the edge equal to the line width, or it can be a circle with diameter equal to the line width. Both cases are calculated below.

$$\text{(Square Vias)} \quad R_i = \rho_T \frac{h_c}{(w_i)^2} \quad 7.67$$

$$\text{(Circular Vias)} \quad R_i = \rho_T \frac{4h_c}{\pi(w_i)^2} \quad 7.68$$

## 2. Vertical Outside Via

This is identical to the calculation of the vertical inside via, except with a different via dimension.

$$\text{(Square Vias)} \quad R_o = \rho_T \frac{h_c}{(w_o)^2} \quad 7.69$$

$$\text{(Circular Vias)} \quad R_o = \rho_T \frac{4h_c}{\pi(w_o)^2} \quad 7.70$$

## 3. Top metal line

This segment is far more interesting, because the dimensions are not constant with length. For this analysis, there will be a small approximation. The wedges will be assumed to be vertically symmetric along the length. Consider FIG. 7.26. The line will be analyzed as it is shown in FIG. 7.26b. What is apparent from FIG. 7.26b is that if the positive  $x$  direction is considered the length, then the line width is not constant. With the line width depending on the  $x$  position, the area and resistance will also depend on  $x$ .

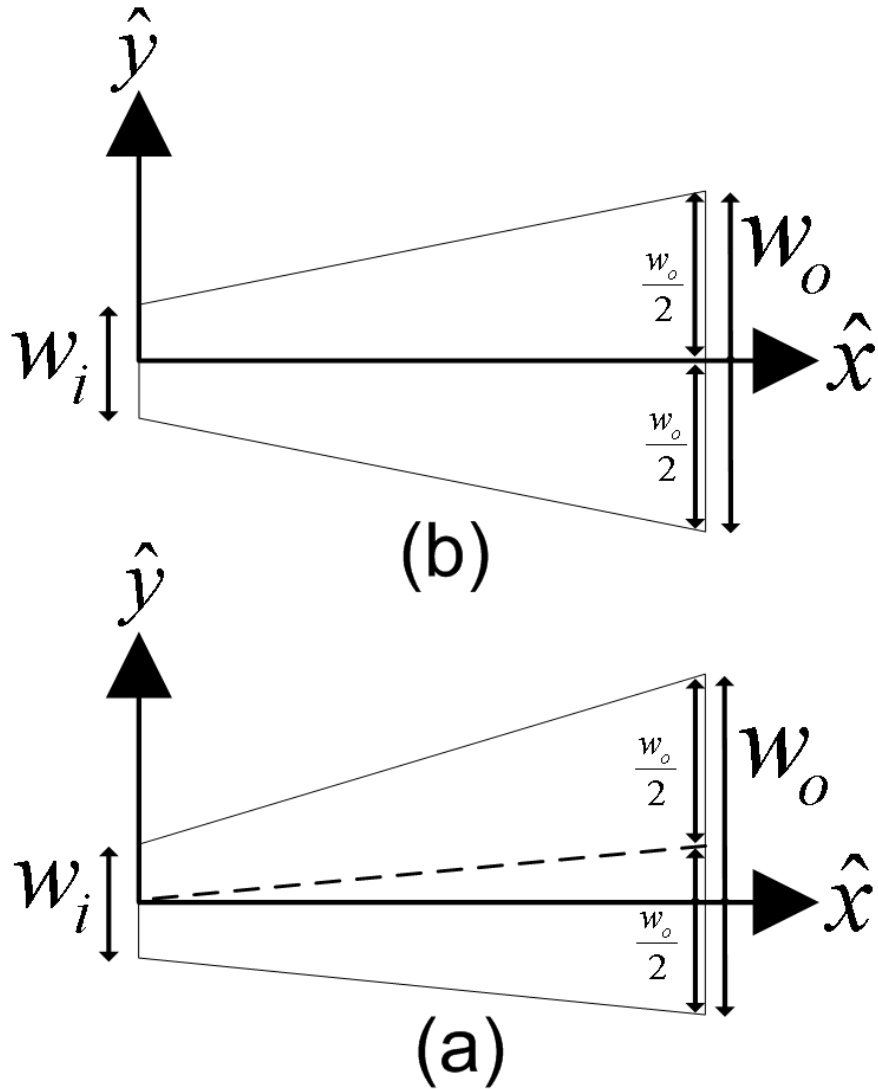


FIG. 7.26. Wedge line layout (a) real line layout with skew (b) approximate layout for analysis

Returning to equation 7.66, it is necessary to integrate the resistance expression along the length. First, the width (and area) must be related to the position  $x$ . To define the width in terms of  $x$ , the length must be known. To determine the length, which is identical for all top and bottom metal lines, the distance between defining coordinates must be found. The distance is calculated the same way as for the rectangular line design, with the result reproduced in equation 7.71 below.

$$l_c = \sqrt{\left(a \cos\left(\frac{\pi}{N}\right) - b\right)^2 + \left(a \sin\left(\frac{\pi}{N}\right)\right)^2} = \sqrt{a^2 + b^2 - 2ab \cos\left(\frac{\pi}{N}\right)} \quad 7.71$$

Note how as  $N$  becomes large,  $l_c$  becomes  $a - b$ . Now, knowing the length, the width can be defined by the linear equation below.

$$w(x) = w_i + \frac{(w_o - w_i)}{l_c} x \quad 7.72$$

The cross sectional area of the top metal is defined as follows.

$$A(x) = h_{m,T} * w(x) \quad 7.73$$

Now with the area expression and equation 7.66, the resistance of a top metal line segment is expressed as follows.

$$R_T = \int_0^{l_c} \rho_T \frac{dx}{A(x)} = \int_0^{l_c} \rho_T \frac{dx}{h_{m,T} * w(x)} = \rho_T \int_0^{l_c} \frac{dx}{h_{m,T} * w_i + \frac{h_{m,T} (w_o - w_i)}{l_c} x} \quad 7.74$$

The integral in equation 7.74 can be expressed as follows.

$$\int_0^{l_c} \frac{dx}{\alpha + \beta x} \quad 7.75$$

where

$$\alpha = h_{m,T} * w_i \quad 7.76$$

$$\beta = \frac{h_{m,T}(w_o - w_i)}{l_c} \quad 7.77$$

To evaluate the integral of equation 7.75, a  $u$  substitution is used.

$$u = \alpha + \beta x \quad 7.78$$

$$x = \frac{u - \alpha}{\beta} \quad 7.79$$

$$dx = \frac{du}{\beta} \quad 7.80$$

Substituting  $u$  into equation 7.75 gives the following.

$$\int_{\alpha}^{\alpha + \beta l_c} \frac{du}{\beta u} = \frac{1}{\beta} \alpha^{\beta l_c} [\ln(u)] = \frac{1}{\beta} (\ln(\alpha + \beta l_c) - \ln(\alpha)) = \frac{1}{\beta} \ln\left(\frac{\alpha + \beta l_c}{\alpha}\right) \quad 7.81$$

Substituting the expressions for  $\alpha$  and  $\beta$  back into equation 7.81 gives the following expression for resistance in terms of empirical parameters.

$$R_T = \frac{\rho_T l_c}{h_{m,T}(w_o - w_i)} \ln\left(\frac{w_i + (w_o - w_i)}{w_i}\right) = \frac{\rho_T l_c}{h_{m,T}(w_o - w_i)} \ln\left(\frac{w_o}{w_i}\right) \quad 7.82$$

#### 4. Bottom Metal line

The analysis for the bottom metal line resistance will be identical to the top metal line resistance, except with bottom metal resistivity and height.

$$R_B = \frac{\rho_B l_c}{h_{m,B}(w_o - w_i)} \ln\left(\frac{w_o}{w_i}\right) \quad 7.83$$

#### 5. Total resistance

The total resistance will now be the sum of all four segment resistances, times the number of turns,  $N$ .

**(Square Vias):**

$$\begin{aligned} R_{Total} &= N(R_i + R_o + R_T + R_B) \quad 7.84 \\ &= N\left(\rho_T \frac{h_c}{(w_i)^2} + \rho_T \frac{h_c}{(w_o)^2} + \frac{\rho_T l_c}{h_{m,T}(w_o - w_i)} \ln\left(\frac{w_o}{w_i}\right) + \frac{\rho_B l_c}{h_{m,B}(w_o - w_i)} \ln\left(\frac{w_o}{w_i}\right)\right) \end{aligned}$$

**(Round Vias)**

$$\begin{aligned} R_{Total} &= N(R_i + R_o + R_T + R_B) \\ &= N\left(\rho_T \frac{4h_c}{\pi(w_i)^2} + \rho_T \frac{4h_c}{\pi(w_o)^2} + \frac{\rho_T l_c}{h_{m,T}(w_o - w_i)} \ln\left(\frac{w_o}{w_i}\right) + \frac{\rho_B l_c}{h_{m,B}(w_o - w_i)} \ln\left(\frac{w_o}{w_i}\right)\right) \quad 7.85 \end{aligned}$$

### 7.2.3.3 Calculation of total capacitance for wedge shaped winding toroid transformer

The capacitance analysis for wedge shaped lines is very similar to the analysis for straight lines. The vertical via regions of capacitance will be identical. However, for the top and bottom metal line runs, the gap ( $d$ ) will be constant and equal to  $w_g$  while the metal line widths ( $a$  and  $b$ ) will depend on position. Following is the new analysis for only the top and bottom metal line regions.

#### 1. Top metal line

With constant gap width, the metal line width will change linearly over the run from the inside circle to the outside circle on the top and bottom layers of the transformer windings. It is assumed that the primary and secondary windings are identical, so dimension  $a$  and  $b$  will have the same position dependent width,  $a = b = w(x)$ . The width has the following linear dependence.

$$w(x) = w_i + \left( \frac{w_o - w_i}{l_c} \right) x \quad 7.86$$

where  $x$  is the distance along the line between the inner and outer radii,  $w_i$  is the inside radius line width,  $w_o$  is the outside radius line width, and  $l_c$  is defined in equation 7.71. Substituting equation 7.86 into equations 7.31 and 7.34 for  $a$  and  $b$  gives the following  $x$  dependent equations for capacitance.

$$k_{1,T}(x) = \left( 1 + \frac{2 \left( w_i + \left( \frac{w_o - w_i}{l_c} x \right) \right)}{2 w_g + \left( w_i + \left( \frac{w_o - w_i}{l_c} x \right) \right)} \right) \left( 1 + \frac{\left( w_i + \left( \frac{w_o - w_i}{l_c} x \right) \right)}{w_g} + \frac{\left( w_i + \left( \frac{w_o - w_i}{l_c} x \right) \right)}{w_g} \right) \left( 1 + \frac{\left( w_i + \left( \frac{w_o - w_i}{l_c} x \right) \right)}{w_g} \right) \right) \quad (7.87)$$

$$k_{2,T}'(x) = \frac{\sinh \left( \frac{\pi \left( w_i + \left( \frac{w_o - w_i}{l_c} x \right) \right)}{4k} \right)}{\sinh \left( \frac{\pi}{2k} \left( w_i + \left( \frac{w_o - w_i}{l_c} x \right) \right) \right)} \frac{\sinh^2 \left( \frac{\pi}{2k} \left( w_i + \left( \frac{w_o - w_i}{l_c} x \right) \right) \right)}{\sinh^2 \left( \frac{\pi}{2k} \left( w_i + \left( \frac{w_o - w_i}{l_c} x \right) \right) + w_g + \left( w_i + \left( \frac{w_o - w_i}{l_c} x \right) \right) \right)} - \sinh^2 \left( \frac{\pi}{2k} \left( w_i + \left( \frac{w_o - w_i}{l_c} x \right) \right) \right) \frac{\sinh^2 \left( \frac{\pi}{2k} \left( w_i + \left( \frac{w_o - w_i}{l_c} x \right) \right) \right)}{\sinh^2 \left( \frac{\pi}{2k} \left( w_i + \left( \frac{w_o - w_i}{l_c} x \right) \right) + w_g + \left( w_i + \left( \frac{w_o - w_i}{l_c} x \right) \right) \right)} \quad (7.88)$$

To find the capacitance of the top metal line over the entire run, the capacitance expression (equations 7.30 and 7.33) must be integrated with respect to  $x$  from 0 to  $l_c$ . Given the complexity of the equations involving both hyperbolic trigonometry as well as elliptical integrals, these integrals can be evaluated numerically using MATLAB.

$$C_{1,T} = 4\epsilon_0 \int_0^{l_c} \left( \frac{K(\sqrt{1-(k_{1,T}(x))^2})}{K(k_{1,T}(x))} \right) dx \quad 7.89$$

$$C_{2,T} = 4\epsilon_0 \int_0^{l_c} \left( \frac{K(k'_{2,T}(x))}{K(\sqrt{1-(k'_{2,T}(x))^2})} \right) dx \quad 7.90$$

### 1. Bottom Metal Line

The capacitance of the horizontal bottom metal line run will be identical to the capacitance of the top metal horizontal line run. This calculation does not need to be repeated.

$$C_{1,B} = 4\epsilon_0 \int_0^{l_c} \left( \frac{K(\sqrt{1-(k_{1,B}(x))^2})}{K(k_{1,B}(x))} \right) dx = 4\epsilon_0 \int_0^{l_c} \left( \frac{K(\sqrt{1-(k_{1,T}(x))^2})}{K(k_{1,T}(x))} \right) dx \quad 7.91$$

$$C_{2,B} = 4\epsilon_0 \int_0^{l_c} \left( \frac{K(k_{2,B}'(x))}{K\left(\sqrt{1-(k_{2,B}'(x))^2}\right)} \right) dx = 4\epsilon_0 \int_0^{l_c} \left( \frac{K(k_{2,T}'(x))}{K\left(\sqrt{1-(k_{2,T}'(x))^2}\right)} \right) dx \quad 7.92$$

### 7.2.3.4 Inductance

Recall the theoretical inductance equation 7.7.

$$L_{torus} = \frac{\Psi_{torus}}{\hat{I}} = \frac{\mu(\omega)N^2h}{2\pi} \ln\left(\frac{a}{b}\right)$$

The inductance equation does not depend on line geometry, only core geometry and turn number. Thus, the expression will be the same for all transformers.

### 7.2.3.5 Fabrication

The fabrication process for these wedge shaped transformers is exactly the same as for the rectangular line transformers. See section 7.2.2.1 for process details. FIG. 7.27 and FIG. 7.28 show photographs of the completed devices. On this sample, toroids with different radii were fabricated: (1mm and 3mm) or G-scale, and (2mm and 5mm) or H-scale. The physical device parameters are summarized in Table 7.5. The terminals of physically identical transformer were also routed in both differential-mode and common-mode. Common-mode analysis, however, is a topic for future research as only differential-mode devices are considered here. Using the resistance, capacitance, and inductance equations from above, the theoretical device parameters can be calculated. Predicted values are presented in Table 7.6 below.

Table 7.5. Fabricated wedge-lined transformer physical parameters.

$N$	Scale	$a_r$ (mm)	$b_r$ (mm)	$w_g$ ( $\mu\text{m}$ )	$h_{m,t}$ (nm)	$h_{m,b}$ (nm)	$h_c$ (nm)
8	H	5	2	50	750	200	500
16	H	5	2	50	750	200	500
8	G	3	1	50	750	200	500
16	G	3	1	50	750	200	500

Table 7.6. Theoretical parameters for wedge-lined fabricated transformers.

$N$	Scale	$R$ ( $\Omega$ ) theory	$L$ (pH) theory	$C$ (pF) theory
8	H	2.49	5.86	16.0
16	H	9.83	23.46	28.8
8	G	3.03	7.03	10.7
16	G	12.72	28.12	18.2

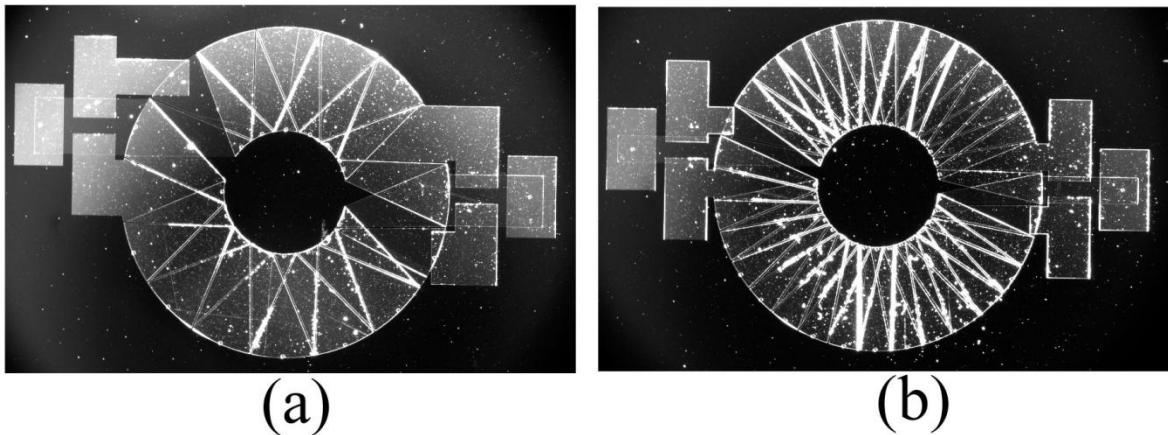


FIG. 7.27. Probe station images of wedge transformers (a) 8-turn H-scale (b) 16-turn H-scale

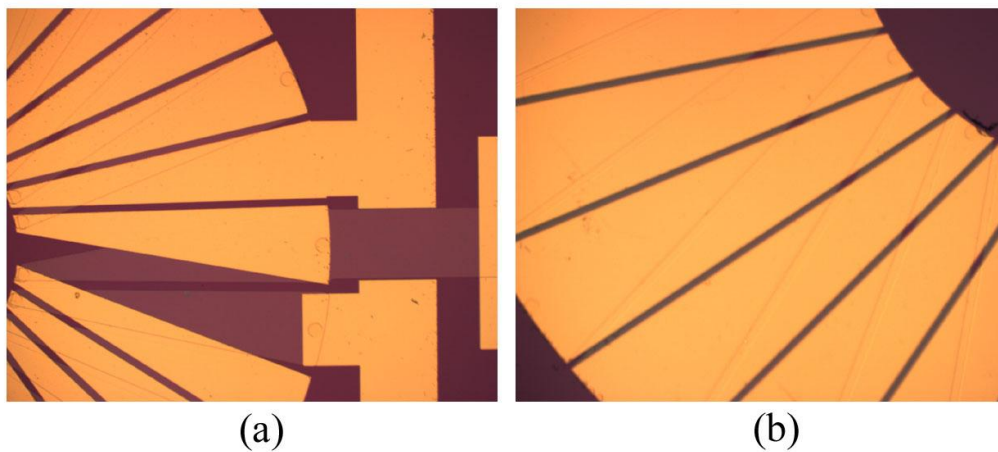


FIG. 7.28 Microscope photographs of transformer lines (a) 16-turn G-scale transformer lines and contact pads (b) 16-turn H-scale transformer lines

### 7.2.3.6 Results

In the same manner as the rectangular-lined transformers discussed above, the wedge-lined transformers were measured using a microprobe station in both high frequency and DC regimes. Wedge-lined transformers with 8 and 16 turns were successfully fabricated for the differential mode. The resistance measurements in the DC regime are given in Table 7.7 below.

**Table 7.7. Fabricated wedge-lined transformers measured DC resistance.**

N	Scale	Primary Resistance ( $\Omega$ )	Secondary Resistance ( $\Omega$ )	$R_{iso}$ (M $\Omega$ )
8	G	11.2	11.2	1.36
8	H	9.03	9	0.91
8	H	8.48	8.54	1.3
8	G	8.97	9	1.36
16	H	27.7	27.55	1.07
16	H	26.07	26	1.3
16	H	25.62	25.6	0.57

The column to the far right of Table 7.7 shows the isolation resistance between the windings. Similar to the rectangular-lined transformers, the fabricated devices measured resistance is slightly higher than what was theoretically predicted. This could, again, be attributed to the evaporated thin-film metal having a higher resistivity than the resistivity of bulk gold [41]. The relationship between the resistances of windings with different numbers of turns is the same as with rectangular-lined transformers (see equation 7.55).

Using the same de-embedding procedure as was used for the rectangular-line transformers, the transfer relation of the wedge-lined transformers was measured and is shown in FIG. 7.29.

Fabricated transformer DM Transfer relations - wedge lines:  $Z_L = \text{inf}\Omega$

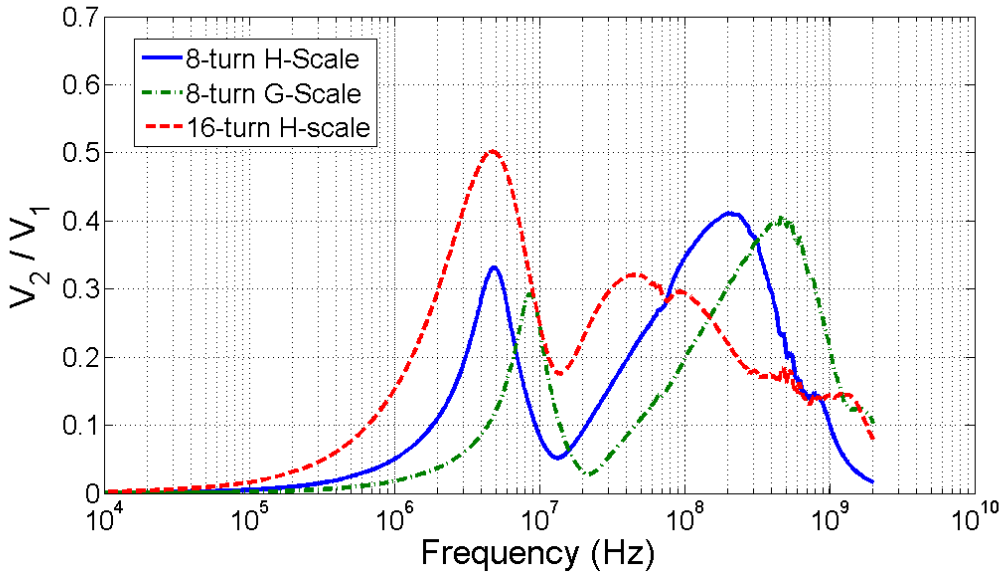


FIG. 7.29. Measured transfer relations for fabricated wedge-lined transformers.

It is difficult to reason the behavior of the wedge-lined fabricated transformer transfer relation. It appears that with low inductive coupling and low resistance, overall coupling between the windings is low. The only major behavioral features are two resonances. One occurs between 5MHz and 10 MHz and does not depend on line length or turn number; only core geometry scale. A broader resonance occurs closer to 100MHz, but distorts with both changing line length and changing core geometry. One can conclude from the data when compared to the rectangular-lined transformers that reducing resistance without boosting other coupling factors results in a device that cannot couple signals without distortion.

## **7.3. Numerical analysis of magnetic flux and inductance of air-core toroid inductors and transformers**

### **7.3.1. Introduction**

In the following sections, a rectangular cross section toroid inductor will be analyzed. The purpose of the analysis is to theoretically determine the leakage inductance of an air-core toroid transformer with dimensions of the designer's choosing. The multiple subsections below will lead to this conclusion. However, the conclusion of each subsection offers further understanding and intuition about the magnetic behavior of these devices.

The subsections are as follows:

- 1) **Magnetic flux density** – Determine the vector of magnetic flux density in all of 3D space
- 2) **Structure and Reciprocity** – Determine the structure of the inductor in space with known coordinates
- 3) **Total Flux**– Calculate the flux through the cross sections of each turn then find the total flux by reciprocity.
- 4) **Inductance (Self, Mutual, leakage)** – Use the flux calculated at the turns of the primary winding to find self-inductance. Use the flux calculated at the turns of the secondary to find mutual inductance. Subtract the two values to find the leakage inductance.

### 7.3.2. Magnetic flux density

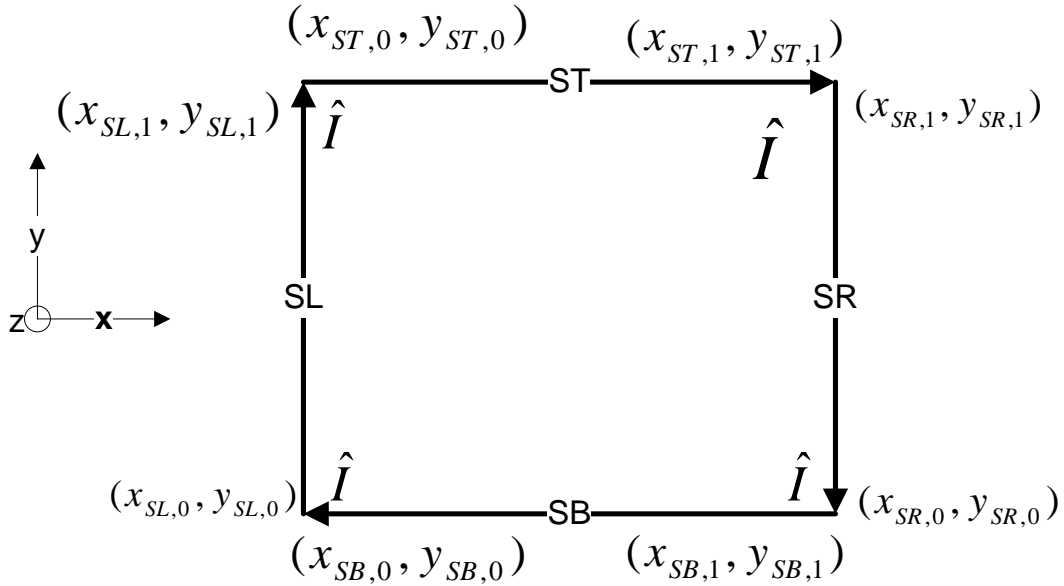


FIG. 7.30. Schematic of a single wire loop with current flowing around it.

The following analysis will determine the magnetic flux density for an arbitrary point in space as the result of a single rectangular loop with current  $\hat{I}$ . As will be explained in a later section, considering a stationary source and multiple observation points by symmetry is the same as a fixed observation point and multiple sources.

Consider a single planar wire loop with current  $\hat{I}$  flowing as shown in the above FIG. 7.30. The start and end points of each wire segment are labeled as in the figure, though many of the coordinates will be identical to an adjacent wire. The magnetic flux density from an infinitesimally small current element is given by

$$d\vec{B} = \frac{\mu_0}{4\pi} \frac{|\vec{I}| d\vec{l} \times \vec{r}}{r^3} \quad 7.93$$

where  $d\vec{l}$  is the infinitesimal current element vector (in direction of current flow) and  $\vec{r}$  is the vector from the current element to the observation point. For an arbitrary point in space  $(x_p, y_p, z_p)$ , the total magnetic flux will be the sum of the magnetic flux densities from each of the four current carrying wires (SL, SR, ST, and SB). The four flux densities are as follows. First consider the source line on the left of the above FIG. 7.30 (SL). The integrals can be collapsed into the xy plane, since the above configuration has no current density in the z direction.

**SL:**

$$\begin{aligned} \vec{l} &= \hat{y}(y_{SL,1} - y_{SL,0}) \\ d\vec{l} &= \hat{y}dy \end{aligned} \quad 7.94$$

The above equation has the current flowing in the positive y direction. Following is the general integral expression for total magnetic flux density due to line SL.

$$\vec{B}_{SL}(x_p, y_p, z_p) = \int d\vec{B} = \int \frac{\mu_0}{4\pi} \frac{|\hat{I}| d\vec{l} \times \vec{r}}{r^3} = \frac{\mu_0}{4\pi} |\hat{I}| \int \frac{d\vec{l} \times \vec{r}}{r^3} \quad 7.95$$

$$r^3 = ((x_p - x)^2 + (y_p - y)^2 + (z_p - z)^2)^{3/2} \quad 7.96$$

$$\vec{r} = ((x_p - x)\hat{x} + (y_p - y)\hat{y} + (z_p - z)\hat{z}) \quad 7.97$$

Evaluating the cross product in the integral gives the following.

$$d\vec{l} \times \vec{r} = \begin{vmatrix} \hat{x} & \hat{y} & \hat{z} \\ 0 & dy & 0 \\ (x_p - x) & (y_p - y) & (z_p - z) \end{vmatrix} = \hat{x}dy(z_p - z) - \hat{z}dy(x_p - x) \quad 7.98$$

Breaking the flux density into vector components gives the following.

$$B_{SL,\hat{x}}(x_p, y_p, z_p) = \frac{\mu_0}{4\pi} |\hat{I}| \int_{y_{SL,0}}^{y_{SL,1}} dy \frac{(z_p)}{((x_p - x_{SL,0})^2 + (y_p - y)^2 + (z_p)^2)^{3/2}} \quad 7.99$$

$$B_{SL,\hat{z}}(x_p, y_p, z_p) = -\frac{\mu_0}{4\pi} |\hat{I}| \int_{y_{SL,0}}^{y_{SL,1}} dy \frac{(x_p - x_{SL,0})}{((x_p - x_{SL,0})^2 + (y_p - y)^2 + (z_p)^2)^{3/2}} \quad 7.100$$

The first integral for the  $x$  component of flux density is shown below.

$$B_{SL,\hat{x}}(x_p, y_p, z_p) = \frac{\mu_0}{4\pi} |\hat{I}| z_p \int_{y_{SL,0}}^{y_{SL,1}} dy ((x_p - x_{SL,0})^2 + (y_p - y)^2 + (z_p)^2)^{-3/2} \quad 7.101$$

This integral is of the form

$$\frac{\mu_0}{4\pi} \left| \hat{I} \right|_{z_p} \int_{y_{SL,0}}^{y_{SL,1}} dy (c + by + ay^2)^{-3/2} \quad 7.102$$

where

$$\begin{aligned} a &= 1 \\ b &= -2y_p \\ c &= (x_p - x_{SL,0})^2 + (z_p)^2 + y_p^2 \end{aligned} \quad 7.103$$

The integral equation 7.102 can be found in an integral table ([43]) and is given as

$$\begin{aligned} B_{SL,\hat{x}}(x_p, y_p, z_p) &= \frac{\mu_0}{4\pi} \left| \hat{I} \right|_{z_p} \int_{y_{SL,0}}^{y_{SL,1}} dy (c + by + ay^2)^{-3/2} \quad 7.104 \\ &= \frac{\mu_0}{4\pi} \left| \hat{I} \right|_{z_p} \left[ \frac{2(2ay+b)}{(4ac-b^2)\sqrt{ay^2+by+c}} \right]_{y_{SL,0}}^{y_{SL,1}} \\ &= \frac{\mu_0}{2\pi(4c-b^2)} \left| \hat{I} \right|_{z_p} \left[ \frac{(2y_{SL,1}+b)}{\sqrt{y_{SL,1}^2+by_{SL,1}+c}} - \frac{(2y_{SL,0}+b)}{\sqrt{y_{SL,0}^2+by_{SL,0}+c}} \right] \end{aligned}$$

The  $z$  direction flux density can be found in a similar way.

$$\begin{aligned} B_{SL,\hat{z}}(x_p, y_p, z_p) &= -\frac{\mu_0}{4\pi} \left| \hat{I} \right| \int_{y_{SL,0}}^{y_{SL,1}} dy \frac{(x_p - x_{SL,0})}{((x_p - x_{SL,0})^2 + (y_p - y)^2 + (z_p)^2)^{3/2}} \quad 7.105 \\ &= -\frac{\mu_0}{4\pi} \left| \hat{I} \right| (x_p - x_{SL,0}) \int_{y_{SL,0}}^{y_{SL,1}} dy ((x_p - x_{SL,0})^2 + (y_p - y)^2 + (z_p)^2)^{-3/2} \\ &= -\frac{\mu_0}{2\pi(4ac-b^2)} \left| \hat{I} \right| (x_p - x_{SL,0}) \left[ \frac{(2y_{SL,1}+b)}{\sqrt{y_{SL,1}^2+by_{SL,1}+c}} - \frac{(2y_{SL,0}+b)}{\sqrt{y_{SL,0}^2+by_{SL,0}+c}} \right] \end{aligned}$$

Now consider the flux density contributions from the right source line (SR).

**SR:**

$$\begin{aligned}\vec{l} &= \hat{y}(y_{SL,1} - y_{SL,0}) \\ d\vec{l} &= -\hat{y}dy\end{aligned}\tag{7.106}$$

Equation 7.106 is the negation of equation 7.94 because the current is traveling in the  $-\hat{y}$  direction. The analysis is repeated as follows.

$$\vec{B}_{SR}(x_p, y_p, z_p) = \int d\vec{B} = \int \frac{\mu_0}{4\pi} \frac{|\hat{l}| d\vec{l} \times \vec{r}}{r^3} = \frac{\mu_0}{4\pi} |\hat{l}| \int \frac{d\vec{l} \times \vec{r}}{r^3}\tag{7.107}$$

$$r^3 = ((x_p - x_{SR,0})^2 + (y_p - y)^2 + (z_p)^2)^{3/2}\tag{7.108}$$

$$\vec{r} = ((x_p - x_{SR,0})\hat{x} + (y_p - y)\hat{y} + (z_p - z)\hat{z})\tag{7.109}$$

$$d\vec{l} \times \vec{r} = \begin{vmatrix} \hat{x} & \hat{y} & \hat{z} \\ 0 & -dy & 0 \\ (x_p - x_{SR,0}) & (y_p - y) & (z_p) \end{vmatrix} = -\hat{x}dy(z_p) + \hat{z}dy(x_p - x_{SR,0})\tag{7.110}$$

Breaking the flux density into vector components gives the following.

$$B_{SR,\hat{x}}(x_p, y_p, z_p) = \frac{-\mu_0}{4\pi} \left| \hat{I} \right| \int_{y_{SR,0}}^{y_{SR,1}} dy \frac{(z_p)}{((x_p - x_{SR,0})^2 + (y_p - y)^2 + (z_p)^2)^{3/2}} \quad 7.111$$

$$B_{SR,\hat{z}}(x_p, y_p, z_p) = \frac{\mu_0}{4\pi} \left| \hat{I} \right| \int_{y_{SR,0}}^{y_{SR,1}} dy \frac{(x_p - x_{SR,0})}{((x_p - x_{SR,0})^2 + (y_p - y)^2 + (z_p)^2)^{3/2}} \quad 7.112$$

The first integral for the x component of flux density is shown below.

$$B_{SR,\hat{x}}(x_p, y_p, z_p) = \frac{-\mu_0}{4\pi} \left| \hat{I} \right| z_p \int_{y_{SR,0}}^{y_{SR,1}} dy ((x_p - x_{SR,0})^2 + (y_p - y)^2 + (z_p)^2)^{-3/2} \quad 7.113$$

This integral is of the form

$$-\frac{\mu_0}{4\pi} \left| \hat{I} \right| z_p \int_{y_{SL,0}}^{y_{SL,1}} dy (c + by + ay^2)^{-3/2} \quad 7.114$$

where

$$\begin{aligned} a &= 1 \\ b &= -2y_p \\ c &= (x_p - x_{SR,0})^2 + (z_p)^2 + y_p^2 \end{aligned} \quad 7.115$$

The integral equation 7.113 can be found in an integral table ([43]) and is given as

$$\begin{aligned}
B_{SR,\hat{x}}(x_p, y_p, z_p) &= \frac{-\mu_0}{4\pi} \left| \hat{I} \right|_{z_p} \int_{y_{SL,0}}^{y_{SL,1}} dy (c + by + ay^2)^{-3/2} \\
&= \frac{-\mu_0}{4\pi} \left| \hat{I} \right|_{z_p} \left[ \frac{2(2ay+b)}{(4ac-b^2)\sqrt{ay^2+by+c}} \right]_{y_{SL,0}}^{y_{SL,1}} \\
&= \frac{-\mu_0 \left| \hat{I} \right|_{z_p}}{2\pi(4ac-b^2)} \left[ \frac{(2y_{SR,1}+b)}{\sqrt{y_{SR,1}^2+by_{SR,1}+c}} - \frac{(2y_{SR,0}+b)}{\sqrt{y_{SR,0}^2+by_{SR,0}+c}} \right]
\end{aligned}$$

The  $z$  direction flux density can be found in a similar way.

$$\begin{aligned}
B_{SR,\hat{z}}(x_p, y_p, z_p) &= \frac{\mu_0}{4\pi} \left| \hat{I} \right| \int_{y_{SL,0}}^{y_{SL,1}} dy \frac{(x_p - x_{SR,0})}{((x_p - x_{SR,0})^2 + (y_p - y)^2 + (z_p)^2)^{3/2}} \\
&= \frac{\mu_0}{4\pi} \left| \hat{I} \right| (x_p - x_{SR,0}) \int_{y_{SL,0}}^{y_{SL,1}} dy ((x_p - x_{SR,0})^2 + (y_p - y)^2 + (z_p)^2)^{-3/2} \\
&= \frac{\mu_0 \left| \hat{I} \right| (x_p - x_{SR,0})}{2\pi(4c-b^2)} \left[ \frac{(2y_{SR,1}+b)}{\sqrt{y_{SR,1}^2+by_{SR,1}+c}} - \frac{(2y_{SR,0}+b)}{\sqrt{y_{SR,0}^2+by_{SR,0}+c}} \right]
\end{aligned} \tag{7.117}$$

Following is the analysis for the top source line (ST).

**ST:**

$$\begin{aligned}
\vec{l} &= \hat{x}(x_{ST,1} - x_{ST,0}) \\
d\vec{l} &= \hat{x}dx
\end{aligned} \tag{7.118}$$

The above equation has the current flowing in the positive  $x$  direction.

$$\vec{B}_{ST}(x_p, y_p, z_p) = \int d\vec{B} = \int \frac{\mu_0}{4\pi} \frac{|\hat{I}| d\vec{l} \times \vec{r}}{r^3} = \frac{\mu_0}{4\pi} |\hat{I}| \int \frac{d\vec{l} \times \vec{r}}{r^3} \quad 7.119$$

$$r^3 = ((x_p - x)^2 + (y_p - y_{ST,0})^2 + (z_p)^2)^{3/2} \quad 7.120$$

$$\vec{r} = ((x_p - x)\hat{x} + (y_p - y_{ST,0})\hat{y} + (z_p)\hat{z}) \quad 7.121$$

$$d\vec{l} \times \vec{r} = \begin{vmatrix} \hat{x} & \hat{y} & \hat{z} \\ dx & 0 & 0 \\ (x_p - x) & (y_p - y_{ST,0}) & (z_p) \end{vmatrix} = -\hat{y}dx(z_p) + \hat{z}dx(y_p - y_{ST,0}) \quad 7.122$$

Breaking the flux density into vector components gives the following.

$$B_{ST,\hat{y}}(x_p, y_p, z_p) = \frac{-\mu_0}{4\pi} |\hat{I}| \int_{x_{ST,0}}^{x_{ST,1}} dx \frac{(z_p)}{((x_p - x)^2 + (y_p - y_{ST,0})^2 + (z_p)^2)^{3/2}} \quad 7.123$$

$$B_{ST,\hat{z}}(x_p, y_p, z_p) = \frac{\mu_0}{4\pi} |\hat{I}| \int_{x_{ST,0}}^{x_{ST,1}} dx \frac{(y_p - y_{ST,0})}{((x_p - x)^2 + (y_p - y_{ST,0})^2 + (z_p)^2)^{3/2}} \quad 7.124$$

The first integral for the y component of flux density is shown below.

$$B_{ST,\hat{y}}(x_p, y_p, z_p) = \frac{-\mu_0}{4\pi} z_p |\hat{I}| \int_{x_{ST,0}}^{x_{ST,1}} dx ((x_p - x)^2 + (y_p - y_{ST,0})^2 + (z_p)^2)^{-3/2} \quad 7.125$$

This integral is of the form

$$\int_{x_{ST,0}}^{x_{ST,1}} dx(ax^2 + bx + c)^{-3/2} \quad 7.126$$

where

$$\begin{aligned} a &= 1 \\ b &= -2x_p \\ c &= x_p^2 + (y_p - y_{ST,0})^2 + z_p^2 \end{aligned} \quad 7.127$$

The integral equation 7.126 can be found in an integral table ([43]) and is given as

$$\begin{aligned} B_{ST,\hat{y}}(x_p, y_p, z_p) &= \frac{-\mu_0}{4\pi} \left| \hat{I} \right|_{z_p} \int_{x_{ST,0}}^{x_{ST,1}} dx(ax^2 + bx + c)^{-3/2} \quad 7.128 \\ &= \frac{-\mu_0}{4\pi} \left| \hat{I} \right|_{z_p} \left[ \frac{2(2ax+b)}{(4ac-b^2)\sqrt{ax^2+bx+c}} \right]_{x_{ST,0}}^{x_{ST,1}} \\ &= \frac{-\mu_0}{2\pi(4ac-b^2)} \left| \hat{I} \right|_{z_p} \left[ \frac{(2x_{ST,1}+b)}{\sqrt{x_{ST,1}^2+bx_{ST,1}+c}} - \frac{(2x_{ST,0}+b)}{\sqrt{x_{ST,0}^2+bx_{ST,0}+c}} \right] \end{aligned}$$

The  $z$  direction flux density can be found in a similar way.

$$\begin{aligned} B_{ST,\hat{z}}(x_p, y_p, z_p) &= \frac{\mu_0}{4\pi} \left| \hat{I} \right| \int_{x_{ST,0}}^{x_{ST,1}} dx \frac{(y_p - y_{ST,0})}{((x_p - x)^2 + (y_p - y_{ST,0})^2 + (z_p)^2)^{3/2}} \\ &= \frac{\mu_0}{4\pi} \left| \hat{I} \right| (y_p - y_{ST,0}) \int_{x_{ST,0}}^{x_{ST,1}} dx ((x_p - x)^2 + (y_p - y_{ST,0})^2 + (z_p)^2)^{-3/2} \quad 7.129 \\ &= \frac{\mu_0}{2\pi(4c-b^2)} \left| \hat{I} \right| (y_p - y_{ST,0}) \left[ \frac{(2x_{ST,1}+b)}{\sqrt{x_{ST,1}^2+bx_{ST,1}+c}} - \frac{(2x_{ST,0}+b)}{\sqrt{x_{ST,0}^2+bx_{ST,0}+c}} \right] \end{aligned}$$

The following analysis considers the bottom source line (SB).

**SB:**

$$\begin{aligned}\vec{l} &= \hat{x}(x_{ST,1} - x_{ST,0}) \\ d\vec{l} &= -\hat{x}dx\end{aligned}\tag{7.130}$$

Equation 7.130 is the negation of equation 7.118 because the current is traveling in the  $-\hat{x}$  direction.

$$\vec{B}_{SB}(x_p, y_p, z_p) = \int d\vec{B} = \int \frac{\mu_0}{4\pi} \frac{|\hat{l}| d\vec{l} \times \vec{r}}{r^3} = \frac{\mu_0}{4\pi} |\hat{l}| \int \frac{d\vec{l} \times \vec{r}}{r^3}\tag{7.131}$$

$$r^3 = ((x_p - x)^2 + (y_p - y_{SB,0})^2 + (z_p)^2)^{3/2}\tag{7.132}$$

$$\vec{r} = ((x_p - x)\hat{x} + (y_p - y_{SB,0})\hat{y} + (z_p)\hat{z})\tag{7.133}$$

$$d\vec{l} \times \vec{r} = \begin{vmatrix} \hat{x} & \hat{y} & \hat{z} \\ -dx & 0 & 0 \\ (x_p - x) & (y_p - y_{SB,0}) & (z_p) \end{vmatrix} = \hat{y}dx(z_p) - \hat{z}dx(y_p - y_{SB,0})\tag{7.134}$$

Breaking the flux density into vector components gives the following.

$$B_{SB,\hat{y}}(x_p, y_p, z_p) = \frac{\mu_0}{4\pi} |\hat{l}| \int_{x_{SB,0}}^{x_{SB,1}} dx \frac{(z_p)}{((x_p - x)^2 + (y_p - y_{SB,0})^2 + (z_p)^2)^{3/2}}\tag{7.135}$$

$$B_{SB,\hat{z}}(x_p, y_p, z_p) = \frac{-\mu_0}{4\pi} |\hat{l}| \int_{x_{SB,0}}^{x_{SB,1}} dx \frac{(y_p - y_{SB,0})}{((x_p - x)^2 + (y_p - y_{SB,0})^2 + (z_p)^2)^{3/2}}\tag{7.136}$$

The first integral for the y component of flux density is shown below.

$$B_{SB,\hat{y}}(x_p, y_p, z_p) = \frac{\mu_0}{4\pi} z_p \left| \hat{I} \right| \int_{x_{SB,0}}^{x_{SB,1}} dx ((x_p - x)^2 + (y_p - y_{SB,0})^2 + (z_p)^2)^{-3/2} \quad 7.137$$

This integral is of the form

$$\int_{x_{SB,0}}^{x_{SB,1}} dx (ax^2 + bx + c)^{-3/2} \quad 7.138$$

where

$$\begin{aligned} a &= 1 \\ b &= -2x_p \\ c &= x_p^2 + (y_p - y_{SB,0})^2 + z_p^2 \end{aligned} \quad 7.139$$

The integral equation 7.138 can be found in an integral table ([43]) and is given as

$$\begin{aligned} B_{SB,\hat{y}}(x_p, y_p, z_p) &= \frac{\mu_0}{4\pi} \left| \hat{I} \right| z_p \int_{x_{SB,0}}^{x_{SB,1}} dx (ax^2 + bx + c)^{-3/2} \quad 7.140 \\ &= \frac{\mu_0}{4\pi} \left| \hat{I} \right| z_p \left[ \frac{2(2ax+b)}{(4ac-b^2)\sqrt{ax^2+bx+c}} \right]_{x_{SB,0}}^{x_{SB,1}} \\ &= \frac{\mu_0 \left| \hat{I} \right| z_p}{2\pi(4ac-b^2)} \left[ \frac{(2x_{SB,1}+b)}{\sqrt{x_{SB,1}^2+bx_{SB,1}+c}} - \frac{(2x_{SB,0}+b)}{\sqrt{x_{SB,0}^2+bx_{SB,0}+c}} \right] \end{aligned}$$

The  $z$  direction flux density can be found in a similar way.

$$\begin{aligned}
B_{SB,\hat{z}}(x_p, y_p, z_p) &= \frac{-\mu_0}{4\pi} |\hat{I}| \int_{x_{SB,0}}^{x_{SB,1}} dx \frac{(y_p - y_{SB,0})}{((x_p - x)^2 + (y_p - y_{SB,0})^2 + (z_p)^2)^{3/2}} & 7.141 \\
&= \frac{-\mu_0}{4\pi} |\hat{I}| (y_p - y_{SB,0}) \int_{x_{SB,0}}^{x_{SB,1}} dx ((x_p - x)^2 + (y_p - y_{SB,0})^2 + (z_p)^2)^{-3/2} \\
&= \frac{-\mu_0 |\hat{I}| (y_p - y_{SB,0})}{2\pi(4ac - b^2)} \left[ \frac{(2x_{SB,1} + b)}{\sqrt{x_{SB,1}^2 + bx_{SB,1} + c}} - \frac{(2x_{SB,0} + b)}{\sqrt{x_{SB,0}^2 + bx_{SB,0} + c}} \right]
\end{aligned}$$

Thus, the total flux density at an arbitrary point in space  $(x_p, y_p, z_p)$  is given by the vector sum of the flux contributions from each of the source lines.

$$B_x(x_p, y_p, z_p) = B_{SL,x}(x_p, y_p, z_p) + B_{SR,x}(x_p, y_p, z_p) \quad 7.142$$

**(Sum of Equations 7.116 and 7.104)**

$$B_y(x_p, y_p, z_p) = B_{ST,y}(x_p, y_p, z_p) + B_{SB,y}(x_p, y_p, z_p) \quad 7.143$$

**(Sum of Equations 7.140 and 7.128)**

$$\begin{aligned}
&B_z(x_p, y_p, z_p) \\
&= B_{SL,z}(x_p, y_p, z_p) + B_{SR,z}(x_p, y_p, z_p) + B_{ST,z}(x_p, y_p, z_p) + B_{SB,z}(x_p, y_p, z_p) & 7.144
\end{aligned}$$

**(Sum of Equations 7.104, 7.116, 7.128, and 7.140)**

Below is a plot of the magnetic flux density slope field in the  $y=0$  plane. The weight of the vectors represents the magnitude of the flux density, and the red dots act as vector arrow heads.

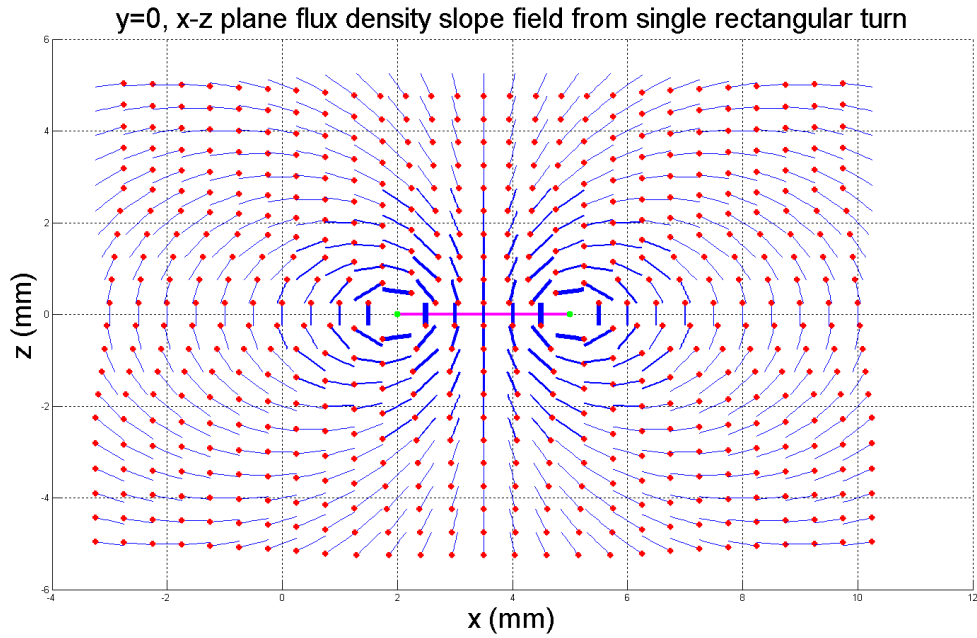


**FIG. 7.31. Flux density slope field around a wire loop in the XY plane.**

FIG. 7.32 shows the single source turn slope field superimposed over the other turn locations in the transformer.

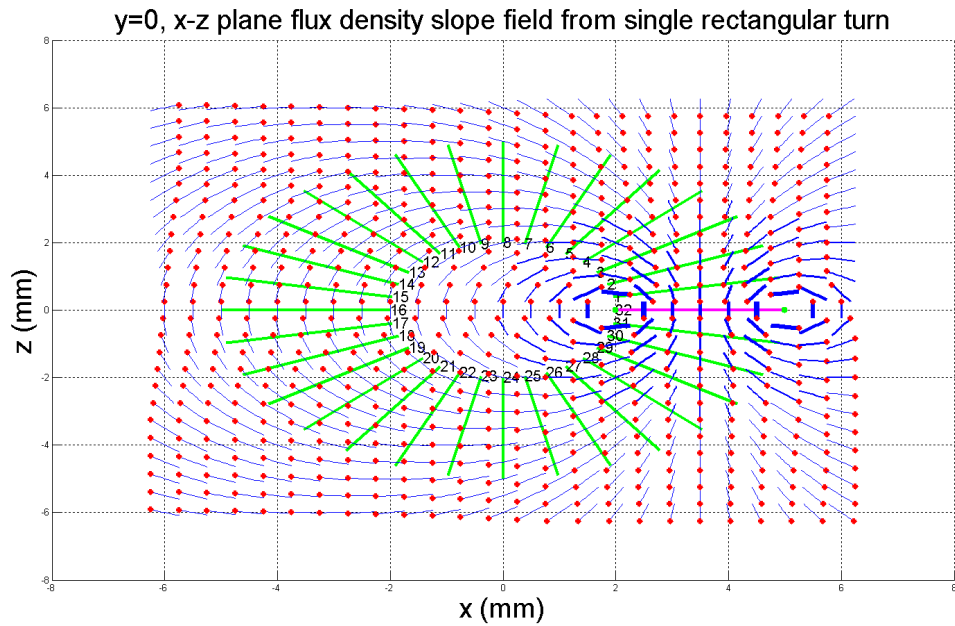


**FIG. 7.32. Flux density slope field superimposed over turn map of toroidal inductor.**

FIG. 7.33 through FIG. 7.37 show the magnetic slope field as a sum of the magnetic fields from all of the turns for a non-magnetic core toroidal winding. As  $N$  increases, the normal field in the core is reinforced, while the leakage flux is attenuated.

$y=0$ ,  $x$ - $z$  plane flux density slope field from rectangular toroidal winding

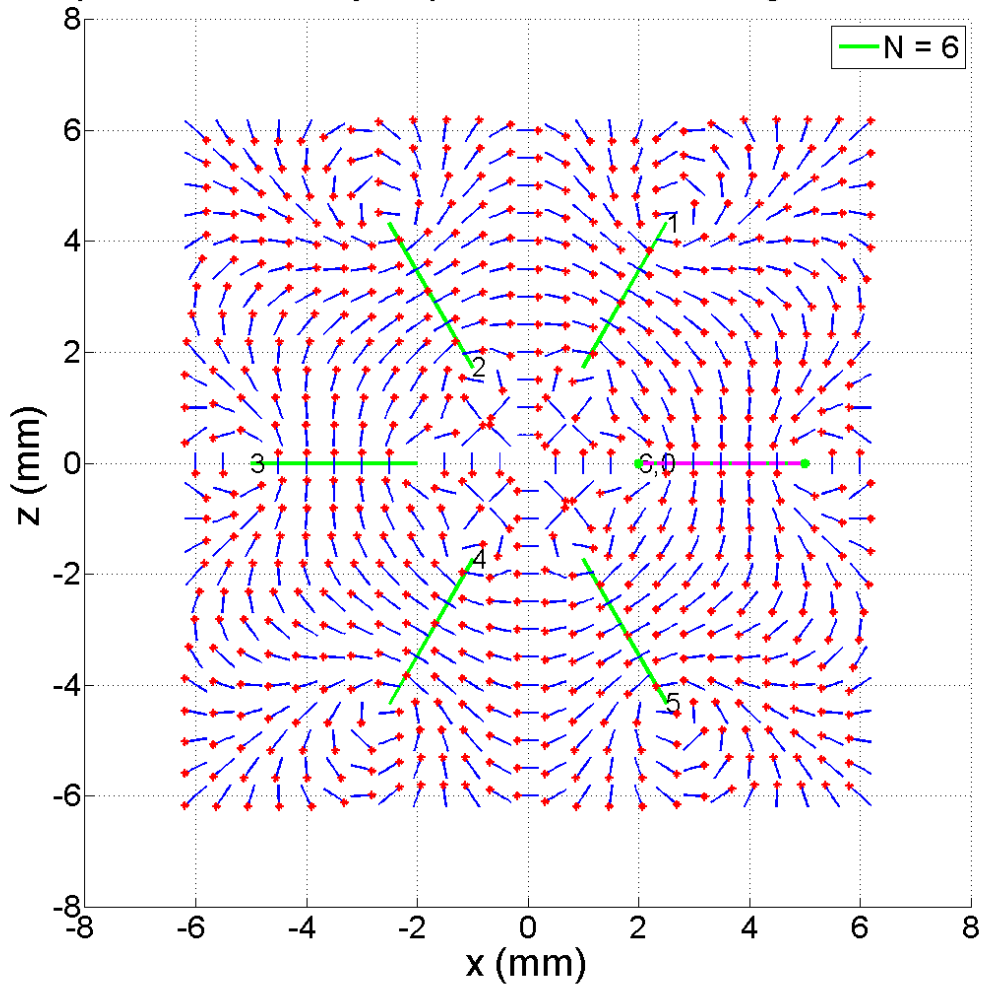


FIG. 7.33. Magnetic slope field for a dielectric-core toroid transformer:  $N=6$ .

y=0, x-z plane flux density slope field from rectangular toroidal winding

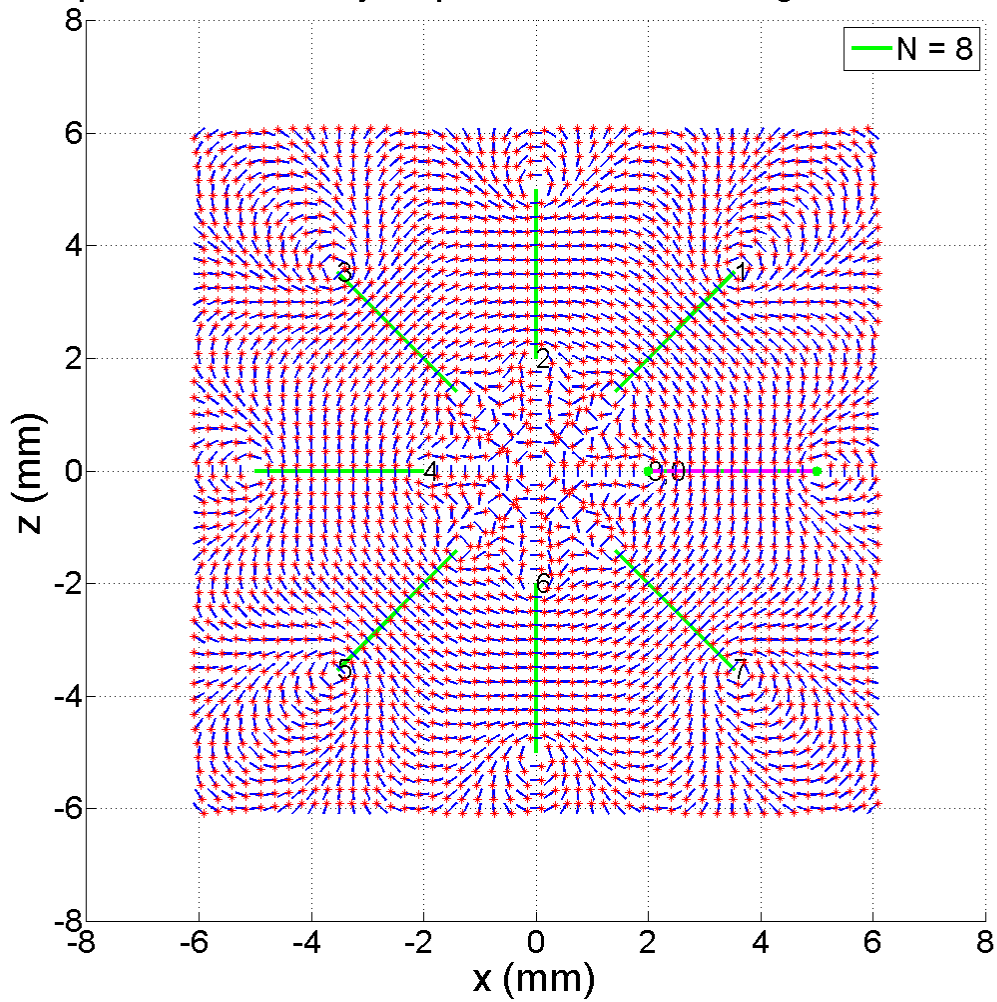


FIG. 7.34. Magnetic slope field for a dielectric-core toroid transformer: N=8.

y=0, x-z plane flux density slope field from rectangular toroidal winding

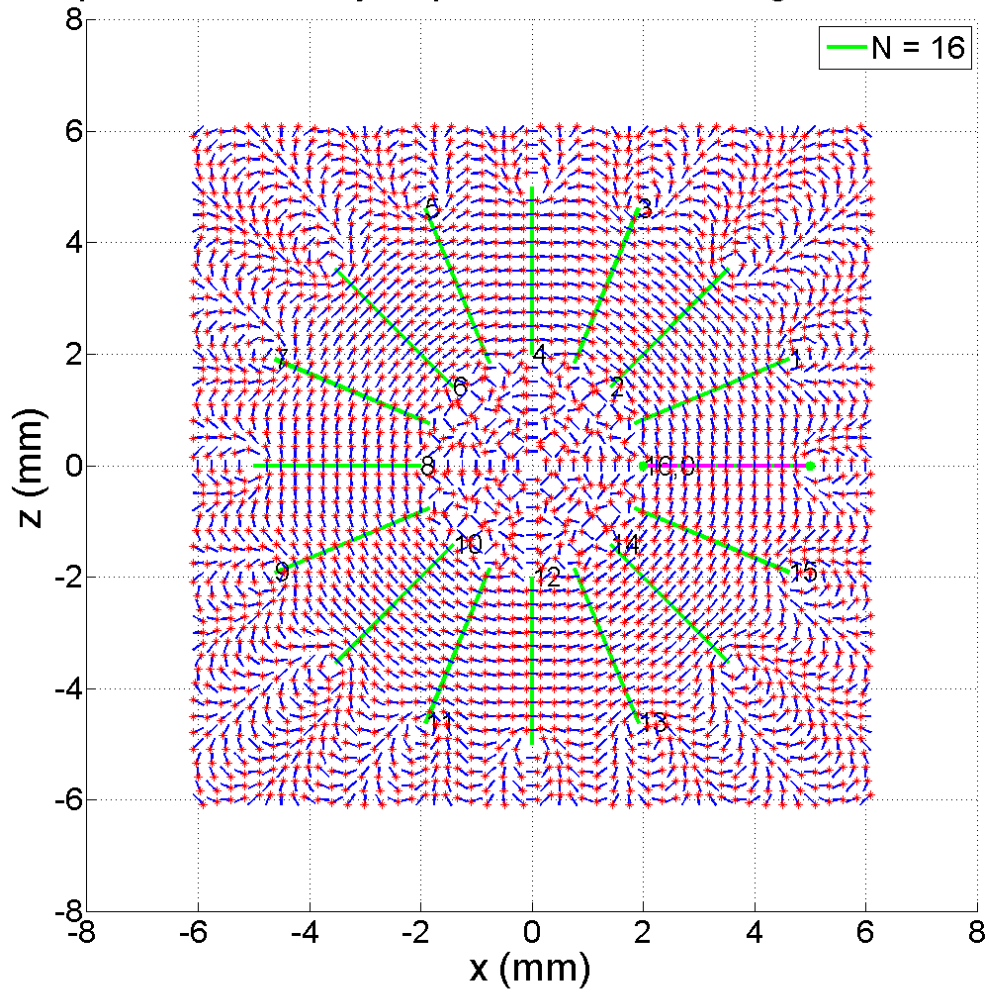


FIG. 7.35. Magnetic slope field for a dielectric-core toroid transformer: N=16.

y=0, x-z plane flux density slope field from rectangular toroidal winding

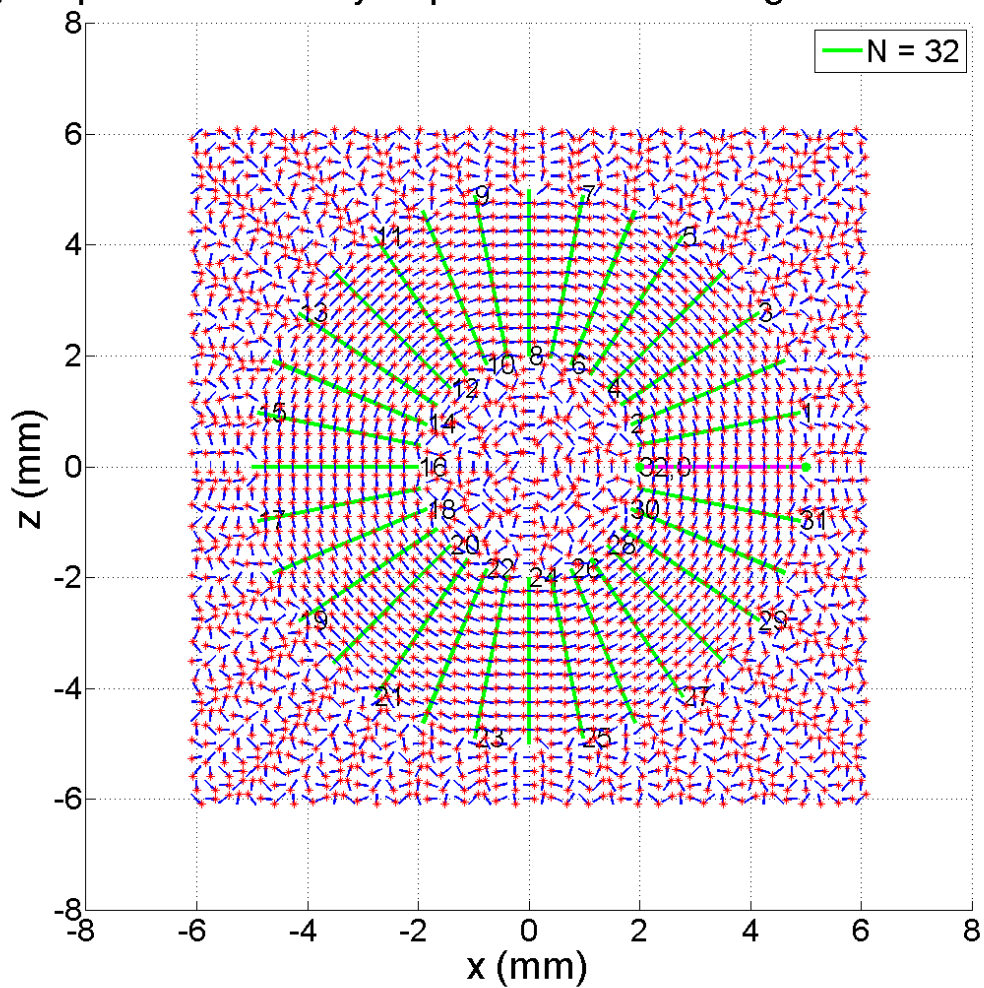


FIG. 7.36. Magnetic slope field for a dielectric-core toroid transformer: N=32.

y=0, x-z plane flux density slope field from rectangular toroidal winding

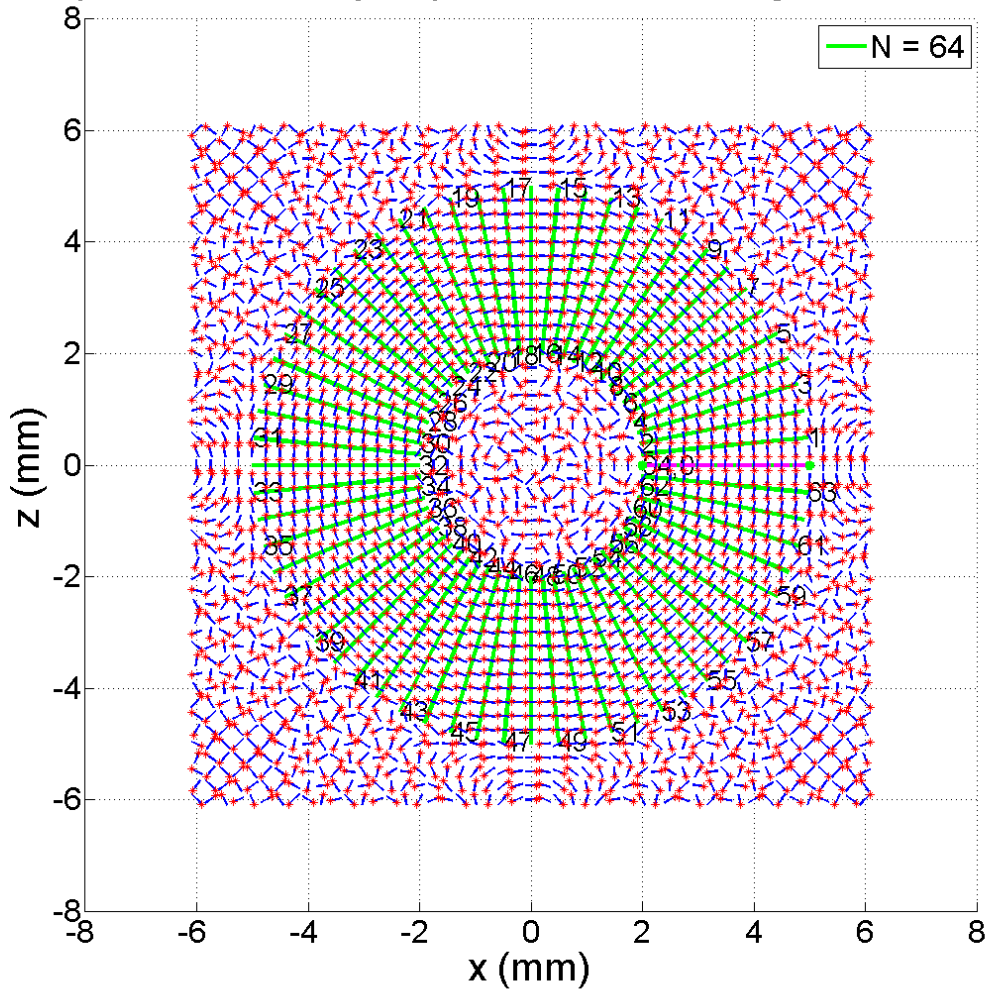


FIG. 7.37. Magnetic slope field for a dielectric-core toroid transformer: N=64.

FIG. 7.38 and FIG. 7.39 show a group of plots depicting the normal ( $\hat{\theta}$  direction) magnetic field. In FIG. 7.38 it can be seen how as the core becomes thicker, the field cut through  $y=0$  becomes smoother, with less dramatic field spikes in the vicinity of the winding turns. This effect can be attributed to the proximity of the observing point in the  $y=0$  plane to the source

lines parallel to the  $y=0$  plane. As the core becomes thinner, the source lines approach the observing point at  $y=0$ .

In FIG. 7.39, however, the height is constant and the turn number is increased. As  $N$  increases, it is apparent that the field fluctuations in the  $\hat{\theta}$  direction decrease and the field magnitude increases. Though the radial field dependence is accounted for in the theoretical inductance calculation (equation 7.4), the  $\hat{\theta}$  direction fluctuations are not. The theoretical derivation assumes a tightly packed winding in which the field is uniform around the  $\hat{\theta}$  direction. These fluctuations are most likely the source of error when calculating the inductance using equation 7.7. Numerical methods that determine the inductance empirically would account for these fluctuations, making numerical methods more accurate for windings that are not tightly packed.

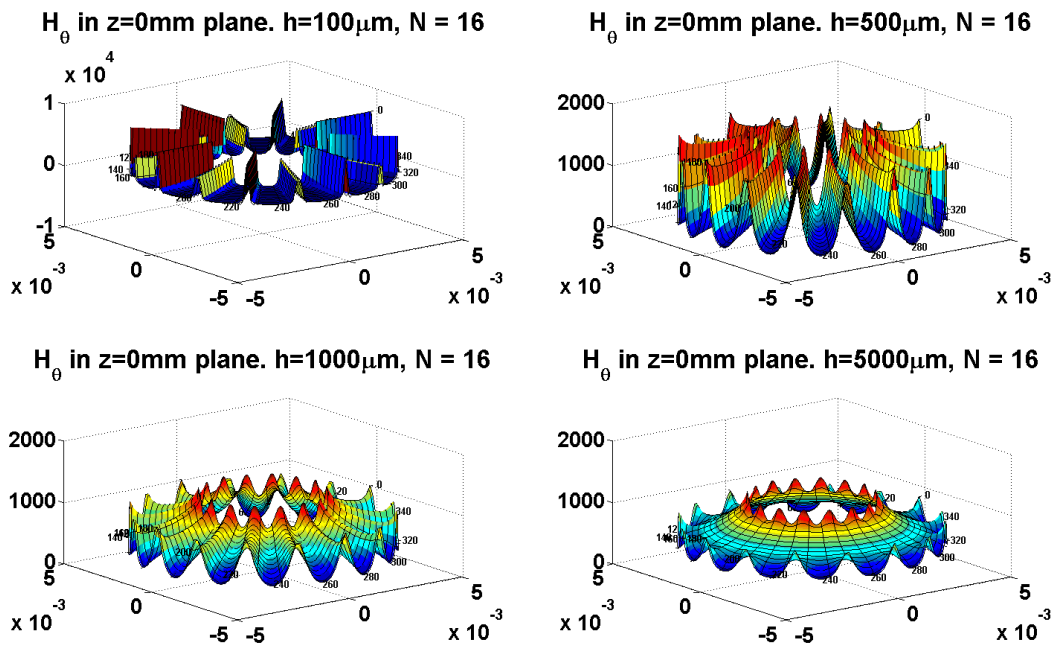


FIG. 7.38. Theta direction magnetic field around the core of an  $N=16$  toroid transformer with varying core height.

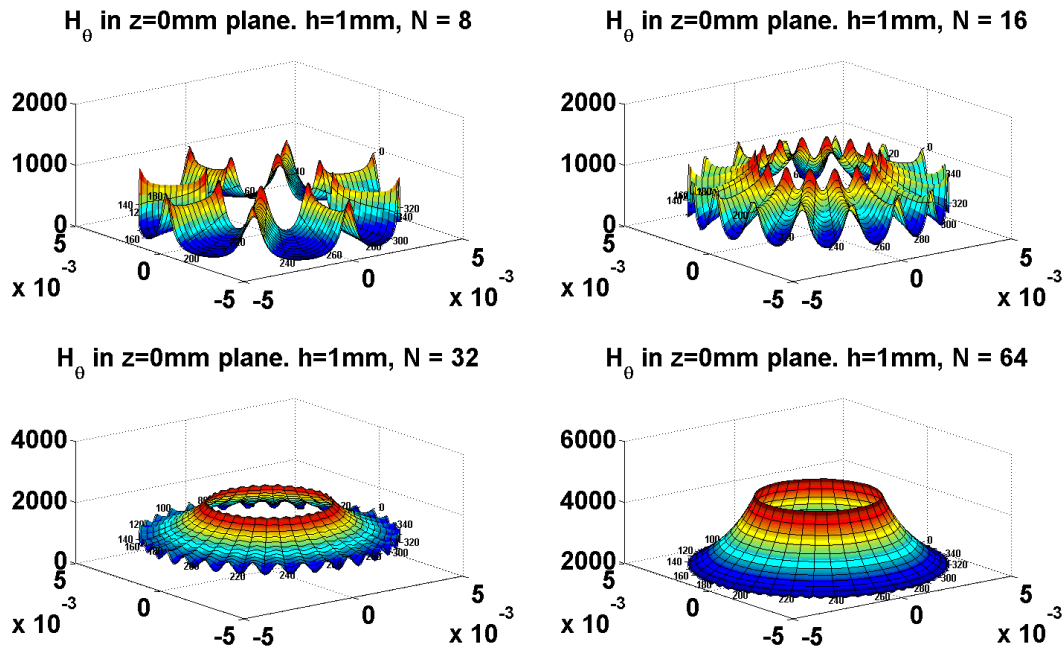


FIG. 7.39. Theta direction magnetic field around the core of an  $h=1\text{mm}$  toroid transformer with varying turn number.

### 7.3.3. Structure

The flux density has been determined for all points in space due to the excitation from a singular rectangular turn. The next goal is to determine the total flux that passes through each of the turns for a planar torus inductor. FIG. 7.32 has the turns for a 32-turn device superimposed on the field lines from a single turn. In the following analysis, the turn with current flowing through it giving rise to magnetic flux will be referred to as the *excited* or *source* turn (in magenta on FIG. 7.32). The other turns will be referred to as *observing* turns (green on FIG. 7.32). When the device is operating, however, each turn will be excited simultaneously (assumed to be in phase). If the observing turn were kept in a fixed position and the flux through the observing turn from the exciting turn were measured as the exciting turn was moved to each turn position, the sum of all flux measurements would be the total flux measured at the observing turn during operation. However, given the symmetry of the device, exciting a turn in a fixed position

and observing at all turn positions achieves the same result. The flux through a single turn when operating will be the sum of the flux measured at each turn with a single exciting turn, a reciprocal property.

Thus, to determine the flux through the turns when operating, it will suffice to leave the single exciting turn in a fixed position and measure the flux at all observing turns. The first thing to do would be to find the coordinates of all turns in space. This is where a key approximation of this analysis should be discussed. The real devices have helical windings. To analyze a helical winding would be considerably complex since the flux would need to be considered for each line of wire with a well-defined  $\hat{\phi}$  direction. In this analysis, we approximate the turns as planar and perpendicular to the  $\hat{\phi}$  direction of the torus. This approximation becomes more valid with high turn densities. So, finding the planar turn coordinates is a relatively simple task. Since the exciting turn is defined in the x-y plane, the orientation of the observing turns will be defined in x-z space.

First, the inner circle coordinates are found by dividing  $2\pi$  by the number of turns,  $N$ .

$$\theta_n = 2\pi \left( \frac{n}{N} \right) \quad 7.145$$

$$x_{n,inner} = b \cos(\theta_n) \quad 7.146$$

$$z_{n,inner} = b \sin(\theta_n) \quad 7.147$$

The dimensions of torus are defined as  $a$  for outer radius,  $b$  for inner radius, and  $h$  for height. The angle between the inner circle coordinates and the outer circle coordinates is the

same as the angle between the origin and the inner circle coordinates (a result of planar windings). Thus, to find the outer coordinates, use the same angle with a magnitude of  $(a-b)$ .

$$dx_n = (a - b) \cos(\theta_n) \quad 7.148$$

$$dz_n = (a - b) \sin(\theta_n) \quad 7.149$$

The absolute coordinates of the outer circle will then be given by the following.

$$x_{n,outer} = (a - b) \cos(\theta_n) + x_{n,inner} \quad 7.150$$

$$z_{n,outer} = (a - b) \sin(\theta_n) + z_{n,inner} \quad 7.151$$

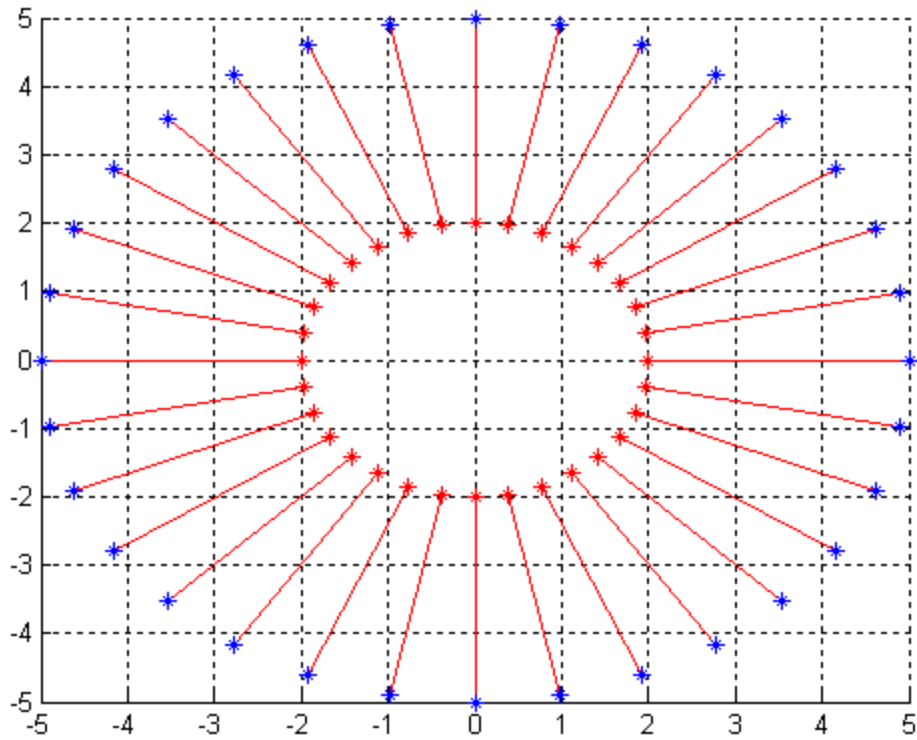


**FIG. 7.40. Observing turn locations around toroid.**

FIG. 7.40 shows the determined coordinates and the connecting lines of the turns for a 32-turn model.

To determine the total flux passing through each turn would mean integrating the dot product of the magnetic flux density and the cross sectional area element of the turn. First, the cross sectional area element must be defined for each turn. The turn is defined in three dimensional space, but the flux integral is only two dimensional across the plane of the turn. Consider FIG. 7.41.

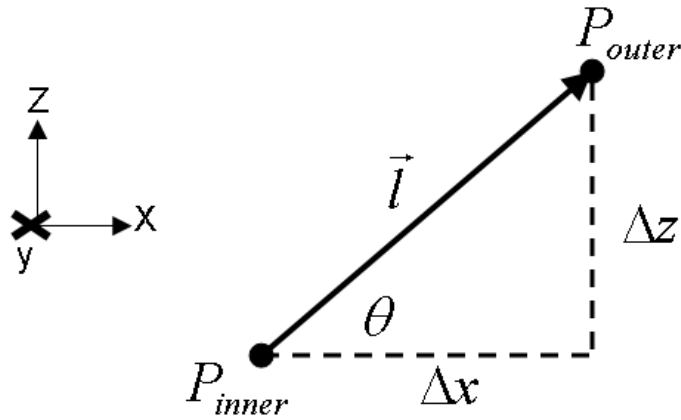


FIG. 7.41. Diagram of  $dA$  calculation.

$$\begin{aligned}\Delta x &= P_{x,outer} - P_{x,inner} \\ \Delta z &= P_{z,outer} - P_{z,inner}\end{aligned}\quad 7.152$$

The differential area element is the product of the  $y$  increment and the increment along line  $\vec{l}$  in the direction normal to the plane.

$$d\vec{A} = dy * dl * \hat{y} \times \hat{l} \quad 7.153$$

The direction of line  $\vec{l}$  is required to evaluate the cross product with the  $y$  direction.

$$\hat{l} = \frac{\vec{l}}{|\vec{l}|} = \frac{\hat{x}(\Delta x) + \hat{z}(\Delta z)}{\sqrt{(\Delta x)^2 + (\Delta z)^2}} \quad 7.154$$

The cross product is then given by the following. This is the direction of the differential area element.

$$\hat{y} \times \hat{l} = d\hat{A} = \begin{vmatrix} \hat{x} & \hat{y} & \hat{z} \\ 0 & 1 & 0 \\ \frac{(\Delta x)}{\sqrt{(\Delta x)^2 + (\Delta z)^2}} & 0 & \frac{(\Delta z)}{\sqrt{(\Delta x)^2 + (\Delta z)^2}} \end{vmatrix} = \hat{x} \frac{(\Delta z)}{\sqrt{(\Delta x)^2 + (\Delta z)^2}} - \hat{z} \frac{(\Delta x)}{\sqrt{(\Delta x)^2 + (\Delta z)^2}}$$

$$d\hat{A} = \hat{x} \frac{(\Delta z)}{\sqrt{(\Delta x)^2 + (\Delta z)^2}} - \hat{z} \frac{(\Delta x)}{\sqrt{(\Delta x)^2 + (\Delta z)^2}}$$

7.155

The magnitude of the differential area element is given by formula 7.156. The logic is taken directly from FIG. 7.41.

$$|d\vec{A}| = dy^* dl = dy^* \frac{dx}{\cos(\theta)} = \frac{dx^* dy}{\cos(\theta)} \quad 7.156$$

$$d\vec{A} = |d\vec{A}| d\hat{A} = \frac{dx^* dy}{\cos(\theta)} \left( \hat{x} \frac{(\Delta z)}{\sqrt{(\Delta x)^2 + (\Delta z)^2}} - \hat{z} \frac{(\Delta x)}{\sqrt{(\Delta x)^2 + (\Delta z)^2}} \right) \quad 7.157$$

An early conclusion is that since there is no y component of the differential area, then no flux in the y direction will add to the total flux since the y component of the dot product will be zero.

This is a result of the z-plane symmetry of each turn in the structure.

The z dummy variable in the flux integral can be expressed as x in the following way.

$$z_p = (x_p - x_0) \tan(\theta) + z_0 \quad 7.158$$

With expressions for flux density and differential area, the total flux can be calculated for a turn.

#### **4. Total Flux**

The total flux through a turn will be the integral of the dot product of flux density and differential area over the cross section of the turn.

$$\psi_n = \int_{A_n} \vec{B}(x, y, z) \cdot d\vec{A}$$

7.159

$$\begin{aligned}
\psi_n &= \int_{A_h} \vec{B}_x(x, y, z) \cdot dA_x + \int_{A_h} \vec{B}_z(x, y, z) \cdot dA_z \\
&= \frac{(\Delta z)}{\cos(\theta) \sqrt{(\Delta x)^2 + (\Delta z)^2}} \int_{A_h} dx^* dy (B_{SLx}(x, y, z) + B_{SRx}(x, y, z)) \\
&\quad - \frac{1}{\cos(\theta)} \left( \frac{(\Delta x)}{\sqrt{(\Delta x)^2 + (\Delta z)^2}} \int_{A_h} dx^* dy (B_{SLz}(x_p, y_p, z_p) + B_{SRz}(x_p, y_p, z_p)) + B_{SEz}(x_p, y_p, z_p) \right)
\end{aligned}$$

7.160

Beginning with the x component terms of equation 7.158, consider the following.

$$\frac{(\Delta z)}{\cos(\theta)\sqrt{(\Delta x)^2 + (\Delta z)^2}} \int_{A_n} dx^* dy \left( \begin{array}{l} \frac{\mu_0 |\hat{I}| z_p}{2\pi(4c-b^2)} \left[ \frac{(2y_{SL,1}+b)}{\sqrt{y_{SL,1}^2 + by_{SL,1} + c}} - \frac{(2y_{SL,0}+b)}{\sqrt{y_{SL,0}^2 + by_{SL,0} + c}} \right] \\ - \frac{\mu_0 |\hat{I}| z_p}{2\pi(4c-b^2)} \left[ \frac{(2y_{SR,1}+b)}{\sqrt{y_{SR,1}^2 + by_{SR,1} + c}} - \frac{(2y_{SR,0}+b)}{\sqrt{y_{SR,0}^2 + by_{SR,0} + c}} \right] \end{array} \right) \quad 7.161$$

Taking the first term of 7.161 gives the following.

$$\begin{aligned} & \frac{(\Delta z)}{\cos(\theta)\sqrt{(\Delta x)^2 + (\Delta z)^2}} \int_{A_n} dx^* dy \left( \frac{\mu_0 |\hat{I}| z_p}{2\pi(4c-b^2)} \left[ \frac{(2y_{SL,1}+b)}{\sqrt{y_{SL,1}^2 + by_{SL,1} + c}} - \frac{(2y_{SL,0}+b)}{\sqrt{y_{SL,0}^2 + by_{SL,0} + c}} \right] \right) \\ &= \frac{\mu_0 |\hat{I}|}{2\pi} \frac{(\Delta z)}{\cos(\theta)\sqrt{(\Delta x)^2 + (\Delta z)^2}} [Integral, SLx] \end{aligned} \quad 7.162$$

$$[Integral, SLx] = \int_x dx \frac{1}{(4[(x_p - x_{SL,0})^2 + (z_p)^2])} \int_y dy \left[ \frac{(2y_{SL,1} - 2y_p)}{\sqrt{y_{SL,1}^2 - 2y_p y_{SL,1} + (x_p - x_{SL,0})^2 + (z_p)^2 + y_p^2}} - \frac{(2y_{SL,0} - 2y_p)}{\sqrt{y_{SL,0}^2 - 2y_p y_{SL,0} + (x_p - x_{SL,0})^2 + (z_p)^2 + y_p^2}} \right] \quad 7.163$$

$$[Integral, SLx] = \int_x \frac{1}{(4[(x_p - x_{SL,0})^2 + (z_p)^2])} \int_y dy_p \left[ \frac{-(2y_p + b_1)}{\sqrt{c_1 + b_1 y_p + y_p^2}} + \frac{(2y_p + b_2)}{\sqrt{c_2 + b_2 y_p + y_p^2}} \right] \quad 7.164$$

$$\begin{aligned} a_1 &= 1 \\ b_1 &= -2y_{SL,1} \\ c_1 &= y_{SL,1}^2 + (x_p - x_{SL,0})^2 + (z_p)^2 \end{aligned} \quad 7.165$$

$$\begin{aligned} a_2 &= 1 \\ b_2 &= -2y_{SL,0} \\ c_2 &= y_{SL,0}^2 + (x_p - x_{SL,0})^2 + (z_p)^2 \end{aligned} \quad 7.166$$

The indefinite integral of 7.164 can be found in a table but depends on the numerical value a, b, and c. The integral has four separate forms depending on which of a, b, and c is larger. Since this integral must be calculated for multiple positions in space, it is impractical to calculate the integral for all four cases of a, b, and c. Since a, b, and c are made up in part by dummy variables, the integral would have to be broken up into different regions where a particular form is valid.

For this reason, the above analysis from equation 7.161 up through equation 7.164 was given just to show the complexity of the analysis and to justify the following action. To evaluate this integral, numerical methods will be used. The approach is based on Simpson's Rule where integrable polynomial curves are fitted to the non-integrable function (in this case, the dot product of area and the three dimensional magnetic flux). The polynomials are then integrated to give a numerical result.

Thus, by properly substituting equation 7.158 into the flux density expressions, taking the dot product with  $d\vec{A}$ , a MATLAB function can be written that can be integrated in MATLAB's numerical quadrature integrator. In the following section are the results.

### **5. Inductance (Self, Mutual, Leakage)**

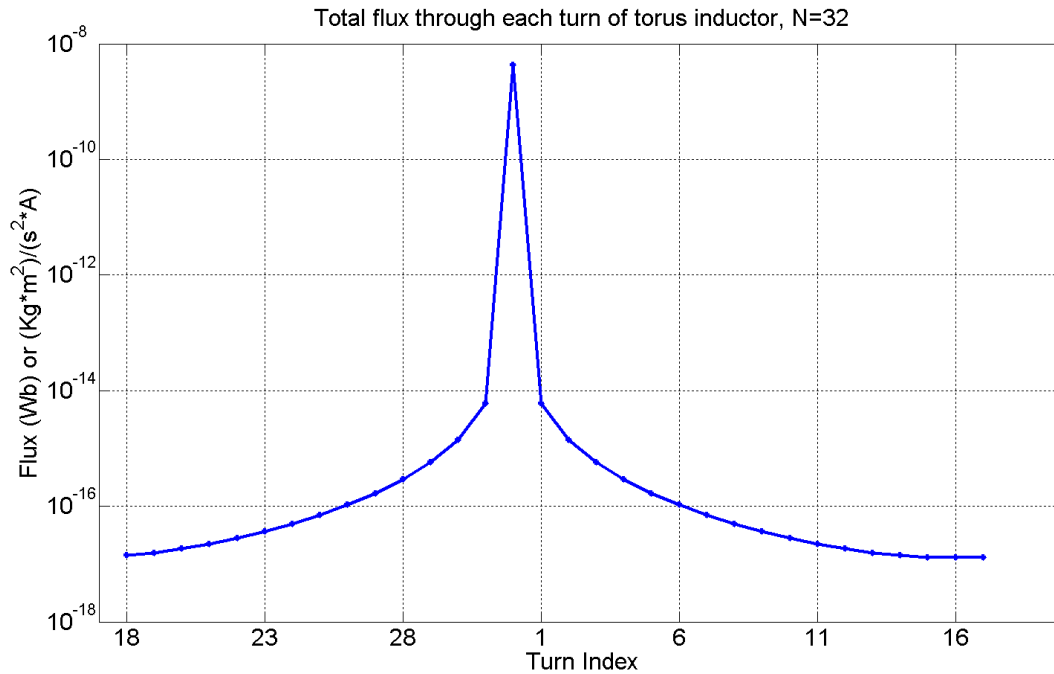


**FIG. 7.42. Total normal flux through turns as numbered in FIG. 7.43, N = 32.**

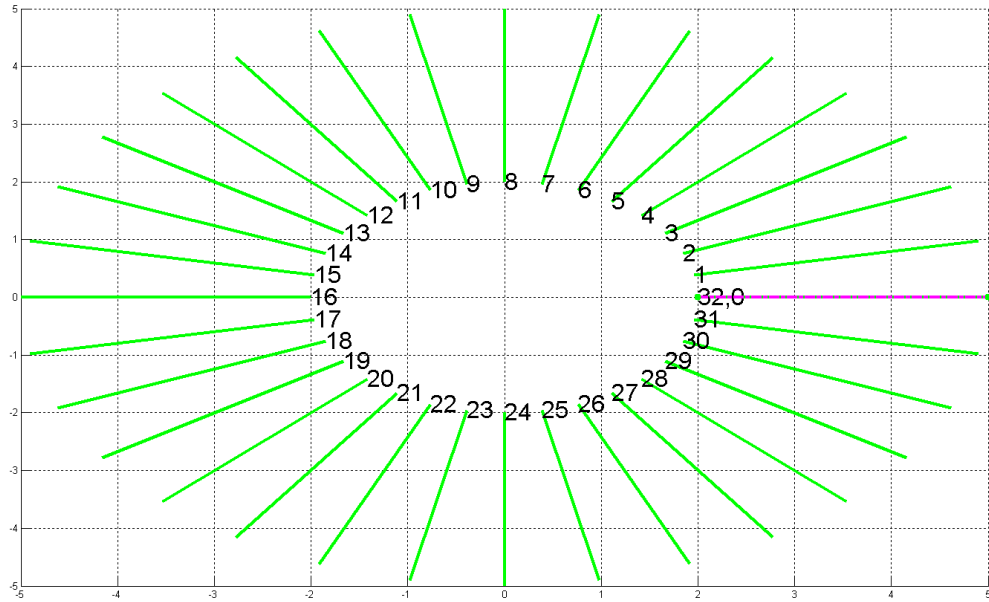


**FIG. 7.43. Primary toroid winding indexed turn map, N = 32.**

Summing the flux from all of the turns for N=32 and h=2 microns gives a total flux through the core of a single turn during operation to be **2.64 nWb**. Since these simulations were carried out with a 1 A current, the inductance (defined as N times Flux per current,  $L = \frac{N\phi}{I}$ ) is **84.41 nH** for N = 32. Following an identical approach for N=128 gives the following.

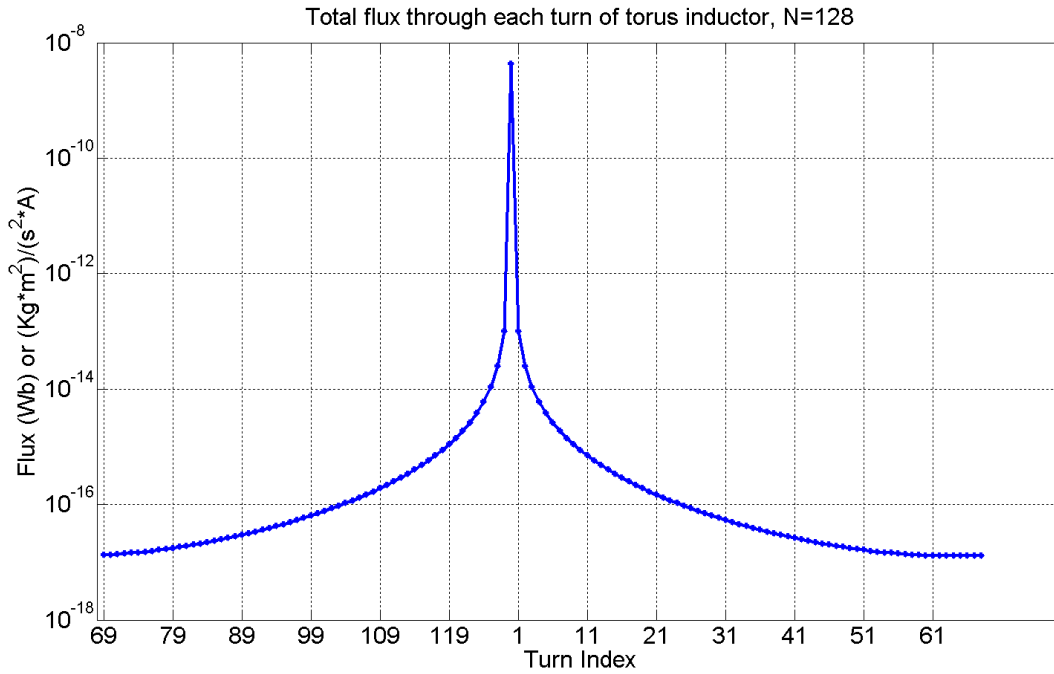


**FIG. 7.44. Total normal flux through turns as numbered in FIG. 7.45, N = 128.**

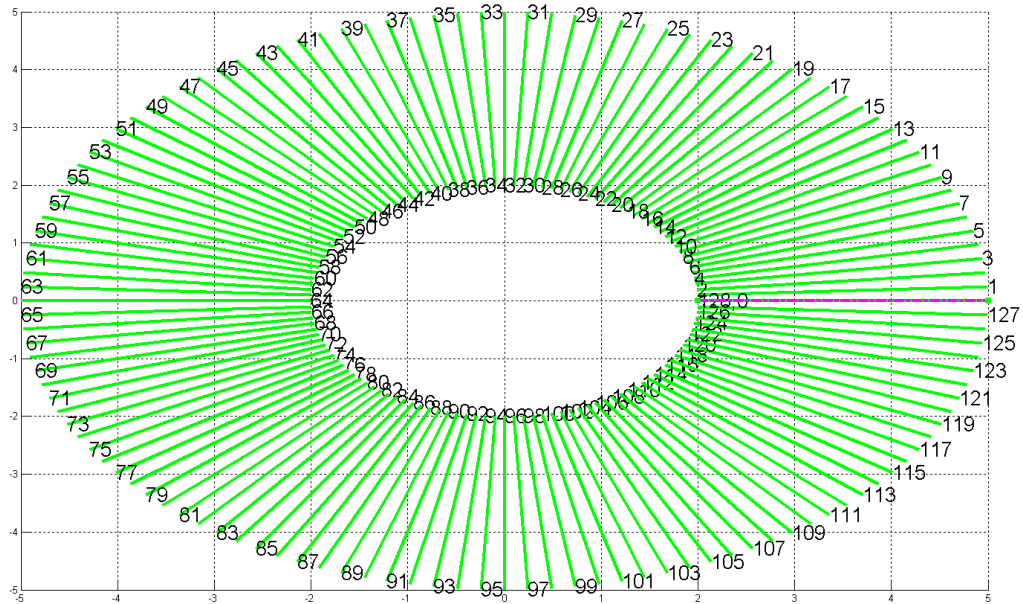


**FIG. 7.45. Primary toroid winding indexed turn map, N = 128.**

The inductance of the N=128 winding is found to be  $337.69nH$ . The results for different turn densities are given in the table below.

**Table 7.8. Analytical inductance for toroid rectangular cross-section transformers with various turn numbers (h = 2 $\mu$ m, a = 5mm, b = 2mm).**

<i>N</i>	<i>Inductance</i>
16	42.2049nH
32	84.4103nH
64	168.8253nH
128	337.689nH
256	675.6888nH
512	1353.8754nH
1024	2727.6835nH

The values in the above table are self inductance values. If this device is to act as a transformer, the flux must be determined at the locations of the secondary turns, which will be in between the primary turns. The difference of the self inductance and the mutual inductance will be the leakage inductance of the model.

A small modification to the coordinates function gives the results for the secondary turn flux. The secondary turn flux (mutual flux) and leakage flux are used again to find the corresponding inductances which are given below.

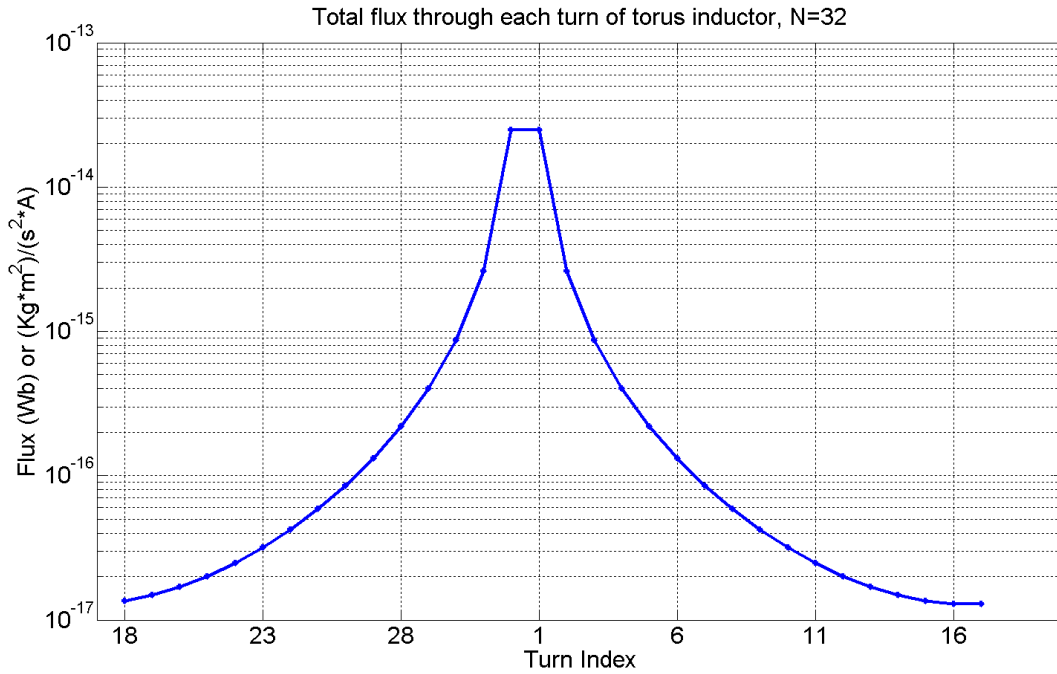


**FIG. 7.46.** Total normal flux through turns as numbered in FIG. 7.47, N = 32.

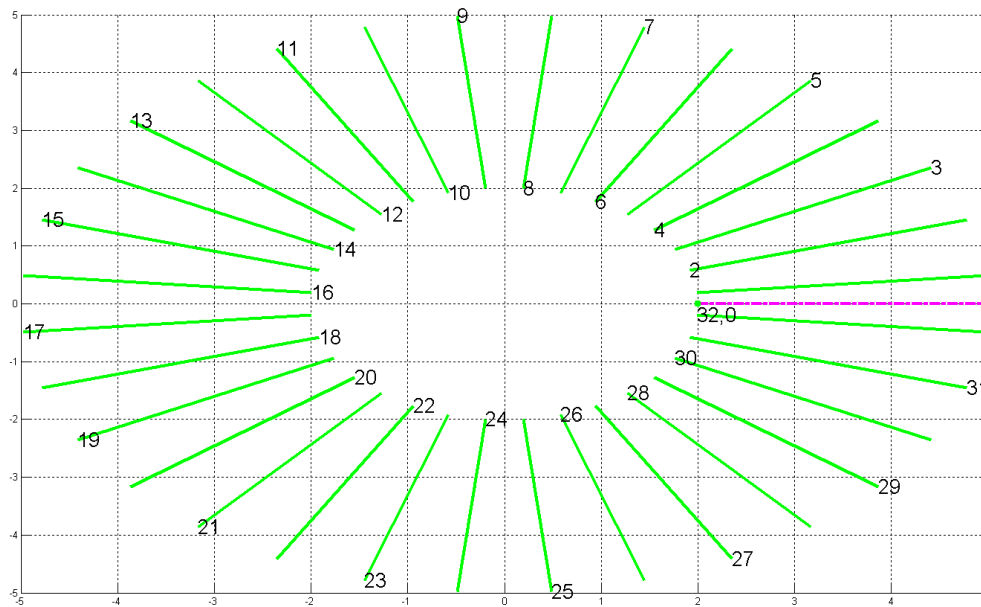


**FIG. 7.47.** Secondary toroid winding indexed turn map, N = 32.

**Table 7.9. Analytical mutual and leakage inductance for toroid rectangular cross-section transformers with various turn numbers ( $h = 2\mu\text{m}$ ,  $a = 5\text{mm}$ ,  $b = 2\text{mm}$ ).**

$N$	<i>Mutual Inductance</i>	<i>Leakage Inductance</i>
16	0.27876pH	42.2046nH
32	2.3438pH	84.408nH
64	19.205pH	168.8061nH
128	155.41pH	337.5336nH
256	1.2489nH	674.44nH
512	9.9663nH	1343.9091nH
1024	168.1132nH	2559.5703nH

**Table 7.10. Ratios of calculated mutual and leakage inductance to self inductance for various turn numbers.**

$N$	<i>Mutual Inductance ratio (<math>L_m / L</math>)</i>	<i>Leakage Inductance ratio (<math>L_l / L</math>)</i>
16	6.6049e-006	0.99999
32	2.7767e-005	0.99997
64	1.1376e-004	0.99989
128	4.6022e-004	0.99954
256	0.0018	0.99815
512	0.0074	0.99264
1024	0.0616	0.93837

### 7.3.4. Nested windings

The idea of using nested windings to minimize leakage inductance is a current topic for research in air-core power transformers. Nested windings are a winding layout in which the secondary is wrapped around the primary, rather than next to the primary (bifilar wound) around the core (See FIG. 7.48). In this manner, the primary windings can be wound considerably tighter, reducing leakage flux. Since the secondary winding still shares a large percentage of its cross-sectional area with the primary, the flux of the primary will be shared with the secondary. As a final consideration for their use in Ethernet transformers, the numerical inductance analysis can be used to evaluate the structure's reduction in leakage inductance.

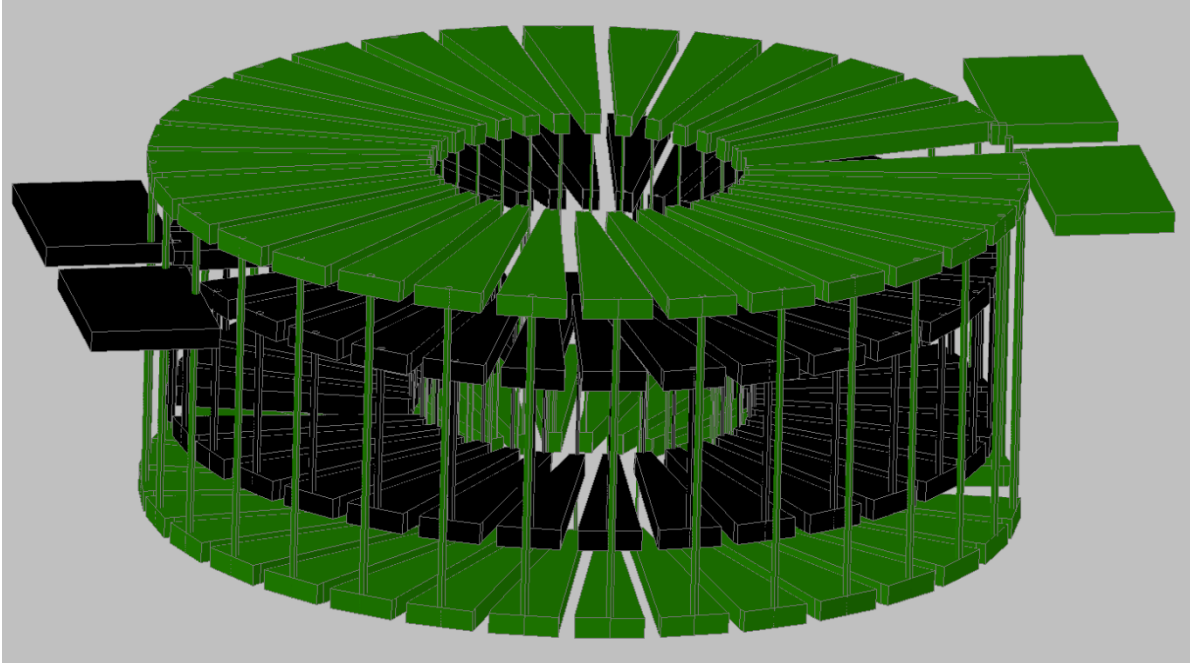


**FIG. 7.48. 3D rendering of a nested winding thin-film transformer structure.**

Consider a single nested turn, with the secondary on the outside and the primary on the inside. The initial catch to nested windings is that some of the secondary turn cross-sectional area is outside the interior cross-sectional area of the primary turn. Recall that within the interior area, the primary flux will all be in the same direction (call it the *positive* direction). Outside of this area in the plane of the turn, the flux will return in the negative direction. The net flux within the secondary turn will be the sum of the primary turn positive interior area flux and the negative return flux. However, this return flux is leakage flux. By tightly packing the primary winding this flux should be minimized. Also, by making the nesting gap (distance between primary and secondary wires) small, the area of negative return flux is minimized. The areas of positive and negative flux through the nested windings are shown in FIG. 7.49. The figure shows a top view of the nested turns in the X-Z, with the cross-section of the turns in the X-Y plane.

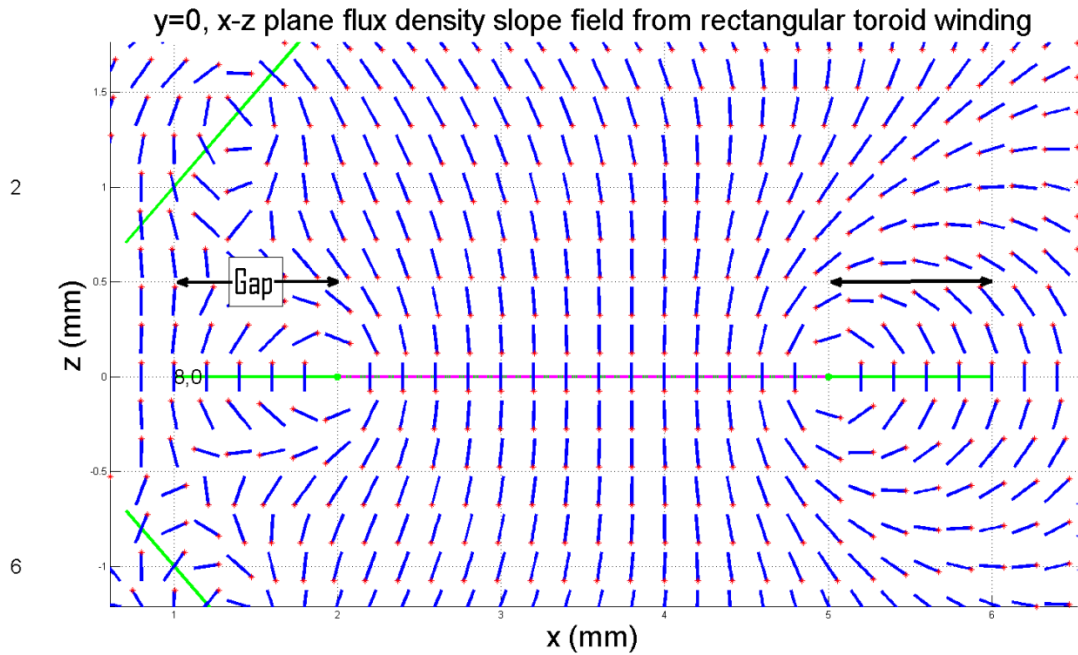


FIG. 7.49. Magnetic slope field around nested windings: Primary = Magenta, Secondary = Green.

As can be seen in table, nesting the windings would significantly decrease leakage inductance. Also shown in the table is the leakage inductance dependence on gap size, where larger gaps have poorer coupling. As expected, increasing the number of turns also improves leakage inductance as a percentage of self inductance.

Table 7.11. Nested-winding numerical inductance analysis values.

N	Gap	$L_{\text{Self}}$ (nH)	$L_{\text{Mutual}}$ (nH)	$L_{\text{Leakage}}$ (nH)	$L_{\text{Leakage}}/L_{\text{self}}$
8	1mm	139	25	114	0.82
16	1mm	306	94	212	0.69
32	1mm	758	375	383	0.51
64	1mm	2181	1501	680	0.31
8	1 $\mu$ m	139	117	22	0.16
16	1 $\mu$ m	306	262	44	0.14
32	1 $\mu$ m	758	670	88	0.12
64	1 $\mu$ m	2181	2006	175	0.08

#### **7.4. PVC-core measured and predicted value comparison**

To validate the numerical inductance calculation methods and the cross-winding capacitance calculation method, a comparison of the measured values and the numerically calculated values is given in Table 7.12 for the PVC core transformer. The table shows that for mutual and leakage inductance, the numerical method predicts slightly lower than what was measured. It is difficult to reason why this is the case, but it can be written that the model structure is ideal and the real structure does not match the model perfectly. It is possible that the real helical windings give higher inductance than what is numerically predicted for planar turns.

For cross-winding capacitance, the numerical method predicts slightly higher than what was measured. This can be easily explained from a few different causes. The windings were not perfectly wrapped around the PVC, leaving a small air gap in between the wires and the surface of the PVC-core. This would cause the measured capacitance to be lower than the predicted capacitance. Also, it is possible that the dielectric constant used in the numerical prediction was not the exact dielectric constant of the PVC-core material used, the difference being the result of subtle manufacturing process variations that would not be important to the average user.

Ultimately, however, with all of the assumptions and all of the unknown variables, the numerical predictions land relatively close to what was measured, supporting the validity of the numerical methods. More comparisons should be performed in the future.

**Table 7.12. Comparison of measured and predicted inductance and capacitance for the large PVC-core transformer.**

<i>Device</i>	<i>Mutual Inductance(<math>\mu H</math>)</i>			<i>Leakage Inductance(<math>\mu H</math>)</i>		<i>Cross-winding capacitance (pF)</i>	
	<i>Measured</i>	<i>Theory</i>	<i>Numerical</i>	<i>Measured</i>	<i>Numerical</i>	<i>Measured</i>	<i>Numerical</i>
PVC-core transformer	30	26.3	25.6	2-2.5	1.9	600	691

## 7.5. Summary

In this chapter, dielectric-core rectangular cross-section toroid transformers were thoroughly discussed. A successful fabrication process for thin-film transformers was given. Theoretical devices with rectangular metal lines and wedge-shaped metal lines were analyzed to extract resistance, capacitance, and inductance. Fabricated rectangular-line devices were tested and their performance was presented. A fabricated wedge-lined transformer was also tested and its performance results were shown. Of the fabricated devices, the best performance was found for a 32-turn rectangular-lined transformer when loaded with  $100\Omega$ .

In the last section of the chapter, work to analytically and numerically calculate inductance from the theoretical dielectric-core toroid structures was described. Slope field plots offered insight into the coupling field behavior between the turns of the dielectric-core device with changing  $N$ , core height, and winding placement. Though the fabrication process length would increase by a factor of three, preliminary results for nested winding inductance suggests that nested structures would give superior performance.

## Chapter 8 : Summary

### 8.1. Problem restatement and chapter review

In the past two decades, Ethernet computer networking has evolved from thick coaxial cable that was difficult to connect and expensive to maintain. It has evolved into inexpensive and easy to use unshielded twisted pair cable and a data rate increase by a factor of 1000. Ethernet has left the office and entered the home as cable television companies expanded to supply broadband internet access. Twisted pair Ethernet has, indeed, flourished.

With the proliferation of twisted pair Ethernet, Ethernet transformers have stepped out as a special type of especially broadband and especially miniature electrical isolation coupler. However, current ferrite-core Ethernet transformer technology is reaching a performance limit as Ethernet devices become smaller. The future of twisted pair Ethernet requires an isolation coupler that is small and can be fabricated on a chip while still satisfying the isolation and bandwidth requirements of Ethernet.

Before new isolation couplers can be considered, the performance requirements of Ethernet (specifically the *IEEE Ethernet standard* [25]) must be understood. The standard outlines bandwidths for differential and common-mode signals as well as electrical isolation requirements. These modes and the concept of electrical isolation is discussed in chapter 2 and used throughout this dissertation.

To truly understand the problem and the performance requirements, current ferrite transformers were tested and modeled. The discussion of modeling and testing transformers spans chapters 3, 4, 5, and 6. Chapter three describes the use of a well-known lumped equivalent circuit. Chapter 4 outlines scalar transformer tests to extract equivalent circuit parameters.

Chapter 5 discusses and describes the novel work done on distributed transformer modeling in both the differential and common modes. Chapter 6 ties the previous chapters together. Chapter 6 outlines high frequency vector measurements of the transformer and the use of equivalent models to extract device parameters. The extracted parameters were then used in the models of chapter 3 and 5 and compared with the measured data. It was found that initially, the lumped element equivalent circuit gave a better match to the measurement. However, there were measurement features that the lumped element equivalent circuit would not be capable of reproducing. By tuning the distributed model parameter values, the distributed models were found to give an exceptional match to the data. It was concluded that the relationship between the measured extracted parameters and the distributed model parameters must be more thoroughly researched in the future.

Chapter 7 describes the work done to fabricate and test a thin-film dielectric-core transformer. Over the course of many months, a process was developed and multiple toroidal transformers were fabricated. It was concluded that the best performance was found for a 32-turn transformer loaded with  $100\Omega$ . Also in chapter 7 are thorough analyses to predict resistance, inductance, and cross winding capacitance of the fabricated transformer structures. Analytical and numerical methods to determine the mutual and leakage inductances of the fabricated transformers were derived and implemented. Tangential to that effort, magnetic flux density slope fields were plotted and insight was gained into the behavior of toroidal winding flux with a non-magnetic core. In the final section of chapter 7, a new nested winding structure was proposed and it was shown to have minimal leakage inductance.

## 8.2. Future work

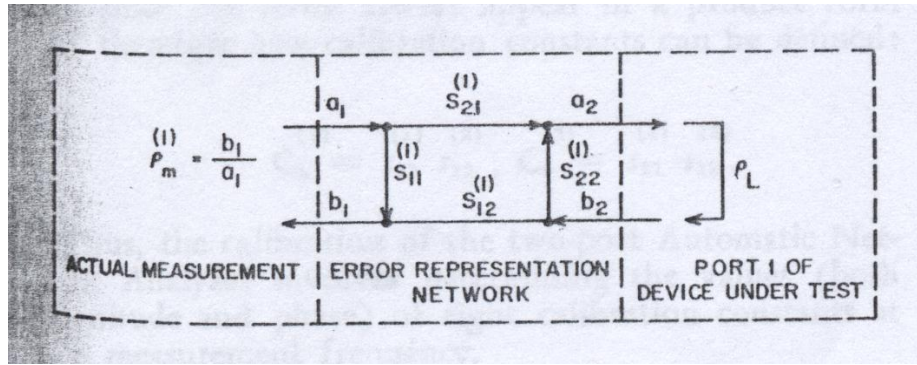
Of the many topics considered over the course of this dissertation, following are the topics that warrant future research as well as some entirely new topics.

1. Distributed model parameters need to be related more intelligently to the extracted parameters. Perhaps, also, the extraction procedure can be revised to specifically extract distributed model parameters. A reliable and practically usable model would be a great advantage to Ethernet transformer design.
2. The fabrication process should be modified for thicker metal layers and thicker core heights. Thicker cores will boost inductance, while thicker metal will reduce resistance and improve power coupling. Thick photoresists are a viable option to thicken the core, while electroplated copper is the best option to make thick metal layers.
3. A process should be developed to fabricate a nested winding transformer. Nesting the windings will add at least 4 layers to the structure, significantly increasing the process length. The nested windings should also be theoretically evaluated for resistance, inductance, and capacitance before a process is developed.
4. The possibility of a capacitive isolation coupler should be explored. Though capacitive couplers will pass common-mode interference, secondary common-mode suppression techniques can be used, such as a differential amplifier. Capacitors would be easily fabricated and, if made thick enough, would easily pass the isolation requirements.

## **Appendix A : VNA calibration theory**

Vector network analyzers (or automatic network analyzers) first appeared in the early 1960's. Engineers soon realized that to improve the accuracy of their measurements, certain measurement errors needed to be corrected. The errors can be classified in the following three ways: systematic errors, random errors, and drift errors. Systematic errors are due to deviations and imperfections in the system, like the varying frequency response of the receiver or impedance mismatches in connection hardware. Random errors occur from spontaneous noise or interference, or other random fluctuations in system components. Drift errors occur due to cyclical drifts of system hardware, usually dependent on temperature or humidity. In theory, frequent calibrations should control systematic and drift errors, but not random errors. Each error source need not be precisely identified, only the total error effect needs to be characterized and factored out of the overall measurement.

The above classification of error sources gives a conceptual picture of why error correction is needed, but doesn't offer any information about analysis and correction methods. The above errors must be formed into a model that can be analyzed. In 1968, Richard Hackborn of Hewlett Packard published the first and often referenced article describing the error model and how to analyze it, using a technique still used today [44]. As will be described in detail below, Hackborn outlined the necessary 1-port and 2-port calibration measurements to measure the eight error terms of his model. Hackborn began his analysis by connecting the 1-port error model (shown in Appendix Fig. A.1) to the error sources discussed above. Hackborn conducts his analysis using signal flow graphs, as nearly all papers on this topic do. In signal flow graphs, ' $a$ ' terms generally indicate signals into a port and ' $b$ ' terms generally indicate signals out of a port. However, this convention can be superseded by directed branches of the flow graph.



Appendix Fig. A.1. 1-port error model from Hackborn's 1968 article [44].

As discussed in Hackborn's article, the above error terms arise from the error sources as follows.  $s_{11}^{(1)}$  represents directivity errors and reference (applied) and test (through the DUT) signal isolation.  $s_{22}^{(1)}$  represents impedance mismatch errors between the characteristic system impedance and the real source impedance, partly due to the connectors.  $s_{12}^{(1)}$  and  $s_{21}^{(1)}$  represent the different frequency responses (tracking) of the reference channel (input signal) and measurement channel (reflection). The superscript in parentheses indicates to which port the error term is connected. Though Appendix Fig. A.1 shows  $s_{XY}^{(1)}$  as the error terms, the same model applies to port 2 as  $s_{XY}^{(2)}$ .

To characterize the 1-port error model, Hackborn describes the SOL ('S' = *short*, 'O' = *open*, 'L' = *matched load*) set of calibration measurements. Through these measurements, three error terms of the above model can be found. With the 1-port model, there exists only one scattering measurement: reflection. The analysis of the 1-port error signal flow graph gives equations to determine the error parameter values.

$$\rho_m = \frac{b_1}{a_1} \quad \text{A.1}$$

To determine the reflected signal from the above signal flow graph, the non-touching loop rule is used [45]. The non-touching loop rule is an application of infinite geometric series sums generalized to 2-port networks. Details on the rule can be found in reference [45].

$$T = \frac{P_1(1 - \sum L_1^{(1)} + \sum L_2^{(1)} - \sum L_3^{(1)} \dots) + P_2(1 - \sum L_1^{(2)} + \sum L_2^{(2)} - \sum L_3^{(2)} \dots) + P_3(1 - \dots) + \dots}{(1 - \sum L_1 + \sum L_2 - \sum L_3 \dots)} \quad \text{A.2}$$

The general procedure requires the identification of all paths between the signal nodes of interest and the identification of all first and second order loops. The first order loop is defined as any closed path with all branches in the same direction along the path. Second order loops are defined as the product of two non-touching first order loops; third order loops are the product of three non-touching first order loops; etc. See reference [45] for examples of determining loop orders. Loops are identified by the notation  $L_A^{(B)}$ , where  $A$  indicates the loop order, and  $B$  indicates to which path the loop shares *no* branches. To indicate *all* loops of a given order in a signal flow graph, the  $B$  index is omitted. In the 1-port analysis of Appendix Fig. A.1, two paths exist between  $b_1$  and  $a_1$ .

$$P_1 = s_{11}^{(1)} \quad \text{A.3}$$

$$P_2 = s_{21}^{(1)} \rho_L s_{12}^{(1)}$$

Also, only one loop exists, which is of first order.

$$\begin{aligned} \sum L_1^{(1)} &= \sum L_1 = s_{22}^{(1)} \rho_L \\ \sum L_1^{(2)} &= 0 \end{aligned} \quad \text{A.4}$$

The measured reflection coefficient ( $\rho_m^{(1)}$ ) is then given by the non-touching loop rule (equation A.2).

$$\rho_m^{(1)} = \frac{b_1}{a_1} = \frac{s_{11}^{(1)}(1 - s_{22}^{(1)}\rho_L) + s_{21}^{(1)}\rho_L s_{12}^{(1)}}{1 - s_{22}^{(1)}\rho_L} = s_{11}^{(1)} + \frac{s_{21}^{(1)}\rho_L s_{12}^{(1)}}{1 - s_{22}^{(1)}\rho_L} \quad \text{A.5}$$

Similarly, for the port 2 error parameters, the reflection coefficient is defined as follows.

$$\rho_m^{(2)} = s_{11}^{(2)} + \frac{s_{21}^{(2)}\rho_L s_{12}^{(2)}}{1 - s_{22}^{(2)}\rho_L} \quad \text{A.6}$$

Now, to extract the error network parameter values, Hackborn outlined the three necessary measurements by measuring the reflection with different loads: open, short, and broadband matched load. The three loads imply the following three reflection coefficients.

$$\rho_{L,Open} = 1 + j0 \quad \text{A.7}$$

$$\rho_{L,Short} = -1 + j0 \quad \text{A.8}$$

$$\rho_{L,Load} = 0 + j0 \quad \text{A.9}$$

The three loaded reflection coefficients give three equations for the measured reflection, from which three error model parameter values can be derived.

$$\rho_{m,Load}^{(1)} = s_{11}^{(1)} = C_1^{(1)} \quad \text{A.10}$$

$$\rho_{m,Open}^{(1)} = s_{11}^{(1)} + \frac{s_{21}^{(1)}s_{12}^{(1)}}{1 - s_{22}^{(1)}} = C_1^{(1)} + \frac{s_{21}^{(1)}s_{12}^{(1)}}{1 - s_{22}^{(1)}} \quad \text{A.11}$$

$$(\rho_{m,Open}^{(1)} - C_1^{(1)})(1 - s_{22}^{(1)}) = s_{21}^{(1)}s_{12}^{(1)}$$

$$\rho_{m,Short}^{(1)} = s_{11}^{(1)} - \frac{s_{21}^{(1)}s_{12}^{(1)}}{1 + s_{22}^{(1)}} = C_1^{(1)} - \frac{s_{21}^{(1)}s_{12}^{(1)}}{1 + s_{22}^{(1)}} \quad \text{A.12}$$

$$(\rho_{m,Short}^{(1)} - C_1^{(1)})(1 + s_{22}^{(1)}) = -s_{21}^{(1)}s_{12}^{(1)} = (-\rho_{m,Open}^{(1)} + C_1^{(1)})(1 - s_{22}^{(1)})$$

$$\rho_{m,Short}^{(1)} + \rho_{m,Open}^{(1)} - 2C_1^{(1)} = s_{22}^{(1)}(\rho_{m,Open}^{(1)} - \rho_{m,Short}^{(1)})$$

$$s_{22}^{(1)} = \frac{\rho_{m,Short}^{(1)} + \rho_{m,Open}^{(1)} - 2C_1^{(1)}}{(\rho_{m,Open}^{(1)} - \rho_{m,Short}^{(1)})} = C_2^{(1)}$$

$$s_{21}^{(1)}s_{12}^{(1)} = (\rho_{m,Open}^{(1)} - C_1^{(1)})(1 - s_{22}^{(1)}) = (\rho_{m,Open}^{(1)} - C_1^{(1)})\left(1 - \frac{\rho_{m,Short}^{(1)} + \rho_{m,Open}^{(1)} - 2C_1^{(1)}}{(\rho_{m,Open}^{(1)} - \rho_{m,Short}^{(1)})}\right) \quad \text{A.13}$$

$$s_{21}^{(1)}s_{12}^{(1)} = \frac{2(\rho_{m,Open}^{(1)} - C_1^{(1)})(C_1^{(1)} - \rho_{m,Short}^{(1)})}{(\rho_{m,Open}^{(1)} - \rho_{m,Short}^{(1)})} = C_3^{(1)}$$

Similarly, for port 2, the error parameters are given by the following equations.

$$\rho_{m,Load}^{(2)} = s_{11}^{(2)} = C_1^{(2)}$$

A.14

$$s_{22}^{(2)} = \frac{\rho_{m,Short}^{(2)} + \rho_{m,Open}^{(2)} - 2C_1^{(2)}}{(\rho_{m,Open}^{(2)} - \rho_{m,Short}^{(2)})} = C_2^{(2)}$$

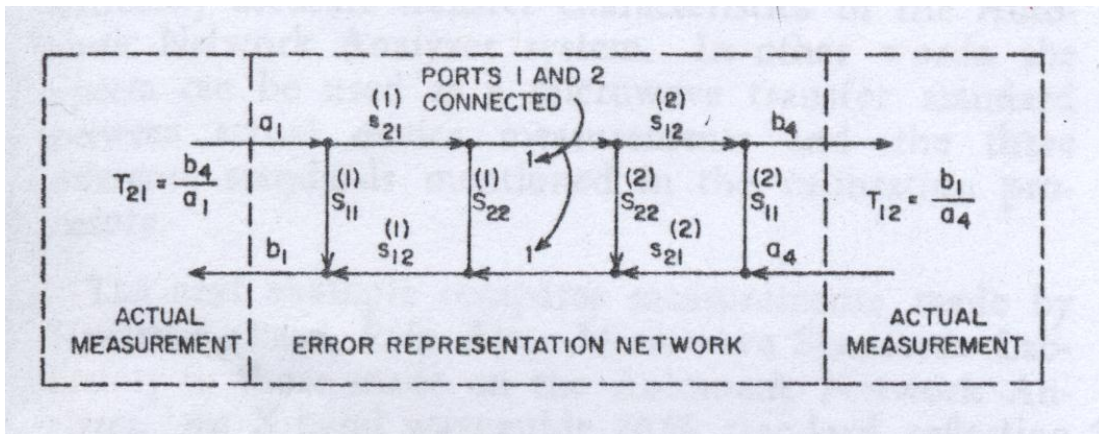
A.15

$$s_{21}^{(2)} s_{12}^{(2)} = \frac{2(\rho_{m,Open}^{(2)} - C_1^{(2)})(C_1^{(2)} - \rho_{m,Short}^{(2)})}{(\rho_{m,Open}^{(2)} - \rho_{m,Short}^{(2)})} = C_3^{(2)}$$

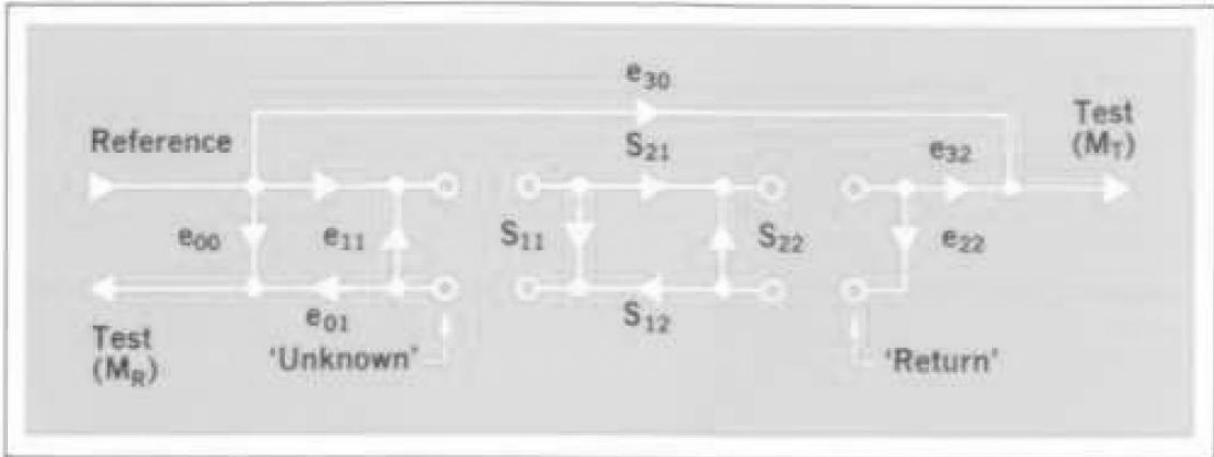
A.16

Equations A.10 through A.16 give six error terms. Two more terms can be found by analyzing the *through* connection. Hackborn's *through* model was symmetric and is shown in Appendix Fig. A.2. However, the error model has evolved since Hackborn's 1968 paper.

B. P. Hand, also of Hewlett-Packard, published an article in February of 1970 modifying the error model making it non-symmetric and requiring different forward and reverse direction models [46]. The modification made by Hand added a reflection signal path on the model port opposite the applied signal port, as shown in Appendix Fig. A.3.

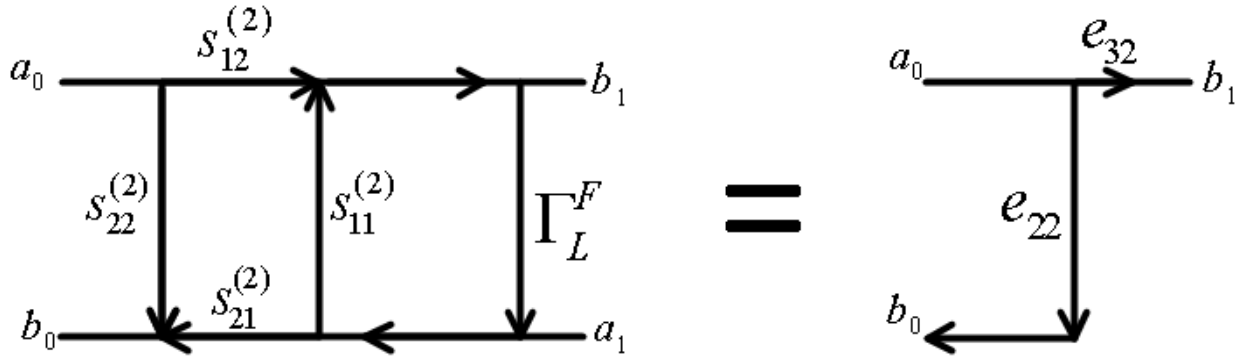


Appendix Fig. A.2. Hackborn's obsolete *through* connection error model [44].



Appendix Fig. A.3. B. P. Hand's depiction of the modern VNA error model [46].

In the forward model, Hand has replaced the complicated port 2 error network and reflection branch with simple transmission ( $e_{32}$ ) and reflection ( $e_{22}$ ) branches. Hand has also added the port isolation term,  $e_{30}$ , which represents signal flow from ports that are disconnected and terminated. In Hand's model,  $e_{22}$  is an effective reflection branch, defined by both the original port 2 error network and the new reflection branch ( $\Gamma_L$ , see Appendix Fig. A.4). The new reflection coefficient,  $\Gamma_L$ , represents the impedance mismatch between the port 2 connectors and the system in the forward direction. Signals into the analyzer port 2 (to the right in Appendix Fig. A.4) will reflect from the analyzer port 2 (if unmatched) and back into the error network. This error source is referred to as *load impedance match* error, as opposed to the error network's  $s_{22}$  which represents the *source impedance match* error. The equivalent error transmission branch accounts for transmission frequency tracking, or the differences in the frequency response of the port 2 receiver and the reference receiver. The following analysis shows how the port 2 error network and reflection branch can be collapsed into the two branches for the forward model.



Appendix Fig. A.4. Forward direction port 2 error network with load match reflection branch.

Applying the non-touching loop rule for the reflection branch ( $e_{22}$ ) to the about flow graph gives the following.

**Reflection: Forward equivalent branch**

$$P_1 = s_{22}^{(2)} \quad \text{A.17}$$

$$P_2 = s_{21}^{(2)} \Gamma_L^F s_{12}^{(2)}$$

$$\sum L_1^{(1)} = \sum L_1 = s_{11}^{(2)} \Gamma_L^F \quad \text{A.18}$$

$$\sum L_1^{(2)} = 0$$

$$e_{22} = \frac{b_0}{a_0} = \frac{s_{22}^{(2)} (1 - s_{11}^{(2)} \Gamma_L^F) + s_{21}^{(2)} \Gamma_L^F s_{12}^{(2)}}{1 - s_{11}^{(2)} \Gamma_L^F} = s_{22}^{(2)} + \frac{s_{21}^{(2)} \Gamma_L^F s_{12}^{(2)}}{1 - s_{11}^{(2)} \Gamma_L^F} = C_2^{(2)} + \frac{C_3^{(2)} \Gamma_L^F}{1 - C_1^{(2)} \Gamma_L^F} \quad \text{A.19}$$

$$e_{22} = C_2^{(2)} + \frac{C_3^{(2)} \Gamma_L^F}{1 - C_1^{(2)} \Gamma_L^F} \quad \text{A.20}$$

$$(e_{22} - C_2^{(2)}) - (e_{22} - C_2^{(2)}) C_1^{(2)} \Gamma_L^F = C_3^{(2)} \Gamma_L^F$$

$$\Gamma_L^F = \frac{(e_{22} - C_2^{(2)})}{C_3^{(2)} + (e_{22} - C_2^{(2)}) C_1^{(2)}}$$

Similarly, the transmission branch can be found as follows:

**Transmission: Forward equivalent branch**

$$P_1 = s_{12}^{(2)} \tag{A.21}$$

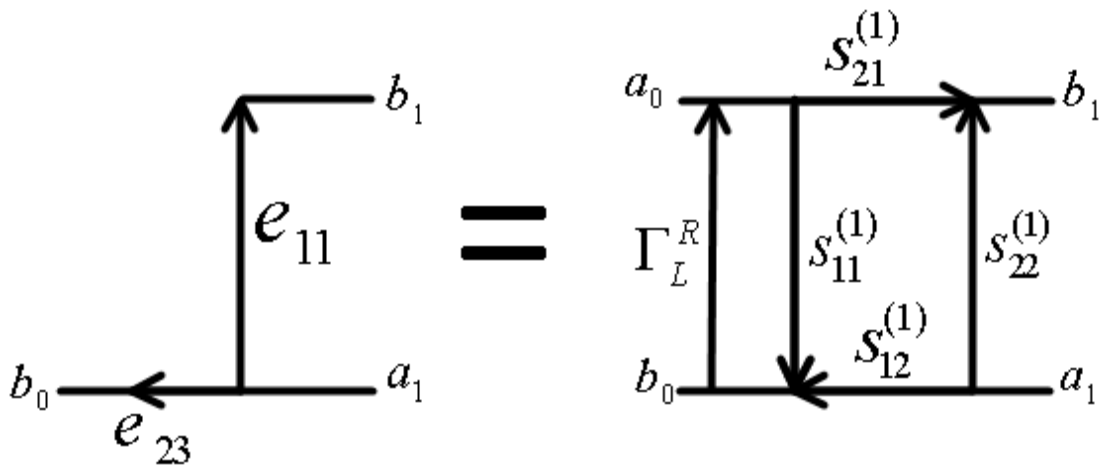
$$\sum L_1^{(1)} = 0 \tag{A.22}$$

$$\sum L_1 = s_{11}^{(2)} \Gamma_L^F \tag{A.23}$$

$$e_{32} = \frac{b_1}{a_0} = \frac{s_{12}^{(2)}}{1 - s_{11}^{(2)} \Gamma_L^F} = \frac{s_{12}^{(2)}}{1 - C_1^{(2)} \Gamma_L^F}$$

A similar analysis can be performed for the reverse direction (See Appendix Fig. A.5).

Applying the non-touching loop rule to the signal flow graph of Appendix Fig. A.5 gives the following expressions for equivalent transmission and reflection parameters.



**Appendix Fig. A.5. Reverse direction port 2 error network with load match reflection branch.**

**Reflection: Reverse equivalent branch**

$$P_1 = s_{22}^{(1)} \quad \text{A.24}$$

$$P_2 = s_{21}^{(1)} \Gamma_L^R s_{12}^{(1)}$$

$$\sum L_1^{(1)} = \sum L_1 = s_{11}^{(1)} \Gamma_L^R \quad \text{A.25}$$

$$\sum L_1^{(2)} = 0$$

$$e_{11} = \frac{b_1}{a_1} = \frac{s_{22}^{(1)} (1 - s_{11}^{(1)} \Gamma_L^R) + s_{21}^{(1)} \Gamma_L^R s_{12}^{(1)}}{1 - s_{11}^{(1)} \Gamma_L^R} = s_{22}^{(1)} + \frac{s_{21}^{(1)} \Gamma_L^R s_{12}^{(1)}}{1 - s_{11}^{(1)} \Gamma_L^R} = C_2^{(1)} + \frac{C_3^{(1)} \Gamma_L^R}{1 - C_1^{(1)} \Gamma_L^R} \quad \text{A.26}$$

**Transmission: Reverse equivalent branch**

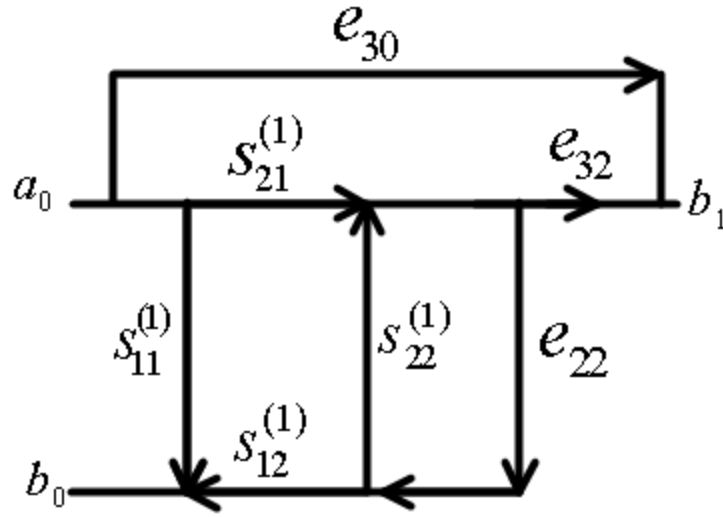
$$P_1 = s_{12}^{(1)} \quad \text{A.27}$$

$$\sum L_1^{(1)} = 0 \quad \text{A.28}$$

$$\sum L_1 = s_{11}^{(1)} \Gamma_L^R$$

$$e_{23} = \frac{b_0}{a_1} = \frac{s_{12}^{(1)}}{1 - s_{11}^{(1)} \Gamma_L^R} = \frac{s_{12}^{(1)}}{1 - C_1^{(1)} \Gamma_L^R} \quad \text{A.29}$$

To measure the values of the two new error parameters for both the forward and reverse directions, the *through* connection measurement is used. Both reflection and transmission can be measured for the *through* connection, so both measurements will be used to find the unknown error branch values. Consider first the forward direction model *through* connection shown in Appendix Fig. A.6 and the following analysis.



Appendix Fig. A.6. Through connection error model in the forward direction.

**Reflection: Forward *through***

$$P_1 = s_{11}^{(1)} = C_1^{(1)} \quad \text{A.30}$$

$$P_2 = s_{21}^{(1)} s_{12}^{(1)} e_{22} = C_3^{(1)} e_{22} \quad \text{A.31}$$

$$\sum L_1^{(1)} = s_{22}^{(1)} e_{22} = C_2^{(1)} e_{22}$$

$$\sum L_1 = s_{22}^{(1)} e_{22} = C_2^{(1)} e_{22}$$

$$\sum L_1^{(2)} = 0$$

$$R_F^{thru} = \frac{b_0}{a_0} = \frac{C_1^{(1)}(1 - C_2^{(1)} e_{22}) + C_3^{(1)} e_{22}}{1 - C_2^{(1)} e_{22}} = C_1^{(1)} + \frac{C_3^{(1)} e_{22}}{1 - C_2^{(1)} e_{22}} \quad \text{A.32}$$

$$(R_F^{thru} - C_1^{(1)}) - (R_F^{thru} - C_1^{(1)}) C_2^{(1)} e_{22} = C_3^{(1)} e_{22}$$

$$e_{22} = \frac{(R_F^{thru} - C_1^{(1)})}{C_3^{(1)} + (R_F^{thru} - C_1^{(1)}) C_2^{(1)}}$$

**Transmission: Forward *through***

$$P_1 = s_{21}^{(1)} e_{32} \quad \text{A.33}$$

$$P_2 = e_{30}$$

$$\sum L_1^{(1)} = 0 \quad \text{A.34}$$

$$\sum L_1 = s_{22}^{(1)} e_{22} = C_2^{(1)} e_{22}$$

$$\sum L_1^{(2)} = C_2^{(1)} e_{22}$$

$$T_F^{thru} = \frac{b_1}{a_0} = \frac{e_{30}(1 - C_2^{(1)} e_{22}) + s_{21}^{(1)} e_{32}}{1 - C_2^{(1)} e_{22}} = e_{30} + \frac{s_{21}^{(1)} e_{32}}{1 - C_2^{(1)} e_{22}} \quad \text{A.35}$$

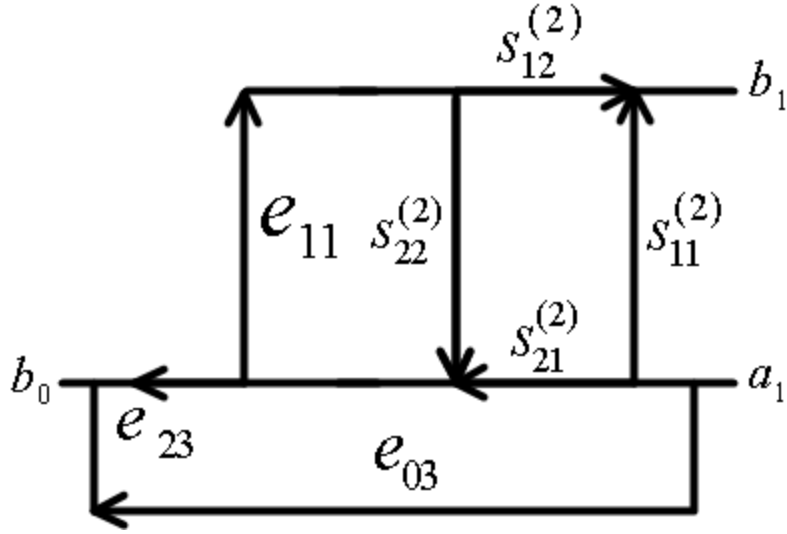
$$\frac{(T_F^{thru} - e_{30}) - (T_F^{thru} - e_{30}) C_2^{(1)} e_{22}}{s_{21}^{(1)}} = e_{32}$$

$$e_{32} = \frac{(T_F^{thru} - e_{30}) - (T_F^{thru} - e_{30}) C_2^{(1)} \left( \frac{(R_F^{thru} - C_1^{(1)})}{C_3^{(1)} + (R_F^{thru} - C_1^{(1)}) C_2^{(1)}} \right)}{s_{21}^{(1)}}$$

$$= \frac{(T_F^{thru} - e_{30}) C_3^{(1)}}{s_{21}^{(1)} (C_3^{(1)} + (R_F^{thru} - C_1^{(1)}) C_2^{(1)})}$$

$$\boxed{s_{21}^{(1)} e_{32} = \frac{(T_F^{thru} - e_{30}) C_3^{(1)}}{(C_3^{(1)} + (R_F^{thru} - C_1^{(1)}) C_2^{(1)})} = \frac{s_{21}^{(1)} s_{12}^{(2)}}{1 - C_1^{(2)} \Gamma_L^F} = C_4^{(1)}} \quad \text{A.36}$$

Below, the same analysis is repeated for the reverse direction error model.



Appendix Fig. A.7. Through connection error model in the reverse direction.

**Reflection: Reverse through**

$$P_1 = s_{11}^{(2)} = C_1^{(2)} \quad \text{A.37}$$

$$P_2 = s_{21}^{(2)} s_{12}^{(2)} e_{11} = C_3^{(2)} e_{11}$$

$$\sum L_1^{(1)} = s_{22}^{(2)} e_{11} = C_2^{(2)} e_{11} \quad \text{A.38}$$

$$\sum L_1 = s_{22}^{(2)} e_{11} = C_2^{(2)} e_{11}$$

$$\sum L_1^{(2)} = 0$$

$$R_R^{thru} = \frac{b_0}{a_1} = \frac{C_1^{(2)}(1 - C_2^{(2)}e_{11}) + C_3^{(2)}e_{11}}{1 - C_2^{(2)}e_{11}} = C_1^{(2)} + \frac{C_3^{(2)}e_{11}}{1 - C_2^{(2)}e_{11}} \quad \text{A.39}$$

$$(R_R^{thru} - C_1^{(2)}) - (R_R^{thru} - C_1^{(2)})C_2^{(2)}e_{11} = C_3^{(2)}e_{11}$$

$$e_{11} = \frac{(R_R^{thru} - C_1^{(2)})}{C_3^{(2)} + (R_R^{thru} - C_1^{(2)})C_2^{(2)}}$$

**Transmission: Reverse *through***

$$P_1 = s_{21}^{(2)} e_{23} \quad \text{A.40}$$

$$P_2 = e_{03}$$

$$\sum L_1^{(1)} = 0 \quad \text{A.41}$$

$$\sum L_1 = s_{22}^{(2)} e_{11} = C_2^{(2)} e_{11}$$

$$\sum L_1^{(2)} = C_2^{(2)} e_{11}$$

$$T_R = \frac{b_0}{a_1} = \frac{e_{03}(1 - C_2^{(2)} e_{11}) + s_{21}^{(2)} e_{23}}{1 - C_2^{(2)} e_{11}} = e_{03} + \frac{s_{21}^{(2)} e_{23}}{1 - C_2^{(2)} e_{11}} \quad \text{A.42}$$

$$\frac{(T_R - e_{03}) - (T_R - e_{03})C_2^{(2)} e_{11}}{s_{21}^{(2)}} = e_{23}$$

$$e_{23} = \frac{(T_R^{thru} - e_{03}) - (T_R^{thru} - e_{03})C_2^{(2)} \left( \frac{(R_R^{thru} - C_1^{(2)})}{C_3^{(2)} + (R_R^{thru} - C_1^{(2)})C_2^{(2)}} \right)}{s_{21}^{(2)}}$$

$$= \frac{(T_R^{thru} - e_{03})C_3^{(2)}}{s_{21}^{(2)} (C_3^{(2)} + (R_R^{thru} - C_1^{(2)})C_2^{(2)})}$$

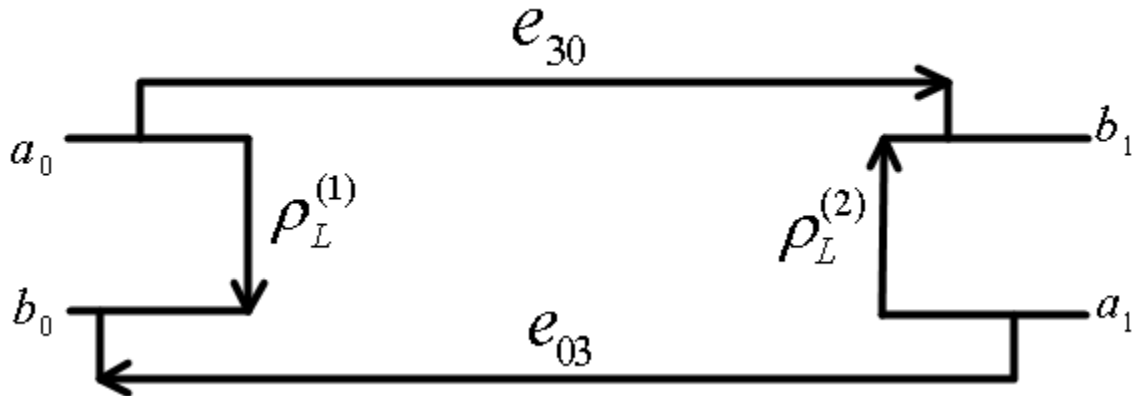
$$e_{23} = \frac{(T_R^{thru} - e_{03}) - (T_R^{thru} - e_{03})C_2^{(2)} \left( \frac{(R_R^{thru} - C_1^{(2)})}{C_3^{(2)} + (R_R^{thru} - C_1^{(2)})C_2^{(2)}} \right)}{s_{21}^{(2)}}$$

$$= \frac{(T_R^{thru} - e_{03})C_3^{(2)}}{s_{21}^{(2)} (C_3^{(2)} + (R_R^{thru} - C_1^{(2)})C_2^{(2)})}$$

$$s_{21}^{(2)} e_{23} = \frac{(T_R^{thru} - e_{03})C_3^{(2)}}{(C_3^{(2)} + (R_R^{thru} - C_1^{(2)})C_2^{(2)})} = \frac{s_{21}^{(2)} s_{12}^{(1)}}{1 - s_{11}^{(1)} \Gamma_L^R} = C_4^{(2)} \quad \text{A.43}$$

The final parameters of Hand's error model are the port to port isolation terms,  $e_{30}$  and  $e_{03}$ . Of all calibration measurements, this is the most straightforward. To extract the isolation parameter values, both ports are terminated in matched loads and transmission is measured.

Often, the isolation terms are assumed to be zero when it is difficult to find a broadband load of high precision for calibration. Appendix Fig. A.8 gives the signal flow graph for the analysis of isolation. For proper terminations (perfect system match over entire frequency range), the  $\rho_L^{1,2}$  will be zero.



Appendix Fig. A.8. Hand's isolation terms signal flow graph.

$$T_{iso}^F = \frac{b_1}{a_0} = e_{30}$$

A.44

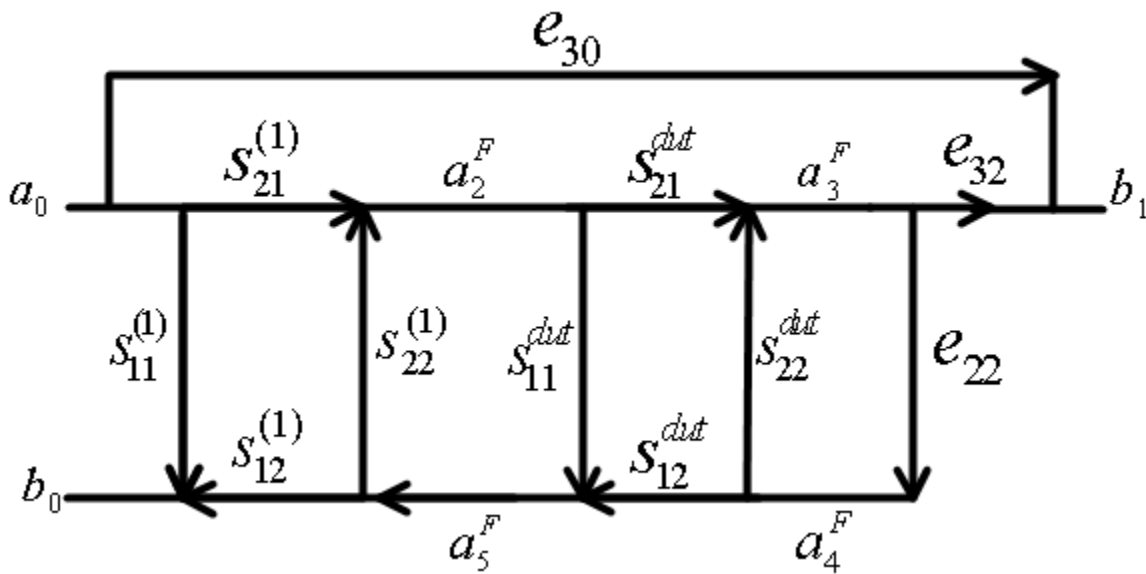
$$T_{iso}^R = \frac{b_0}{a_1} = e_{03}$$

A.45

To summarize, from the measurements of the *open*, *short*, and *load* on each port and the *through* and *isolation* for both ports, in both directions, the following twelve error model parameter values are known:

$$\begin{aligned}
s_{11}^{(1,2)} &= C_1^{(1,2)} \\
s_{22}^{(1,2)} &= C_2^{(1,2)} \\
s_{21}^{(1,2)} s_{12}^{(1,2)} &= C_3^{(1,2)} \\
e_{22} \\
e_{11} \\
e_{30} \\
e_{03} \\
s_{21}^{(2)} e_{23} &= C_4^{(2)} \\
s_{21}^{(1)} e_{32} &= C_4^{(1)}
\end{aligned}$$

Now, with all of the error parameter values determined through measurement, the full model must be analyzed. This requires analyzing the signal flow graph with the DUT in place, and recovering the DUT parameters out of the measured parameters. Consider first the forward error model with the DUT in place.



Appendix Fig. A.9. Full error model with DUT in place in the forward direction.

With a two port measurement, both transmission and reflection can be measured.

Through analysis of the forward error signal flow graph in Appendix Fig. A.9, transmission and reflection expressions can be found in terms of the error and DUT parameters.

### Transmission: Forward full model

$$P_1 = s_{21}^{(1)} s_{21}^{dut} e_{32} \quad \text{A.46}$$

$$P_2 = e_{30} \quad \text{A.47}$$

$$\sum L_1^{(1)} = 0$$

$$\sum L_1^{(2)} = s_{22}^{(1)} s_{11}^{dut} + s_{22}^{dut} e_{22} + s_{21}^{dut} s_{12}^{dut} e_{22} s_{22}^{(1)} = C_2^{(1)} s_{11}^{dut} + s_{22}^{dut} e_{22} + s_{21}^{dut} s_{12}^{dut} e_{22} C_2^{(1)}$$

$$\sum L_1 = C_2^{(1)} s_{11}^{dut} + s_{22}^{dut} e_{22} + s_{21}^{dut} s_{12}^{dut} e_{22} C_2^{(1)}$$

$$\sum L_2^{(1)} = 0$$

$$\sum L_2^{(2)} = s_{22}^{(1)} s_{11}^{dut} s_{22}^{dut} e_{22} = C_2^{(1)} s_{11}^{dut} s_{22}^{dut} e_{22}$$

$$\sum L_2 = C_2^{(1)} s_{11}^{dut} s_{22}^{dut} e_{22}$$

A.48

$$T_F^M = \frac{b_1}{a_0}$$

$$= \frac{s_{21}^{(1)} s_{21}^{dut} e_{32} + e_{30} (1 - C_2^{(1)} s_{11}^{dut} - s_{22}^{dut} e_{22} - s_{21}^{dut} s_{12}^{dut} e_{22} C_2^{(1)} + C_2^{(1)} s_{11}^{dut} s_{22}^{dut} e_{22})}{1 - C_2^{(1)} s_{11}^{dut} - s_{22}^{dut} e_{22} - s_{21}^{dut} s_{12}^{dut} e_{22} C_2^{(1)} + C_2^{(1)} s_{11}^{dut} s_{22}^{dut} e_{22}}$$

$$= e_{30} + \frac{s_{21}^{(1)} e_{32} s_{21}^{dut}}{D_F} = e_{30} + \frac{C_4^{(1)} s_{21}^{dut}}{D_F}$$

$$T_F^M = e_{30} + \frac{C_4^{(1)} s_{21}^{dut}}{D_F}$$

A.49

A.50

$$T_F^M = e_{30} + \frac{C_4^{(1)} s_{21}^{dut}}{D_F}$$

$$s_{21}^{dut} = \frac{D_F (T_F^M - e_{30})}{C_4^{(1)}}$$

$$D_F = 1 - C_2^{(1)} s_{11}^{dut} - s_{22}^{dut} e_{22} - s_{21}^{dut} s_{12}^{dut} e_{22} C_2^{(1)} + C_2^{(1)} s_{11}^{dut} s_{22}^{dut} e_{22}$$

A.51

**Reflection: Forward full model**

$$P_1 = s_{11}^{(1)} = C_1^{(1)} \quad \text{A.52}$$

$$P_2 = s_{21}^{(1)} s_{12}^{(1)} s_{11}^{dut} = C_3^{(1)} s_{11}^{dut}$$

$$P_3 = C_3^{(1)} s_{21}^{dut} s_{12}^{dut} e_{22}$$

$$\sum L_1^{(1)} = C_2^{(1)} s_{11}^{dut} + s_{22}^{dut} e_{22} + s_{21}^{dut} s_{12}^{dut} e_{22} C_2^{(1)} \quad \text{A.53}$$

$$\sum L_1^{(2)} = s_{22}^{dut} e_{22}$$

$$\sum L_1 = C_2^{(1)} s_{11}^{dut} + s_{22}^{dut} e_{22} + s_{21}^{dut} s_{12}^{dut} e_{22} C_2^{(1)}$$

$$\sum L_2^{(1)} = C_2^{(1)} s_{11}^{dut} s_{22}^{dut} e_{22} \quad \text{A.54}$$

$$\sum L_2^{(2)} = 0$$

$$\sum L_2 = C_2^{(1)} s_{11}^{dut} s_{22}^{dut} e_{22}$$

$$R_F^M = \frac{b_0}{a_0} \quad \text{A.55}$$

$$= \frac{C_1^{(1)} (D_F) + C_3^{(1)} s_{11}^{dut} (1 - s_{22}^{dut} e_{22}) + C_3^{(1)} s_{21}^{dut} s_{12}^{dut} e_{22}}{D_F}$$

$$= C_1^{(1)} + \frac{C_3^{(1)} s_{11}^{dut} (1 - s_{22}^{dut} e_{22}) + C_3^{(1)} s_{21}^{dut} s_{12}^{dut} e_{22}}{D_F}$$

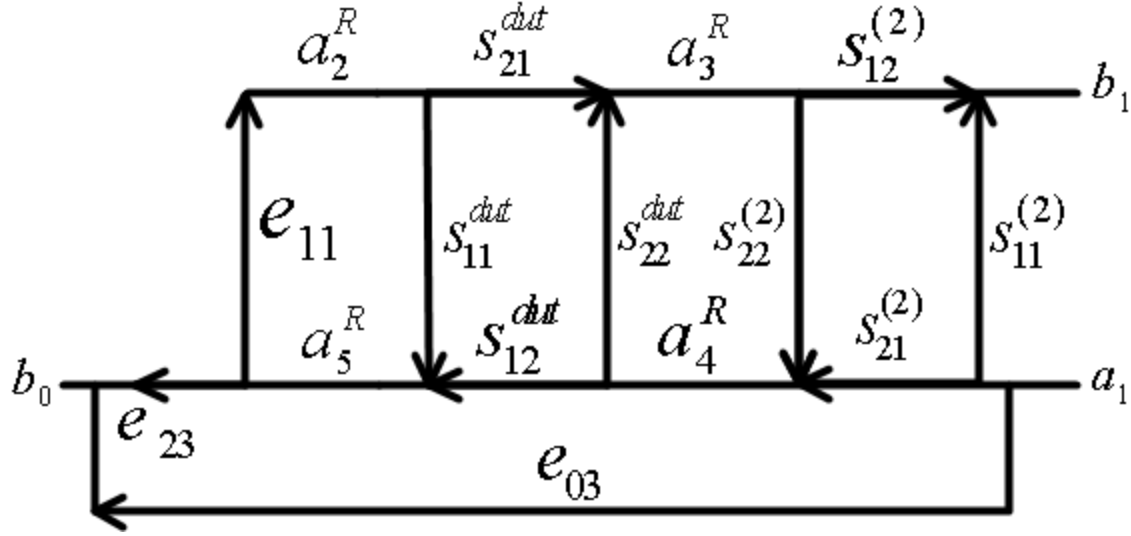
$$\frac{(R_F^M - C_1^{(1)}) D_F}{C_3^{(1)}} = s_{11}^{dut} (1 - s_{22}^{dut} e_{22}) + s_{21}^{dut} s_{12}^{dut} e_{22} \quad \text{A.56}$$

$$s_{11}^{dut} = \frac{(R_F^M - C_1^{(1)}) D_F - s_{21}^{dut} s_{12}^{dut} e_{22} C_3^{(1)}}{C_3^{(1)} (1 - s_{22}^{dut} e_{22})}$$

$$D_F = 1 - C_2^{(1)} s_{11}^{dut} - s_{22}^{dut} e_{22} - s_{21}^{dut} s_{12}^{dut} e_{22} C_2^{(1)} + C_2^{(1)} s_{11}^{dut} s_{22}^{dut} e_{22} \quad \text{A.57}$$

From measuring transmission and reflection and using the full error and DUT signal flow graph in the *forward* direction, expressions (not *explicit*) can be found for  $s_{11}^{dut}$  and  $s_{21}^{dut}$ .

Repeating the analysis for the *reverse* direction gives the following.



Appendix Fig. A.10. Full error model with DUT in place in the reverse direction.

### Reflection: Reverse full model

$$P_1 = s_{11}^{(2)} = C_1^{(2)} \quad \text{A.58}$$

$$P_2 = s_{21}^{(2)} s_{22}^{dut} s_{12}^{(2)} = C_3^{(2)} s_{22}^{dut}$$

$$P_3 = C_3^{(2)} s_{21}^{dut} s_{12}^{dut} e_{11}$$

$$\sum L_1^{(1)} = s_{22}^{(2)} s_{22}^{dut} + s_{11}^{dut} e_{11} + s_{21}^{dut} s_{12}^{dut} s_{22}^{(2)} e_{11} = C_2^{(2)} s_{22}^{dut} + s_{11}^{dut} e_{11} + s_{21}^{dut} s_{12}^{dut} C_2^{(2)} e_{11} \quad \text{A.59}$$

$$\sum L_1^{(2)} = s_{11}^{dut} e_{11}$$

$$\sum L_1 = s_{22}^{(2)} e_{11} = C_2^{(2)} s_{22}^{dut} + C_1^{(2)} e_{11} + s_{21}^{dut} s_{12}^{dut} C_2^{(2)} e_{11}$$

$$\sum L_2^{(1)} = s_{22}^{(2)} s_{22}^{dut} s_{11}^{dut} e_{11}$$

$$\sum L_2 = s_{22}^{(2)} s_{22}^{dut} s_{11}^{dut} e_{11}$$

$$R_R^M = \frac{b_0}{a_1} = \frac{C_1^{(2)} (D_R) + C_3^{(2)} s_{22}^{dut} (1 - s_{11}^{dut} e_{11}) + C_3^{(2)} s_{21}^{dut} s_{12}^{dut} e_{11}}{D_R} \quad \text{A.60}$$

$$= C_1^{(2)} + \frac{C_3^{(2)} s_{22}^{dut} (1 - s_{11}^{dut} e_{11}) + C_3^{(2)} s_{21}^{dut} s_{12}^{dut} e_{11}}{D_R}$$

$$s_{22}^{dut} = \frac{(R_R^M - C_1^{(2)}) D_R - C_3^{(2)} s_{21}^{dut} s_{12}^{dut} e_{11}}{C_3^{(2)} (1 - s_{11}^{dut} e_{11})}$$

$$D_R = 1 - C_2^{(2)} s_{22}^{dut} - s_{11}^{dut} e_{11} - s_{21}^{dut} s_{12}^{dut} C_2^{(2)} e_{11} + s_{22}^{(2)} s_{22}^{dut} s_{11}^{dut} e_{11} \quad \text{A.61}$$

**Transmission: Reverse full model**

$$P_1 = s_{21}^{(2)} s_{12}^{dut} e_{23} \quad \text{A.62}$$

$$P_2 = e_{03}$$

$$\sum L_1^{(1)} = 0 \quad \text{A.63}$$

$$\sum L_1 = C_2^{(2)} s_{22}^{dut} + C_1^{(2)} e_{11} + s_{21}^{dut} s_{12}^{dut} C_2^{(2)} e_{11}$$

$$\sum L_1^{(2)} = C_2^{(2)} s_{22}^{dut} + C_1^{(2)} e_{11} + s_{21}^{dut} s_{12}^{dut} C_2^{(2)} e_{11}$$

$$\sum L_2^{(1)} = 0$$

$$\sum L_2^{(2)} = s_{22}^{(2)} s_{22}^{dut} s_{11}^{dut} e_{11}$$

$$\sum L_2 = s_{22}^{(2)} s_{22}^{dut} s_{11}^{dut} e_{11}$$

$$T_R^M = \frac{b_0}{a_1} = e_{03} + \frac{s_{21}^{(2)} e_{23} s_{12}^{dut}}{D_R} = e_{03} + \frac{C_4^{(2)} s_{12}^{dut}}{D_R} \quad \text{A.64}$$

$$T_R^M = e_{03} + \frac{C_4^{(2)} s_{12}^{dut}}{D_R} \quad \text{A.65}$$

$$s_{12}^{dut} = \frac{(T_R^M - e_{03}) D_R}{C_4^{(2)}}$$

From the measurement of the reflection and transmission in both the forward and reverse directions, the following equations can be written.

$$s_{12}^{dut} = \frac{(T_R^M - e_{03})D_R}{C_4^{(2)}} \quad \text{A.66}$$

$$s_{21}^{dut} = \frac{D_F(T_F^M - e_{30})}{C_4^{(1)}} \quad \text{A.67}$$

$$s_{22}^{dut} = \frac{(R_R^M - C_1^{(2)})D_R - C_3^{(2)}s_{21}^{dut}s_{12}^{dut}e_{11}}{C_3^{(2)}(1 - s_{11}^{dut}e_{11})} \quad \text{A.68}$$

$$s_{11}^{dut} = \frac{(R_F^M - C_1^{(1)})D_F - s_{21}^{dut}s_{12}^{dut}e_{22}C_3^{(1)}}{C_3^{(1)}(1 - s_{22}^{dut}e_{22})} \quad \text{A.69}$$

$$\boxed{D_R = 1 - C_2^{(2)}s_{22}^{dut} - s_{11}^{dut}e_{11} - s_{21}^{dut}s_{12}^{dut}C_2^{(2)}e_{11} + s_{22}^{(2)}s_{22}^{dut}s_{11}^{dut}e_{11}} \quad \text{A.70}$$

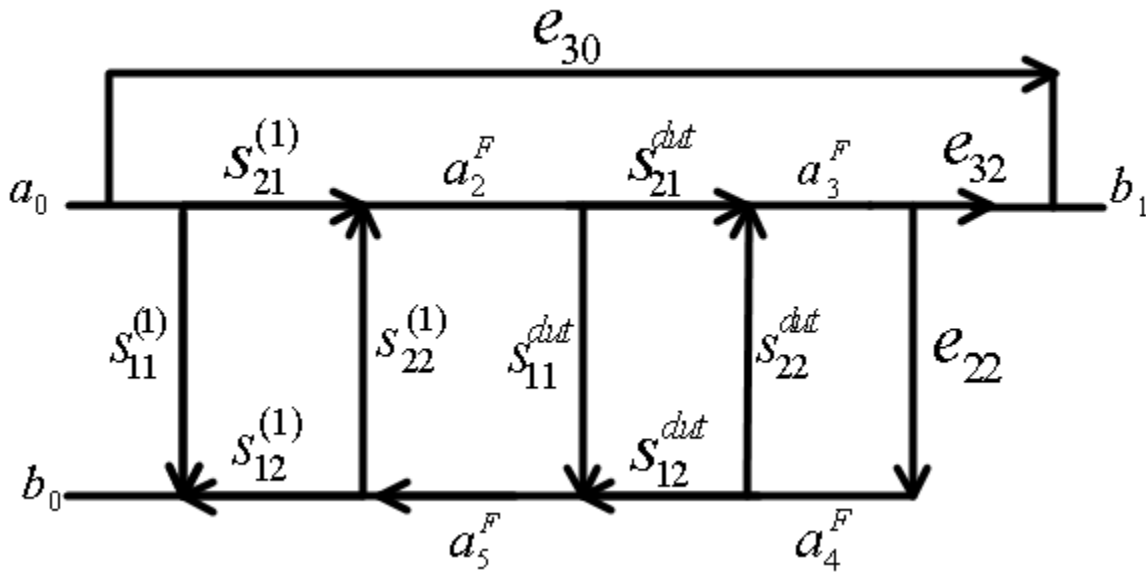
$$\boxed{D_F = 1 - C_2^{(1)}s_{11}^{dut} - s_{22}^{dut}e_{22} - s_{21}^{dut}s_{12}^{dut}e_{22}C_2^{(1)} + C_2^{(1)}s_{11}^{dut}s_{22}^{dut}e_{22}} \quad \text{A.71}$$

Equations A.66 through A.71 are coupled, and thus not explicit expressions of the DUT scattering parameters. Hand arrived at similar forms of these equations in 1970, as well as Hackborn in 1968 for a different model. At that time, both Hand and Hackborn relied on a computerized iterative approach to extract the DUT scattering parameters from the measurement. The  $D$  terms were initially assumed to be 1, and the computer would iteratively compute the scattering parameters until the values satisfied a specified convergence tolerance.

In 1971, shortly after Hand's article appeared in the Hewlett Packard engineering journal, W. Kruppa and Kenneth Sodomsy published an article giving the explicit formulas for the DUT scattering parameters using the Hackborn error model [47]. All measurement and characterization steps were the same as Hackborn's method, but the signal flow graph was analyzed node by node, resulting in explicit expressions for the DUT parameters. Later, in June 1973, Stig Rehnmark, using Kruppa and Sodomsy's technique, would present an article with

explicit formulas using Hand's model, thus giving explicit solutions for DUT parameters in the more sophisticated and more commonly used error model [48].

Kruppa and Sodomsy's method involves first expressing the model node signals as the sum of the nearest neighbor signals. The following equations define the node signals for the forward model.



$$a_2^F = a_5^F S_{22}^{(1)} + a_0 S_{21}^{(1)} \quad \text{A.72}$$

$$a_3^F = a_4^F S_{22}^{dist} + a_2^F S_{21}^{dist} \quad \text{A.73}$$

$$a_4^F = a_3^F e_{22} \quad \text{A.74}$$

$$a_5^F = a_2^F S_{11}^{dist} + a_4^F S_{12}^{dist} \quad \text{A.75}$$

$$b_0 = a_0 R_F^M = a_5^F S_{12}^{(1)} + a_0 S_{11}^{(1)} \quad \text{A.76}$$

$$b_1 = a_0 T_F^M = a_0 e_{30} + a_3^F e_{32} \quad \text{A.77}$$

First using equations A.76 and A.77, the signal at nodes  $a_5^F$  and  $a_3^F$  can be defined in terms of measured transmission and reflection as well as previously known error parameter values. The equations will be normalized by the initial input signal,  $a_0$ .

$$a_3^F = \frac{(T_F^M - e_{30})}{e_{32}} \quad \text{A.78}$$

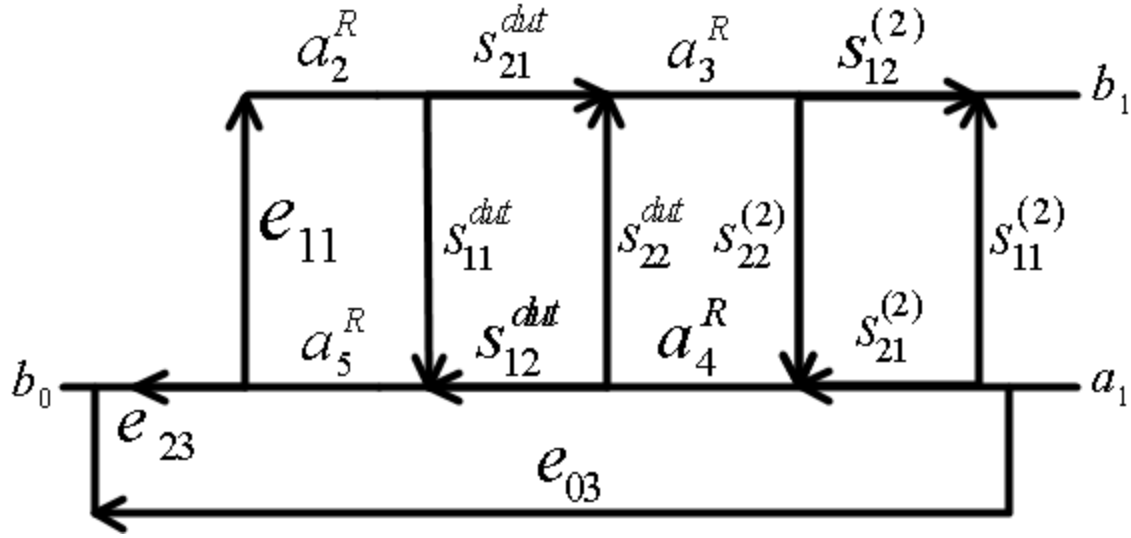
$$a_5^F = \frac{(R_F^M - S_{11}^{(1)})}{S_{12}^{(1)}} \quad \text{A.79}$$

Substituting the expressions from equations A.78 and A.79 into the remaining node signal expressions gives the following node signals in terms of measured and known quantities.

$$a_2^F = \left( \frac{(R_F^M - S_{11}^{(1)})}{S_{12}^{(1)}} \right) S_{22}^{(1)} + S_{21}^{(1)} \quad \text{A.80}$$

$$a_4^F = \left( \frac{(T_F^M - e_{30})}{e_{32}} \right) e_{22} \quad \text{A.81}$$

Repeating the same analysis for the reverse signal model gives the following equations.



$$a_2^R = a_5^R e_{11} \quad \text{A.82}$$

$$a_3^R = a_4^R S_{22}^{dut} + a_2^R S_{21}^{dut} \quad \text{A.83}$$

$$a_4^R = a_1 S_{21}^{(2)} + a_3^R S_{22}^{(2)} \quad \text{A.84}$$

$$a_5^R = a_4^R S_{12}^{dut} + a_2^R S_{11}^{dut} \quad \text{A.85}$$

$$b_0 = a_1 T_R^M = a_5^R e_{23} + a_1 e_{03} \quad \text{A.86}$$

$$b_1 = a_1 R_R^M = a_3^R S_{12}^{(2)} + a_1 S_{11}^{(2)} \quad \text{A.87}$$

First using equations A.86 and A.87, the signal at nodes  $a_5^R$  and  $a_3^R$  can be defined in terms of measured transmission and reflection as well as previously known error parameter values. The equations will be normalized by the initial input signal,  $a_1$ .

$$a_5^R = \left( \frac{T_R^M - e_{03}}{e_{23}} \right) \quad \text{A.88}$$

$$a_3^R = \frac{R_R^M - S_{11}^{(2)}}{S_{12}^{(2)}} \quad \text{A.89}$$

Exactly as in the forward model, substituting the expressions from equations A.88A.78 and A.89 into the remaining node signal expressions gives the following node signals in terms of known quantities.

$$a_2^R = \left( \frac{T_R^M - e_{03}}{e_{23}} \right) e_{11} \quad \text{A.90}$$

$$a_4^R = \left( \frac{R_R^M - S_{11}^{(2)}}{S_{12}^{(2)}} \right) S_{22}^{(2)} + S_{21}^{(2)} \quad \text{A.91}$$

Now, the following node signals are known from error model parameters and transmission and reflection measurements:  $\{a_2^R, a_3^R, a_4^R, a_5^R\}$  and  $\{a_2^F, a_3^F, a_4^F, a_5^F\}$ . Using the node equations that depend on the DUT parameters (equations A.73, A.75, A.83, A.85), the DUT parameters can be isolated and solved for in terms of measureable quantities.

First, using equation A.73 (forward direction) and A.83 (reverse direction), the following DUT parameters can be explicitly solved.

$$a_3^F = a_4^F S_{22}^{dut} + a_2^F S_{21}^{dut} \Rightarrow \quad \text{A.92}$$

$$S_{22}^{dut} = \frac{a_3^F - a_2^F S_{21}^{dut}}{a_4^F}$$

$$a_3^R = a_4^R \left( \frac{a_3^F - a_2^F S_{21}^{dut}}{a_4^F} \right) + a_2^R S_{21}^{dut} \quad \text{A.93}$$

$$a_3^R a_4^F = a_4^R a_3^F - (a_4^R a_2^F - a_4^F a_2^R) S_{21}^{dut}$$

$$S_{21}^{dut} = \frac{a_4^R a_3^F - a_3^R a_4^F}{(a_4^R a_2^F - a_4^F a_2^R)} = \frac{a_4^F (a_4^R a_3^F - a_3^R a_4^F)}{a_4^F (a_4^R a_2^F - a_4^F a_2^R)}$$

$$S_{22}^{dut} = \frac{a_3^F - a_2^F \left( \frac{a_4^F (a_4^R a_3^F - a_3^R a_4^F)}{a_4^F (a_4^R a_2^F - a_4^F a_2^R)} \right)}{a_4^F} = \frac{a_3^F (a_4^R a_2^F - a_4^F a_2^R) - a_2^F (a_4^R a_3^F - a_3^R a_4^F)}{a_4^F (a_4^R a_2^F - a_4^F a_2^R)} \quad \text{A.94}$$

Second, using equation A.75 (forward direction) and A.85 (reverse direction), the following DUT parameters can be explicitly solved.

$$a_5^R = a_4^R S_{12}^{dut} + a_2^R S_{11}^{dut} \Rightarrow \quad \text{A.95}$$

$$S_{11}^{dut} = \frac{a_5^R - a_4^R S_{12}^{dut}}{a_2^R}$$

$$a_5^F = a_2^F S_{11}^{dut} + a_4^F S_{12}^{dut} \quad \text{A.96}$$

$$a_5^F = a_2^F \left( \frac{a_5^R - a_4^R S_{12}^{dut}}{a_2^R} \right) + a_4^F S_{12}^{dut}$$

$$a_2^R a_5^F = a_2^F a_5^R - (a_2^F a_4^R - a_4^F a_2^R) S_{12}^{dut}$$

$$S_{12}^{dut} = \frac{a_2^F a_5^R - a_2^R a_5^F}{a_2^F a_4^R - a_4^F a_2^R} = \frac{a_2^R (a_2^F a_5^R - a_2^R a_5^F)}{a_2^R (a_2^F a_4^R - a_4^F a_2^R)}$$

$$S_{11}^{dut} = \frac{a_5^R - a_4^R \left( \frac{a_2^R (a_2^F a_5^R - a_2^R a_5^F)}{a_2^R (a_2^F a_4^R - a_4^F a_2^R)} \right)}{a_2^R} = \frac{a_5^R (a_2^F a_4^R - a_4^F a_2^R) - a_4^R (a_2^F a_5^R - a_2^R a_5^F)}{a_2^R (a_2^F a_4^R - a_4^F a_2^R)} \quad \text{A.97}$$

Equations A.93, A.94, A.96, and A.97 give explicit expressions for the DUT scattering parameters in terms of previously determined error model parameters and measurements with the device in place. The final and neatest expressions for the DUT scattering parameters are given in equations A.98, A.99, A.100, and A.101. The complete and clearly outlined derivation presented here has not been found explicitly presented in any other publication by this author. However, the final equations agree with equations published documents from Agilent Technologies, when notation is properly matched and expanded [49].

$$S_{11}^{dut} = \frac{(a_5^F a_4^R - a_5^R a_4^F)}{(a_2^F a_4^R - a_4^F a_2^R)} \quad \text{A.98}$$

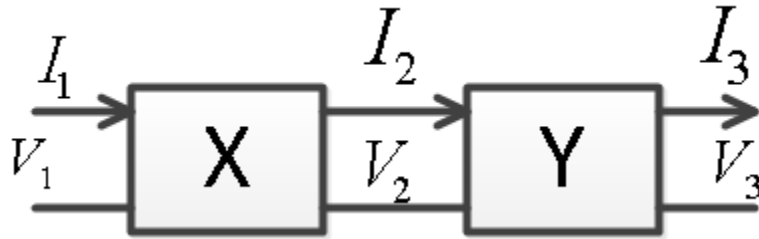
$$S_{12}^{dut} = \frac{(a_2^F a_5^R - a_2^R a_5^F)}{(a_2^F a_4^R - a_4^F a_2^R)} \quad \text{A.99}$$

$$S_{21}^{dut} = \frac{(a_4^R a_3^F - a_3^R a_4^F)}{(a_2^F a_4^R - a_4^F a_2^R)} \quad \text{A.100}$$

$$S_{22}^{dut} = \frac{(a_3^R a_2^F - a_2^R a_3^F)}{(a_2^F a_4^R - a_4^F a_2^R)} \quad \text{A.101}$$

In final summary, error correction on automatic vector network analyzers follows this process: The complete error model is actually two error models, forward and reverse. Each directional model has six error terms. By measuring calibration standards (*short*, *open*, *load*) and measuring the system in the *isolation* and *through* configurations, all twelve error model parameter values can be determined. Then, by analyzing the complete signal flow graph with error networks and the DUT network in place, the DUT parameters can be explicitly solved for in terms of the measurement and error parameter values. These final equations are given in A.98 through A.101.

## Appendix B : ABCD parameters cascade



Appendix Fig. B.1. Cascade of two 2-port devices: X and Y with voltages and currents labeled.

Consider a cascade of two 2-port devices as shown in Appendix Fig. B.1. Using ABCD parameters to define voltage and current at location ‘1’ from the voltage and current at location ‘2’, and to define the voltage and currents at location ‘2’ from the voltages and currents at location ‘3’, it can be shown simply that the 2-port matrix characterization of a cascade of devices is the product of the ABCD matrices of the individual devices (see equations below).

$$\begin{bmatrix} V_1 \\ I_1 \end{bmatrix} = \begin{bmatrix} A & B \\ C & D \end{bmatrix}_X \begin{bmatrix} V_2 \\ I_2 \end{bmatrix} \quad \text{B.1}$$

$$\begin{bmatrix} V_2 \\ I_2 \end{bmatrix} = \begin{bmatrix} A & B \\ C & D \end{bmatrix}_Y \begin{bmatrix} V_3 \\ I_3 \end{bmatrix} \quad \text{B.2}$$

Plugging B.2 into B.1, the cascade product below is formed.

$$\begin{bmatrix} V_1 \\ I_1 \end{bmatrix} = \begin{bmatrix} A & B \\ C & D \end{bmatrix}_X \begin{bmatrix} A & B \\ C & D \end{bmatrix}_Y \begin{bmatrix} V_3 \\ I_3 \end{bmatrix} = [2port_X][2port_Y] \begin{bmatrix} V_3 \\ I_3 \end{bmatrix} \quad \text{B.3}$$

## Appendix C : 2-port parameter conversions

	S	Z	Y	ABCD
$S_{11}$	$S_{11}$	$\frac{(Z_{11} - Z_0)(Z_{22} + Z_0) - Z_{12}Z_{21}}{\Delta Z}$	$\frac{(Y_{11} - Y_0)(Y_{22} + Y_0) + Y_{12}Y_{21}}{\Delta Y}$	$\frac{A + B/Z_0 - CZ_0 - D}{A + B/Z_0 + CZ_0 + D}$
$S_{12}$	$S_{12}$	$\frac{2Z_{12}Z_0}{\Delta Z}$	$\frac{-2Y_{12}Y_0}{\Delta Y}$	$\frac{2(AD - BC)}{A + B/Z_0 + CZ_0 + D}$
$S_{21}$	$S_{21}$	$\frac{2Z_{21}Z_0}{\Delta Z}$	$\frac{-2Y_{21}Y_0}{\Delta Y}$	$\frac{2}{A + B/Z_0 + CZ_0 + D}$
$S_{22}$	$S_{22}$	$\frac{(Z_{11} + Z_0)(Z_{22} - Z_0) - Z_{12}Z_{21}}{\Delta Z}$	$\frac{(Y_{11} + Y_0)(Y_{22} - Y_0) + Y_{12}Y_{21}}{\Delta Y}$	$\frac{-A + B/Z_0 - CZ_0 + D}{A + B/Z_0 + CZ_0 + D}$
$Z_{11}$	$Z_0 \frac{(1 + S_{11})(1 - S_{22}) + S_{12}S_{21}}{(1 - S_{11})(1 - S_{22}) - S_{12}S_{21}}$	$Z_{11}$	$\frac{Y_{22}}{ Y }$	$\frac{A}{C}$
$Z_{12}$	$Z_0 \frac{2S_{12}}{(1 - S_{11})(1 - S_{22}) - S_{12}S_{21}}$	$Z_{12}$	$\frac{-Y_{12}}{ Y }$	$\frac{AD - BC}{C}$
$Z_{21}$	$Z_0 \frac{2S_{21}}{(1 - S_{11})(1 - S_{22}) - S_{12}S_{21}}$	$Z_{21}$	$\frac{-Y_{21}}{ Y }$	$\frac{1}{C}$
$Z_{22}$	$Z_0 \frac{(1 - S_{11})(1 + S_{22}) + S_{12}S_{21}}{(1 - S_{11})(1 - S_{22}) - S_{12}S_{21}}$	$Z_{22}$	$\frac{Y_{11}}{ Y }$	$\frac{D}{C}$

	S	Z	Y	ABCD
$Y_{11}$	$Y_0 \frac{(1 - S_{11})(1 + S_{22}) + S_{12}S_{21}}{(1 + S_{11})(1 + S_{22}) - S_{12}S_{21}}$	$\frac{Z_{22}}{ Z }$	$Y_{11}$	$\frac{D}{B}$
$Y_{12}$	$Y_0 \frac{-2S_{12}}{(1 + S_{11})(1 + S_{22}) - S_{12}S_{21}}$	$\frac{-Z_{12}}{ Z }$	$Y_{12}$	$\frac{BC - AD}{B}$
$Y_{21}$	$Y_0 \frac{-2S_{21}}{(1 + S_{11})(1 + S_{22}) - S_{12}S_{21}}$	$\frac{-Z_{21}}{ Z }$	$Y_{21}$	$\frac{-1}{B}$
$Y_{22}$	$Y_0 \frac{(1 - S_{11})(1 - S_{22}) + S_{12}S_{21}}{(1 + S_{11})(1 + S_{22}) - S_{12}S_{21}}$	$\frac{Z_{11}}{ Z }$	$Y_{22}$	$\frac{A}{B}$
$A$	$\frac{(1 + S_{11})(1 - S_{22}) + S_{12}S_{21}}{2S_{21}}$	$\frac{Z_{11}}{Z_{21}}$	$\frac{-Y_{22}}{Y_{21}}$	$A$
$B$	$Z_0 \frac{(1 + S_{11})(1 + S_{22}) - S_{12}S_{21}}{2S_{21}}$	$\frac{ Z }{Z_{21}}$	$\frac{-1}{Y_{21}}$	$B$
$C$	$\frac{1}{Z_0} \frac{(1 - S_{11})(1 - S_{22}) - S_{12}S_{21}}{2S_{21}}$	$\frac{1}{Z_{21}}$	$\frac{- Y }{Y_{21}}$	$C$
$D$	$\frac{(1 - S_{11})(1 + S_{22}) + S_{12}S_{21}}{2S_{21}}$	$\frac{Z_{22}}{Z_{21}}$	$\frac{-Y_{11}}{Y_{21}}$	$D$

$ Z  = Z_{11}Z_{22} - Z_{12}Z_{21}$	$ Y  = Y_{11}Y_{22} - Y_{12}Y_{21}$	$\Delta Y = (Y_{11} + Y_0)(Y_{22} + Y_0) - Y_{12}Y_{21}$	$\Delta Z = (Z_{11} + Z_0)(Z_{22} + Z_0) - Z_{12}Z_{21}$
			$Y_0 = \frac{1}{Z_0}$

**Appendix Fig. C.1. Table taken from microwave engineering text by Pozar [28] showing the conversion formulas between 2-port network parameters, assuming a single system characteristic impedance.**

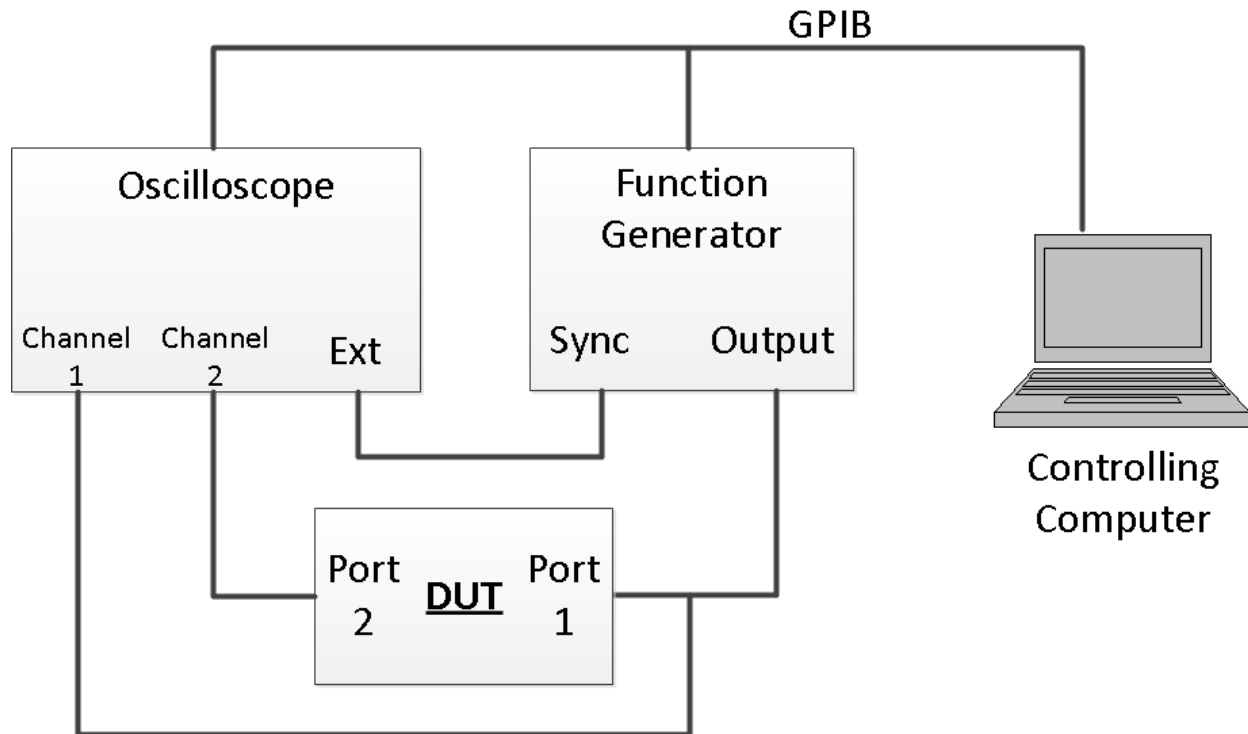
TABLE I  
EQUATIONS FOR THE CONVERSION BETWEEN S PARAMETERS AND Z, Y, h, AND ABCD PARAMETERS WITH A SOURCE IMPEDANCE Z<sub>01</sub> AND LOAD IMPEDANCE Z<sub>02</sub>

$S_{11} = \frac{(Z_{01} - Z_{01}^*)(Z_{22} + Z_{02}) - Z_{12}Z_{21}}{(Z_{01} + Z_{01}^*)(Z_{22} + Z_{02}) - Z_{12}Z_{21}}$	$Z_{11} = \frac{(Z_{01}^* + S_{11}Z_{01})(1 - S_{22}) + S_{12}S_{21}Z_{01}}{(1 - S_{11})(1 - S_{22}) - S_{12}S_{21}}$
$S_{12} = \frac{2Z_{12}(R_{01}R_{02})^{1/2}}{(Z_{01} + Z_{01}^*)(Z_{22} + Z_{02}) - Z_{12}Z_{21}}$	$Z_{12} = \frac{2S_{12}(R_{01}R_{02})^{1/2}}{(1 - S_{11})(1 - S_{22}) - S_{12}S_{21}}$
$S_{21} = \frac{2Z_{21}(R_{01}R_{02})^{1/2}}{(Z_{01} + Z_{01}^*)(Z_{22} + Z_{02}) - Z_{12}Z_{21}}$	$Z_{21} = \frac{2S_{21}(R_{01}R_{02})^{1/2}}{(1 - S_{11})(1 - S_{22}) - S_{12}S_{21}}$
$S_{22} = \frac{(Z_{01} + Z_{01}^*)(Z_{22} + Z_{02}) - Z_{12}Z_{21}}{(Z_{01} + Z_{01}^*)(Z_{22} + Z_{02}) - Z_{12}Z_{21}}$	$Z_{22} = \frac{(1 - S_{11})(Z_{02}^* + S_{22}Z_{02}) + S_{12}S_{21}Z_{02}}{(1 - S_{11})(1 - S_{22}) - S_{12}S_{21}}$
$S_{11} = \frac{(1 - Y_{11}Z_{01}^*)(1 + Y_{22}Z_{02}) + Y_{12}Y_{21}Z_{01}Z_{02}}{(1 + Y_{11}Z_{01})(1 + Y_{22}Z_{02}) - Y_{12}Y_{21}Z_{01}Z_{02}}$	$Y_{11} = \frac{(1 - S_{11})(Z_{02}^* + S_{22}Z_{02}) + S_{12}S_{21}Z_{02}}{(Z_{01}^* + S_{11}Z_{01})(Z_{02}^* + S_{22}Z_{02}) - S_{12}S_{21}Z_{01}Z_{02}}$
$S_{12} = \frac{-2Y_{12}(R_{01}R_{02})^{1/2}}{(1 + Y_{11}Z_{01})(1 + Y_{22}Z_{02}) - Y_{12}Y_{21}Z_{01}Z_{02}}$	$Y_{12} = \frac{-2S_{12}(R_{01}R_{02})^{1/2}}{(Z_{01}^* + S_{11}Z_{01})(Z_{02}^* + S_{22}Z_{02}) - S_{12}S_{21}Z_{01}Z_{02}}$
$S_{21} = \frac{-2Y_{21}(R_{01}R_{02})^{1/2}}{(1 + Y_{11}Z_{01})(1 + Y_{22}Z_{02}) - Y_{12}Y_{21}Z_{01}Z_{02}}$	$Y_{21} = \frac{-2S_{21}(R_{01}R_{02})^{1/2}}{(Z_{01}^* + S_{11}Z_{01})(Z_{02}^* + S_{22}Z_{02}) - S_{12}S_{21}Z_{01}Z_{02}}$
$S_{22} = \frac{(1 + Y_{11}Z_{01})(1 - Y_{22}Z_{02}) + Y_{12}Y_{21}Z_{01}Z_{02}}{(1 + Y_{11}Z_{01})(1 + Y_{22}Z_{02}) - Y_{12}Y_{21}Z_{01}Z_{02}}$	$Y_{22} = \frac{(Z_{01}^* + S_{11}Z_{01})(1 - S_{22}) + S_{12}S_{21}Z_{01}Z_{02}}{(Z_{01}^* + S_{11}Z_{01})(Z_{02}^* + S_{22}Z_{02}) - S_{12}S_{21}Z_{01}Z_{02}}$
$S_{11} = \frac{(h_{11} - Z_{01}^*)(1 + h_{22}Z_{02}) - h_{12}h_{21}Z_{02}}{(Z_{01} + h_{11})(1 + h_{22}Z_{02}) - h_{12}h_{21}Z_{02}}$	$h_{11} = \frac{(Z_{01}^* + S_{11}Z_{01})(Z_{02}^* + S_{22}Z_{02}) - S_{12}S_{21}Z_{01}Z_{02}}{(1 - S_{11})(Z_{02}^* + S_{22}Z_{02}) + S_{12}S_{21}Z_{02}}$
$S_{12} = \frac{2h_{12}(R_{01}R_{02})^{1/2}}{(Z_{01} + h_{11})(1 + h_{22}Z_{02}) - h_{12}h_{21}Z_{02}}$	$h_{12} = \frac{2S_{12}(R_{01}R_{02})^{1/2}}{(1 - S_{11})(Z_{02}^* + S_{22}Z_{02}) + S_{12}S_{21}Z_{02}}$
$S_{21} = \frac{-2h_{21}(R_{01}R_{02})^{1/2}}{(Z_{01} + h_{11})(1 + h_{22}Z_{02}) - h_{12}h_{21}Z_{02}}$	$h_{21} = \frac{-2S_{21}(R_{01}R_{02})^{1/2}}{(1 - S_{11})(Z_{02}^* + S_{22}Z_{02}) + S_{12}S_{21}Z_{02}}$
$S_{22} = \frac{(Z_{01} + h_{11})(1 - h_{22}Z_{02}) + h_{12}h_{21}Z_{02}}{(Z_{01} + h_{11})(1 + h_{22}Z_{02}) - h_{12}h_{21}Z_{02}}$	$h_{22} = \frac{(1 - S_{11})(1 - S_{22}) - S_{12}S_{21}}{(1 - S_{11})(Z_{02}^* + S_{22}Z_{02}) + S_{12}S_{21}Z_{02}}$
$S_{11} = \frac{AZ_{02} + B - CZ_{01}Z_{02} - DZ_{01}^*}{AZ_{02} + B + CZ_{01}Z_{02} + DZ_{01}}$	$A = \frac{(Z_{01}^* + S_{11}Z_{01})(1 - S_{22}) + S_{12}S_{21}Z_{01}}{2S_{21}(R_{01}R_{02})^{1/2}}$
$S_{12} = \frac{2(AD - BC)(R_{01}R_{02})^{1/2}}{AZ_{02} + B + CZ_{01}Z_{02} + DZ_{01}}$	$B = \frac{(Z_{01}^* + S_{11}Z_{01})(Z_{02}^* + S_{22}Z_{02}) - S_{12}S_{21}Z_{01}Z_{02}}{2S_{21}(R_{01}R_{02})^{1/2}}$
$S_{21} = \frac{2(R_{01}R_{02})^{1/2}}{AZ_{02} + B + CZ_{01}Z_{02} + DZ_{01}}$	$C = \frac{(1 - S_{11})(1 - S_{22}) - S_{12}S_{21}}{2S_{21}(R_{01}R_{02})^{1/2}}$
$S_{22} = \frac{-AZ_{02}^* + B - CZ_{01}Z_{02} + DZ_{01}}{AZ_{02} + B + CZ_{01}Z_{02} + DZ_{01}}$	$D = \frac{(1 - S_{11})(Z_{02}^* + S_{22}Z_{02}) + S_{12}S_{21}Z_{02}}{2S_{21}(R_{01}R_{02})^{1/2}}$

(c) 1994 IEEE

Appendix Fig. C.2. Table taken from [50] showing the conversion from 2-port scattering parameters only to all other parameters, accounting for different characteristic impedances on port 1 and port 2. (Reprinted with permission from IEEE).

## Appendix D : In-house transfer relation measurement system



Appendix Fig. D.1. In-house built setup for measuring the transfer relation of a DUT.

The transfer relation, as used in this dissertation, is defined as the voltage amplitude at port 2 divided by the voltage amplitude at port 1.

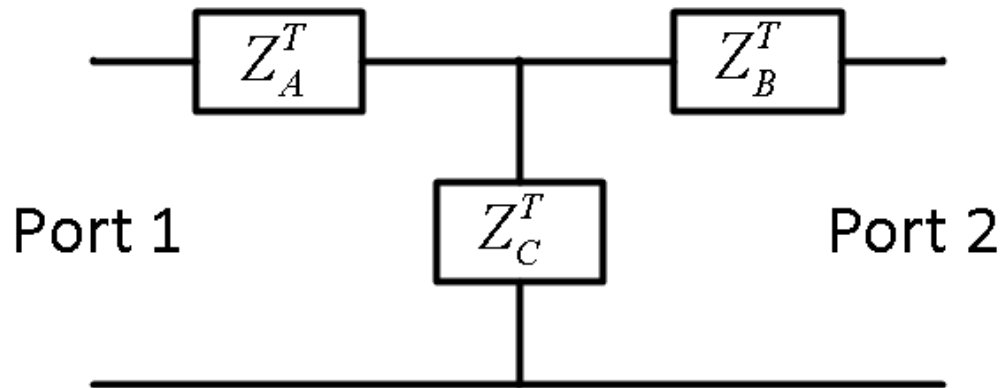
At a high level, the setup of Appendix Fig. D.1 operates as follows. The controlling computer sets the frequency of the function generator and measures the port 1 and port 2 voltages from the oscilloscope. This data is instantly plotted but also is stored for later analysis. The oscilloscope channels are  $1\text{M}\Omega$  terminated.

There are also some subtle issues that must be accounted for when using the system. The function generator is designed to drive a  $50\Omega$  matched system. To accomplish this, the  $50\Omega$  internal source resistance is taken into account and the real voltage source value is scaled such that the nominal voltage (the voltage set by the computer) appears at the output. However, the

impedance of the DUT is unknown, so the output voltage will change with changing DUT impedance. To account for this, the nominal voltage is not trusted, but the port 1 voltage is measured for direct use.

Another issue is measuring the low frequency behavior of a device. At low frequency, a transformer DUT has very low input impedance but also low transmission. The voltages at port 1 and port 2 are very small, even at maximum generator output. As a result, the signal to noise ratio is very small. When the noisy voltages are divided, the noise compounds to an even noisier quotient. To get the most precise measurement, the oscilloscope math channels are used to average the signal for a specified number of sweeps to reduce random noise on the signal. Also, with the small voltages at low frequencies, the oscilloscope loses the ability to properly autose. Thus, initially, the computer assumes quasi manual control by setting the timebase to correspond to the proper frequency and monitoring the signal amplitudes. When the amplitudes are large enough for autose to work properly, quasi-manual control is automatically turned off and the oscilloscope autose function determines the voltage and time scales.

## Appendix E : Formation of T-type and $\pi$ -type equivalent circuits



Appendix Fig. E.1. T-type equivalent circuit

To convert the measured impedance parameters to the T-type equivalent circuit, the conditions of the measured impedance parameters are applied to the circuit and the port impedances are compared in equations. Fundamentally, the port impedances of the circuit model must be the same as the measured impedances. It is shown by equations E.3 and E.4 that the T-type equivalent circuit is only valid if the device is reciprocal ( $Z_{12} = Z_{21}$ ).

$$Z_{11} = \left. \frac{V_1}{I_1} \right|_{I_2=0} = Z_A^T + Z_C^T \quad \text{E.1}$$

$$Z_{22} = \left. \frac{V_2}{I_2} \right|_{I_1=0} = Z_B^T + Z_C^T \quad \text{E.2}$$

$$Z_{12} = \left. \frac{V_1}{I_2} \right|_{I_1=0} = Z_C^T \quad \text{E.3}$$

$$Z_{21} = \left. \frac{V_2}{I_1} \right|_{I_2=0} = Z_C^T \quad \text{E.4}$$

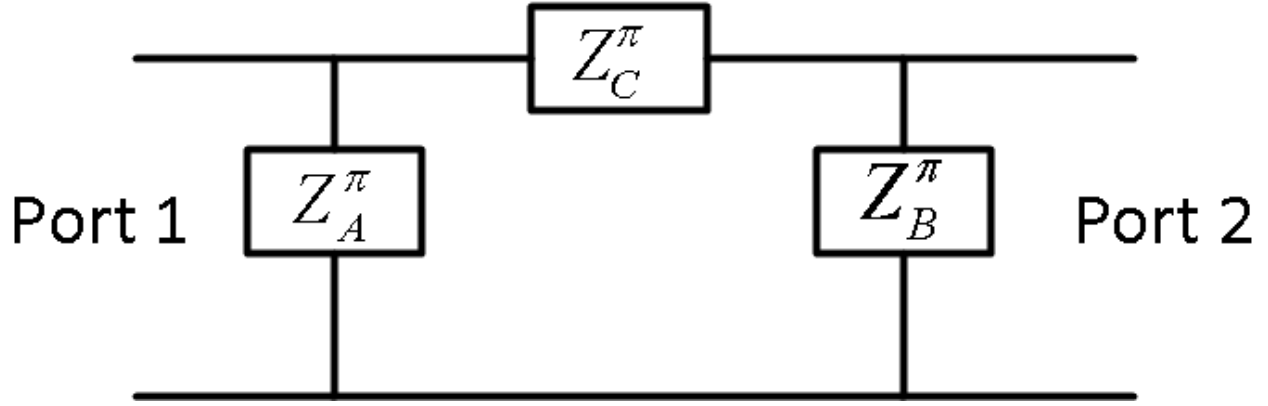
By manipulating the above equations, the values of the equivalent circuit impedances can be found from the measured impedance values.

$$Z_A^T = Z_{11} - Z_C^T = Z_{11} - Z_{12} \quad \text{E.5}$$

$$Z_B^T = Z_{22} - Z_C^T = Z_{22} - Z_{12} \quad \text{E.6}$$

$$Z_C^T = Z_{12} = Z_{21} \quad \text{E.7}$$

Consider now, the  $\pi$ -type equivalent circuit. For reasons of simpler arithmetic, the  $\pi$ -type equivalent circuit will be considered as admittances. The measured device will also be assumed to be reciprocal.



Appendix Fig. E.2.  $\pi$ -type equivalent circuit.

$$Y_{11} = \left. \frac{I_1}{V_1} \right|_{V_2=0} = Y_A^T + Y_C^T \quad \text{E.8}$$

$$Y_{22} = \left. \frac{I_2}{V_2} \right|_{V_1=0} = Y_B^T + Y_C^T \quad \text{E.9}$$

$$Y_{12} = \left. \frac{I_1}{V_2} \right|_{V_1=0} = \frac{-V_2 Y_C^T}{V_2} = -Y_C^T \quad \text{E.10}$$

$$Y_{21} = \left. \frac{I_2}{V_1} \right|_{V_2=0} = \frac{-V_1 Y_C^T}{V_1} = -Y_C^T \quad \text{E.11}$$

Manipulating the above equations gives the equivalent circuit admittance parameters in terms of the measured device admittances.

$$Y_A^T = Y_{11} - Y_C^T = Y_{11} - Y_{12} \quad \text{E.12}$$

$$Y_B^T = Y_{22} - Y_C^T = Y_{22} - Y_{12} \quad \text{E.13}$$

$$Y_C^T = -Y_{12} = -Y_{21} \quad \text{E.14}$$

## Bibliography

1. **Spurgeon, C.** *Ethernet: The Definitive Guide*. O'Reilly, 2000.
2. **Morrison, R.** *Grounding and Shielding Circuits and Interfaces*. IEEE Press, John Wiley and Sons, 2007.
3. **Ferrero, A.** *Eternal Ethernet*. Addison-Wesley, 1999.
4. **Jackson, M.** CAT5 UTP Copper is not yet dead! [Online] 2003.  
<http://www.pulseelectronics.com/download/3125/g205>.
5. **Ulaby, Fawwaz.** *Fundamentals of Applied Electromagnetics*. Pearson, Prentice Hall, 2004.
6. **Mayergoyz, I. D. Lawson, W.** *Basic Electric Circuit Theory*. Academic Press, 1997.
7. **Cheng, D.** *Field and Wave Electromagnetics, 2nd ed.* Addison Wesley , 1989.
8. **Chikazumi, Soshin.** *Physics of Magnetism*. John Wiley and Sons, Inc., 1964.
9. **Matsch, L. W.** *Electromagnetic and Electromechanical Machines*. 2nd. , Harper and Row Publishers, 1977.
10. **Young, Hugh. Freedman, Roger.** *University Physics*. San Francisco, Pearson, Addison Wesley, 2004.
11. **Mohan, N. Undeland, T. Robbins, W.** *Power Electronics*. , John Wiley and Sons, Inc, 2003.
12. **de Lacheisserie, E. Gignoux, D. Schlenker, M.** *Magnetism Fundamentals*. New York, Springer Science, 2005.
13. **Huang, R. Zhang, D.** Experimentally Verified Mn-Zn Ferrites' Intrinsic Complex Permittivity and Permeability Tracing Technique Using Two Ferrite Capacitors. *IEEE Transactions on Magnetics*. 2007, Vol. 43, 3, pp. 974-981.
14. **Bowen, D. Mayergoyz, I. Zhang, Z. McAvoy, P. Krafft, C. Kroop, D.** Modeling and testing of Ethernet Transformers. *IEEE Transactions on Magnetics*. 2009, Vol. 45, 10, p. 4793.
15. **Biernacki, J. Czarkowski, D.** High Frequency Transformer Modeling. *IEEE Transactions on Power Delivery*. 1993, Vol. 8, 3, pp. 1615-1626.

16. *Stray Capacitances of Two Winding Transformers: Equivalent Circuit, Measurements, Calculation and Lowering*. **Blache, F. Keradec, J.P. Cogitore, B.** 1994. Conference Record of the Industry Applications Society Annual Meeting. pp. 1211-1217.
17. *Comparison of Experimental Techniques for the Determination of Stray Capacitances in High Frequency Transformers*. **Lu, H. Y. Ramsden, V.S.** 2000. Power Electronics Specialists Conference. Vol. 3, pp. 1645-1650.
18. *The Two Winding Ferrite Core Transformer: An Experimental Method to Obtain A Wide Frequency Range Equivalent Circuit*. **Cogitore, B. Keradec, J.P. Barbaroux, J.** Conference Record., IEEE, 1993. Instrumentation and Measurement Technology Conference. pp. 558-561.
19. **Martinez, J. Mork, B.** Transformer Modeling for Low- and Mid-Frequency Transients- A Review. *IEEE Transactions on Power Delivery*. Vol. 20, 2, pp. 1625-1631.
20. **Huang, R. Zhang, D.** Using a Single Toroidal Sample to Determine the Intrinsic Complex Permeability and Permittivity of Mn–Zn Ferrites. *IEEE Transactions on Magnetics*. 2007, Vol. 43, 10, pp. 3807-3815.
21. *Effect of high Permittivity and Core Dimensions on the Permeability Measurement for Mn-Zn Ferrite Cores Used in High-Frequency Transformer*. **Zhang, D. Tseng, K.J.** 2006. IEEE International Workshop on Electronic Design, Test and Applications.
22. **Itoh, S. Yamamoto, Y. Makino, A. Yamaguchi, T. Sasada, I.** A Low Profile Type High Frequency Transformer Using A fine Grained Mn-Zn Ferrite. 1998, Vol. 2, pp. 1492-1498.
23. **Ribbenfjård, D.** *A lumped element transformer model including core losses and winding impedances*. Stockholm, Sweden, Licentiate thesis in Electromagnetic Engineering, KTH , 2007.
24. **Bowen, D. Mayergoyz, I. Krafft, C. Kroop, D. Beyaz, M.** On design of air-core Ethernet transformers. *Journal of Applied Physics*. 2009, Vol. 105, p. 07A307.
25. *IEEE Standard for Information Technology--Telecommunications and Information Exchange Between Systems--Local and Metropolitan Area Networks--Specific Requirements Part 3: Carrier Sense Multiple Access With Collision Detection (CSMA/CD) Access Method and P*. IEEE Standard 802.3, 2008.
26. **Hamidy, F.** Designing magnetics for 10-Gbit Ethernet. *EE Times*. [Online]
27. *Gigabit Ethernet (1000Base-T) H5007 Performance Data, G021.B*. Pulse, A Technitrol Company Published documents, 2000.
28. **Pozar, David.** *Microwave Engineering*. John Wiley and Sons, 2005.

29. **Bowen, D. Mayergoyz, I. Krafft, C.** Fabrication and Testing of a MEMS Type Dielectric Core Ethernet Transformer. *Journal of Applied Physics*. 2011.
30. **Jackson, M.** Understanding Common Mode Noise. [Online] 1999.  
<http://www.pulseelectronics.com/download/3100/g019>.
31. **Bowen, D. Mayergoyz, I. Krafft, C.** Testing and Analysis of Common Mode Characteristics of Ethernet Transformers. *Journal of Applied Physics*. 2011.
32. **Yun, E. Jung, M. Cheon, C. Nam, H.G.** Microfabrication and Characteristics of Low-Power High performance Magnetic Thin-Film Transformers. *IEEE Transactions on Magnetics*. 2004, Vol. 40, 1, pp. 65-70.
33. **Wong, F. Lu, J.** High Frequency Planar Transformer with Helical winding Structure. 2000, Vol. 36, 5, pp. 3524-3526.
34. **Liakopoulos, T. Ahn, C.** 3-D Microfabricated Toroidal Planar Inductors with Different Magnetic Core Schemes for MEMs and Power Electronic Applications. *IEEE Transactions on Magnetics*. 1999, Vol. 35, 5, pp. 3679-3681.
35. **Xu, M. Liakopoulos, T. Ahn, C.** A Microfabricated Transformer for High Frequency Power or Signal Conversion. *IEEE Transactions on Magnetics*. 1998, Vol. 34, 4, pp. 1369-1371.
36. **O'Donnel, T. Brunet, M. McCloskey, P. O'Brien, J. Mathuna, S.** Microtransformers and Inductors using Permalloy Thin Films. *Preparation, Properties, and Applications of Thin ferromagnetic Films*. pp. 45-52.
37. **Hayano, S. Nakajima, Y. Saotome, H. Saito, Y.** A New Type High Frequency Transformer. *IEEE Transactions on Magnetics*. 1991, Vol. 27, 6, pp. 5205-5207.
38. **Plonus, M.** *Applied Electromagnetics*. McGraw Hill, 1978.
39. **Veyres, C. Hanna, V.** Extension of the application of conformal mapping techniques to coplanar lines with finite dimensions. *International Journal of Electronics*. 1980, Vol. 48, 1, pp. 47-56.
40. **Ramo, S. Whinnery, J. Van Duzer, T.** *Fields and Waves in Communication Electronics*. 3rd. John Wiley and Sons, 1994.
41. **Appleyard, E. T. S.** The Structure of Evaporated Metal Films and Their Optical Properties. *Proceedings of the Physical Society*. 1937, Vol. 49, p. 118.
42. **Sullivan, C. Sanders, S.** Design of microfabricated transformers and inductors for high-frequency power conversion. *IEEE Transactions on Power Electronics*. 1996, Vol. 11, 2, p. 228.

43. **Gradsteyn, I.S., Ryzhik, I.M.** *Table of Integrals, Series, and Products*. 6th. San Diego, Academic Press, Elsevier, 2000.
44. **Hackborn, Richard A.** An Automatic Network Analyzer System. *Microwave Journal*. 1968, Vol. 11, 5.
45. **Kerns, David M., Beatty, Robert W.** *Basic Theory of Waveguide Junctions and Introductory Microwave Network Analysis*. , Pergamon Press, 1967.
46. **Hand, B. P.** Developing Accuracy Specifications for Automatic Network Analyzer Systems. *Hewlett-Packard Journal*. 1970, February.
47. **Kruppa, W., Sodomsy, K.** An Explicit Solution for the Scattering Parameters of a Linear Two-Port Measured with an Imperfect Test Set. *IEEE Transactions On Microwave Theory and Techniques*. 1971, Vol. 19, 1.
48. **Rehmark, Stig.** On the Calibration Process of Automatic Network Analyzer Systems. *IEEE Transactions on Microwave Theory and Techniques* . 1974, Vol. 22, 4.
49. **Rytting, Doug.** Network Analyzer Error Models and Calibration Methods. [Online] <http://www.cpd.ogi.edu/IEEE-MTT-ED/Network%20Analyzer%20Error%20Models%20and%20Calibration%20Methods.pdf>.
50. **Frickey, Dean A.** Conversions Between S, Z, Y, h, ABCD, and T, parameters which are Valid for Complex Source and Load Impedances. *IEEE Transactions on Microwave Theory and Techniques*. 1994, Vol. 42, 2.